



The
University
Of
Sheffield.

Department
Of
Mechanical
Engineering.

Analysis of the Premature Failure of Wind Turbine Gearbox Bearings

**A thesis submitted in partial fulfilment of the
requirements for the degree of
Doctor of Philosophy**

Author:

Tom Bruce

Supervisors:

Dr. Hui Long

Prof. Rob Dwyer-Joyce

04/06/2016

ABSTRACT

Wind turbine gearbox bearings are the component that leads to the most downtime of operating wind turbines due to their high failure rates. Failures occur within 10 % of bearing design life, despite the fact that they are designed to the same bearing standards that satisfactorily predict bearing lifetime in many other industrial applications. No theory has yet been widely accepted to explain the reasons for this premature failure, despite intensive research effort and many theories have been suggested both from industrial and academic researchers alike. The most widely accepted theory at the current time is that the bearing subsurface is weakened by what have been termed as *white etching cracks* that eventually lead to material removal from the bearing contact surfaces.

Extreme loading conditions caused by a number of possible sources, which expose bearings to higher than designed contact pressures and surface traction in wind turbine operation, are investigated throughout this project. A dynamic model of a wind turbine gearbox was developed in order to calculate bearing contact stresses during transient operating conditions, which found that bearings were loading to above recommended values, even during normal operating conditions. A failed bearing from a wind turbine gearbox was then destructively investigated, leading to the conclusion that manganese sulphide inclusions were the primary cause of white etching crack initiation. These inclusions were investigated in greater detail to determine the geometry and depth of the most damaging inclusions, both in the failed bearing and on bench top test rigs. A series of hammering impact test and rolling contact fatigue tests were designed and led to the successful recreation of white etching cracks in test specimens. It was found that white etching cracks certainly initiate at MnS inclusions. These microcracks initiate due to a tensile load across inclusion tips, which are thought to be further propagated by shear loading along the cracks. Inclusion initiated microcracks have been found to develop into white etching cracks, which may link up and weaken the subsurface of bearing raceways sufficiently to cause eventual failure. Testing is carried out to find thresholds in terms of contact pressure, surface traction, impact and fatigue loading cycles, required for the formation of white etching cracks.

The key contributions of this study are identification and recreation of four different types of subsurface damage at MnS inclusions by examining a failed WTGB and carrying out testing using a reciprocating hammering impact rig and a rolling contact fatigue twin disc machine. A hypothesis of the order and mechanism of these damage events is proposed in this study, as well as the development of testing methods to investigate the damage in order to support the hypotheses. Test methods are also developed to investigate the effects of some key bearing loading parameters, including impact loading, levels of contact pressure, surface traction and number of load cycles.

CONTENTS

ABSTRACT	i
CONTENTS	ii
LIST OF TABLES	vi
LIST OF FIGURES	vii
PUBLICATIONS AND PRESENTATIONS	xii
ABBREVIATIONS.....	xiii
NOMENCLATURE	xiv
ACKNOWLEDGEMENTS.....	xvi
1. INTRODUCTION	1
1.1. Justification of research.....	1
1.2. Aims and objectives of this study	1
1.3. Structure of thesis	2
1.4. Key novelty points and contributions.....	4
2. LITERATURE REVIEW.....	5
2.1. Wind turbine gearbox bearings and their operating conditions.....	6
2.1.1. Wind turbine gearboxes	6
2.1.2. Wind turbine gearbox bearings	7
2.1.3. Stresses induced during rolling contact fatigue	10
2.1.4. Bearing life rating	19
2.1.5. Rolling element bearing failure modes	21
2.1.6. Bearing lubrication	24
2.2. Bearing steel	27
2.2.1. Shaping into bearing rings	27
2.2.2. Heat treatment and resulting microstructure	28
2.2.3. Microstructural changes during long term rolling contact fatigue	30
2.2.4. Inclusions in bearing steel	31
2.2.5. Manganese sulphide (MnS) inclusions	32
2.2.6. Residual Stress.....	33
2.3. White etching microstructural change and features	34
2.3.1. Butterflies	38
2.3.2. White etching cracks	40
2.3.3. Dark etching regions and white etching bands	40
2.3.4. White etching layers.....	41
2.3.5. Factors affecting the development of WECs	41
2.3.6. Laboratory tests to recreate white etching microstructure.....	46
2.4. Dynamic modelling of wind turbine gearboxes.....	47
2.4.1. Rotating machine dynamics	47
2.4.2. Modelling strategies	48
2.4.3. Key findings from previous modelling studies.....	49

2.4.4.	Generator modelling methods.....	50
2.5.	Summary of findings from the literature	51
2.5.1.	Bearing life rating.....	51
2.5.2.	The effect of inclusions	51
2.5.3.	The effect of hydrogen.....	52
2.5.4.	Summary of factors leading to white etching crack formation	52
2.5.5.	WEC failure mechanism hypotheses.....	53
3.	DYNAMIC MODELLING OF WIND TURBINE GEARBOX BEARING LOADING DURING TRANSIENT EVENTS.....	57
3.1.	Development of a dynamic WTG model using VALDYN	58
3.1.1.	Mass and inertias of gearbox components.....	59
3.1.2.	Displacement of gearbox components	60
3.1.3.	Bearings.....	60
3.1.4.	Gears	62
3.1.5.	Shafts.....	63
3.1.6.	Planetary carrier.....	65
3.1.7.	Splined sun shaft connection	65
3.1.8.	Generator resistance torque.....	65
3.1.9.	Gearbox casing and elastomer supports	65
3.1.10.	Disc braking	66
3.1.11.	Maximum Hertzian contact stress calculation.....	66
3.2.	Application to the NREL750 kW WTG	67
3.2.1.	Model validation	68
3.2.2.	Torque loading	71
3.3.	Results from simulated model and analysis	72
3.3.1.	Normal operation.....	72
3.3.2.	Shut-down.....	74
3.3.3.	Maximum Hertzian contact stresses.....	76
3.4.	Discussion.....	76
3.5.	Summary	78
4.	PROCEDURE FOR EXPERIMENTAL AND METALLURGICAL INVESTIGATIONS	79
4.1.	Specimen metallurgical preparation.....	80
4.2.	Observation of specimens	83
4.2.1.	Optical Microscopy	83
4.2.2.	Scanning Electron Microscopy	83
4.2.3.	Surface profile measurements.....	84
4.2.4.	Nano-hardness measurements.....	85
4.3.	Destructive investigation of a failed planetary bearing.....	85
4.3.1.	Inspection of surface damage and location of prepared specimens.....	86
4.3.2.	Observation of WTGB microstructure	88

CONTENTS

4.3.3.	Illustration of undamaged inclusions	90
4.3.4.	Damage initiating MnS inclusion database	90
4.4.	Hammering impact testing of 100CrMo7-3 bearing steel.....	91
4.4.1.	Apparatus	91
4.4.2.	Technical analysis of rig.....	93
4.4.3.	Specimens.....	94
4.4.4.	Test design using FEA	97
4.4.5.	Testing procedure.....	100
4.5.	Twin disc testing of 100Cr6 bearing steel.....	102
4.5.1.	Equipment	102
4.5.2.	Operation of SUROS rig	104
4.5.3.	Specimens.....	105
4.5.4.	Testing procedure.....	108
4.5.5.	Lubrication of specimens.....	109
4.6.	Summary.....	112
5.	RESULTS FROM THE DESTRUCTIVE INVESTIGATION OF A FAILED WIND TURBINE GEARBOX BEARING	113
5.1.	Observed subsurface damage	114
5.1.1.	Distinction of “butterfly” and WEC initiating inclusions.....	115
5.1.2.	Subsurface inclusion-initiated WEC formation.....	120
5.1.3.	Oxide parts within MnS inclusions	123
5.1.4.	Detailed examination of inclusion initiated WEC.....	126
5.1.5.	Additional extended WEC networks.....	127
5.1.6.	Other interesting damage features	129
5.1.7.	Damage initiation and propagation at MnS inclusions	131
5.2.	Analysis of inclusion database.....	133
5.2.1.	Relationship between damage types at MnS inclusions	133
5.2.2.	Variation of MnS inclusion initiated damage with depth.....	134
5.2.3.	Variation of WEC length with MnS inclusion orientation angle	135
5.2.4.	Variation of WEC length with MnS inclusion length.....	136
5.3.	Summary.....	137
6.	RESULTS FROM HAMMERING IMPACT TESTING OF 100CrMo7-3 BEARING STEEL.....	138
6.1.	Initial observations	139
6.2.	Test 1: Varying number of impacts at contact stress of 2.60 GPa.....	141
6.3.	Test 2: Varying level of contact stress	142
6.4.	Test 3: Varying number of impacts at contract stress 2.48 GPa	143
6.5.	Identification of damage thresholds	144
6.6.	Test 3: Long term tests	145
6.7.	Summary.....	149

7. RESULTS FROM TWIN DISC ROLLING CONTACT FATIGUE TESTING OF 100Cr6 BEARING STEEL	150
7.1. Non-destructive examination of the specimens.....	151
7.2. Summary of types of damage found.....	152
7.2.1. Subsurface initiated cracks	152
7.2.2. Surface initiated cracks	154
7.2.3. Separation and cracking at manganese sulphide inclusions.....	155
7.2.4. WEAs and WECs at manganese sulphide inclusions	157
7.2.5. White etching layer in failed test	161
7.3. Identification of damage initiating condition thresholds	164
7.4. Depth of WEA damage.....	166
7.5. Summary	167
8. CONCLUSIONS AND FURTHER WORK	169
8.1. Conclusions	170
8.1.1. Conclusions from the dynamic modelling of a 750 kW wind turbine gearbox.	170
8.1.2. Conclusions from the destructive sectioning of a failed planetary bearing	171
8.1.3. Conclusions from the hammering impact testing of 100CrMo7-3 bearing steel ...	172
8.1.4. Conclusions from the twin disc testing of 100Cr6 bearing steel	172
8.2. Summary of research novelty and key contributions	173
8.3. Further work	175
8.3.1. Possible research in relation to improving bearing steel.....	175
8.3.2. Possible research relating to mechanically redesigning WTGBs	175
REFERENCES.....	177
9. APPENDICES	190
Appendix A: Failure mode matrix (SKF field experience)	190
Appendix B: VALDYN WTG model illustration.....	194
Appendix C: Values used to model NREL 750 kW gearbox	195
Appendix D: Example shaft damping calculations using FEA	198
Appendix E - 600 kW gearbox information	200
Appendix F: SUROS sample wear tracks.....	206

LIST OF TABLES

Table 2-1: Approximate operating speeds for bearings in a typical WTG [12]	7
Table 2-2: Estimated number of revolutions and stress cycles experienced per year for typical WTGBs.	10
Table 2-3: Shear stress loading extremities in rolling contact	16
Table 2-4: Chemical composition of commonly used bearing steels	27
Table 2-5: Physical properties of commonly used bearing steels	27
Table 2-6: Grouping of inclusion types found in steel.....	31
Table 2-7: Physical properties of selected inclusions in steel	32
Table 2-8: Clarification of the different stages and forms of the white etching microstructural stage in steel.....	37
Table 3-1: Comparison of model types 1-3 to proposed gearbox model.....	58
Table 3-2: Parameters of VALDYN model of NREL 750 kW wind turbine gearbox	67
Table 3-3: Maximum bearing contact stresses during normal operation	76
Table 3-4: Maximum bearing contact stresses during shut-down.....	76
Table 4-1: Preparation process for specimen observation	82
Table 4-2: Operating conditions of sectioned bearing	86
Table 4-3: WTGB specimens prepared for metallographic observation	88
Table 4-4: Elements present in WTGB from EDAX analysis.....	88
Table 4-5: Spring stiffnesses used in hammering impact testing.....	94
Table 4-6: Chemical composition of 100CrMo7-3 specimens used during testing.....	95
Table 4-7: Mechanical properties of specimens [18] and impact steel balls used during testing	95
Table 4-8: Procedure for normal hammering impact testing.....	101
Table 4-9: Chemical composition of twin disc specimens. *Carbon value approximate.	106
Table 4-10: Fixed test conditions.....	108
Table 4-11: Variable test conditions showing positions of maximum shear and equivalent stress	109
Table 4-12: Mean traction coefficients during each test	112
Table 5-1: Summary of sectioned specimens and damage found	115
Table 5-2: Nano hardness results for steel matrix and WEC.....	118
Table 5-3: Mean volume percentage of major detected elements in Bakelite EDAX scan.....	125
Table 7-1: Mass loss from raceway disc specimens during twin disc testing.....	151
Table 9-1: Mass and inertia properties of gearbox components.	195
Table 9-2: Bearing stiffness and damping properties.....	195
Table 9-3: Gear tooth contact stiffness and damping properties	196
Table 9-4: Shaft properties.....	196
Table 9-5: Shaft critical damping fraction calculation results	199

LIST OF FIGURES

Figure 1-1: Thesis work flow chart.....	2
Figure 2-1: Thesis work flow chart.....	5
Figure 2-2: Typical WT drivetrain.....	6
Figure 2-3: Typical gearbox schematic.....	7
Figure 2-4: Failed planetary bearing inner raceways from a 600 kW turbine	8
Figure 2-5: Direction of maximum forceacting on planetary gears from WT input torque	9
Figure 2-6: Typical <i>S-N</i> curve for steel	11
Figure 2-7: Static Hertzian line contact.....	12
Figure 2-8: Subsurface Hertzian stress field for static line contact of two steel cylinders	14
Figure 2-9: Stresses experienced by a point moving through a Hertzian stress field	16
Figure 2-10: Effect of traction force (F_T) on cracks	18
Figure 2-11: The effects of surface traction on the subsurface stress field	18
Figure 2-12: Traction coefficient (μ_T) with increasing slip (slide/roll ratio)	19
Figure 2-13: Stribeck curve illustrating lubrication regimes	25
Figure 2-14: Elastohydrodynamic pressure distribution.....	26
Figure 2-15: Bearing steel microstructure.....	29
Figure 2-16: Reduction in plastic strain in martensitic bearing steel with increasing number of loading cycles (adapted from [23])	30
Figure 2-17: Residual stress concentrations around spherical inclusions	34
Figure 2-18: Timeline showing approximate number of cycles that butterflies, DERs and WEBs appear showing L10 and L50 lifetimes.....	36
Figure 2-19: Butterfly formation in wind turbine gearbox bearings.....	38
Figure 2-20: Butterfly initiation threshold in terms of depth and contact pressure	40
Figure 2-21: Modes of loading affecting crack initiation and growth.....	45
Figure 2-22: Simple induction generator resistance torque curve	50
Figure 2-23: Thévenin-equivalent-induction-generator torque/speed curve	51
Figure 2-24: Factors affecting WEC formation in WTGBs	52
Figure 2-25: Importance of surface traction.....	53
Figure 2-26: Equivalent stress concentrations around a hole	54
Figure 2-27: Unidirectional shear stress concentrations around a hole.....	54
Figure 2-28: Orthogonal shear stress concentrations around a hole	54
Figure 2-29: Importance of the order of loading events	55
Figure 3-1: Thesis work flow chart.....	57
Figure 3-2: Wind turbine drivetrain schematic and coordinate system used	59
Figure 3-3: Gearbox model viewed in VALDYN kinetic simulation interface.....	68
Figure 3-4: Validation of model in comparison to partners A-F	70
Figure 3-5: Input torque for normal operation and shutdown events.....	71
Figure 3-6: LSS and HSS velocity during normal operation.....	72

LIST OF FIGURES

Figure 3-7: Resultant forces acting on bearings roller/raceway contacts during normal operation	73
Figure 3-8: LSS and HSS velocity during shut-down	74
Figure 3-9: Resultant forces acting on planetary bearings roller/raceway contacts during shut-down	75
Figure 4-1: Thesis work flow chart	79
Figure 4-2: Specimen preparation summary	80
Figure 4-3: Examples of prepared specimens	81
Figure 4-4: Microscopes used in this study	84
Figure 4-5: Sectioned planetary bearing exploded schematic	85
Figure 4-6: Photographs of raceway damage	87
Figure 4-7: Bearing steel microstructure highlighting spheroidal carbides	89
Figure 4-8: EDAX spectrum showing chemical composition of MnS inclusion	89
Figure 4-9: Examples of undamaged inclusions at depths of greater than 5 mm	90
Figure 4-10: Measurements made for each damage initiating inclusion in the database	91
Figure 4-11: Modified impact test rig a) standard setup b) angled striker setup for compound impact testing	92
Figure 4-12: Illustration of surface sliding induced by angled contact	92
Figure 4-13: Impact velocity (U) at different impact frequencies (0-11 Hz) for the impact test rig	93
Figure 4-14: Moments taken about impact rig pivot	94
Figure 4-15: Orientation of MnS inclusions in specimens	96
Figure 4-16: Typical MnS inclusions in undamaged specimen	96
Figure 4-17: Identification of MnS-type inclusions	96
Figure 4-18: Plastic strain amplitude vs. stress for 100Cr6 steel	97
Figure 4-19: Boundary conditions restraining model	99
Figure 4-20: Mesh around the point of impact	99
Figure 4-21: Equivalent stress distribution for 0.4 m/s impact velocity	100
Figure 4-22: SUROS test rig schematic	103
Figure 4-23: Twin disc testing specimen position	104
Figure 4-24: Twin disc testing specimen dimensions	106
Figure 4-25: Positions of pre-seeded impact damage	107
Figure 4-26: Stribeck curve showing approximate friction (traction) coefficient during boundary and mixed lubrication regimes	111
Figure 4-27: Example traction coefficient readout from SUROS rig	112
Figure 5-1: Thesis work flow chart	113
Figure 5-2: Spalling on the raceway surface in Zone 2	114
Figure 5-3: Inclusion orientation in inner raceway	115
Figure 5-4: Series of butterflies and connected WECs in circumferential section	117
Figure 5-5: Examples of WEA-interacting MnS inclusions	119

Figure 5-6: Damage linked to MnS inclusions in axially sectioned specimens	120
Figure 5-7: Standalone WEC	120
Figure 5-8: Evidence supporting theory that Mode I loading caused crack initiation/propagation (circumferentially sectioned inclusions)	121
Figure 5-9: Evidence supporting subsurface crack and WEA initiation at MnS inclusions	122
Figure 5-10: MnS inclusion and adjacent separation from the steel matrix with EDAX of features	123
Figure 5-11: Internally cracked MnS inclusion initiated cracks with no interacting oxide part at inclusion tip (axially sectioned inclusions)	124
Figure 5-12: Evidence suggesting internal cracking of MnS inclusions is not necessary (inclusions do not appear to have oxide parts near inclusion tips)	124
Figure 5-13: EDAX analysis of separated areas adjacent to inclusion	125
Figure 5-14: MnS inclusion initiated WEA detail	126
Figure 5-15: Extended surface breaking WEC network (circumferential section, phase 2 damage)	127
Figure 5-16: Large surface breaking, vertically propagating WEC (circumferential section, phase 2 damage)	128
Figure 5-17: Axially propagating crack surface linked crack deflection by MnS inclusion	129
Figure 5-18: Vertically propagating surface linked crack deflection by MnS inclusion	130
Figure 5-19: Crack propagation through an M ₃ C carbide	130
Figure 5-20: White etching layer attached to raceway surface	131
Figure 5-21: Damage initiation and propagation at MnS inclusions	132
Figure 5-22: Relationship between damage types	133
Figure 5-23: Variation of inclusion initiated damage with inclusion depth and depths of maximum stresses	135
Figure 5-24: Variation of mean and max WEC length with MnS inclusion depth in	135
Figure 5-25: Variation of mean and max WEC length with MnS inclusion orientation angle in	136
Figure 5-26: Variation of mean and max WEC length with MnS inclusion length in	136
Figure 6-1: Thesis work flow chart	138
Figure 6-2: Examples of damage initiation at MnS inclusions during initial tests	140
Figure 6-3: Depths of damage initiating inclusions found in initial impact tests	140
Figure 6-4: Examples of damage at MnS inclusions during varying number of impact tests ...	141
Figure 6-5: Depths of damage initiating inclusions found in varying number of impacts testing at 2.603 GPa	142
Figure 6-6: Example of damage at MnS inclusions during tests when subsurface stress was altered	142
Figure 6-7: Depths of damage initiating inclusions found in varying contact pressure impact tests	143
Figure 6-8: Examples of damage at MnS inclusions during varying number of impact tests ...	143

LIST OF FIGURES

Figure 6-9: Depths of damage initiating inclusions found in varying number of impacts testing at 2.477 GPa	144
Figure 6-10: Number of damaged inclusions for each test when subjected to various testing conditions	145
Figure 6-11: Example inclusions damaged under normal impact loading	146
Figure 6-12: Example inclusions damaged under sliding impact testing	147
Figure 6-13: Long term impact test damage initiating inclusion lengths and depths	148
Figure 7-1: Thesis work flow chart	150
Figure 7-2: Subsurface cracks beneath impact zone of specimen 11	153
Figure 7-3: Subsurface microcracks.....	154
Figure 7-4: Extended cracking	154
Figure 7-5: Surface cracking in specimen 11	155
Figure 7-6: Separation around MnS inclusions.....	155
Figure 7-7: Separation from inclusion tips spreading into surrounding material	156
Figure 7-8: Cracking from MnS inclusion tips.....	156
Figure 7-9: Internally cracked MnS inclusions.....	156
Figure 7-10: WEAs initiated at MnS inclusions.....	158
Figure 7-11: Damage at other inclusion types.....	159
Figure 7-12: Damage at carbides in specimen 8.....	160
Figure 7-13: Carbide related damage in SUROS specimens	161
Figure 7-14: Separation around carbides adjacent to MnS inclusions in SUROS specimens	161
Figure 7-15: Elongated carbides around separated and cracked MnS inclusion	161
Figure 7-16: Severely elongated separated carbide under impact zone.....	161
Figure 7-17: WEL formed in failed test.....	162
Figure 7-18: Cracking within WEL.....	163
Figure 7-19: Variation of carbide size within WEL.....	163
Figure 7-20: Contact pressure and slip (%) threshold identification for different forms of MnS inclusion initiated damage	164
Figure 7-21: Contact pressure and traction coefficient threshold identification for different forms of MnS inclusion initiated damage.....	165
Figure 7-22: Depths of WEA initiated in twin disc testing with comparison to depths of maximum stress concentrations	167
Figure 8-1: Thesis work flow chart	169
Figure 9-1: VALDYN model viewed on user interface	194
Figure 9-2: Generator resistance torque model used in dynamic model	197
Figure 9-4: ISS2 under radial load.....	198
Figure 9-3: ISS2 under torsional load	198
Figure 9-5: Torsional oscillation response of ISS2	199
Figure 9-6: Radial oscillation response of ISS2	199
Figure 9-7: Dimensions of a) inner raceway b) cylindrical roller	200

Figure 9-8: Image showing surface damage and clear transition from undamaged to damaged region	201
Figure 9-9: Image showing undamaged region	201
Figure 9-10: Epicyclic stage ring gear	202
Figure 9-11: Gearbox housing shaft bearing mounting positions	202
Figure 9-12: Outer race, cage and rolling elements of failed planetary gear bearing.....	203
Figure 9-13: Wear scars observed on cylindrical rollers	203
Figure 9-14: Smaller wear scars distributed over entire circumference of outer ring	203
Figure 9-15: Failed planetary gear	204
Figure 9-16: Low speed intermediate shaft.....	204
Figure 9-17: Planetary carrier	205
Figure 9-18: Wear tracks from SUROS discs 1-4	206
Figure 9-19: Wear tracks from SUROS discs 5-8	207
Figure 9-20: Wear tracks from SUROS discs 9-12	208
Figure 9-21: Wear track from failed test WEL producing SUROS disc	209

PUBLICATIONS AND PRESENTATIONS

Publications

T. Bruce, H. Long, R. S. Dwyer-Joyce, Dynamic modelling of wind turbine gearbox bearing loading during transient events, *IET Renewable Power Generation*, 9 (7), 2015, 821-830.

T. Bruce, E. Rounding, H. Long, R. S. Dwyer-Joyce, Characterisation of white etching crack damage in wind turbine gearbox bearings, *Wear*, 338-339, 2015, 164-177.

T. Bruce, H. Long, T. Slatter, R. S. Dwyer-Joyce, Formation of white etching cracks at manganese sulphide (MnS) inclusions in bearing steel due to hammering impact loading, *Wind Energy*, In Press, accepted 27.11.15.

T. Bruce, H. Long, R. S. Dwyer-Joyce, White etching crack initiation at manganese sulphide (MnS) inclusions in a wind turbine gearbox bearing, in *Proceedings of the 13th International Conference on Engineering Structural Integrity Assessment*, Manchester, 19-20 May, 2015, In press, accepted 21.04.15.

Presentations

"Failure analysis of Wind Turbine Gearbox Bearings" at *DOE/NREL Gearbox Reliability Collaborative (GRC) annual meeting*, Golden, CO, USA, 10-11 February 2014.

"Wind turbine gearbox loading during transient events" at *11th TriboUK Conference 2014*, Sheffield, 6-7 April 2014.

"White Etching Crack Initiation at Manganese Sulphide (MNS) inclusions in a wind turbine gearbox bearing" at *13th International Conference on Engineering Structural Integrity Assessment*, Manchester, 19-20 May 2015.

Poster presentations

"Investigation into bearing failure modes and their effect on lifetimes of gearbox bearings" at *10th TriboUK Conference*, Leeds, 25-22 March 2013. **2nd place prize for best poster presentation awarded.**

"White etching crack failure of wind turbine gearbox bearings" at *EPSRC Supergen Wind Hub General Assembly 2015*, Loughborough, 14 April 2015.

"White etching crack failure of wind turbine gearbox bearings" at *13th International Conference on Engineering Structural Integrity Assessment*, Manchester, 19-20 May 2015.

ABBREVIATIONS

AC	Alternating current
BCC	Body Centred Cubic
CRB	Cylindrical Rolling element Bearing
CTE	Coefficient of Thermal Expansion
DOF	Degree Of Freedom
DER	Dark Etching Region
EDAX	Energy Dispersive X-ray Analysis
EHL	Elastohydrodynamic lubrication
EWEA	European Wind Energy Agency
EU	European Union
FCC	Face Centred Cubic
FEA	Finite Element Analysis
GRC	Gearbox Reliability Collaborative
HELP	Hydrogen-Enhanced Localised Plasticity
HSS	High Speed Shaft
ISO	International Organization for Standardization
IrWEA	Irregular White Etching Area
IZ	Impact Zone
LSS	Low Speed Shaft
MnS	Manganese Sulphide
NREL	National Renewable Energy Laboratory
O & M	Operation and Maintenance
ORD	Over-Rolling Direction
RCF	Rolling Contact Fatigue
REB	Rolling Element Bearing
RMS	Root mean squared
SCADA	Supervisory Control And Data Acquisition
SEM	Scanning Electron Microscopy
SI	International System of units
SKF	Svenska Kullagerfabriken AB
SRB	Spherical Rolling element Bearing
SUROS	Sheffield University Rolling Sliding
TRB	Tapered Rolling element Bearings
UTS	Ultimate Tensile Strength
vol%	Volume percentage
WEA	White Etching Area
WEB	White Etching Band
WEC	White Etching Crack
WEL	White Etching Layer
WSF	White Structure Flaking
wt%	Weight percentage
WT	Wind Turbine
WTG	Wind Turbine Gearbox
WTGB	Wind Turbine Gearbox Bearing

NOMENCLATURE

Unless otherwise stated, all units used throughout this report are S.I.

α	Angle of bearing taper, pressure-viscosity coefficient
β	Gear helix angle
δ	Logarithmic decrement
ζ	Fraction of critical damping
λ_d	Decay constant
φ	Phase of decay
λ	Lambda ratio
η	Dynamic viscosity
η_0	Dynamic viscosity of lubricant at atmospheric pressure
ω_{HSS}	High speed shaft rotational velocity
ω_{LSS}	Low speed shaft rotational velocity
ω_{syn}	Generator synchronous speed
$\sigma_{xx}, \sigma_{yy}, \sigma_{zz}$	Orthogonal normal stresses
$\sigma_1, \sigma_2, \sigma_3$	Principal stresses
σ_v	von Mises equivalent stress
$\sigma_{v,max}$	Maximum von Mises equivalent stress
σ_Y	Yield strength
τ	Unidirectional shear stress
τ_{max}	Maximum unidirectional shear stress
$\tau(t)$	Time dependent torque
τ_O	Orthogonal shear stress
μ	Dynamic viscosity
μ_F	Coefficient of friction
μ_T	Coefficient of traction
ν	Poisson' s ratio
A	Area
b	Line contact geometry area halfwidth
B	Amplitude of vibration oscillation
C_a	Axial dynamic load rating
c	Damping coefficient
$[C]$	Damping matrix
c_r	Rotational damping coefficient
C_r	Radial dynamic load rating
$C_x, C_y, C_z,$	Bending damping about x, y and z axis
C_t	Torsional damping
D	Diameter
d	Distance from point of impact
d_{max}	Depth at peak load
E	Young' s modulus
E'	Reduced Young' s modulus
F	Force
$f(t)$	Time dependent force loading
F_T	Traction force
g	Acceleration due to gravity
GR	Gearbox Ratio
h	Lubricant film thickness

H	Hardness
h_0	Minimum lubricant film thickness
h_c	Central lubricant film thickness
I	Inertia of body
I_p	Polar moment of inertia
I_{rotor}	Rotor inertia
I_x, I_y, I_z	Mass moment of inertia about x, y and z axis
I_{xx}, I_{yy}	Second moment of inertia in x and y directions
k	Stiffness
$[K]$	Stiffness matrix
k_r	Rotational Stiffness
k_T	Tooth stiffness
L	Length
$L_{0.5}$	Half-life of damping decay
L_{10}	Life after which 10 % of bearings are be expected to fail
L_{50}	Life after which 50 % of bearings are be expected to fail
m	Mass
$[M]$	Mass matrix
M	Moment acting on body
M_e	Effective mass of impact rig striker
n	Load life exponent
N	Number of cycles to failure
o_i, o_j	Initial axial inner and outer race offsets respectively
P	Period of oscillation vibration, Load per unit length
p	Hydraulic load
P_r	Equivalent axial dynamic load
P_{max}	Maximum contact pressure
P_r	Equivalent radial dynamic load
PR	Generator pullout ratio
P_{rec}	Recommended maximum contact pressure
Q_{max}	Force on most heavily loaded roller
R	Radius
R'	Reduced radius of curvature
R_a	Mean surface roughness
R_q	Root mean squared surface roughness
S	Stress, Slip
S_i	Instantaneous slip
t	Time
T_{HSS}	High speed shaft torque
T_{LSS}	Low speed shaft torque
$T_{pullout}$	Generator pullout torque
U	Surface velocity, Velocity of impact
$x, y, z, \theta_x, \theta_y, \theta_z$	Displacement of body in each of the 6 DOFs
$\dot{x}, \dot{y}, \dot{z}, \dot{\theta}_x, \dot{\theta}_y, \dot{\theta}_z$	Velocity of body in each of the 6 DOFs
$\ddot{x}, \ddot{y}, \ddot{z}, \ddot{\theta}_x, \ddot{\theta}_y, \ddot{\theta}_z$	Acceleration of body
$\{X\}, \{\dot{X}\}, \{\ddot{X}\}$	Displacement, velocity and acceleration matrices
W	Contact load
W_{max}	Maximum contact load
W_n	Weight of component, where n is component number

ACKNOWLEDGEMENTS

The author would like to sincerely thank his supervisors for their extensive and invaluable support, guidance and mentoring throughout the studies:

- Dr. Hui Long
- Prof. Rob Dwyer-Joyce

This author is also most grateful to the Engineering and Physical Sciences Research Council (EPSRC) for their funding support of this project. He would also like to express his gratitude to his industrial sponsor, Ricardo, for their funding support as well as the direct guidance and advice from the engineers who worked directly with the author:

- Prof. Jon Wheals
- Mr James Packer
- Mr Giles Hundleby
- Mr Sean Canty

The author would like to thank the following co-authors of his papers for their invaluable advice and assistance:

- Dr. Tom Slatter, The University of Sheffield, for the loan of his hammering impact test rig and allowing me to dismantle and alter it!
- Mr. Ed Rounding, for helping with the sectioning and metallurgical analysis of the failed bearing presented in Chapter 5, a time consuming and sometimes frustrating process that did not discourage him from producing an award winning MEng dissertation [1]!

Many others have provided invaluable input to this project, including:

- Dr Rob Thornton and Mr Mike Bell, for their training and advice in the use of metallurgical preparation and specimen observation equipment.
- Our anonymous partner, for the provision of the failed bearing.
- Researchers at the National Renewable Energy Laboratory, for the provision of drawings of their 750 kW test gearbox as well as test data and help with dynamic modelling.
- Mr Dave Butcher, for helping to fix the various test rigs that the author managed to repeatedly damage, for helping with modification of the hammering impact rig and for always finding time despite his rather intimidating workload!
- Dr Oliver Burke and the students at the Huazhong University of Science & Technology, for their company and hospitality when the author travelled to China to complete his exchange research studies in November 2013.

1. INTRODUCTION

1.1. Justification of research

During the past 15 to 20 years the wind energy industry has rapidly expanded, a trend that will continue throughout this decade. The European Wind Energy Agency (EWEA) has a planned target of 230 GW of installed wind power capacity by 2020, representing 20 % of total European Union (EU) electricity consumption [2]. This expansion is being limited by the high operating cost of wind energy, which is made more expensive by a number of maintenance issues, most critically concerning wind turbine gearboxes (WTGs) which are not reaching their anticipated lifespan of 20 years [3, 4, 5, 6, 7]. A typical onshore WTG failure takes around 250 hours to repair and 20 % of the overall lifetime downtime of a wind turbine (WT) can be expected to be caused by gearbox failure [4], with this percentage greatly increased for offshore applications. It is estimated that operation and maintenance (O&M) account for 20 % of the cost of offshore wind energy in the EU [8, 9].

Theoretical WT availability is being significantly reduced by downtime caused by WTG failures [3, 10]. Approximately two-thirds of these failures initiate in the bearings [10], despite best practice manufacturing being followed [11]. As average WT size increases, failure rates also increase since larger turbine size leads to more flexible supporting structures resulting in complex loading conditions on turbine components [10]. Additionally, larger bearings have a higher probability of material defects being located in a critical position, which increases the probability of failure. Two modes of premature failure have been observed in wind turbine gearbox bearings (WTGBs), namely; white structure flaking (WSF), also known as irregular white etching area (IrWEA) formation; and axial cracking of bearing raceways [12, 13]. Both failure modes are thought to be linked to the development of white etching cracks (WECs) in material just beneath bearing raceway contact surfaces which may be formed at so-called butterfly cracks, an established damage feature found in rolling element bearing (REBs) [12]. Currently, the method by which WECs lead to WTGB failure is not fully understood, despite intensive research effort, and hence there is no useful method of calculating remaining useful bearing life in WTG applications [12, 13, 14, 15].

1.2. Aims and objectives of this study

The overall aim of this study is to gain insight into the premature failure of WTGBs using a combination of modelling techniques and benchtop testing to investigate how extreme loading conditions experienced by WTGBs may contribute to their premature failure. More specifically, the main objectives of the project are as follows:

1. To complete a review of the current literature to understand the many different theories that may lead to failure of WTGBs, particularly by WEC related failure modes. Factors

affecting the likelihood of WEC initiation and subsequent propagation will be thoroughly investigated in order to later design experimental methods to investigate the failure mode.

2. To create a detailed analytical model of a complete WT drivetrain in order to investigate the level of loading experienced by WTGBs during transient operating conditions.
3. To carry out a thorough subsurface metallurgical investigation of a failed WTGB in order to gain insight into the mechanisms behind its failure.
4. To design testing to investigate the effect of varying different factors affecting the WEC damage initiation of bearing steel; namely the contact pressure, level of surface slip and number of load cycles as well as the effects of impact loading.
5. To investigate any features relating to WECs using metallographic analysis to gain insight into the formation mechanisms of WECs and the potential role of material defects, in order to shed light on the mechanism of failure to improve future design of WT drivetrains.

1.3. Structure of thesis

The structure of the work completed in the thesis is shown in Figure 1-1 and the contents of each chapter are summarised below:

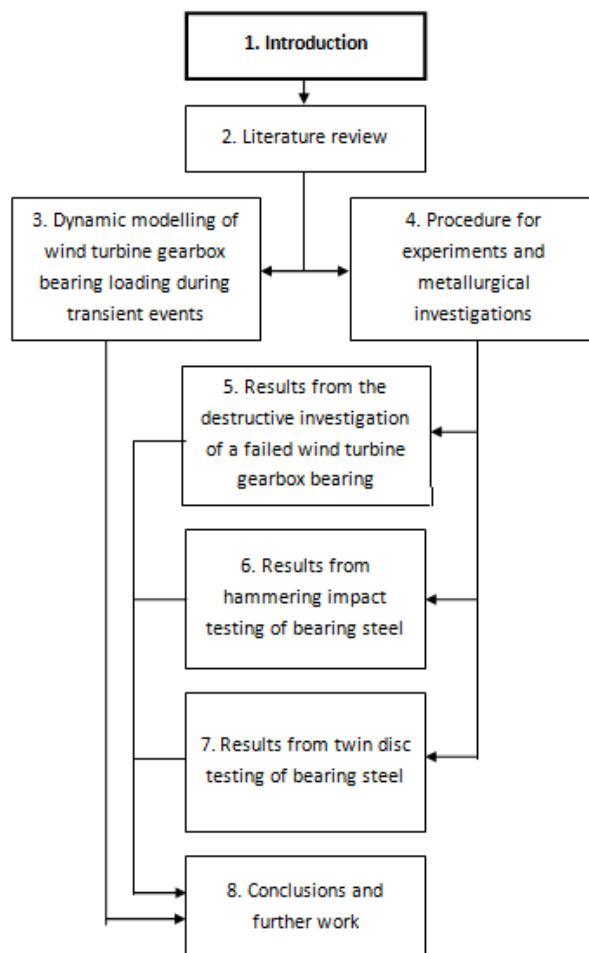


Figure 1-1: Thesis work flow chart

Chapter 2: Literature review. Chapter 2 first summarises the bearings used in wind turbine gearboxes, before discussing bearing technology and tribology. Bearing steel is then reviewed, including manufacturing methods, inclusions in the steel and sources of residual stress. A thorough review of recent investigations into WECs and related features is then presented, including butterfly cracks, factors affecting WEC development and historical testing that has been used to recreate WECs. A review of dynamic modelling methods used to model WTGs is then presented before the chapter is concluded with a number of key findings.

Chapter 3: Dynamic modelling of a wind turbine gearbox bearing loading during transient events. Chapter 3 first presents the development of a multibody dynamic model using *Ricardo PLC's "VALDYN"* software. The model is designed to calculate bearing loading during transient operating conditions acting on a 750 kW gearbox. The model is validated using models of the same gearbox created by external partners, using other modelling tools. Finally, bearing loading results are compared to levels recommended in the international standards.

Chapter 4: Procedure for experimental and metallurgical investigations. Chapter 4 first presents the method used to prepare and observe bearing steel specimens for metallurgical investigations. The method used to examine the subsurface of a failed WTGB is then presented. Finally the design of experiments using both a hammering impact test rig and a twin disc test rig is discussed and experimental procedures presented.

Chapter 5: Results from the destructive investigation of a failed wind turbine gearbox bearing. Chapter 5 reports an investigation of the destructive sectioning of a failed low speed planetary stage WTGB and the damage found at manganese sulphide (MnS) inclusions. The bearing inner raceway was sectioned through its circumferential and axial directions in order to compare the damage around inclusions in different directions. 112 damage initiating inclusions were catalogued and their properties investigated.

Chapter 6: Results from hammering impact testing of 100CrMo7-3 bearing steel. Chapter 6 reports the results of testing using a reciprocating hammer type impact rig. Tests were designed to induce subsurface damage at stress concentrating MnS inclusions. The effects of increasing surface contact stress and number of impact cycles, with and without surface traction, were investigated by destructive investigation of the test specimens.

Chapter 7: Results from twin disc rolling contact fatigue testing of 100Cr6 bearing steel. Chapter 7 reports the results of rolling contact fatigue (RCF) testing using a twin disc test rig. Tests were designed to investigate the effects of changing the contact stress, level of slip and the influence of pre-seeding the specimens with impact damage. A destructive investigation of the specimens was undertaken to investigate the damage at MnS inclusions in the specimens.

Chapter 8: Conclusions and further work. Chapter 8 presents conclusions from the study and highlights the main novelty contributions. Further work on the subject is also suggested.

Appendices: The appendices present supporting information and figures from the study.

1.4. Key novelty points and contributions

The key research novelty and contributions from this study are related to WEC damage at MnS inclusions. Four different types of damage have been found and reproduced at MnS inclusions by exposing bearing steel specimens to impact loading and rolling contact fatigue on bench top test rigs. These four damage types are: separation of MnS inclusion boundary surfaces from the surrounding steel creating free surfaces; the internal cracking of MnS inclusions creating free surfaces; crack propagation from these free surfaces into the surrounding material; the development of WEAs attached to these cracks and/or free surfaces. A hypothesis of the damage sequence and mechanism of these damage types is proposed in this study, as well as the development of testing methods to investigate the damage in order to support the hypotheses. Test methods and experimental procedures are also developed and designed to investigate the effects of some key bearing loading parameters, including impact loading, levels of contact pressure, surface traction and number of load cycles.

2. LITERATURE REVIEW

This chapter presents a review of the literature relating to work completed in this study. It begins by examining WTGBs and the extreme conditions that they operate in, before looking in detail at the steel that bearing raceways are made from and how manufacturing processes and the presence of defects, in particular MnS inclusions, can adversely affect operational performance. The various driving factors leading to the development of WECs are presented and the different types of white etching features, discussed. Methods used to model WTG drivetrains are then investigated before the chapter is concluded with key findings from the literature review and the introduction of hypotheses to be investigated throughout this study. Figure 2-1 shows the thesis work flow chart.

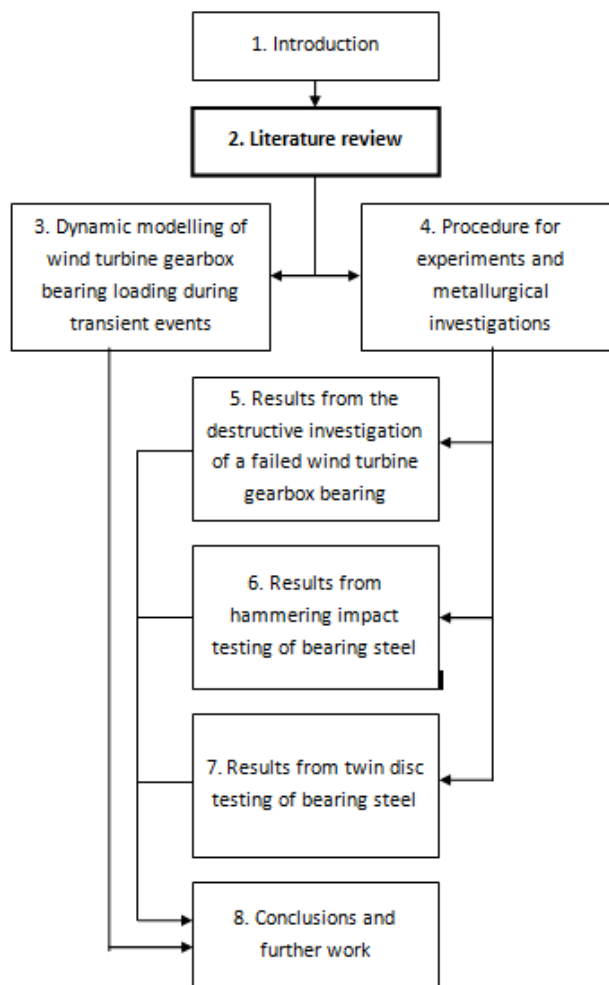


Figure 2-1: Thesis work flow chart

This chapter is split into the following sections:

- Section 2.1 describes WTGBs and their operating conditions.
- Section 2.2 describes bearing steel.
- Section 2.3 described WECs and related features.
- Section 2.4 discusses dynamic modelling of WT drivetrains.
- Section 2.5 summarises findings from the literature review.

2.1. Wind turbine gearbox bearings and their operating conditions

The main difference between wind turbine gearboxes (WTGs), and gearboxes used in many other applications, is that WTGs step up shaft rotation from low speed, high input torque to high speed, low output torque; whereas most other gearboxes operate in the reverse direction. The result of this is that WTGs operate against high referred inertia from the generator that is attached to the high speed end of the gearbox. High transient loads from the rotor are therefore absorbed by the gearbox, and consequently the bearings are loaded in an extreme manner that is relatively unique to WTGs. Additionally, wind turbines operate in extremely harsh environments. Transient wind conditions lead to short time scale extreme loading on gearbox components that need to be considered when designing gearboxes and selecting bearing components. This section discusses: the components within a wind turbine drivetrain; the various bearings that are used in WTGs; stresses experienced during bearing operation; bearing design life calculation methods; bearing failure modes; and the tribology behind bearing operation.

2.1.1. Wind turbine gearboxes

A typical horizontal axis wind turbine drivetrain is shown in Figure 2-2 and consists of: a hub which connects to the rotor blades; a main shaft, supported by two or more main bearings; a gearbox, which typically steps up the input speed from around 20 rpm to around 1,800 rpm output; a braking system on the high speed shaft; an alternating current (AC) generator; and a bedplate that supports the drivetrain[5, 16, 17].

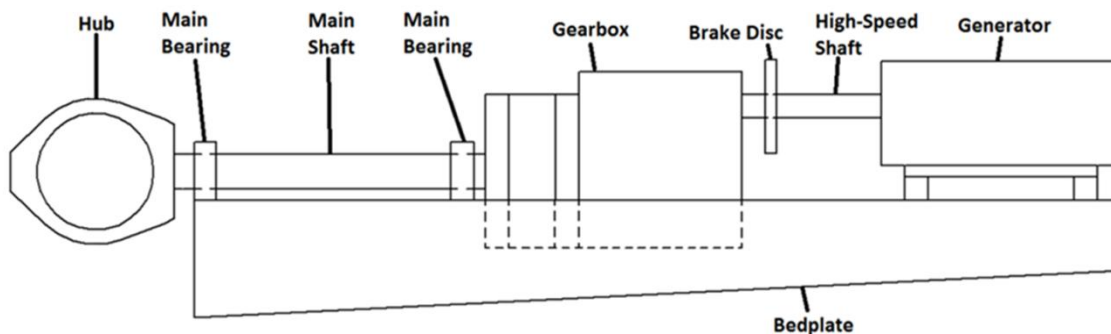


Figure 2-2: Typical WT drivetrain

The wind turbine gearbox links the high torque, low speed main shaft to the low torque, high speed shaft, generally via a three stage gearbox, which provides a total gearbox ratio of around of 90:1 [17]. The most common configuration is for a planetary first stage, with three planetary gears, followed by two parallel gear stages, as shown in Figure 2-3 [7, 18], which also presents the abbreviations used to describe each gearbox component. Rotating components are supported by a total of around 17 bearings [17]. Lubrication is provided by a system that circulates oil around all gears and bearings and through a filter. The oil must therefore be able to provide suitable lubrication at a wide range of speeds and contact pressures, as discussed in

more detail in section 2.1.6. Approximate rotational speeds for bearings in a conventional WTG operating at rated power are given in Table 2-1 [17]. This table is presented as an approximate guideline and bearing speeds will vary dependent on WT rated speed and gearbox ratios.

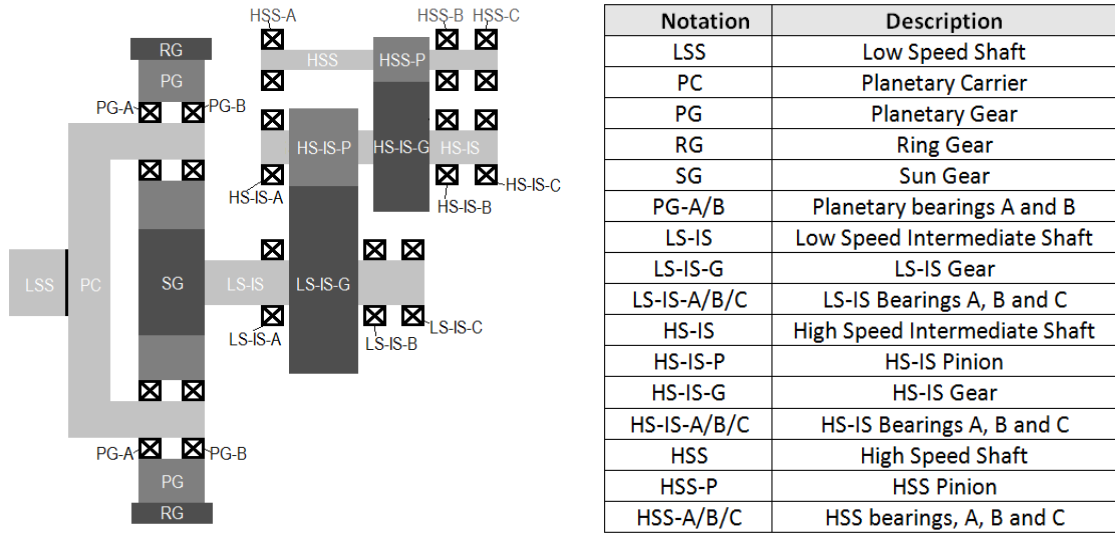


Figure 2-3: Typical gearbox schematic including description of component abbreviations used

WTGB location	Approximate operating speed at rated power (rpm)
Low Speed Shaft	20
Planetary Gear	35
Low Speed Intermediate Shaft	120
High Speed Intermediate Shaft	450
High Speed Shaft	1,800

Table 2-1: Approximate operating speeds for bearings in a typical WTG [17]

2.1.2. Wind turbine gearbox bearings

The general method of operation of the bearings in the gearbox, broadly speaking, fall into two categories [16, 17]:

1. Those with fixed inner races and rotating outer races. These are the planetary gear bearings *PG-A* and *PG-B* in Figure 2-3, of which there are usually three pairs per planetary stage. The inner raceway is connected to the planetary carrier and the outer to the rotating planetary gears by interference fits.
2. Those with fixed outer races and rotating inner races. These include all other bearings in conventional gearboxes, which are used to support the rotating shafts. In the most commonly used design, this will include nine shaft bearings, three on the two intermediate shafts and three on the high speed shaft as shown in Figure 2-3. In these cases the inner raceway is connected to the shaft and the outer to the gearbox casing by interference fits. Two similar bearings are usually used to support the planetary carrier.

LITERATURE REVIEW

The implications of this difference are important when considering gearbox loading, since all bearings have a loaded zone and an unloaded zone, which means that one circumferential section of the bearing will experience higher contact pressures [19]. On the stationary bearing raceway, this loaded section will always be in the same place, so that section of bearing material will be consistently exposed to the highest contact stress levels. For outer races this is less critical than for inner races, because the inner race experiences higher contact pressures due to its lower radius of curvature. The method for calculating Hertzian contact stresses is presented in section 2.1.3.1, which demonstrates this. As a result, a small section of a WT planetary bearing inner raceway is constantly exposed to the highest loading and the failure of such bearings almost always initiates within this loaded zone [20, 21]. Figure 2-4 presents photographs of a pair of failed planetary bearings from a 600 kW wind turbine. A destructive sectioning investigation of the upwind bearing is presented in Chapter 5. Figure 2-5 shows the direction of the maximum loading on each of the planetary bearing inner raceway (PG_{1-3}) due to the WT rotor input torque T_{input} , which is possibly the most load critical location of any bearing in the WT gearbox.

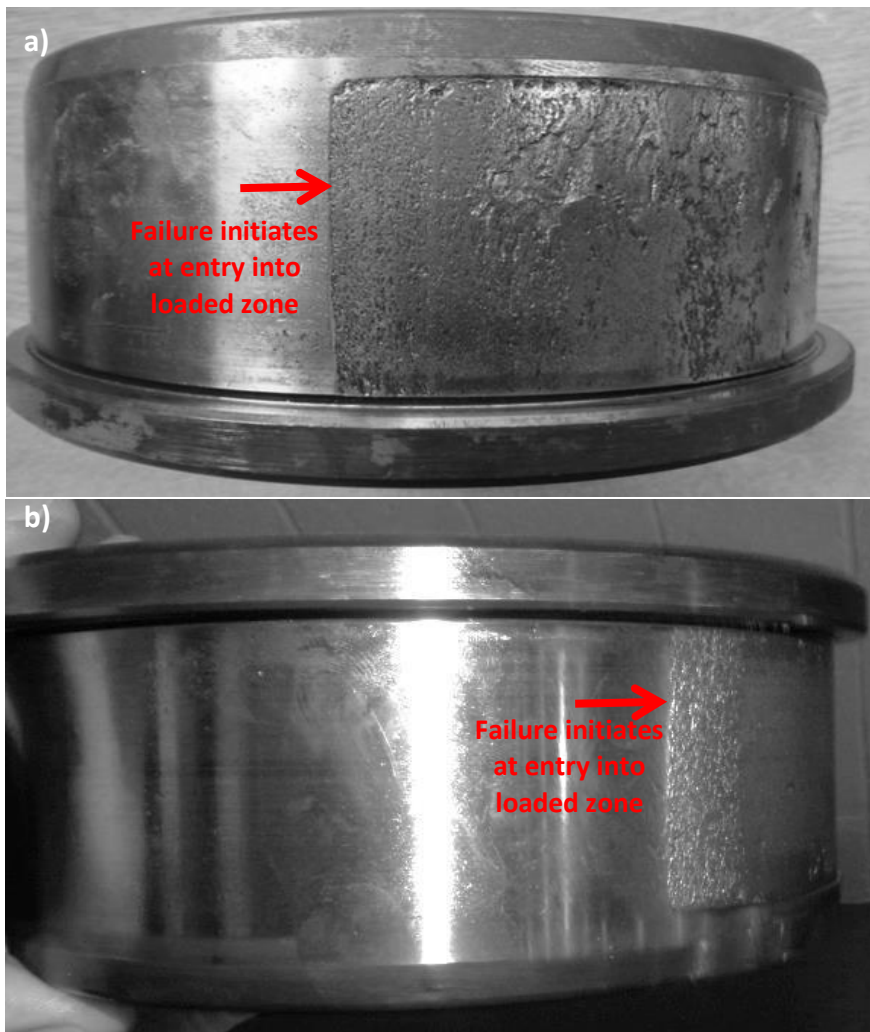


Figure 2-4: Failed planetary bearing inner raceways from a 600 kW turbine: a) upwind bearing, b) downwind bearing

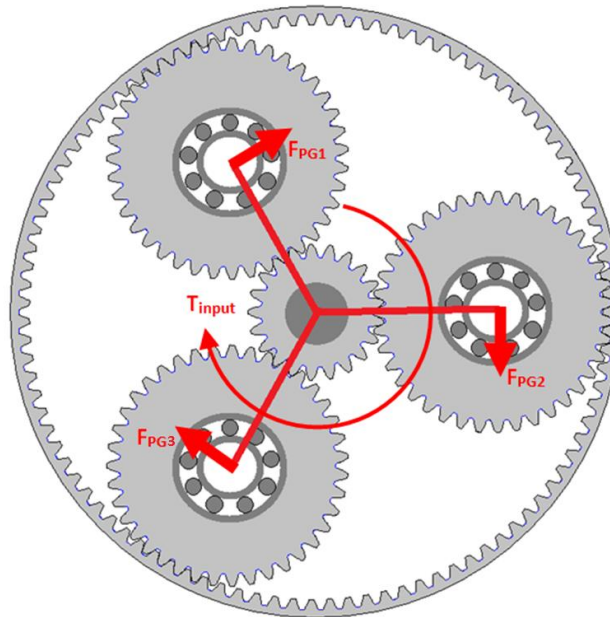


Figure 2-5: Direction of maximum force (F_{PG}) acting on planetary gears 1-3 from WT input torque (T_{input})

In addition to the different operating methods of the bearings, bearing selection in WTGs involves a compromise between many other design requirements [18]. Mechanically, the bearing must be suited to operating at a certain speed, depending on its location within the gearbox, but must also have a high enough load bearing capacity to be suitable for the contact pressures experienced at that location. For example, a larger diameter rolling element will have a higher static capacity, but will more prone to skidding [22]. Other factors to consider include: method of assembly; low-load conditions; vibration; lubrication requirements; lubrication oil flow design; load sharing; operating temperature; operating temperature gradient between inner and outer raceways; thermal expansion of materials; debris resistance; and the suitability of the bearing for its location [18].

In conventional WTGs, such as the one shown in Figure 2-3, cylindrical rolling element bearings (CRBs) are generally used in high radial load carrying locations [18]. Full complement CRBs (which do not have cages separating large rolling elements) may be used in locations with extremely high load carrying requirements, but roller on roller contact may limit the bearing life. When helical gears are used, it is necessary to use bearings that have the capability of supporting axial loading, in which case, tapered rolling element bearings (TRBs) are positioned back to back or double row spherical rolling element bearings (SRBs) are used [18]. For shaft bearings, the outer raceway is generally interference fitted to the bearing housing and the inner raceway rotates. For planetary gear bearings, the inner race is fixed to planetary pins that attach the gears to the planetary carrier, and the outer raceway rotates. Detailed information about the different bearing types used in wind turbines and their selection considerations are listed in Annex C of BS EN 61400 part 4 [18].

Each bearing in the gearbox operates at a different speed; therefore each will experience a different number of rotations during a set operation time. Estimated revolution numbers for WTGBs during one year of operation are listed in Table 2-2 (based on the shaft speeds presented in Table 2-1 and the estimated revolution numbers in [23], assuming 60 % WT operational availability due to standstills, maintenance, low wind speed conditions and other factors. The approximate number of rolling elements for typical WTGBs at each location [24], are also presented in the table, as well as the estimated stress cycles experienced per year, occurring each time a roller passes over a section of raceway. The recommended maximum contact stress valid for a bearing design life of 20 years from the international wind turbine design standards (IEC 61400-4:2012) is displayed to indicate the approximate level of contact stress to be expected at each location [18]. The nature of the stresses experienced by operating WTGBs is discussed in the following section.

WTGB location	Approximate number of revolutions per year	No. of rolling elements in different bearings at each location*	Approximate number of stress cycles per year	Recommended max. contact stress (MPa) [18]
LSS	6.4×10^6	50, 60	3.2×10^8 , 3.8×10^8	1,650
PG	1.1×10^7	20	2.2×10^8	1,500
LS-IS	3.8×10^7	40, 50	1.5×10^9 , 1.9×10^9	1,650
HS-IS	1.4×10^8	15, 30	2.2×10^9 , 4.3×10^9	1,650
HSS	5.8×10^8	15, 20	8.6×10^9 , 1.2×10^{10}	1,300

Table 2-2: Estimated number of revolutions and stress cycles experienced per year for typical WTGBs.

*Number of rolling elements rounded to nearest 5 to protect confidential design data [24].

2.1.3. Stresses induced during rolling contact fatigue

Fatigue is a progressive, localised, permanent structural change that occurs in materials subjected to fluctuating stresses [25]. High cycle fatigue failure occurs over many cycles and results from cyclic stresses well below the yield strength of the material, whereas in low-cycle fatigue, the stresses may be above the yield strength and the failure occurs over fewer cycle numbers. The simultaneous action of cyclic stress, tensile stress and plastic strain must occur to initiate fatigue cracking (note that tensile stress concentrations can occur under compressive load) [25]. *S-N* curves are used to describe the number of cycles to failure at different stress levels and are acquired from fatigue tests; where *S* is the stress; expressed as the maximum stress, the minimum stress, or the cyclic stress amplitude (equal to half of the difference between maximum and minimum stress); and *N* is the number of cycles to failure, plotted on a logarithmic axis. *N* increases with decreasing *S* for all materials; however, for steel (and some other engineering materials) the *S-N* curve becomes horizontal at a certain limiting stress, known as the *fatigue limit*. Theoretically, below this limiting stress, the material can experience an unlimited number of load cycles [25, 26]. A typical *S-N* curve for steel is shown in Figure 2-6.

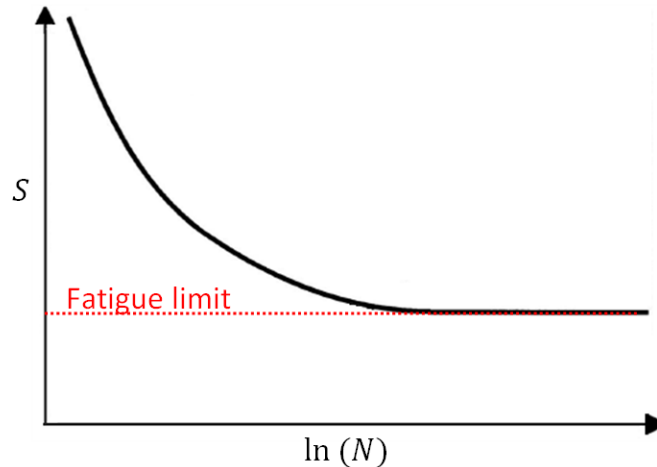


Figure 2-6: Typical S - N curve for steel, where S is the applied stress and N is the number of cycles to failure (adapted from [26])

REB raceways experience a fatigue cycle each time a ball or roller passes over a point on its surface. It is a cyclic dependent phenomenon, which results from repeated stresses under rolling contact and is dependent on: material, speed, surface sliding, lubricant type, contact geometry and the contact pressure [27]. The process eventually leads to bearing failure caused by material loss from the surface, or *spalling*. Cracks usually initiate below the raceway surface at depths close to the location of resolved maximum shear stress, before propagating upwards, but may initiate at the surface in applications where there are large tangential shear stresses involved [27, 28]. Hertz' theory of non-adhesive elastic contact, developed in 1882 [29, 30], is widely used to approximate the magnitude and position of contact stresses in rolling contact applications [19]. Ideally, contact between a rolling element and a bearing raceway is defined to be either at a point, in the case of SRBs, or along a line, in the case of CRBs. Hertzian static contact theory must be considered before looking at the effects of rolling contact, as described below.

2.1.3.1. Hertzian theory of static contact

In 1882, Hertz realised that if the contact load was truly supported by a line or a point, as was thought at the time, this would result in an infinite pressure and as such, a small amount of material deformation must occur before loads could be supported, thus changing the dimensions of the contact area [29, 30]. In the case of a point contact between a sphere and a cylinder, the point contact area becomes elliptical, whereas for two contacting cylinders, the line contact becomes rectangular; the shape of the roller/raceway contact areas for SRBs and CRBs respectively. Within this study, Hertzian line contact theory is used to calculate contact pressures between rolling elements and inner raceways in CRBs and for twin disc testing in Chapter 7. Both situations are non-conformal line contacts, where contact occurs between two convex surfaces with parallel axes. The contact geometry for such conditions is shown in Figure 2-7a and the method of calculated the maximum contact pressure P_{max} in Pascals, in the equations below [19]:

LITERATURE REVIEW

$$P_{max} = \sqrt{\frac{WE^*}{\pi RL}} \quad (2.1)$$

where

$$\frac{1}{E^*} = \frac{1-\nu_1^2}{E_1} + \frac{1-\nu_2^2}{E_2} \quad (2.2)$$

$$\frac{1}{R} = \frac{1}{R_1} + \frac{1}{R_2} \quad (2.3)$$

and W is the contact load, L is the length of the line contact, R is the radius of the contacting body, and ν and E are the Poisson's ratio and Young's Modulus of the steel respectively. Please note that unless otherwise specified, all quantities used throughout this thesis are expressed in terms of the International Standard (SI) system of units. Subscripts 1 and 2 indicate the different contacting bodies and in cases when the bodies have the same elastic properties, equation 2.1 becomes:

$$P_{max} = 0.418 \sqrt{\frac{WE}{RL}} \quad (2.4)$$

The width of the contact rectangle $2b$ in metres, is calculated from the contact half width b , using equation 2.5.

$$b^2 = \frac{4WR}{\pi LE} \quad (2.5)$$

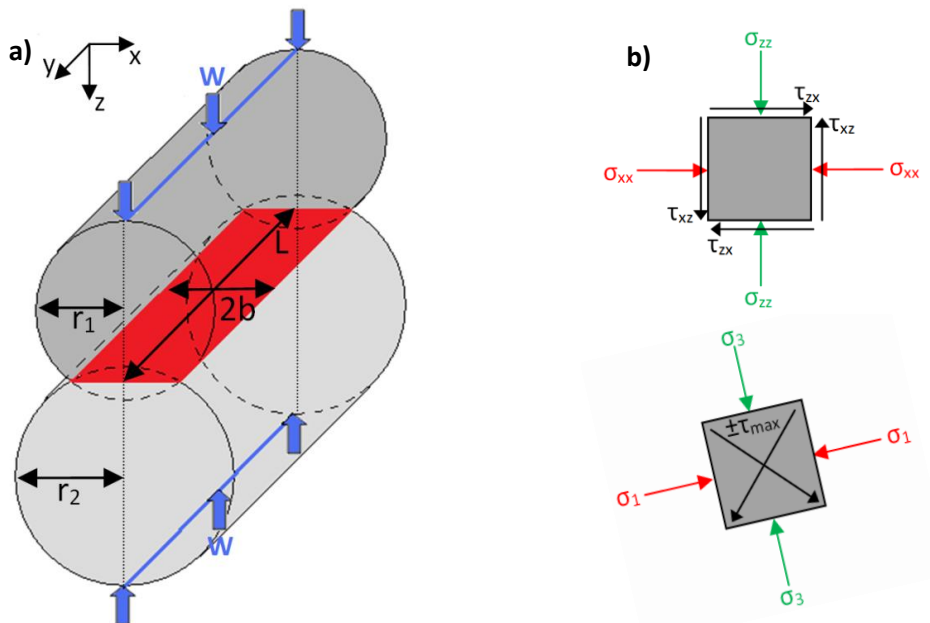


Figure 2-7: Static Hertzian line contact: a) Contact geometry b) Contact stresses on infinitesimal elements on the xz plane (adapted from [19])

In Hertzian contact mechanics, orthogonal normal stresses are compressive in nature and are defined by three components, with differing values; σ_{xx} , σ_{yy} and σ_{zz} , acting along the three

major axis x , y and z , , which are defined in Figure 2-7a. These can be calculated for any infinitesimal element in the contact area, illustrated in Figure 2-7b, along with the orthogonal shear stress τ_o (also commonly written τ_{xy} , τ_{xz} , τ_{yz} to define the plane it is acting on) [19]. The second form of shear stress experienced is termed the unidirectional shear stress τ (also commonly written τ_{45}), which occurs at an angle of 45° to the principal stresses σ_1 , σ_2 and σ_3 in the stress field, as shown in Figure 2-7b on the xz plane. Principal stress act along principal planes, on which orthogonal shear stress is zero [19]. In static Hertzian contact, no movement occurs between the bodies and as a result, for a point at the centre of the contact width, $2b$, there is a principal plane parallel to the surface tangent of the two contacting cylinders (and perpendicular to the contact load, W). At any point underneath the centre of the contact width, the direction of shear stress will be at $\pm 45^\circ$ to the surface tangent. The point of maximum unidirectional shear stress τ_{max} occurs beneath the surface at a depth that is dependent on the load and therefore the dimensions of the contact area. For line contacts of steel bodies with a Poisson's ratio of 0.3, this depth is around $0.78b$. The magnitude of τ_{max} is approximately equal to $0.3P_{max}$. The maximum value of orthogonal shear stress $\tau_{o,max}$, is around $\pm 0.25P_{max}$, found at coordinates $(\pm 0.87x/b, 0.5y/b)$. These positions are shown in Figure 2-8, along with contours of the orthogonal stress field (left side of z axis) and unidirectional stress field (right side of z axis). For Hertz's theory to be accurate, the materials in contact must be homogeneous, the contact area small compared to dimensions of the bodies in contact and the effects of surface roughness negligible [19].

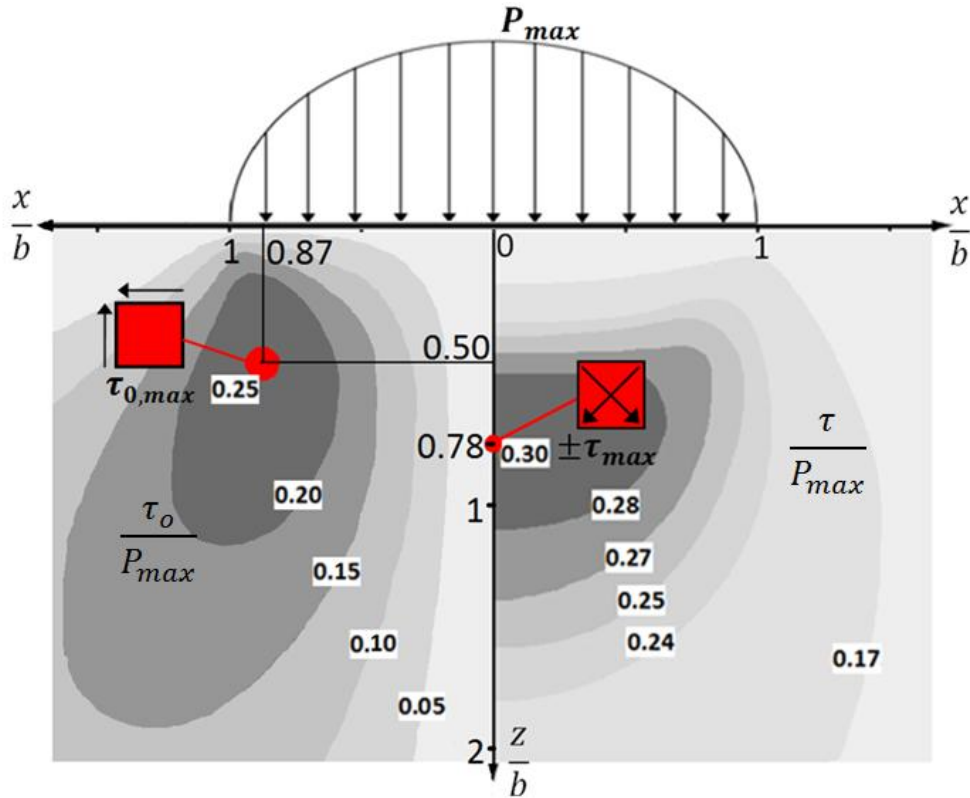


Figure 2-8: Subsurface Hertzian stress field for static line contact of two steel cylinders as a proportion of P_{max} showing contours of orthogonal shear stress (τ_o) and unidirectional shear stress (τ). Positions of maximum orthogonal ($\tau_{o,max} \approx 0.25P_{max}$) and unidirectional shear stress ($\tau_{max} \approx 0.3P_{max}$) are highlighted. z is the depth beneath the material surface, x is distance away from the centre of the contact rectangle and b is the contact rectangle half width. Adapted from [19] and [22]

In reality, surface roughness effects may increase subsurface stress concentrations, so the Hertzian approximation is likely to be conservative. If the lubricant film is thin in comparison to surface roughness, asperity contact will occur, leading to significantly increased pressures [19]. In less extreme situations, when asperity contact does not take place, increased contact pressure is still experienced at raised asperities [19], corresponding to a peak in the subsurface stress field below [23].

The von Mises stress, or equivalent stress, σ_v , is used to predict the yielding of materials and is dependent on the combined effects of the three principal stresses on a principal plane, or on the three orthogonal normal stresses and orthogonal shear stress components on other planes. It can be calculated from the principal stresses using equation 2.6 or from the normal stress in x , y and z and the orthogonal shear stresses, using equation 2.7 [31]. Yielding occurs if $\sigma_v > \sigma_Y$, where σ_Y is the yield strength of the material. For line contacts, the von Mises equivalent stress reaches a maximum $\sigma_{v,max}$, at a depth of approximately $0.7b$ beneath the centre of the contact on the x axis [32].

$$\sigma_v = \sqrt{\frac{1}{2}[(\sigma_1 - \sigma_2)^2 + (\sigma_2 - \sigma_3)^2 + (\sigma_3 - \sigma_1)^2]} \quad (2.6)$$

$$\sigma_v = \sqrt{\frac{1}{2}[(\sigma_{xx} - \sigma_{yy})^2 + (\sigma_{yy} - \sigma_{zz})^2 + (\sigma_{zz} - \sigma_{xx})^2 + 6(\tau_{xy}^2 + \tau_{yz}^2 + \tau_{zx}^2)]} \quad (2.7)$$

It should be noted that in reality, there are beneficial residual stresses in existence, introduced during manufacture and during shakedown of bearing steels (see section 2.1.5.1). Subsurface compressive residual stresses are beneficial in retarding crack growth since they effectively decrease the applied stress [33]. When calculating the actual stress experienced by an infinitesimal element, the residual stress field may be "superimposed" upon the Hertzian stress field, to calculate the actual stress experienced.

2.1.3.2. Hertz's theory use in rolling contacts

So far, only static contact has been considered, which is never the case for moving bearings. This section discusses applying static Hertzian contact theory to rolling contacts. It is generally accepted that Hertz's theory of static contact can be used to a level of reasonable accuracy to model contact stresses in certain cases of lubricated rolling contact [34]. In such cases, the oil film thickness must be large compared to surface roughness and the contacting bodies must be in a condition of pure rolling (no relative motion between the surfaces in contact along the x axis). Hertzian theory is widely used to model such situations and is the basis of the model of elastohydrodynamic lubrication (EHL) (see section 2.1.6) [19].

Any point at or close to the material surface of a rotating body under Hertzian loading will suffer repeated loading and unloading cycles, creating a much more complex situation than in static contact. Considering a point beneath the surface of the inner raceway of a CRB highlights the extreme loading conditions experienced by the bearing steel. As this point moves from left to right through the stress field illustrated in Figure 2-8, it will first experience the peak value of negative orthogonal shear stress, then move into an area of peak normal stress and peak unidirectional shear stress as the orthogonal shear stress magnitude decreases to zero, before experiencing an unloading of normal stress and orthogonal shear stress along with a load cycle of positive orthogonal shear. This rather complex description is illustrated in Figure 2-9. Loading extremities of points at key depths in the shear stress field are shown in Table 2-3, which highlights that the range of orthogonal shear stress is twice its magnitude since it experiences both a positive and negative maximum.

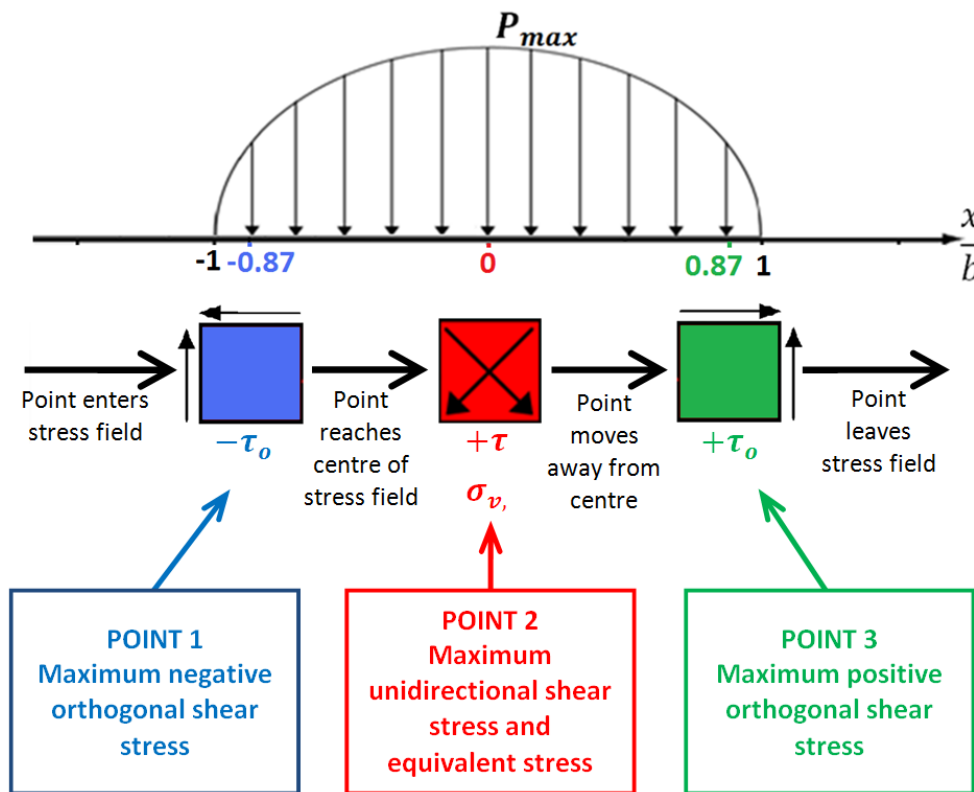


Figure 2-9: Stresses experienced by a point moving through a Hertzian stress field during rolling contact fatigue (note that the distances -0.87 and 0.87 are true for a point at depth $z = 0.5b$)

Depth (z)	Type of max stress intersected	Stress values	Stress range experienced
0.5b	$-\tau_{o,max}$	$-0.25P_{max}$	0.5 P_{max}
	$+\tau_{o,max}$	$+0.25P_{max}$	
0.78b	τ_{max}	0.3 P_{max}	0.3 P_{max}

Table 2-3: Shear stress loading extremities in rolling contact

2.1.3.3. The influence of traction

Up to this point, only pure rolling of the two bodies in contact has been considered. In reality, relative movement of the contacting surfaces along the x axis, known as sliding, is experienced to varying extents by every WTGB. REBs use traction in order to transfer mechanical forces between the raceways, via the rolling elements. Under such conditions, there is always a speed difference between rolling bodies (i.e., between inner raceway and rolling element and between outer raceway and rolling element), leading to slip occurring at the contacting surfaces. RCF is very sensitive to sliding and is accelerated by even very small slip levels [26]. The level of slip is usually described by the percentage difference of the two contacting surface velocities in the direction of rolling. The instantaneous slip percentage (sometimes presented as the slide to roll ratio in the literature) can be found using equation 2.8, where U_1 and U_2 refer to the surface velocities of the two bodies experiencing sliding, rolling contact conditions.

$$S_i(\%) = 200 \left(\frac{U_1 - U_2}{U_1 + U_2} \right) \quad (2.8)$$

During WT operation, WTGBs experience varying levels of slip from moderate to extreme. A study on a spherical REB supporting an intermediate shaft in a WTG found that continuous slip levels of 3-10 % [35] were present due to the geometry of the contacting ball and raceway [36]. During transient events, extreme slip levels between 20-110 % [35] were experienced due to accelerations and decelerations caused by torque reversals. The effects of slip will vary at different locations in the gearbox, with the level of slip expected to be higher on high speed, low load supporting bearings, such as the high speed shaft (HSS) bearings, than on lower speed, high load supporting bearings, such as the low speed shaft (LSS) bearings [37].

Under high surface traction, cracks may form at surface irregularities, including asperities, cracks and dents. Local stress concentrations at these defects initiate the cracks, which propagate at shallow angles (around 15-30° from the surface). After the cracks reach a critical length, they branch back to the surface, isolating a piece of material, which spalls away from the surface, leaving a pit [23]. If the contact stress during shakedown is above the fatigue limit (see Figure 2-6) surface material accumulates deformation by the process of ratcheting, which gradually exhausts the ductility of the material, leading to rolling contact fatigue [38]. Cracks that are initiated in this way are propagated each time the contact zone passes over the crack and by fluid pressure inside the crack, which is more critical for the driving surface than the following. The driving surface has a higher surface velocity and cracks in this surface are pulled open as illustrated in Figure 2-10. Since these cracks are driven towards the oil film, pressurized lubricant is forced into the cracks [38]. The lubricant may directly contribute to crack growth by opening the crack due to fluid pressure, or indirectly, by lubricating the faces and promoting crack growth by shear loading [39].

Figure 2-10 also illustrates why the direction of the resulting traction force, F_T , between the contacting bodies is vital. F_T acts in the opposite direction to surface motion on the surface of the faster body and in the same direction as surface motion in the slower. The result is that F_T tends to pull open RCF cracks on the slower body and push them closed on the faster body. The tensile force is more damaging to the cracks than the compressive force, meaning that RCF life is reduced on the slower rotating body, despite the fact that it will experience a slightly lower number of stress cycles [19]. Figure 2-10 is true for two rotating bodies of equal radius, if the bodies have different radii, the surface velocities must be considered, where the faster surface represents U_2 , and the slower U_1 .

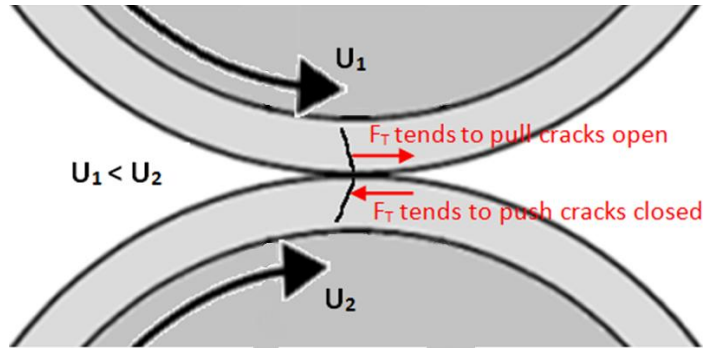


Figure 2-10: Effect of traction force (F_T) on cracks, where U_1 = top body velocity and U_2 = bottom body velocity.

The traction force, calculated using equation 2.9 is dependent on the product of the contact area A (m^2), the dynamic viscosity η (Pa.s), and velocity difference between the surfaces ΔU (m/s^2), divided by the lubricant film thickness h (discussed in 2.1.6) [19]:

$$F_T = \frac{\eta \times A \times \Delta U}{h} \quad (2.9)$$

When sliding occurs, traction between the roller and raceway surface causes the shape of the subsurface stress field to change and the locations of τ_{max} and $\sigma_{v,max}$, to move towards the surface, an arbitrary example of which is shown in Figure 2-11. The extent to which this occurs depends on the traction coefficient, μ_T , defined by equation 2.10, where F_T is the traction force acting between the two surfaces and W is the contact load, acting perpendicular to the traction force. This shifting effect is displayed on τ_{max} is shown in Figure 2-11a and on σ_v in Figure 2-11b. When the traction coefficient reaches a critical level, $\sigma_{v,max}$ reaches the surface and a condition of pure sliding is reached [23].

$$\mu_T = \frac{F_T}{W} \quad (2.10)$$

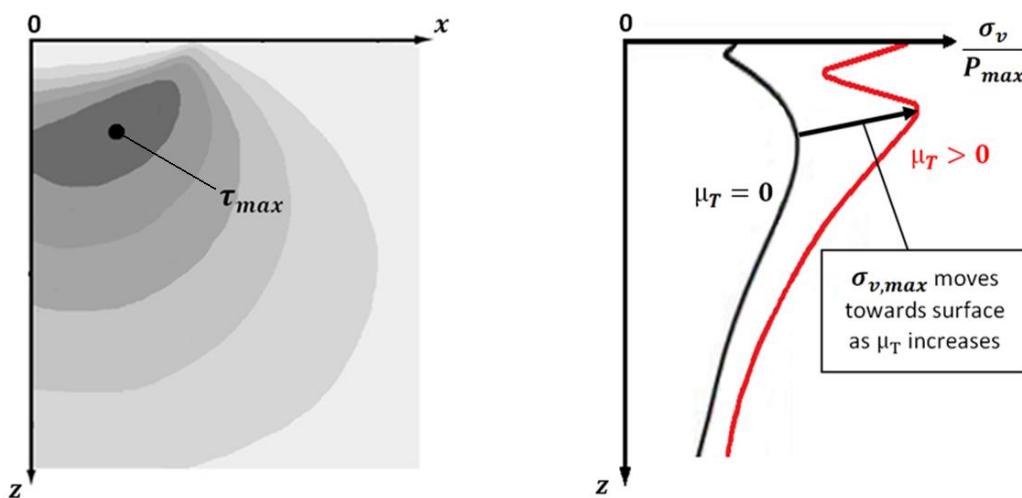


Figure 2-11: The effects of surface traction (acting left to right) on the subsurface stress field: a) contours of arbitrary unidirectional stress b) effect of surface traction on von Mises stress distribution varying with depth (adapted from [19])

The coefficient of traction increases approximately linearly with slip (slide to roll ratio) at low slide to roll ratios (equation 2.8). However, at higher levels of slip, this linear relationship is lost and the traction coefficient increases at a decreasing rate with slide to roll ratio, to a peak, after which the traction coefficient reduces [19]. This peak occurs at a value of approximately $S_i = 10\%$ [19] as shown in Figure 2-12. A friction coefficient is also referred to in the literature and throughout this thesis. Friction coefficients are either “static”, defined for initially stationary surfaces, with no relative movement, or kinetic, for surfaces with relative movement [19]. The frictional force is the theoretical limit to the traction force that may be transmitted between two surfaces [19]. A situation known as stick-slip may occur, where the friction coefficient oscillates between static and kinetic. Under such conditions, the sliding speed of a surface continuously varies between stationary (stick) and very high (slip). Stick-slip is dependent upon the dynamic characteristics of the system and how the friction coefficient changes at low speeds [19].

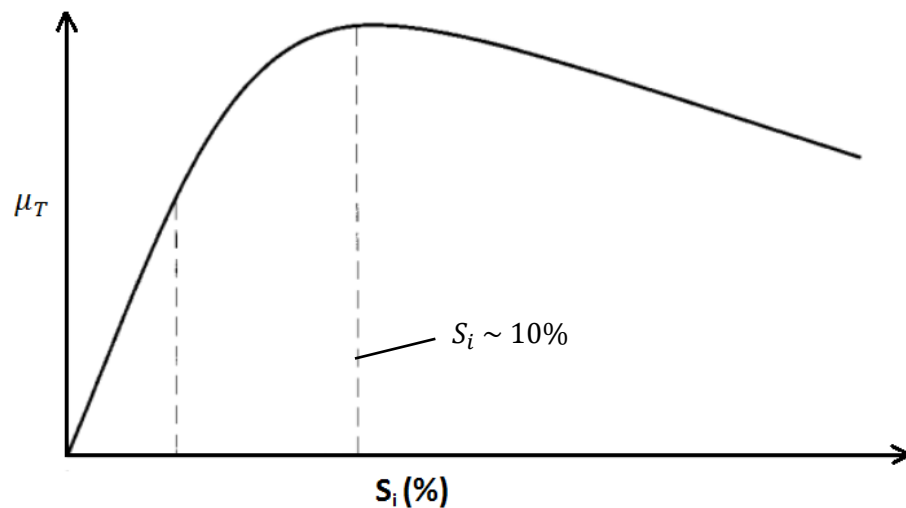


Figure 2-12: Traction coefficient (μ_T) with increasing slip (slide/roll ratio) (S_i) (adapted from [19])

2.1.4. Bearing life rating

Eventually, if not by a different cause of failure, all bearings in operation will fail by spalling [40]. However, current failure-by-fatigue models do not explain why WTGB are failing well before their design lifetime. The L_{10} rating life, which was developed by Lundberg and Palmgren [41, 42] and is used in current rolling element bearing design standards [40], is defined as: ‘the life (in terms of millions of revolutions) at which 10 % of the sample would be expected to fail’. In other words, after a batch of bearings have been running for a period equal to the L_{10} rating life, 90 % could be expected to show no signs of surface spalling and 10 % would have failed; where failure is defined as the first sign of surface spall. The method is based on the theory that the maximum orthogonal shear stress τ_0 , is representative of the failure causing stress, since parallel-to-surface subsurface cracks were found, which means

LITERATURE REVIEW

they propagated in the direction that τ_0 acts [43]. The failure-by-fatigue L_{10} rating life equations for radial bearings (2.10) and for axial bearings (2.11) are displayed below:

$$L_{10} = \left(\frac{C_r}{P_r}\right)^n 10^6 \quad (2.10)$$

$$L_{10} = \left(\frac{C_a}{P_a}\right)^n 10^6 \quad (2.11)$$

Where the L_{10} life is measured in revolutions; C_r and C_a are the basic dynamic load ratings in Newtons for radial and axial loads respectively and represent an applicable constant load where the bearing will achieve an L_{10} rating life of 10^6 revolutions; P_r and P_a are the equivalent dynamic loads in Newtons for radial and axial loads respectively and is a hypothetical constant magnitude load that takes into account off-axis loading; the factor n is the load life exponent, which is $n = 10/3$ for roller bearings and $n = 3$ for ball bearings [40]. Modifications to the basic rating life are listed in standards *ISO 281:2007* [40] and *ISO 16281:2008* [44], which take into account the inner geometry of the bearing, misalignment and/or tilting, internal clearance, edge stresses, lubrication conditions and lubricant contamination. Due to the random nature of the inclusions and defects present in bearing steel, bearing life shows some degree of scatter, where bearing life can be plotted as a Weibull distribution [22].

Despite the updates to the Lundberg and Palmgren rating life, it has become clear that the life rating method is not appropriate for use with WTGBs, since they commonly fail within 20 % of their L_{10} life [45, 46, 47]. Lundberg and Palmgren developed their life rating model by analysis of hundreds of tests on small bearings which were loaded to high contact stresses in excess of 2.5 GPa [48]. Under such conditions, near-surface strain induced microstructural changes known as dark etching bands and white etching bands (described in section 2.3.3) take place [49]. WTGBs are much larger than those used by Lundberg and Palmgren and are designed to operate at much lower contact pressures as shown in Table 2-2. Under such conditions, these microstructural changes are not observed [48] and hence the applicability of the use of the L_{10} life rating for predicting the lifetime of WTGBs is put into question. At these lower contact stresses, it is now widely accepted that sub-surface failure-by-fatigue is initiated at internal flaws in the bearing steel; principally non-metallic inclusions [48, 50, 51, 52, 53, 54, 55, 56], which are discussed in detail in sections 2.2.4 and 2.2.5. Neither material cleanliness nor material structure is modelled by the L_{10} approach [48].

Another problem with the L_{10} life rating approach is that it does not take into account the effects of surface traction, despite the fact that sliding commonly takes place in REBs [56], particularly in the transient conditions experienced by WTGBs. Furthermore, these transient events are not properly modelled by the L_{10} method, since the dynamic equivalent load does not take into account short term impact events that have been cited to occur in WTGBs [10, 12, 14, 36], nor does it have any way of considering the order of events. The order that the

events take place could be critical since crack initiation requires a higher stress than crack propagation [48]. For example, if a bearing was exposed to high enough contact stresses to cause subsurface microcrack initiation and then exposed to a period of moderate contact stresses, the crack may propagate significantly through the material in comparison to a bearing that experienced the events the other way round. This hypothesis is discussed in Section 2.5.5.2. Finally, since the theory is based on the assumption that the failure is associated with a single stress τ_0 , it neglects to consider the wider effects of the subsurface stress distribution (discussed in Sections 2.1.3.1 and 2.1.3.2) [43].

2.1.5. Rolling element bearing failure modes

The following section examines bearing failure modes that are known to affect rolling element bearings. These failure modes are discussed in the current international standard (ISO 15243:2004) [57] that describes the damage and failure of rolling bearings. This section does not discuss failure modes relating to a white etching microstructural change that is thought to be the main cause of premature failure in WTGBs [12], which is discussed in detail in section 2.3. Although the following failure modes are discussed independently, it is important to consider that they may all contribute in some way to the white etching microstructural change so may have cumulative effects. The failure modes covered in this section have been found to occur in a wide range of bearings, and there is a great deal of field experience from observing the resulting failures. A detailed analysis of bearing failure modes from *Svenska Kullagerfabriken AB* (SKF) field experience is provided in Appendix A, which was compiled from information in [58].

2.1.5.1. Fatigue

Failure by fatigue is visible by flaking of material particles from the surface of bearing raceways or rollers. The fatigue process has been described in section 2.1.3 and can occur both on the surface or within the subsurface of a bearing component. Subsurface failure due to rolling contact fatigue is thought to be the main cause of premature failure and results from the initiation of microcracks, often at inclusions or other material defects, and at features known as butterflies (which are described in detail in Section 2.3.1). These microcracks may propagate to the surface leading to the flaking away of material [57].

Surface initiated fatigue most commonly occurs when the combined surface roughness of the rolling elements and the raceway is greater than the lubricant film thickness, meaning that boundary lubrication conditions prevail (discussed further in 2.1.6). This may lead to microcrack initiation at surface asperities and/or micropitting, which appears as grey spots, giving the material a matte appearance [59]. This failure mode is typically associated with tangential shear stress caused by rolling-sliding contact [9]. Micropitting causes problems in bearings because it changes the geometry of the rollers and raceways. The altered geometry increases internal clearance and results in edge stresses that ultimately propagate the damage

to the macro level, before bearing failure eventually occurs. Possible contributions to this failure mode are: widely varying loads, rapid accelerations and high levels of vibration [59]. Contamination by water may also be a contributing factor [60]. Micropitting, reduces tolerances, creates noise and may lead to other issues such as gear tooth bending fatigue and macropitting [61]. Indentations in the raceway surface may lead to surface initiated fatigue and can be caused by contaminant particles or handling [57].

2.1.5.2. Wear

Wear occurs in REBs due to contacting asperities, resulting in the removal of material from the roller and raceway surfaces and occurs due to both adhesive and abrasive processes. Abrasive wear results from reduced lubrication or lubricant contamination by foreign particles. The surfaces become relatively dull in appearance and as wear abrasion occurs, more and more particles are created, leading to accelerating wear rates, resulting in eventual failure. Adhesive wear or smearing of the roller and raceway surfaces is caused by slipping or skidding of the rolling elements on the raceways. Slip occurs frequently during WTGB operation [9] due to torque reversals [10], acceleration and deceleration of the drivetrain, misalignment, roller profiling [56], entry and exit of rolling elements in and out of the loaded zone [20] and transient loading conditions [12]. As previously mentioned, the problem is more likely to occur in high speed, and comparatively low load supporting bearings [59], for example the HSS bearings. When the bearings are lightly loaded and rotating at high speeds, the friction between the rollers and the raceways may be less than the drag force. In this case the surface of the rollers will rotate slower than that of the raceway, leading to a breakdown of the lubricant layer and bouncing and skidding of the rollers on both raceways [59]. Skidding causes localised frictional heating at the surface, where the lubricant film thickness is inadequate [9]. Under such conditions, the roller is dragged across the surface of the raceway, leading to adhesive wear (smearing) [59].

This failure mode is commonly observed in the field [9] and arises because rolling element bearings rely on friction for their operation. The rolling elements are driven at their epicyclic speed by the rotating raceway, but exert some natural resistance to movement due to friction and drag caused by the lubricant. As the rollers move in and out of the loaded zone of the bearing, friction levels between them and the raceways change, leading to unbalance at the boundary between the unloaded and loaded zone [15]. Across this boundary, the rollers may not obtain their correct speed and slipping will occur [59]. Maximum damage occurs just after entry into the loaded zone when the levels of sliding increase roller sliding [15]. Conflicting design needs provide a significant design challenge [10] since large roller size increases sliding risk, but large rollers have a higher load carrying capacity.

2.1.5.3. Corrosion

Defined as a *chemical reaction on metal surfaces*, corrosion may occur in bearings due to contact with moisture or acid, which can lead to the formation of pits on the surface, leading

to flaking of material away from the surface [57]. Another form is *tribocorrosion*, which is frictional corrosion caused by the relative movement of contacting surfaces under certain frictional conditions. Tribocorrosion leads to the oxidation of surfaces and eventually to material removal from the surfaces [57]. This cause of bearing damage begins with an incubation period, known as false brinelling, during which the wear mechanism is mild adhesion and wear debris is magnetite (iron oxide Fe_3O_4) [15]. If wear debris is significant enough to stop lubricant reaching the raceway/roller contact, the wear mechanism becomes strong adhesion, which breaks through the protective oxide layer. In this case the damage is more severe and is known as fretting corrosion [15].

Tribocorrosion can occur when bearings are stationary and are exposed to structure-borne vibrations caused by wind loading or the control system. Under these conditions, lubricant is squeezed out from the contact between the raceways and rollers and not replenished. The metal to metal contact and relative movement removes the protective oxide films from the metal surface [15]. If the thin oxide protective film on the component surface is penetrated, oxidation will proceed deeper into the material. This fretting corrosion damage can be relatively deep in places. The relative movement can also cause small particles to become detached from the surface, which oxidise quickly when exposed to the atmosphere. This leads to uneven support of bearing raceways and has a detrimental effect on load distribution in the bearings. Stationary bearings in inactive turbines are exposed to vibration and other forces which may lead to corrosion at roller contact points [58].

2.1.5.4. Electrical erosion

Electrical erosion causes the removal of material from the roller and raceway surfaces due to the passage of electrical current. Excessive voltage may cause sparking between rolling elements and raceway surfaces due to inadequate insulation, leading to melting and welding of the contact areas [57]. Current leakage may lead to the formation of craters on the surface, even at low currents [57]. Links between electrical erosion and the white etching microstructure change are discussed in Section 2.3.5.4.

2.1.5.5. Plastic deformation

Plastic deformation occurs at rolling element/raceway contacts whenever contact stresses exceed the yield strength of the material, either on a macroscale due to high contact loads, or on a microscale, due to a foreign object bridging the lubricant layer [57] or due to asperity contact if the surface roughness exceeds the thickness of the lubricant layer [12]. Sources of high contact loading during WT operation have been previously discussed. Additionally, inappropriate handling during transport or assembly may also lead to plastic deformation [57], damaging the bearing before it has been used.

2.1.5.6. Cracking

Cracking may occur if the bearing steel is exposed to stresses during surface contact, higher than its ultimate tensile strength (UTS). When a crack propagates to the point that the

component entirely separates, fracture occurs [57]. The UTS may be exceeded at relatively low contact loads due to stress raisers such as inclusions or voids in the material (discussed further in section 2.2.4). Cracking may also be opened due to surface traction during sliding motion. Crack initiation and propagation is discussed further in section 2.3.

2.1.6. Bearing lubrication

The thickness of the lubricant film that separates two surfaces is dependent on a number of factors, the most important of which is the viscosity of the oil or lubricating fluid, which varies with both temperature and pressure. There are four distinct lubrication regimes, which are identified by the “lambda ratio” λ , a ratio of the film thickness divided by the composite surface roughness of the two surfaces that are separated by the fluid film [19] where h_0 is the minimum film thickness (m), R_{q1} is the root mean squared (RMS) roughness of the first body in contact (m) and R_{q2} is the RMS roughness of the second body in contact (m):

$$\lambda = \frac{h_0}{\sqrt{R_{q1}^2 + R_{q2}^2}} \quad (2.12)$$

The thickness of the film is dependent on the relative speed of the separated surfaces, the contact pressure and the viscosity of the lubricating fluid [19]. Once film thickness and surface roughness is known, the lambda ratio can be used to determine the lubrication regime, summarised by the Stribeck curve shown in Figure 2-13 and classified as follows:

- **Boundary lubrication** ($\lambda < 1$) occurs when the fluid film is a similar thickness, or less than, the value of the composite surface roughness. There are a large number of asperity contacts, leading to relatively high friction and therefore, high wear rates and in general, undesirable operating conditions for bearings. The lubricant mechanisms are usually controlled by additives in the lubricant [19].
- **Mixed (or partial) lubrication** ($\sim 1 < \lambda < 1.5$) occurs at higher rotational speeds, lower loads, or with higher fluid viscosity. Surfaces are separated by a thicker film than the boundary lubrication regime, and there are fewer asperity contacts and as a result, less friction, because the film thickness is slightly higher than the surface roughness. The contact load is shared between a thin film and the contacting asperities [19].
- **Elastohydrodynamic lubrication** ($\sim 1.5 < \lambda < 3$) is a special form of hydrodynamic lubrication that occurs in highly loaded non-conformal contacts. Full separation of the surfaces is possible due to a combination of three effects: hydrodynamics, elastic deformation of the metal surfaces and the increase in viscosity of the oil under extreme pressures. An extremely thin lubricant film is formed (0.1 to 1 μm), which separates the surfaces and leads to very low levels of friction and wear [19]. As shown in Figure 2-13, the point of minimum friction between the surfaces is experienced in the EHL regime. The

combination of these factors means that EHL is the desired lubrication regime for non-conformal contact in bearing operation.

- **Hydrodynamic lubrication** ($\lambda > 3$) is formed due to a combination of the surfaces being inclined at some angle to each other, the fluid viscosity being high enough and the surfaces moving with sufficient velocity to generate a lubricant film that is able to support the contact load. Friction and wear levels drop to their lowest at first, but as fluid pressures increase, friction begins to increase due to fluid drag [19].

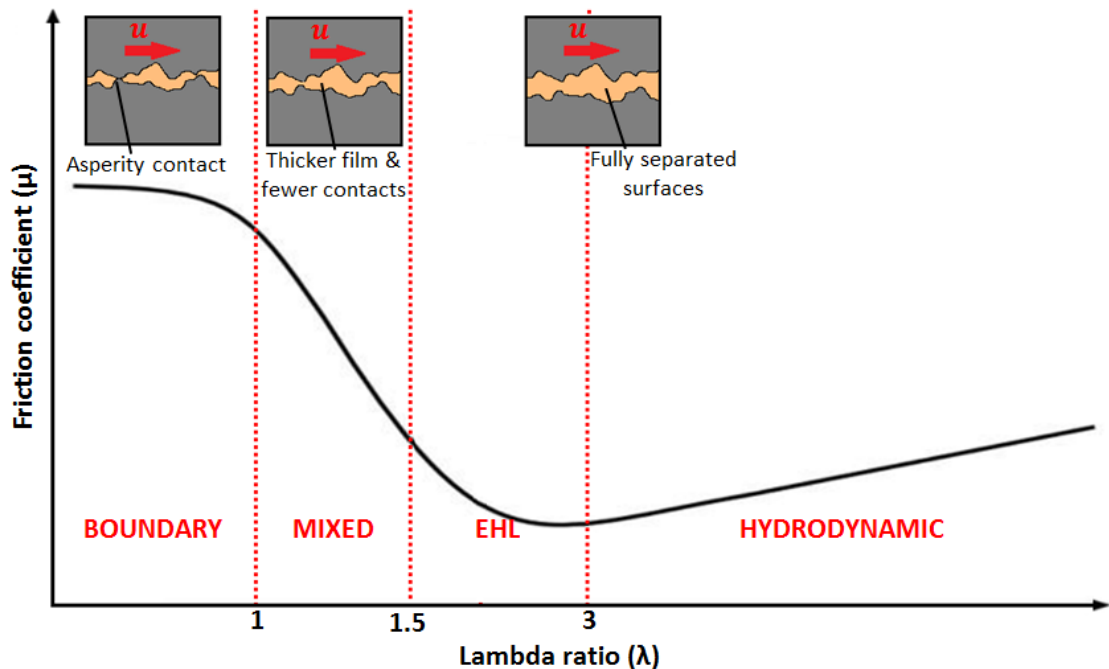


Figure 2-13: Stribeck curve illustrating lubrication regimes (not to scale). u indicates the direction of the movement.

Since lubrication is provided to all WTGBs by the same oil and consequently the same viscosity lubricant, it is not possible to obtain optimum EHL conditions for all bearings in the gearbox at all times. Bearings operate at different speeds depending on: their location in the gearbox (see Table 2-1); the operating condition (start-up, normal operation etc.); and the speed of the wind. As a result, during start-up and shut-down, all bearings in the gearbox will experience boundary and mixed lubrication, leading to asperity contact and relatively high levels of wear [19]. As speed increases, higher speed bearings, on the intermediate and high speed shafts, will move into an EHL regime, however, low speed shaft bearings and planetary bearings, will remain in boundary or mixed lubrication [23].

The mechanism of EHL is displayed in Figure 2-14. Relative motion between the surfaces modifies the ellipsoidal Hertzian pressure distribution, with lower hydrodynamic pressure at the entry and exit regions caused by a slight increase in the size of the contact area. The viscosity of the lubricant sharply increases at entry to the contact and sharply decreases on

exit. On exit, a constriction is created, to compensate for this loss of viscosity and to maintain the lubricant flowrate through the contact region. It is at this constriction that the minimum film thickness h_0 is found [19].

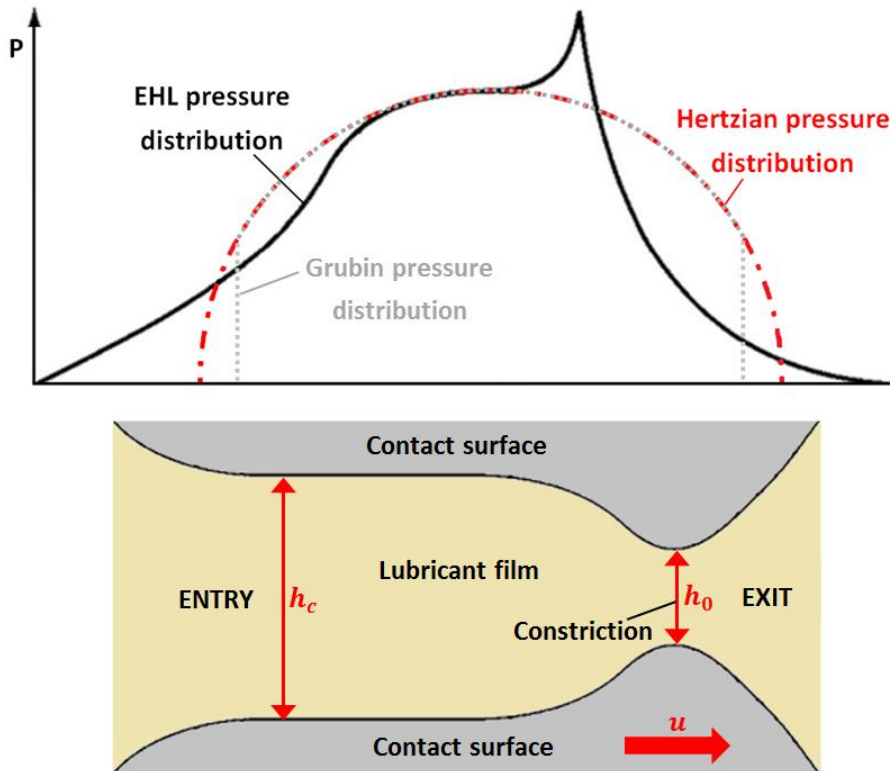


Figure 2-14: Elastohydrodynamic pressure distribution showing contact geometry with comparison to Hertzian and Grubin pressure distributions; h_c is the central film thickness and h_0 is the minimum film thickness. Adapted from [19].

An earlier model developed by Grubin [62], which is also shown in Figure 2-14 approximates the pressure distribution as Hertzian, but with pressure drops at the inlet and outlet. This theory has been superseded by the EHL model discussed above, however it is still useful for modelling contacts with traction affecting the EHL contact. Under the influence of traction, shearing of the lubricant film results in a more uniform distribution and as a result, a commonly used simplification is to ignore the EHL end constriction. Since the contact pressures at entry and exit are low in comparison to P_{max} , Hertzian theory can be used as an approximation of EHL contacts where traction is present instead of complex alternative models [19]. This simplification is used throughout this study.

It is important to be aware of the influence of slip since it is often cited as being essential for the creation of WECs [23]. This may be related primarily to the shifting of the subsurface stress field as depicted in Figure 2-11, however the direct effects of slip on the lubricant film may also be relevant. Slip causes the lubricant layer to shear and consequently heats the lubricant, reducing its viscosity and consequently the film thickness [63, 64]. It should be noted that this does not necessarily mean that high slip means a high shearing effect on the roller and

raceway surfaces, since it is the coefficient of traction μ_T that determines the level of the force due to surface traction F_T [23].

2.2. Bearing steel

Most wind turbine bearings are made from through-hardened steel with carbon concentrations in the range 0.8-1.1 weight percentage (wt%) [26] and with less than 5 wt% total alloying elements [23]. The most commonly used grade of steel used to manufacture WTGBs is DIN 100Cr6 (usually written 100Cr6), which has equivalent grades: AISI 52100 (also written 52100), EN31 and JIS-SUJ2. Other grades that are used to manufacture WTGBs include 100CrMn6 and 100CrMo7 [23]. Through-hardened bearing steel will be focussed on in this section since it is the most widely used in WTGBs and was used throughout this study. The chemical composition of both 100Cr6 [65] and 100CrMo7-3 [66] bearing steels, which were used for testing in the work described in Chapters 6 and 7 respectively, are given in Table 2-4, and their physical properties, in Table 2-5. These steels are generally provided by manufacturers in a hot rolled condition [26], with a pearlitic microstructure as shown in Figure 2-15a.

Steel grade	C%	Si%	Mn%	P%	S%	Cr%	Mo%	Fe%
100Cr6	0.93-1.05	0.15-0.35	0.25-0.45	0.025 max	0.015 max	1.35-1.60	0.10 max	Balance
100CrMo7-3	0.93-1.05	0.15-0.35	0.25-0.45	0.025 max	0.015 max	1.65-1.95	0.15-0.30	Balance

Table 2-4: Chemical composition (wt%) of commonly used bearing steels [8, 67]

Steel grade	Ultimate tensile strength (MPa)	Yield strength (MPa)	Elastic modulus* (GPa)	Poisson's ratio*
100Cr6	2150 - 2450	1400 - 2200	190-210	0.3
100CrMo7-3	2300	1700	210	0.3

Table 2-5: Physical properties of commonly used bearing steels, *typical values [22, 26, 66]

2.2.1. Shaping into bearing rings

There are a number of methods used to shape the steel into ring shaped bearing raceways and the method used influences inclusion orientation, which affects stress concentration under loading and residual stress fields developed during manufacture. The effects of inclusion orientation are investigated in detail in Chapter 5. Bearing raceways are shaped into rings before heat treatment, after which the surface is precision ground to a surface roughness, R_a of around 0.1 μm (value measured from an unused planetary WTGB raceway using the profilometer discussed in Section 4.2.3). The shaping process of the raw material, that is supplied as a bar or tube, is either by deformation of the material by forging (compressive blows used to shape material) or rolling (material is squeezed between two rollers), or by removal of the material by turning [68].

2.2.2. Heat treatment and resulting microstructure

The through-hardening heat treatment of bearing steel takes place over three stages: austenitisation, quenching, and then tempering. The steel is held at austenitisation temperature for around 30 minutes, which is typically at around 840 °C. During austenitisation, the steel structure changes from a body-centred-cubic (BCC) ferrite structure to face-centred-cubic (FCC) austenite. Cementite is dissolved, with small percentages remaining, depending on the austenitisation temperature and time [26]. It is desirable for cementite levels to be low, since its presence has been shown to reduce RCF life [69]. Quenching is the rapid cooling of the steel from the austenitisation temperature and results in a hard, crystalline martensitic structure, with typically around 6-15 volume percentage (vol%) retained austenite [70, 71, 72, 73, 74] and 3-5 vol% uniformly distributed M_3C carbides around 0.4-0.6 μm in size, that remained after austenitisation [22, 26], although these percentages can vary depending on the austenitisation and quenching processes [26]. The "M" in M_3C represents a combination of iron and chromium atoms (as well as minor amounts of some other alloying elements) and consequently such carbides are sometimes denoted $(\text{Fe,Cr})_3\text{C}$ [23, 75, 76, 77]. After quenching, the steel is held at around 160 °C in a process called tempering, which causes the decomposition of some of the retained austenite and the precipitation of a variety of temper carbides (also called ϵ -carbides) [26]. Figure 2-15b shows the steel microstructure after heat treatment, using an image taken of the microstructure of the WTGB described in Chapter 5, prepared for metallurgical observation using the process discussed in section 4.1. The resulting, rather complex microstructure, contains martensite, retained austenite, ferrite, temper carbides and undissolved M_3C carbides left over from austenitisation [23, 26]. This microstructure is examined in more detail in section 4.3.2. It has been claimed that if at least 20% austenite remains after heat treatment, the bearing may be immune to the WEC failure mode [13]. However, a low level of retained austenite is desirable as it helps to keep the bearing raceway dimensionally stable [27].

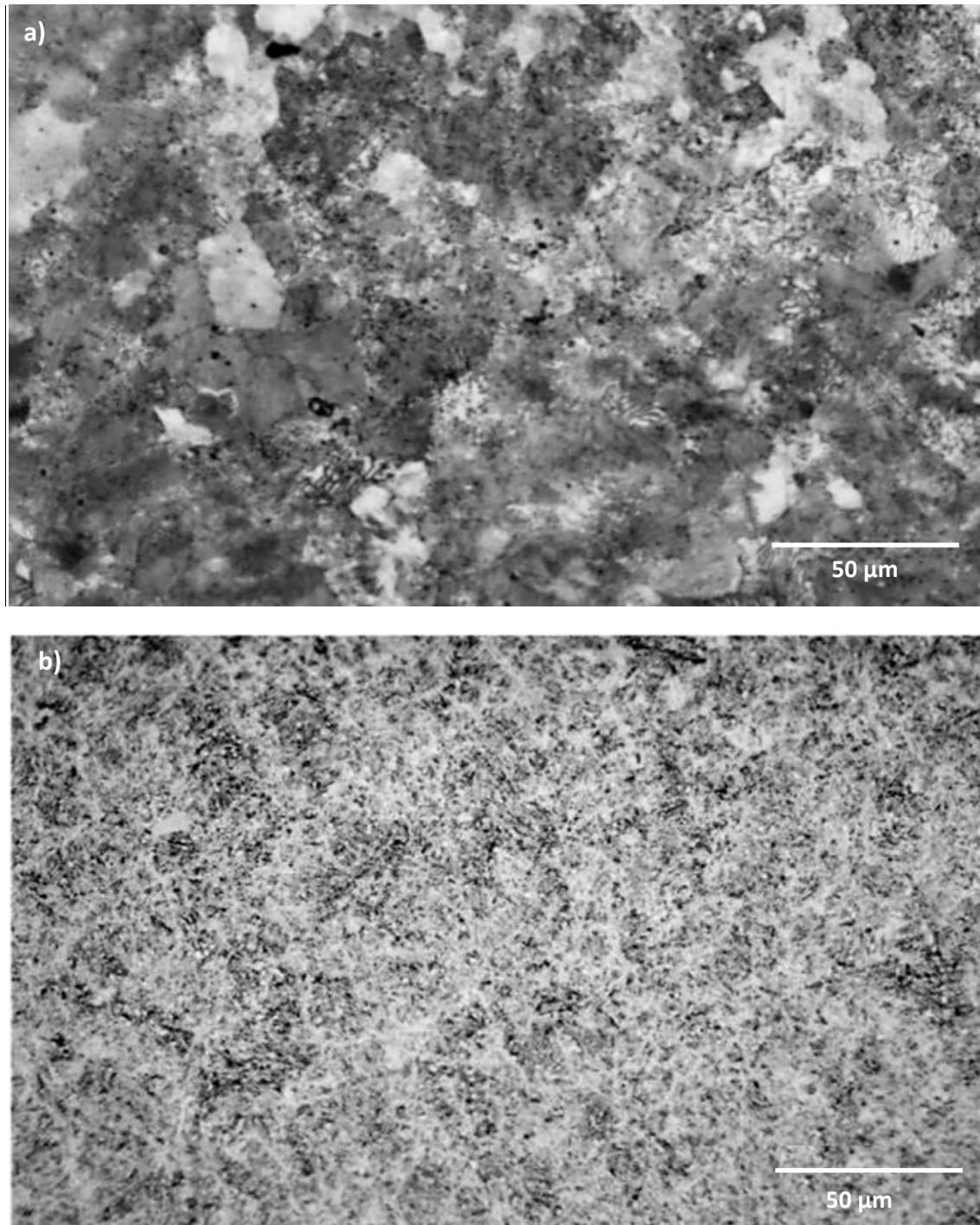


Figure 2-15: Bearing steel microstructure: a) before heat treatment, b) after martensitic heat treatment

After austenitisation, bearing steel can be made bainitic by interrupting quenching at a bainitic transformation temperature of between around 250-500 °C and holding the steel at this temperature using a molten salt bath [23]. After bainitic transformation has taken place, the steel may be cooled at a slower rate [78]. This process is called austempering and leads to a steel with a higher fracture strength, but a lower hardness [79].

2.2.3. Microstructural changes during long term rolling contact fatigue

Long term observation of the subsurface region affected by cyclic RCF stresses has revealed that microstructural changes occur in three distinct phases termed: shakedown, steady state and instable. During shakedown, the material becomes conditioned to the contact stresses due to limited plastic micro-straining [56, 80, 81], or work-hardening. The progressive reduction in plastic strain after repeated cyclic loading due to work hardening is illustrated for martensitic 52100 bearing steel in Figure 2-16. Small-scale dislocation glide takes place, leading to the generation of defects within the crystalline matrix structure, including dislocations and vacancies [82]. During shakedown, a residual stress is induced, which increases the material strength [83]. The shakedown limit is the largest stress that can be applied to the material without causing plastic deformation [26]. During shakedown in WTGB steel, some of the retained austenite is transformed to martensite [83]. After around 10^3 cycles, the shakedown phase ends and further plastic deformation does not occur as easily. At this point, the steady state phase begins and the material responds elastically to RCF induced contact stresses. The length of steady state phase depends on the contact pressure, but it may last as long as 10^9 cycles, during which no fatigue damage occurs [23]. Eventually the material becomes instable and enters the final stage of the RCF process. At this point, plastic deformation occurs (more slowly than during shakedown), the yield strength decreases and crack nucleation begins [56]. During the instable phase, a tensile residual stress is developed, which promotes growth of cracks parallel to the rolling surface [84, 85].

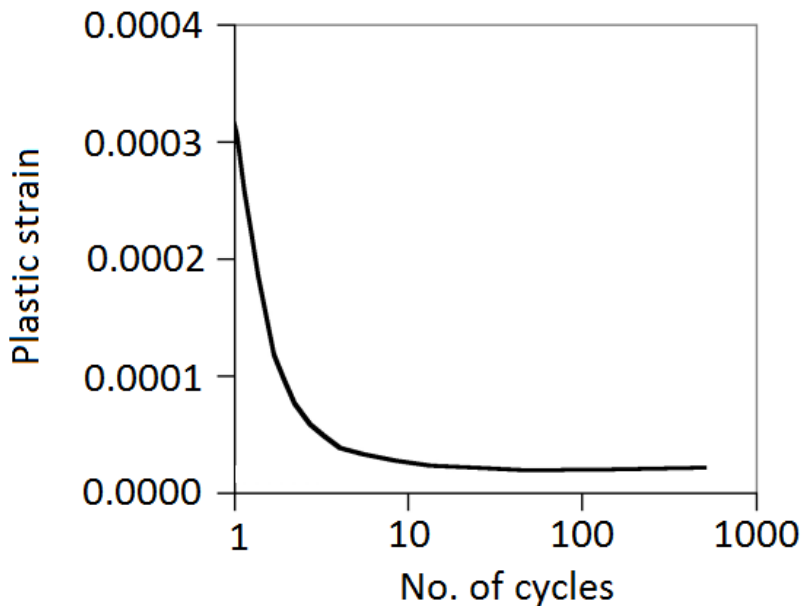


Figure 2-16: Reduction in plastic strain in martensitic bearing steel with increasing number of loading cycles (adapted from [26])

2.2.4. Inclusions in bearing steel

During manufacture, small quantities of various elements are used to aid machining of the material and to aid the manufacturing process [26]. During the manufacturing process, these elements may bond to elements in the steel or to oxygen and create small quantities of non-metallic material in the steel [26]. After manufacture is complete, the non-metallic material remains embedded within the steel matrix as an inclusion. Six groups of inclusions are described in Table 2-6 [26, 86].

Inclusion group	Description
A (sulphide type)	Highly malleable, individual grey particles with a wide range of aspect ratios (inclusion length/width) and have generally rounded ends.
B (alumina type)	Non-deformable, with low aspect ratios (< 3), black or bluish particles, aligned in the deformation direction.
C (silicate type)	Highly malleable, individual black or dark grey particles, wide range of aspect ratios (> 3), sharp ends.
D (globular oxide type)	Non-deformable, angular or circular, low aspect ratio (< 3), black or bluish, randomly distributed.
DS (single globular type)	Circular single particle with a diameter > 13 μm .
T (nitride type)	Non-deformable, strongly connected to matrix, with sharp corners

Table 2-6: Grouping of inclusion types found in steel [26, 86]

These inclusions cause a number of problems in operating WTGBs due to their differing properties from the steel matrix. The properties of selected commonly found inclusions in steel are presented in Table 2-7. Some inclusion types are brittle and may crack during manufacture or under loading. Such cracks form at stress concentration points and so may propagate through the material. If the inclusion has a different Poisson's ratio than the surrounding steel, it will create a stress concentration point under load, thus locally changing the Hertzian stress field [87]. In addition, most inclusions have a significantly different coefficient of thermal expansion (CTE) from the steel and so during quenching, contract at different rates to the matrix. The majority of inclusions have a smaller CTE than the steel (green text in Table 2-7), but manganese sulphide inclusions, for example, have a larger CTE (red text in Table 2-7). Inclusions that have smaller CTEs contract more slowly than the steel and so produce tensile and compressive residual stresses that develop parallel and normal to the inclusion/matrix boundary respectively (discussed further in section 2.2.6). This is particularly problematic for inclusions with higher yield strength than steel, such as aluminas [88]. Tensile residual stresses can be damaging to the steel. Inclusions that have larger CTEs contract faster than the steel and so the bond between inclusion and steel may become weakened or in extreme cases, the inclusion may detach from the matrix. Either directly from cooling, or by the breaking of a weakened bond after a number of stress cycles, a free surface may be created at the inclusion/steel matrix boundary, which is a potential initiation point for RCF cracking [26]. Since inclusions with larger CTEs are not well bonded to the steel matrix, the formation of cavities at the inclusion/matrix interface may occur during deformation, potentially leading to void formation. MnS inclusions with weak or non-existent bonds

(debonded) can be treated similarly to voids in the microstructure [89] as they act similarly under loading. It should be noted that tensile residual stresses are created around inclusions regardless of whether their CTE is larger or smaller than the matrix, but the locations of the tensile stress are different [90], this is discussed in more detail in section 2.2.6.

Inclusion Type	Chemical composition	Inclusion identification group	Average CTE* ($\times 10^{-6}$) ($^{\circ}\text{C}^{-1}$)	Young's modulus E (GPa)	Poisson's ratio ν
Manganese Sulphide	MnS	A	18.1	69-138	0.3
Alumina	Al_2O_3	B	8.0	389	0.250
Nitride	TiN	T	9.4	317	0.192
Calcium Aluminas	$\text{CaS}.6\text{Al}_2\text{O}_3$	B, D	8.8	113	0.234
	$\text{CA}2.2\text{Al}_2\text{O}_3$		5.0		
	$\text{CaO}.2\text{Al}_2\text{O}_3$		6.5		
Steel matrix	See Table 2-4	-	12.5	210	0.3

Table 2-7: Physical properties of selected inclusions in steel [90]*values true for temperature range (0-800°C)

During this study, it has become increasingly clear that MnS inclusions are the primary initiator (although not exclusively) of subsurface damage in WTGBs. Evidence to support this claim is presented throughout this thesis, however, it is with this in mind that the following section primarily focuses on the properties and behaviour of MnS inclusions.

2.2.5. Manganese sulphide (MnS) inclusions

MnS inclusions have been classified into three types since 1938 [91]. Although initially the classification applied to cast steels, it has been extended to include wrought steels [92]. Type I inclusions are globular in shape and appear in steels with practically no aluminium content. Type II are dendritic chain formations on grain boundaries and appear with the first traces of aluminium (0.005 wt%). Type III are strings of broken silicates and initially appear alongside Type II at levels of 0.01% - 0.03 wt% aluminium. At levels greater than 0.04 wt%, Type III is the only MnS inclusion to appear. Typical bearing steel has very low aluminium content [93], so it is therefore globular Type I MnS inclusions that are most commonly found, although in steels with low cleanliness, Type II and III can also be found. MnS inclusions in hot-rolled steels are randomly distributed and of irregular shape. During forming of the bearing raceways, the MnS inclusions are flattened and elongated in the direction of rolling [26, 92, 94], therefore their orientation may vary from bearing to bearing due to differences in the metal forming process used. Inclusions have been observed to have been elongated to different extents in bearing steel and can be defined by their aspect ratio (length/width) when viewed two-dimensionally [86].

MnS inclusions can become further elongated under loading because they deform more than the surrounding matrix [95, 96]. Cracks may be initiated along the highly strained and flattened MnS inclusions [95] due to: micro-crack initiation at localised deformation bands in the vicinity

of the inclusions; high stress concentration in the middle of the elongated inclusions leading to interfacial debonding and void formation, which are potential crack initiation sites; break up the inclusions due to lower plastic limit, causing the cracks to form within the inclusion [96], which may propagate into the bulk material [52]; or by stress concentration at the low radius of curvature inclusion tips that coincide with the position of maximum equivalent stress when inclusions become debonded from the matrix [97]. A debonded MnS inclusion acts like an elliptical hole in the material and provides the greatest stress concentration at its tips when the direction of loading is normal to the plane of its long axis [97], as has been observed to be the case in axial sections of a failed WTGB [98] that is investigated in Chapter 5 of this study.

Although free surfaces may be potential crack initiation sites, it is not necessary for a MnS inclusion to initiate a crack due to the poor bond with the bulk material. A thin, flattened MnS inclusion may itself act as a virtual crack [99] that may propagate into an actual crack. In rail steel, MnS inclusions can become significant crack initiators [100]. It was found that near to the rail surface, all MnS inclusions were deformed first in the strain direction, moved to the shear angle caused by over-rolling, and then flattened as they reached the wear surface. Wear tests on four rail steel types confirmed that almost all deformed MnS inclusions near to the wear surface were associated with cracks [99].

2.2.6. Residual Stress

Residual stress can be classified into three types, defined by the scale at which it self-equilibrates: Type 1 balances over macroscopic distances; Type 2, over a number of grains; Type 3, within a single grain [101, 102]. A thorough review of residual stresses in bearing steel is published in [26]. Type 1, or *macrostress* can arise from the different phases of microstructure in the bearing steel (described in section 2.2.2), reacting differently to external effects due to their different properties, which may include mechanical, thermal or chemical operations. Specifically relevant to this study are the effects of cyclic loading. Macro residual stresses may accumulate during cyclic loading, because the resulting strain hardening over long periods of time will lead to a local decrease in plastic stress redistribution in comparison to undamaged areas of the bearing raceways [103].

Type 2 and 3, or *microstress* are caused by defects such as inclusions that have different CTEs to the steel. Inclusions with smaller CTEs than steel, such as alumina-type, will induce tensile residual stresses around their circumference. It is sometimes overlooked that inclusions with higher CTEs, such as MnS-type, also introduce tensile residual stresses, although in a different direction. A list of commonly found inclusions in steel and their thermal expansion coefficients is presented in Table 2-7. The locations of the induced tensile (damaging) residual stresses at inclusions during quenching are illustrated in Figure 2-17. Those inclusions with CTEs that are less than that of the matrix induce tensile residual stresses around the circumference of the matrix/inclusion interface (Figure 2-17a), while those with CTEs greater than the matrix induce

tensile residual stresses in the radial direction (of the inclusion) at the matrix/inclusion interface [90]. The direction in which these residual stresses act could be crucial and so is considered throughout this study.

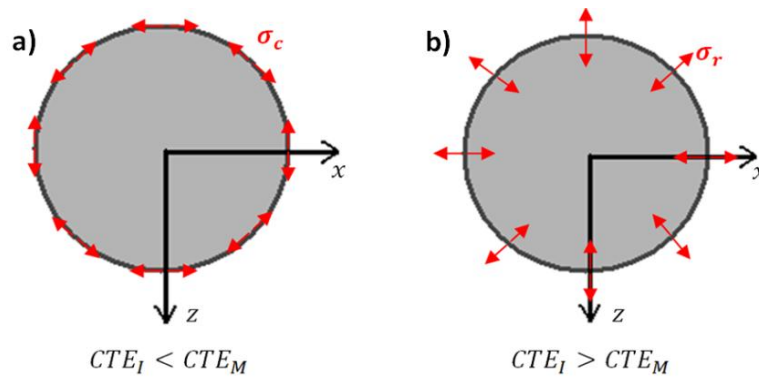


Figure 2-17: Residual stress concentrations around spherical inclusions for: a) cases where the coefficient of thermal expansion of the inclusion (CTE_I) is less than that of the matrix (CTE_M), b) cases where CTE_I is greater than CTE_M . z indicates direction perpendicular to surface tangent, x indicates any direction perpendicular to z , σ_c indicates a tensile residual stress in the inclusion circumferential direction, σ_r indicates a tensile residual stress in the inclusion radial direction. Adapted from [90]

The distribution of microstress in bearing steel varies depending on the phase. Retained austenite contains tensile residual microstress, however, for microstructures containing at least 83% volume of martensite, the residual microstress is compressive [26, 104].

Another residual stress is induced upon bearing raceways due to interference fits between bearing raceways and shafts or housings, named the *hoop stress*. Hoop stresses are tensile (damaging) for inner raceways, that are stretched by the interference fit, and compressive for outer raceways that are compressed [22]. These hoop stresses are "superimposed" on the stress field due to loading during operation, affecting the magnitudes of the maximum stresses experienced [22]. Tensile hoop stresses reduce the RCF life in general and can also be particularly damaging to subsurface microcracks since the added tensile loading will tend to pull open these cracks, encouraging propagation to the surface [23]. It is recommended that the hoop stress should not exceed about 140 MPa [105].

2.3. White etching microstructural change and features

Failure due to axially propagating WECs and WSF has been found to lead to WTGB failure within 5-10% of their L_{10} design life [3, 10, 13]. Due to the rapid expansion of the wind industry in recent years, intense research effort has been undertaken to attempt to find causes and solutions to this problem, which has become a critical issue for wind turbine operators [9, 12, 13, 15, 23, 26, 46, 56, 106, 107]. The eventual failure occurs when the material within the Hertzian zone of an operating bearing raceway subsurface is sufficiently weakened by the formation and propagation of WECs and white etching areas (WEAs), at depths of up to approximately one millimetre from the raceway surface [12]. "White etching" (and white

structure) refers to the colour of the altered steel microstructure, after having been etched in nitric acid/methanol solution (nital) [52] and is coloured as such due to the low etching response of the ultrafine nano-recrystallised carbide-free ferrite structure [10]. The appearance of the surface damage is similar to that caused by spalling due to RCF. Microstructural analyses have identified the link between these white etching features and premature failure of wind turbines [13, 26, 52, 55, 56].

White etching areas have been found to be areas of ultrafine nano-recrystallised carbide-free BCC ferrite microstructure [12, 53, 108], with no, or very few remaining carbides and are supersaturated with dissolved carbon, which makes the material brittle and harder (about 30-50%) than the steel matrix [12, 53, 109]. The movement (glide) of dislocations due to cyclic Hertzian stresses is thought to lead to repeated interaction between dislocations and carbides, which leads to the dissolution of temper carbides and the elongation of M_3C carbides [12, 110]. One theory is that when the accumulation of dislocations reaches a critical density, a dislocation cell-like structure forms to release the strain energy [111], possibly explaining why obstacles to dislocation glide, such as inclusions, voids or large carbides have been found to be areas at which WEAs form [51].

WEAs have been found to propagate from what have been termed “butterfly cracks”, due to their two dimensional appearance. Butterfly “wings” extend from a central initiation point that is usually but not necessarily a material defect. The wings typically consist of thin cracks, with attached WEAs [12]. Butterflies are discussed in detail in section 2.3.1. WEAs may also form in the near vicinity of inclusions as a separate WEA, with or without a linked crack. WEAs attached to cracks (WECs) may propagate many hundreds of micrometres through the material and possibly near enough to the surface to weaken the material sufficiently to lead to spalling failure [12, 13]. WECs are discussed in more detail in section 2.3.2. Butterflies, WECs and WEAs should not be confused with white etching bands (WEBs), which are linear areas of the white etching microstructural change, orientated at 30 and 80 to the horizontal, preceded by dark etching regions (DERs), which also occur in the Hertzian affected region [26, 112, 113, 114] (discussed in more detail in 2.3.3). WEBs however, are found after the L_{10} life of the bearing has passed, so are not considered to be a cause of premature failure [26, 115, 116]. The approximate times at which butterflies, compared to the L_{10} life and the L_{50} life (life after which 50 % of bearings could be expected to fail), DERs and WEBs appear in WTGBs are shown in Figure 2-18.

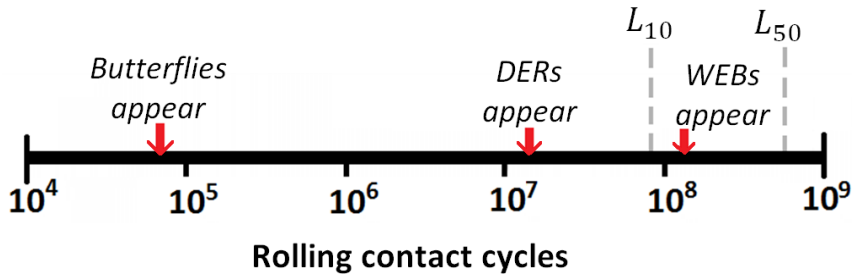


Figure 2-18: Timeline showing approximate number of cycles that butterflies, DERs and WEBS appear showing L_{10} and L_{50} lifetimes. Results from a deep groove REB tested at $\sigma_{v,max} = 3.48$ GPa. Adapted from [26, 115, 116]

It is thought that all of the features discussed above are different occurrences and/or different stages of development of the same microstructural change of steel. Table 2-8 is assembled to clarify the different terms describing the different forms of the WEA microstructural changes observed in bearing steel during the course of this study. Following this, each of the features are discussed in more detail.

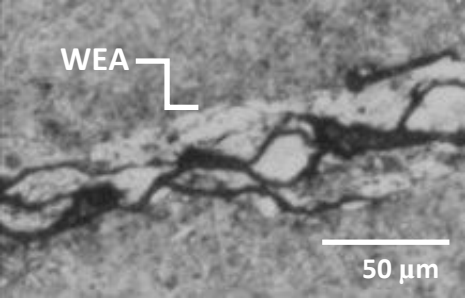
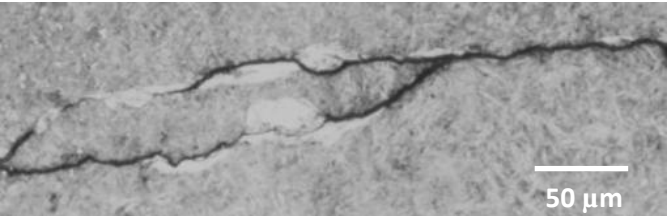
Name of feature	Description of feature	
<p>1. White structure flaking (WSF)</p>	<p>The eventual failure mode caused by the white etching microstructure change. In WTGBs, it occurs at a late stage, when brittle white etching cracks propagate to the surface, which is weakened sufficiently for material to flake away from the surface.</p>	
<p>2. White etching area (WEA)</p>	<p>An area of hard, ultrafine nano-recrystallised carbide-free ferrite microstructure that appears white when etched in nital and observed by an optical microscope.</p>	
<p>3. Irregular white etching area (IrWEA)</p>	<p>A network of WECs and possibly butterflies that has developed into an irregular shape (not a single long and thin straight crack)</p>	
<p>4. Butterfly crack</p>	<p>A region of WEA that has the appearance of a butterfly, with up to four white etching microstructure “wings” at angles of between 30 to 50° and 130-150° from the over-rolling direction. They may or may not have a central initiating defect.</p>	
<p>5. White etching crack (WEC)</p>	<p>An extended, long and thin WEA that is adjacent to a physical crack in the material.</p>	
<p>6. White etching layer (WEL)</p>	<p>An extended layer of white etching microstructural change attached to the contact surface.</p>	

Table 2-8: Clarification of the different stages and forms of the white etching microstructural change in steel. Images reproduced with thanks from [48], with permission from SAGE publishing.

2.3.1. Butterflies

Butterflies are small (of the order of 20-100 μm) damage features that form within the Hertzian subsurface stress field and can diminish the load bearing capacity of the material in their vicinity [106]. Considerable research effort has focussed on the formation of so-called “butterfly cracks” or “butterflies” [12, 13, 26, 50, 52, 53, 54, 55], named such due to their two-dimensional appearance. It has been shown that microcracks initiate at impurities and propagate between $30\text{-}50^\circ$ and $130\text{-}150^\circ$ from the over-rolling direction, which is likely to be due to the position of maximum Hertzian unidirectional shear stress (see Figure 2-8) [12]. Butterflies have been reported to initiate most commonly at inclusions [51], but voids and carbides may also be candidates for butterfly initiation [12, 13] and other studies have found that voids are most likely to initiate butterflies [117, 118]. Impurities may be initiation points due to Hertzian stress concentrations around the inclusion, residual stress from heat treatment, the creation of free surfaces during quenching, and/or dislocation accumulation, all of which have been previously discussed. WEAs form adjacent to the cracks, or possibly form first and promote microcrack growth giving the resulting features the appearance of “butterfly wings” [12, 13]. During torque reversals caused by extreme loading conditions, symmetric cracks may form at the same angles, in the direction opposite to overrolling [12], a process that is illustrated in Figure 2-19.

When considering the Hertzian unidirectional shear stress, it is not clear why two-winged butterflies commonly form during RCF tests, as shown in Figure 2-19a, since the stress field is symmetric and theoretically, four winged butterflies should be found [26]. The reason for this is that the stress field is affected by the direction of roller motion. If the RCF test is stopped and the over-rolling direction reversed, four-wing butterflies are created, as shown in Figure 2-19b [119]. Since four-winged butterflies are sometimes found in WTGBs, this may suggest that torque reversals in WTGB actually cause short reversals in the over-rolling direction of bearing rollers; or alternatively without reversal, when the first two wings form preferentially and the other two, after further exposure to unidirectional shear stress. The propagation of a butterfly wing to the surface may lead to spalling as shown in Figure 2-19c.

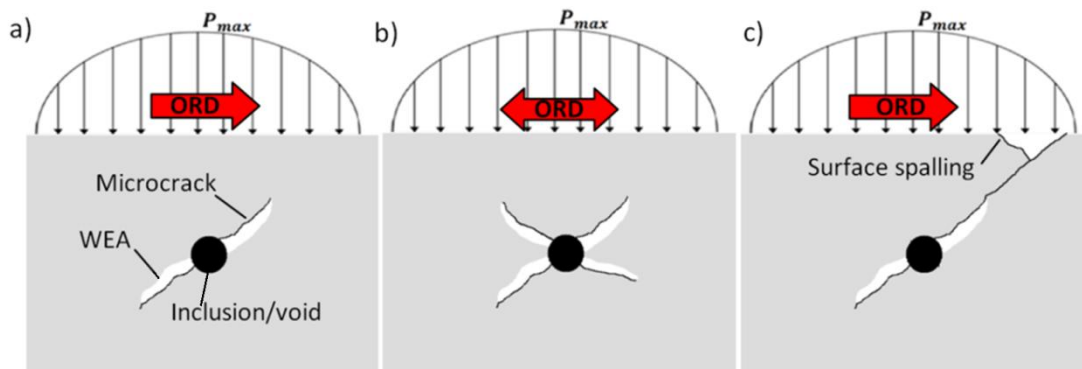


Figure 2-19: Butterfly formation in wind turbine gearbox bearings: a) two-wing butterfly formation with single over-rolling direction (ORD), b) four-wing butterfly formation with reversal of over-rolling direction, c) propagation of butterfly initiated crack to raceway surface leading to spalling.

It is not known whether the cracks propagate along the WEA (or “wing”), or if the cracks proceed the WEA and encourage its growth. Evans et al. propose that crack and wing form cooperatively, which may explain why the WEA is commonly observed to form on only one side of the cracks [106]. An alternative theory proposes that the WEA forms first and the cracks form within the WEA to relax the stress concentration at the harder WEA material, which cannot plastically yield like the surrounding material [120]. It has been argued that the white matter can occur independently of cracks if the strain amplitude caused by cyclic loading is above a certain level and that cracking occurs preferentially if this value is exceeded [121]. There is also some dispute that butterfly cracks are directly linked to the development of a propagated WEC. One theory is that when a crack or WEA is at a typical 45 ° butterfly orientation, it is likely to have propagated from a butterfly defect [51], since it was initiated by the unidirectional shear stress acting in this direction. An alternative opinion is that there is little evidence to support the fact that butterflies may propagate into irWEAs or WECs [13].

Lund [55] found that butterfly initiation is dependent on $\tau_{0,max}$ generated during RCF, exceeding a value of approximately 400 MPa. This value can be used to define a threshold depth at which butterflies are formed at different Hertzian contact stresses, as shown in Figure 2-20. Grabulov [53] found this limit to be at around 450 MPa for Al_2O_3 inclusion initiated butterflies (although this result is based on an unnaturally high number of artificially introduced large $\sim 45 \mu m$ diameter Al_2O_3 inclusions). It has been found that when the contact stress exceeds 3.0 GPa, butterflies may be observed at $L_{10}/1000$ rotations [115], although it should be noted that this contact stress is unrealistically high when considering long term exposure of the material forming WTGB raceways. Other thresholds of butterfly initiation have been based on levels of P_{max} and have been found to be at around 1.4 GPa [33] and in another study; 2.0 GPa for clean steel and 1.3 GPa for dirtier steel [122], proving that steel cleanliness is critical in preventing butterfly formation. Twin disc testing and other methods have been used to successfully recreate butterflies in 100Cr6 bearing steel and are discussed in section 2.3.6. It has been found that “butterflies” propagated into WEC networks in twin disc testing where the samples had been precharged with hydrogen. The acceleration of butterfly initiation and WEC propagation by hydrogen embrittlement, generated by lubricant aging, water contamination, or hydrogen initially present in the steel microstructure [12, 123, 124] is investigated in section 2.3.5.5.

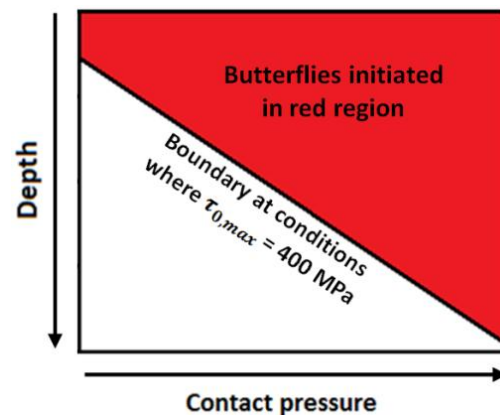


Figure 2-20: Butterfly initiation threshold in terms of depth and contact pressure (adapted from [55])

2.3.2. White etching cracks

Currently, WTGB failure via white etching cracking is not fully understood, despite intense research effort [13, 36, 46, 50, 52, 53, 55, 107, 109, 123]. WEAs are physical cracks in the material subsurface decorated by WEAs [52]. Despite considerable evidence [26, 50, 52, 53, 56, 106, 110, 33, 125], there has been, as yet, no method devised to prove absolutely that butterflies are indeed the point of damage initiation. Findings in [53, 125] suggest that WEAs are formed at butterflies by an evolving microstructural change leading to the nanocrystalline structure by material transfer and “rubbing” between inclusions and the steel matrix. Impurities may be initiation points due to local Hertzian stress concentration, residual stress from heat treatment, the creation of free surfaces during quenching, and/or dislocation accumulation [26]. WEAs form adjacent to microcracks, or possibly form first and promote microcrack growth. As well as in WTGBs, WEAs have been observed to form in bearings used in industrial applications including: marine propulsion systems, paper mills, crusher mill gearboxes, industrial variable drives, or lifting gear drives [10]. Evidence that microcracks precede the formation of the attached WEA is presented in [126], where RCF cracks were created in 100Cr6 bearing steel with artificially introduced voids, appearing before the WEA. This evidence suggests that it is the repeated contact of the free surfaces, formed at microcracks, against each other, that leads to the deformation and hardening required to create the WEA microstructure [26]. WEAs can form as cracks parallel to the surface, or as irregular branching crack networks that follow pre-austenite grain boundaries [16].

2.3.3. Dark etching regions and white etching bands

WEBs have the appearance of thin, elongated, white strips that can form at steep or shallow angles of 80° or 30° to the surface respectively [127]. The level of Hertzian stress and the number of fatigue cycles (see Figure 2-18) influence the formation of WEBs [13]. WEBs form in high quality bearing steels (100Cr6 or similar) and are preceded by the formation of a DER, in

comparison to the colour of the etched undamaged steel, and form at depths of up to around 0.3 mm [112, 128] (value dependent on the contact pressure) and centred around the location of τ_{max} [113, 129]. The DER microstructure is heterogeneous, consisting mainly of martensite separating severely deformed bands [112, 113, 114], appearing dark since the etchant preferentially attacks the bands that appear dark when viewed with an optical microscope [26]. WEBs develop within the DER after further rolling contact cycles as shown in Figure 2-18. Both WEBs and DERs have been found to be linked to martensitic decay and carbide "depletion" [26]. A comprehensive review of DERs and WEBs is presented in [26] but since these features have been identified as distinct from WECs and butterflies, they will not be considered further in this thesis.

2.3.4. White etching layers

The formation of WELs is common on machined surfaces, on railway tracks and in other applications where steel surfaces rub together [130]. The formation occurs during periods of high surface sliding at high friction (or traction) coefficients; for example during a railway wheel lock-up [131]. The formation method is thought to be via one of two methods:

1. The surface traction is high enough to lead to temperatures high enough to austenitise the steel, leading to the formation of a layer of highly deformed martensite [26].
2. Mechanical action causes the initial microstructure to become alloyed, creating a carbon supersaturated ferrite [132].

WELs are not thought to be a major problem in WTGBs although they have been observed to appear (see section 5.2.6). However, observation of the manner of their formation and of their microstructure may offer insight into the formation of subsurface WEAs and WECs, which appear to be similar in microstructural appearance to WELs.

2.3.5. Factors affecting the development of WECs

A number of factors have been found and/or are suspected to contribute to the initiation and/or propagation of WECs. These factors are investigated below:

2.3.5.1. Extreme Loading

The loading conditions experienced at the contact between the roller and raceway affects the initiation and propagation of WECs in a WTGB [12], regardless of the method that has led to their formation. As has been previously discussed, WEC initiation is more likely when the material has experienced higher levels of stress. The transient nature of the wind and the subsequent operational actions of a WT creates extremely harsh operating conditions for drivetrain components leading to overloading, causing stress levels beyond the bearing raceway material yield strength. Local yielding may occur in the bearing subsurface, leading to microstructural change and possibly the initiation of a WEC [17, 109]. Overloading can be

caused by short-term impact loading, torque reversals and/or misalignment of gearbox components due to deflections in the drivetrain structure, which may arise from: fluctuating wind loads, non-synchronisation of blade pitch, sudden braking, sudden and frequent grid drops, generator/grid engagements [12], extended periods of high rotor torque during the high wind speed season, misalignment due to deflections of gearbox components, oval compression of gearbox bearings due to deflections in gearbox support structure, oval compression of blade pitch bearings causing short term torque spikes due to delayed blade pitching [10], non-torsional loading [58], preloading on account of tight fits, excessive drive-up on a tapered seating, extreme events leading to torque reversal (for example emergency shutdown), or impact during fitting [133, 134]. The high variability of wind conditions and subsequent turbine controls leads to frequent connections and disconnections between the generator and grid, causing the gearbox to experience frequent torque reversals and overloads [10]. Such torque reversal events can occur approximately 15,000 times per year [10] (although this number may vary considerably depending on the WT and the bearing location within the gearbox).

During torque reversals and transient wind loading, the acceleration and deceleration of the drivetrain can lead to frequent impact events at WTGBs. Such events are most serious when bearing rolling elements are in the unloaded zone, where they may be instantaneously loaded beyond the material's yield strength in misaligned conditions, along one or two contact points in the load profile [12]. These periods of heavy and dynamic loading lead to transient raceway stresses sometimes exceeding 3.1 GPa and generator engagements/disengagements can lead to stresses up to 2.5-4 times higher than during normal operating conditions [10] well above the yield strength of bearing steels [15]. At such high contact stresses, failure may occur over a relatively low number of load cycles due to low cycle fatigue [135].

As previously discussed, operating WTGBs are more heavily loaded in the "loaded zone", within which rollers experience high traction forces and are well aligned. In the unloaded zone, however, traction forces are much lower, resulting in poor roller alignment [20]. An instantaneous change in shaft loading from a torque reversal relocates the loaded zone, resulting in high loads being applied to the raceway by misaligned rollers. A small misalignment angle can alter what is normally a line contact between the roller and raceway to a point contact, which will lead to far higher contact stresses on a small area of the raceway.

2.3.5.2. Adiabatic heating due to hammering impact loading

It has been hypothesised by Hansen Transmissions, that high frequency impact loading creates the white etching microstructural change due to adiabatic localised heating in the vicinity of inclusions [14]. It is thought that adiabatic shear bands may be formed, which have long been known to appear white after etching [136]. However, this form of damage would require the strain rate of deformation to be large enough to avoid the dissipation of heat [26]. Additionally, adiabatic shear bands are not associated with cracks [26], however, as has been

previously discussed, WECs that have been found in various studies [13, 36, 46, 50, 52, 53, 107, 109, 123] are linked to cracks. It therefore seems likely that adiabatic shear bands are not the same as WECs, although hammering impact loading may be damaging in other ways as discussed in the previous section (2.3.5.1).

2.3.5.3. Slip

Slip could be a driver of WEC development, either directly, due to high levels of surface traction resulting in shear stress concentrations being shifted closer to the surface (as shown in Figure 2-11), meaning that any crack would have less distance to propagate in order to reach the surface; or indirectly, by shearing the lubricant layer [19] and/or the fact that the creation of fresh surfaces may lead to hydrogen liberation [12], subsequently leading to hydrogen embrittlement (see section 2.3.5.5).

2.3.5.4. Electrical discharge damage

When electrical current passes across WTGB raceways, a process similar to arc welding occurs heating the steel to high temperatures and in extreme cases, melting it. The discharge current may come from the generator, lightning strikes, pitch motors, or static discharge and is observed in the field to be caused by damaged insulation and grounding protection damage [9]. It is possible that such damage produces fresh steel surfaces, encouraging the release of hydrogen, which accelerates WSF damage [12] (see section 2.3.5.5). Static discharge has been experienced in automotive bearings, where asperity contacts release static charge, liberating hydrogen from water that had penetrated into the bearing and mixed with the lubricant [46].

2.3.5.5. Hydrogen Embrittlement

It has become increasingly clear that WSF is accelerated by the presence of hydrogen. Numerous tests have been conducted to investigate the influence of hydrogen, including RCF [51, 56], high frequency ultrasonic loading [137], low frequency loading [138, 139] and tensile testing [140], with the general conclusion that the presence of hydrogen is detrimental to fatigue life. Although there are many models to explain this phenomenon, two prevalent theories have emerged that describe the detrimental effects of diffusible hydrogen leading to the embrittlement of bearing steels. The first is via *hydrogen-enhanced localised plasticity* (HELP), which was proposed by Beachem [141] in 1972. The HELP theory suggests that hydrogen is absorbed into the steel matrix and enhances the ease of dislocation motion, while simultaneously decreasing the stress limits for crack propagation [51]. Hydrogen induces localised plasticity at crack tips [142, 143], effectively making crack growth possible at lower contact stresses. The second theory is named *hydrogen induced decohesion*, which was developed by Troiano [144] and modified by Oriani and Josephic [145]. This theory suggests that dissolved hydrogen in the steel matrix reduces the strength of interatomic bonds, therefore promoting decohesion and encouraging cleavage fracture of the material [146]. Cracking occurs at lower stresses due to the lower cohesion strength of the steel [147].

Hydrogen gas (H_2) is diatomic in its natural state and therefore too large to enter steel. These molecules must be broken up into single atoms by chemical reaction or electrochemically if it is to penetrate (diffuse) into the steel subsurface [12]. Sources of diffusible hydrogen include: water in the bearing lubricant [148], degradation of products in the lubricant [149]; trapped hydrogen in the steel from heat treatment [26]; which may be released when fresh surfaces are created both on the surface and subsurface and particularly at crack tips [51], which creates a vicious cycle; the trapping and subsequent release of hydrogen from MnS inclusions [150] (discussed further below); and from stray electrical currents [12]. There seems to be a critical concentration of hydrogen of around 1 part per million [26, 151] below which bearings have relatively long lifetimes, and above which, the fatigue life declines sharply [151].

2.3.5.6. Inclusions as initiators

All inclusions may act as crack initiation sites under high enough contact stress [26]. In 100Cr6 steel, enough evidence is now available to confirm that MnS inclusions are the most likely to interact with butterfly cracks [52, 56, 33] despite older studies disputing this [152, 153, 154]. These older studies did not believe that MnS inclusions were damaging since, unlike harder inclusions, MnS inclusions and other sulphide inclusions do not act directly as stress concentrators [26, 154]. Since MnS inclusions have been found to be the most likely to interact with WECs, this section will focus on this inclusion type, although as discussed in previous sections other inclusion types (particularly aluminas) have also been found to interact with butterflies.

Shorter MnS inclusions have been found to be more likely to initiate damage than longer inclusions, with the ideal length for crack propagation found to be smaller than 20 μm (based on a sample size of 76 WEC-interacting inclusions) [52]. As previously discussed, free surfaces created during quenching and/or separation of the inclusion from the matrix during operation may be locations for the initiation of RCF cracking [26]. Cracking has been found to be sensitive to the direction within the raceway; with vertical WEC branches appearing to propagate when viewed in circumferential cross-sections and branches that are parallel to the surface in axial cross-sections [52]. Another possible influence of MnS inclusions, is that their boundaries are thought to act as trapping sites of hydrogen, which may lead to hydrogen embrittlement [155]. The accumulation of hydrogen atoms at MnS inclusions may aid crack initiation [150].

Fracture mechanics relates crack opening and propagation to the type of applied loading, which is defined by three modes that are illustrated in Figure 2-21 and listed below [48]:

1. Mode I: Tensile loading across the crack
2. Mode II: Shear loading in the plane of the crack (in-plane)
3. Mode III: Shear loading out of the plane of the crack (off-plane)

It is thought that for microcracks that initiate at inclusions, the initial extent of short crack growth is caused by Mode I loading of the inclusion, which consequently means that a tensile

stress field must exist across the inclusion [48]. Since cracks have been observed to form at inclusion tips, it follows that the tensile stress field must exist at that location, although there may be alternative reasons explaining crack initiation at the tips, which are discussed below. Cracks are thought therefore, to be initiated in the vicinity of inclusions due to this residual tensile stress, which decreases to zero with distance from the inclusion, meaning that crack growth is limited. However, the cyclic stress field can load the crack by Mode II/III, which can cause further propagation and spread to greater (and more damaging) distances from the inclusion [48, 90]. Whether or not the crack will open, and propagate by Mode I/II/III loading is governed by stress intensity factors that are discussed in [90]. For crack initiation based on Mode I to induce tensile loading across the crack, an inclusion needs to have a CTE lower than that of the steel matrix (see Figure 2-17), which would not explain why MnS inclusions have been found to be the most likely to interact with WECs. It has been postulated that it is essential for MnS inclusion to contain oxide parts in contact with the surrounding steel matrix at these crack tip locations [50, 55]. Oxide parts have a smaller CTE than the steel matrix [26] which would create this harmful tensile residual stress and it has been found that MnS inclusions that contain oxide parts are more harmful than those that do not [50, 55].

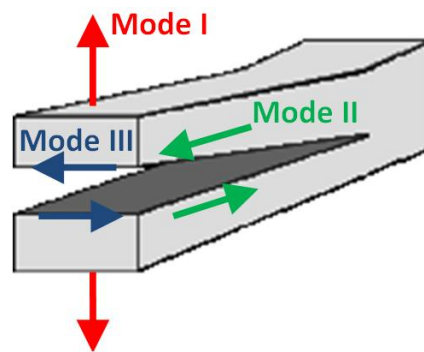


Figure 2-21: Modes of loading affecting crack initiation and growth

However, an alternative three-stage process for MnS initiated WEC formation has been proposed [109]. First the inclusion fractures along the length of its major axis. Secondly the crack propagates into the bulk material surrounding the inclusion. Finally, white etching areas (WEAs) form along the cracks. For a butterfly to exist at a MnS inclusion, Evans et al. [52] found that the inclusion was always cracked in the direction of the major axis and that the inclusions themselves were initiators of cracks/butterflies that propagated to form WECs. Such crack initiation is by Mode I loading [48], but since it takes place inside the inclusion, it may be possible for an inclusion with a higher CTE than steel, such as MnS to initiate the crack. As discussed earlier, residual stress concentrations around such inclusions, formed during quenching may affect this process, shown in Figure 2-17.

2.3.6. Laboratory tests to recreate white etching microstructure

A number of researchers have successfully recreated butterflies and white etching cracks in test specimens. Their main results and the operating conditions used to create the damage are discussed in this section.

Evans, et al. [51] used a TE-74S twin-disc machine, with steel rollers of size 26mm and 52mm to simulate wind turbine transient conditions. Slip levels from 0-15% were tested, at contact pressures of up to 5 GPa. Contact pressure and slip were changed to various levels during a single test, to simulate transient conditions during wind turbine operation. Tests were carried out using rollers made from 100Cr6 steel, initially with comparable hydrogen content to bearing steel, then with increased levels of hydrogen, since hydrogen embrittlement is known to accelerate WEC formation. Upon examination of the tested rollers, no WECs were found in the non-hydrogen charged tests, although limited numbers of butterflies were found. In the hydrogen charged tests, the number of butterflies formed increased with contact pressures in the range of 1.2 - 2.0 GPa and with the number of rolling cycles. WECs were formed at various contact pressures between above 1.2 – 2.0 GPa depending on the hydrogen charging method used.

Evans, et al. [52] also conducted tests on a non-hydrogen charged high-speed-shaft WTGB using a large-scale test rig designed to simulate transient WTG operating conditions at maximum contact pressures of around 2.15 GPa and for 1.4×10^6 stress cycles, equivalent to 130% of the bearing L_{10} life. Amongst other findings it was found that butterflies could propagate to form WECs and that WECs initiate at inclusions.

Reullan [54] also used a twin disc machine with hydrogen charged and non-hydrogen charged test specimens to recreate butterflies. Contact pressures between 1.0 – 3.5 GPa were tested at slip ratios of up to 30%. Like Evans, Reullan recreated WECs on the hydrogen-charged samples but not the non-hydrogen charged. Reullan also tested a REB on a full scale test rig at contact pressures of 2.56 – 3.40 GPa and slip ratios of 13-22%. WECs were created on both hydrogen-charged and non-hydrogen charged bearing inner races. WECs initiated primarily (and more extensively) at inclusions in the hydrogen-charged samples and at the boundary between a near surface DER and the steel matrix in the non-hydrogen charged samples. This important finding suggests that hydrogen concentration at inclusions may be relevant.

As was briefly mentioned in section 2.3.1, Grabulov [53] successfully recreated butterflies at (large $\sim 45 \mu\text{m}$) artificially introduced Al_2O_3 inclusions using a test rig that simultaneously applied a contact pressure of 3.2 GPa for 1.3×10^8 stress cycles at an extremely high rotational speed of 15,000 rpm. It was found that the damage was as a result of shear stress leading to material transfer from a debonded inclusion to the surrounding steel matrix. Material transfer across the gap led to the creation of butterfly cracks that then propagated away from the inclusions. Butterflies were created at maximum orthogonal shear stress $\tau_{O,max}$, of around 450

MPa. While these results are very interesting, it must be noted that the steel may not have been truly representative of bearing steel since the inclusions were artificially introduced.

Lund [55] exposed spherical ball bearing to RCF at contact pressures of up to 4.9 GPa to find conditions at which butterflies were formed. As mentioned in section 2.3.1, it was found that a maximum orthogonal shear stress $\tau_{O,max}$ of 400 MPa was required to initiate butterflies and that the maximum depth at which they were found decreased as the magnitude of the contact pressure decreased. The trend was not affected by the whether the steel had a martensitic or bainitic microstructure.

A study by Carroll at the University of Sheffield [156] investigated rolling contact fatigue on rail track using a twin disc machine, to create a hard WEL just below the rail surface. Tests were conducted at contact pressures of 1,500 MPa for a period of 5 seconds, with discs rotating at around 400 rpm in the same direction, so that the contacting surfaces moved in opposite directions, rubbing against each other and creating extremely high slip levels. Testing found that the growth of cracks depended greatly on the strain history of the subsurface pearlite structure. The WEL was found to initiate at weak spots at the surface, such as grain boundaries, or WEL/pearlite boundaries. 'Corrogations', or ripples on the rail material surface, displayed WELs at their peak, although it is not clear whether they lead to the formation of the WEL or vice versa [156].

2.4. Dynamic modelling of wind turbine gearboxes

From the findings in sections 2.1– 2.3, it has become clear that the complex loading conditions and their effect on WTGBs are not fully understood, despite the many theories suggesting different modes of failure and factors affecting them. It seems important therefore, to model a WT drivetrain to establish the levels of contact stress that are found in WTGBs during normal operating conditions. A review of dynamic modelling methods and previous work in this area is presented.

2.4.1. Rotating machine dynamics

Every rotating machine comprises of three principle component types: rotors, bearings and supporting structures. A rotor component has mass and inertia and is at the heart of any rotating machine, and therefore, any analysis must first determine the dynamic properties of the rotor element. Each rotor is connected to the supporting structure by bearings, which support the rotor up to a certain load capacity and with certain stiffness and damping. The bearings make a significant contribution to the rotating machine dynamics so it is important to model them accurately. The structure supporting the bearings consists of stators and foundations; the stator being an integral part of the machine and the foundation holds the machine in place [157].

From Newton's second law, we have the well-known linear equation of dynamic motion,

$$m\ddot{x} + c\dot{x} + kx = f(t) \quad (2.13)$$

where: m represents the mass of an object; c and k , the damping and stiffness of its supporting structure respectively; \ddot{x} , \dot{x} and x represent its acceleration, velocity and displacement at a point in time; and $f(t)$ is time dependent force loading.

In rotational dynamics, equation 2.13 is adapted to a polar coordinates system and to include rotational inertia rather than mass [157]. This equation shows that a rotating system can be defined by a series of polar moment of inertias I_p , damping coefficients c_r , stiffnesses k_r and time-dependent torque loading $\tau(t)$.

$$I_p\ddot{\theta} + c_r\dot{\theta} + k_r\theta = \tau(t) \quad (2.14)$$

In matrix form, these equations are combined to represent six degree of freedom (DOF) motion, both linearly and rotationally, as shown in equation 2.15 [157], where $[M]$, $[C]$, and $[K]$ are the inertia, damping and stiffness matrices representing the modelled components respectively; $\{\ddot{X}\}$, $\{\dot{X}\}$ and $\{X\}$ represent the 6 DOF acceleration, velocity and displacement of each modelled component respectively and $\{F\}$ represents the calculated forces and torques at the modelled bearing supports.

$$[M]\{\ddot{X}\} + [C]\{\dot{X}\} + [K]\{X\} = \{F\} \quad (2.15)$$

2.4.2. Modelling strategies

Peeters et al. [158] compared multibody WT gearbox models with varying complexity and their strengths and weaknesses, identifying three types of model:

- **Type 1:** Purely torsional multibody models, modelled with one degree of freedom (DOF);
- **Type 2:** Six DOF rigid multibody models with discrete flexible elements;
- **Type 3:** Fully flexible multibody models.

Type 1 models are generally carried out to model drivetrains in the early design stage, but insights into gearbox modal behaviour are limited [159]. They are suitable for investigating dynamic torque levels throughout the gearbox, but are not capable of modelling detailed reaction forces on the bearings. A study by the University of Strathclyde and Romax Technology [160] describes the development of a basic type 1 gearbox model, which is used to simulate normal operation and emergency stop conditions. It was found that most of the off-axis loads are absorbed by the main rotor shaft bearings before they enter the gearbox, a conclusion that has also been reached by the USA-based National Renewable Energy Laboratory (NREL) [161]. Using the current failure-by-fatigue analysis method as presented in the international standards [40], it was concluded that the planetary bearings in the first stage of the gearbox were subject to the highest loads and showed the greatest amount of fatigue damage, but that the damage was well within acceptable limits. Normal stops led to no more

damage than normal operation but emergency stops led to higher damage levels, especially in the modelling of 10 second period after grid loss. The model did not predict any excess loads on the HSS [160].

Type 2 models consist of rigid components free to move in 6 DOFs, supported by linear springs that represent component stiffness. They can be used to investigate the influence of bearing stiffness on the internal dynamics of the drivetrain [158]. Helsen et al. [159] investigated a type 2 model, finding that it was applicable for use in both planetary and parallel stages as well as complete gearboxes. These models are not able to take the internal stresses and strains of drivetrain components into account, although they are capable of calculating detailed reaction forces on the gearbox bearings. A bearing stiffness matrix with off-diagonal zero terms was used, meaning that the effects between degrees of freedoms were not coupled, and with constant diagonal terms, meaning constant stiffness values, and zero bearing damping. This model could be refined to provide a more realistic simulation.

It has been shown that fully flexible models (type 3) are the most accurate and are able to calculate internal component stresses and strains, but with high computational expense [158, 159]. Further research by the GRC [16, 161] investigated the computational cost of each model type. A gearbox model was developed, initially as a two mass system (rotor and generator), and then the complexity was incrementally increased, while being matched to experimental acceleration data from a tested braking event. It was found that the computational cost of using type 2 models was 400 % higher than that of type 1, with type 3 a further 26 % higher than type 2. The conclusion drawn was that type 1 models are time effective and that accurate modelling is possible using type 2, without the need for using finite element analysis (FEA).

2.4.3. Key findings from previous modelling studies

The GRC also examined the effects of changing the complexity of the gear tooth model. One analytical analysis method ‘slices’ the gear contact across the tooth width into many ‘spring-damper’ force elements, allowing both the radial and axial forces to be calculated over the whole width of each gear tooth. This is important when analysing helical gear contact, since axial forces are introduced by the angled gear teeth, which must be supported by the bearings and may lead to shaft bending and therefore misalignment. It was determined that a 35-slice contact model was found to be the optimum compromise between accuracy and computational cost [162]. It was also noted by the same GRC report, that changing bearing clearances has a negligible effect on results, but that such models are sensitive to bearing stiffness values [162]. NREL has found that turbine size has little effect on the type of failure occurring in WTGs. Therefore, failures that occur in smaller WTGs are also found to occur in larger gearboxes. This confirms that any conclusions taken from a study based on a small-scale WT, such as the NREL 750 kW test-turbine, will be relevant for larger, more modern, WTGs [17].

2.4.4. Generator modelling methods

A challenging part of any WT drivetrain model is the method used to simulate the generator, since instantaneous fluctuations in torque, in response to input conditions are required. One modelling method is utilised by the NREL developed *FAST* drivetrain simulation package, which uses two different generator models to provide generator resistance torque: the simple induction generator model and the Thevenin-equivalent model. The "simple induction generator model" is a good starting point and is capable of providing generator resistance for most operation modes, although it is too simple to model turbine start-up [17]. This method requires four inputs:

1. Synchronous generator speed, ω_{syn} .

2. HSS rated speed:

$$\omega_{HSSrated} = \omega_{LSSrated} \times GR \quad (2.16)$$

where GR is the gearbox ratio and $\omega_{LSSrated}$ is the LSS rated speed.

3. HSS rated torque:

$$T_{HSSrated} = T_{LSSrated} \times GR \quad (2.17)$$

where $T_{LSSrated}$ is the LSS rated torque.

4. Pullout torque (the highest level of resistance that the generator can supply)

$$T_{pullout} = PR \times T_{HSSrated} \quad (2.18)$$

where PR is the pullout ratio.

Using these values, a simple generator resistance torque curve can be calculated for any conventional wind turbine, as shown in Figure 2-22.

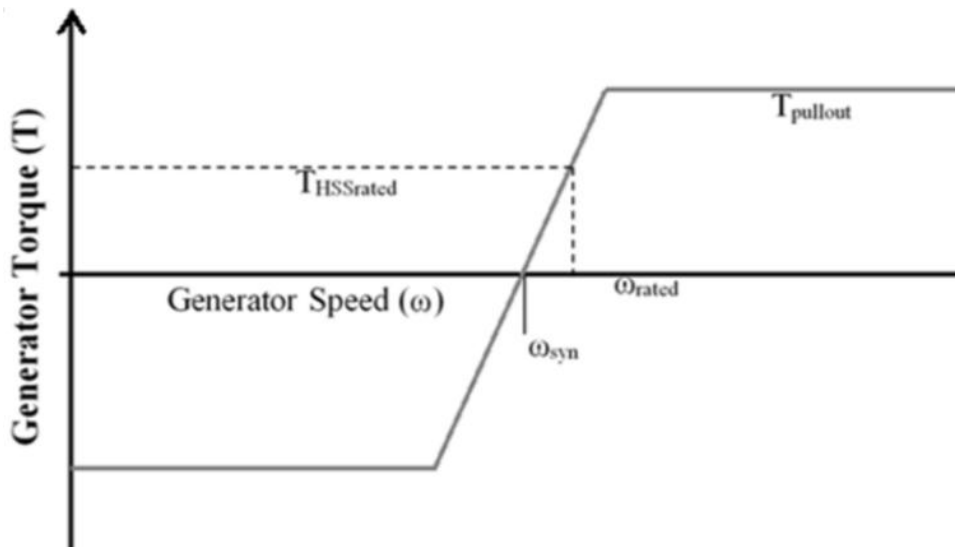


Figure 2-22: Simple induction generator resistance torque curve (adapted from [17])

Mohit Singh [163] developed a more complex, but more accurate, generator model from an equivalent circuit. This equivalent circuit can be used to construct a Thévenin-equivalent generator model based on the theorem in [164]. Figure 2-23 shows an example Thévenin-equivalent-induction generator torque/speed curve. This model is suitable for modelling generator resistance torque during all operating conditions, including turbine start-up [17].

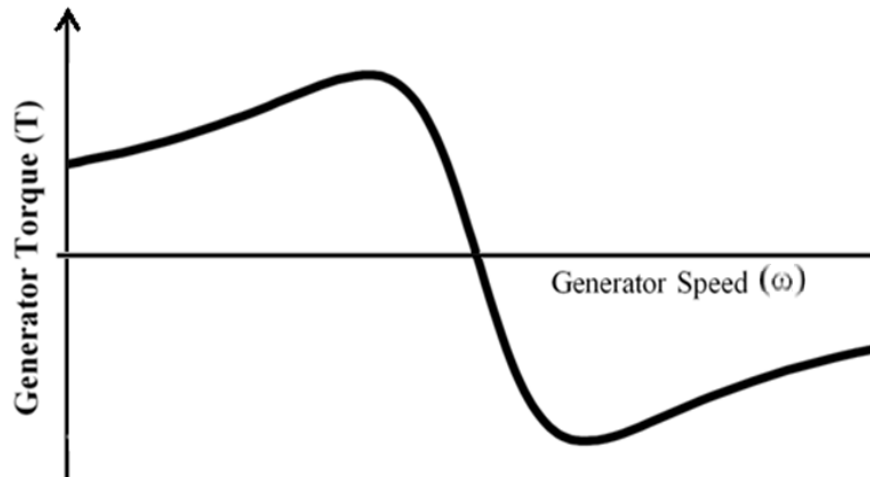


Figure 2-23: Thévenin-equivalent-induction-generator torque/speed curve (adapted from [17])

2.5. Summary of findings from the literature

A review of literature relating to the work undertaken in this study has been presented. This section will summarise key findings from the literature and introduce hypotheses that will be investigated in this study. Generally, the key theme from the literature is that current research into premature WTGB failure is focussing on the WEC failure mode.

2.5.1. Bearing life rating

It has become clear that the current method used to predict the lifespan of a bearing is not accurate for use in the selection of WTGBs. It is clear that the Lundberg-Palmgren method does not take into account many essential factors that affect WTGB life and will therefore be considered to be inaccurate for the remainder of this thesis. It seems that it is vitally important to consider transient operating conditions when designing WTGBs and because of this, it has been decided to create a full dynamic model of a wind turbine drivetrain, as described in Chapter 3.

2.5.2. The effect of inclusions

Despite many theories being suggested for the initiation of WEC damage in WTGBs, it seems that the dominant theory is that the damage starts at inclusions. A variety of failure mechanisms are suggested and it seems that different researchers suggest that different

inclusions are responsible for causing the damage. MnS and Al₂O₃ inclusions in particular have been mentioned as damage initiators, and the importance of oxide parts within MnS inclusions has also been highlighted, since they may cause tensile residual stress during the steel manufacturing process. Despite considerable research effort, it seems clear that the various studies have not reached much common ground in their findings so this study will seek to find the most damaging inclusion type and suggest why that is the case. Since the best way to work out how a component has failed is by examining a failed part, Chapter 5 examines the inner raceway of a WTGB that has been decommissioned after failure.

2.5.3. The effect of hydrogen

It is clear that raised hydrogen levels accelerate WEC damage and butterfly formation. Considerable research has already been completed on this subject and the detrimental effects of hydrogen have been categorically proven. For this reason, the effect of hydrogen will not be investigated in this study, although its negative effect on bearing life will be considered throughout.

2.5.4. Summary of factors leading to white etching crack formation

Since there are many factors that have been cited to contribute to WEC initiation and propagation, they have been summarised in Figure 2-24: Factors affecting WEC formation in WTGBs. The factors highlighted in red are investigated in this project.

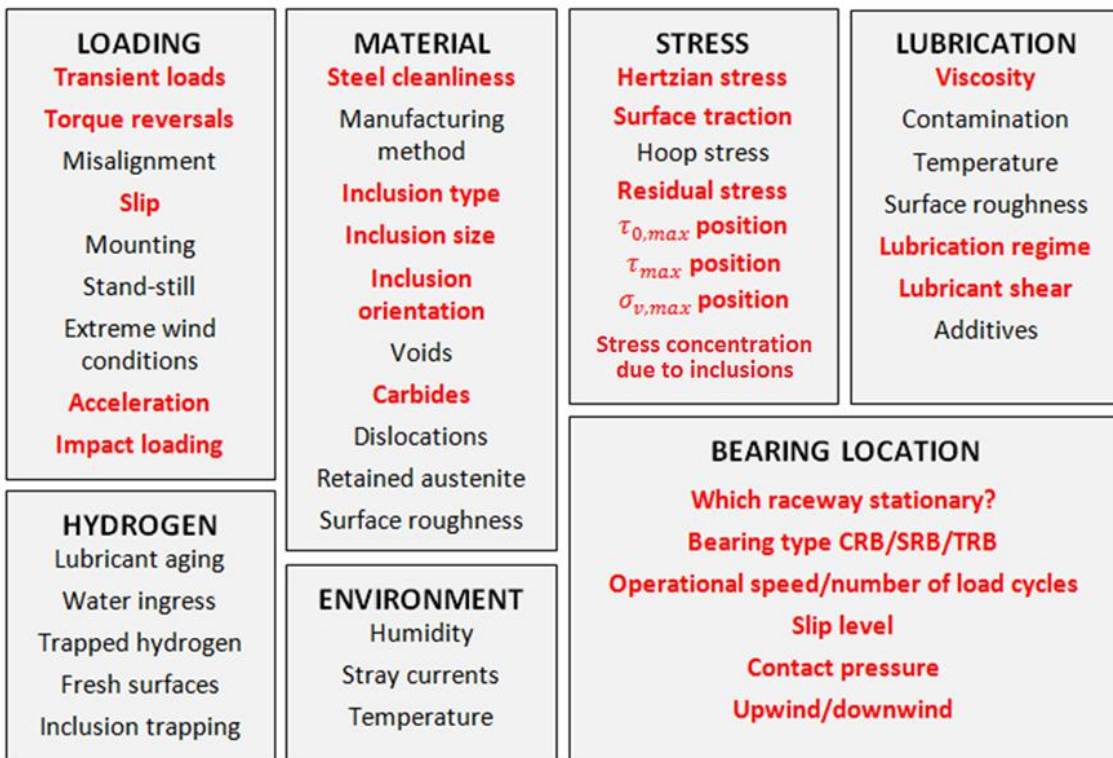


Figure 2-24: Factors affecting WEC formation in WTGBs

2.5.5. WEC failure mechanism hypotheses and influence of MnS inclusions

2.5.5.1. The effect of slip

The importance of the effect of surface traction caused by slipping between rolling elements and bearing raceways has been identified. It is hypothesised that slip could be a key factor in initiating surface spalling from WECs at inclusions. Since surface traction shifts the Hertzian contact stress field closer to the surface, the locations of maximum shear stress τ_{max} , $\tau_{0,max}$ and equivalent stress $\sigma_{v,max}$ occur at shallower depths. Since cracks have to propagate a lesser distance from shallower inclusions, those cracks initiated at shallower depths have a higher chance of leading to surface damage. The potential importance of slip is illustrated in Figure 2-25. The influence of slip on the development of WECs will be investigated in this study.

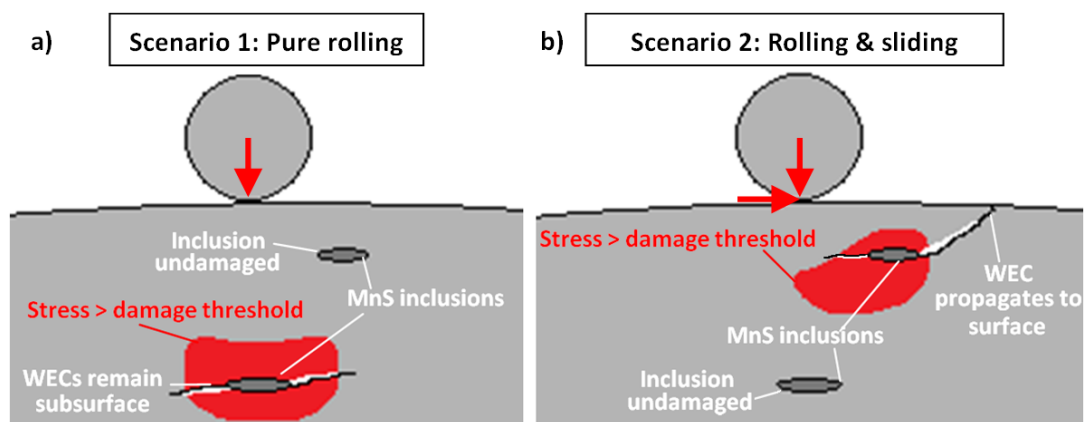


Figure 2-25: Importance of surface traction (not to scale): a) Scenario 1 – pure rolling: critical stress threshold exceeded relatively deep below surface – WEC may never reach surface and cause failure b) Scenario 2 – rolling and sliding: critical stress field shifted closer to surface – WEC propagates to surface, leading to failure.

Additional considerations arise when considering the effect of slip on stress concentrations at material defects. The previous work in this area, as discussed earlier in this section, tends to ignore the effect of surface traction on the position of maximum stress at material defects. A simple two-dimensional FEA simulation was set up to simulate this hypothesis. The purpose of the simulation was not to accurately simulate stress concentration magnitudes or their exact positions, but to illustrate how their locations shift under the influence of surface traction. An arbitrarily sized hole in a large elastic steel plate was exposed to: a) an arbitrary compressive load acting on the top surface of the plate and, b) arbitrary combined compressive tractive loads acting on and along the top surface of the plate respectively. The hole may represent a void or an inclusion that is detached from the surrounding material [97]. The implications of these effects is that the angled propagation of butterfly wings, from the horizontal, may not be due to the direction of τ_{max} , but due to the shifting under traction of the position of $\sigma_{v,max}$ or $\tau_{0,max}$. The effects of surface traction on the location of the maximum equivalent stress, unidirectional shear stress and orthogonal shear stress around a hole are shown in Figure 2-26, Figure 2-27 and Figure 2-28 respectively. Each form of stress can be seen to be shifted around

the circumference of the hole. In Figure 2-26 - Figure 2-28, the images labelled a) are exposed to an arbitrary vertical compressive load and those labelled b), to arbitrary compressive and surface tractive loads. It should be noted that inclusion shape, depth and load magnitudes will change the stress fields shown in the figures and that they are for illustrative purposes only. The findings presented in these images are consistent with [165].

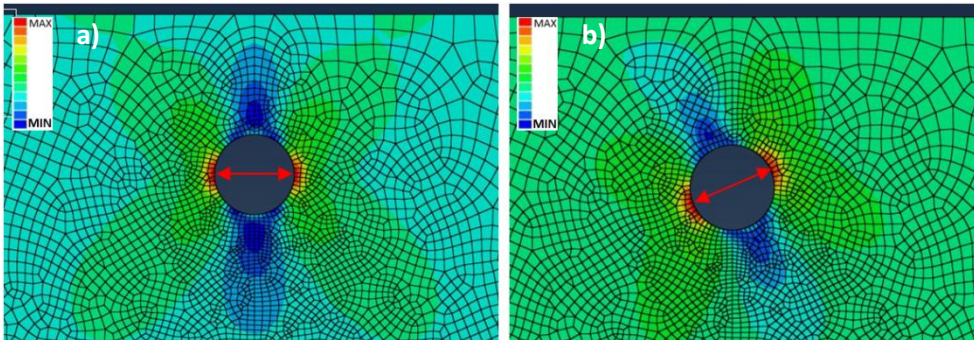


Figure 2-26: Equivalent stress concentrations around a hole under a) arbitrary compressive load b) arbitrary compressive load and arbitrary surface traction acting left to right (arrows indicate max positions)

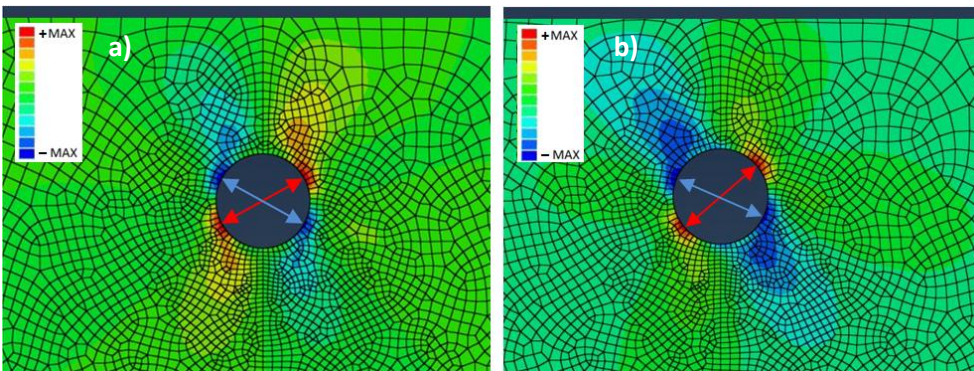


Figure 2-27: Unidirectional shear stress concentrations around a hole under a) arbitrary compressive load b) arbitrary compressive load and arbitrary surface traction acting left to right (arrows indicate +max and -min positions)

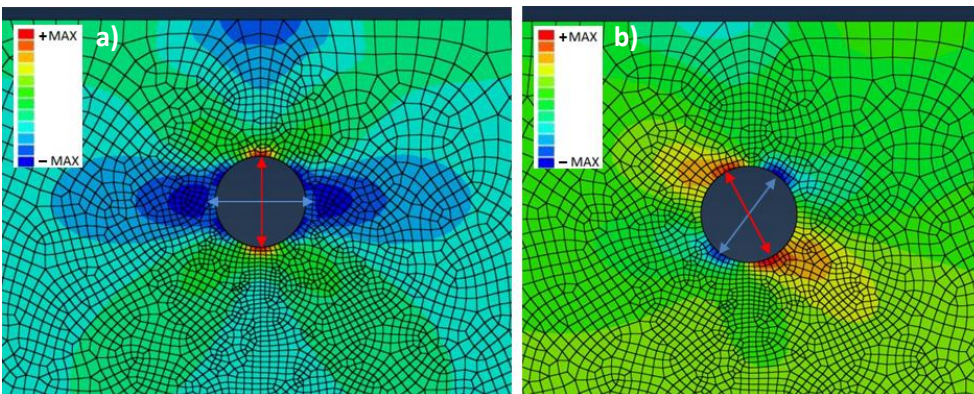


Figure 2-28: Orthogonal shear stress concentrations around a hole under a) arbitrary compressive load b) arbitrary compressive load and arbitrary surface traction acting left to right (arrows indicate +max and -min positions)

Since it is not currently known whether τ_{max} , $\tau_{O,max}$ or $\sigma_{v,max}$ or a combined effect of the different stress components is critical to WEC initiation, this study will aim to find out which correlates most strongly with the damage caused. As the position of each maxima occurs at different depths (particularly $\tau_{O,max}$, which is the shallowest) within the material, it is possible to see which corresponds most strongly with the damage found. This is investigated in Chapters 5 - 7.

2.5.5.2. Loading order effects

One of the key flaws in the Lundberg-Palmgren method is that it does not consider the order of loading events. It is hypothesised that this is a vitally important factor that is investigated in Chapter 7 of this thesis. Figure 2-29 describes a hypothesis, showing that if a high load event happens prior to a series of lesser load events, then the damage is more serious than that if these events occur in the reverse order.

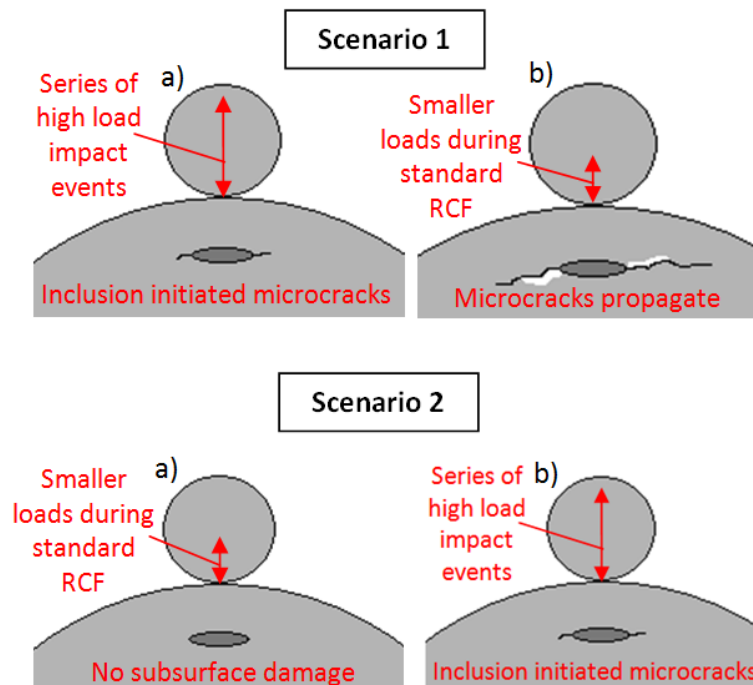


Figure 2-29: Importance of the order of loading events (not to scale). Scenario 1 shows a high load impact event a) that initiates subsurface microcracking, which is then propagated by stresses induced by standard RCF loading in b). Scenario 2 shows that when these event occur in reverse, the damage would be far less severe.

2.5.5.3. Summary of testing methods designed to test hypotheses

To investigate the hypotheses discussed in this section, this study has developed the following experimental testing methods to recreate WTGB damage, including WECs, in bearing steel test specimens:

1. Hammering impact testing, using a reciprocating impact test rig designed to apply up to one million impacts at contact pressures of over 2.5 GPa. Tests were designed to apply impacts both perpendicularly to specimen surfaces, as well as at an angle, in order to investigate the effects of surface traction. Varying contact pressures and

LITERATURE REVIEW

impact numbers were applied in order to determine thresholds at which resulting damage was observed. The test design is described in more detail in section 4.4.

2. Twin disc testing of specimens that had been damaged by the impact rig, as well as specimens that had not, was carried out in order to investigate the order effects discussed in Figure 2-29. The testing also tested damage thresholds of the variables that were altered during testing; the traction coefficient and the contact pressure. Twin disc test design is described in more detail in section 4.5.

3. DYNAMIC MODELLING OF WIND TURBINE GEARBOX BEARING LOADING DURING TRANSIENT EVENTS

In order to understand WTGB failure modes, bearing contact pressures during operation in transient wind conditions and different operating modes need to be considered. The purpose of the multibody dynamic model developed in this study is to find the maximum contact pressures during normal operation and manual shutdown of the wind turbine drivetrain to determine whether recommended levels are being exceeded during typical WTGB loading. This study first presents the development of a dynamic gearbox model, created using *Ricardo PLC's VALDYN* software, of the NREL two-speed, stall-regulated 750 kW test drivetrain. The model is then validated against models of the same gearbox, created independently by the GRC round-robin project. Simulation results of the bearing dynamic loading during normal operation and shutdown modes are then presented and Hertzian contact loads in the bearing calculated.

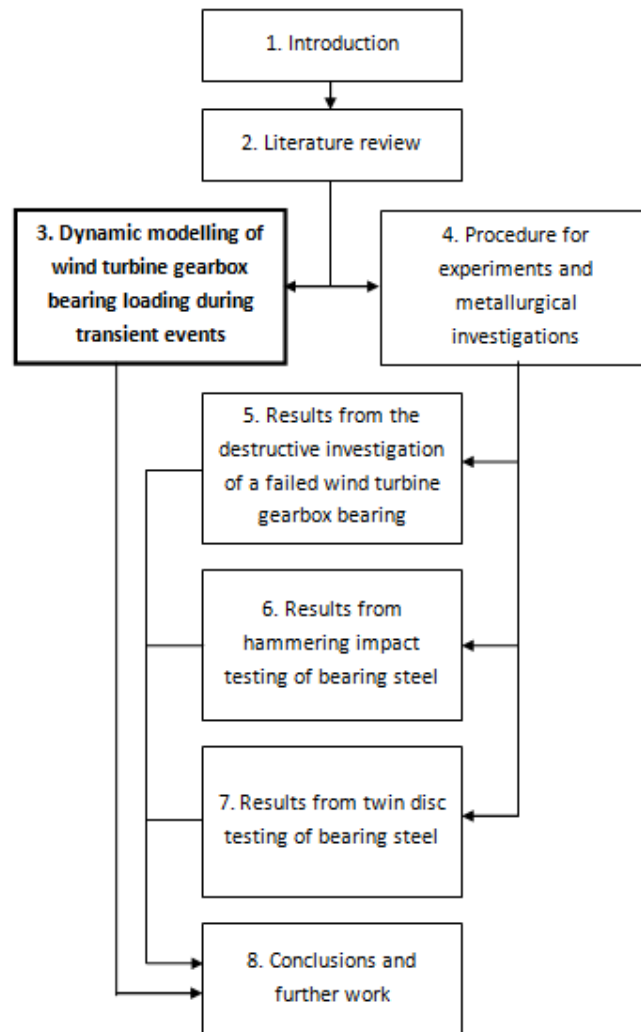


Figure 3-1: Thesis work flow chart

This Chapter is split into five sections:

- Section 3.1 describes the development of the gearbox model.
- Section 3.2 describes the application of the model to a 750 kW WTG.
- Section 3.3 presents the simulation results.
- Section 3.4 discusses findings from the simulation.
- Section 3.5 summarises the chapter.

3.1. Development of a dynamic WTG model using VALDYN

Taking into account the findings discussed in section 2.4, it is proposed that a modified gearbox model will provide a more efficient way of modelling bearing loading, without a significant loss of accuracy, and at relatively low computational cost. The proposed new model is compared to the three model types discussed in Table 3-1. The new model can be described as *modified type 2* and its main advantages over the type 2 model, are that it is able to model variable bearing stiffness, bearing damping and that it uses a sliced gear mesh stiffness model, important for modelling helical gear contact. This model is streamlined for efficiently calculating bearing loading.

Modelled stiffness	Type 1 – 1 DOF torsional model	Type 2 – 6 DOF rigid multibody model	Type 3 – Flexible multibody model	Proposed model in this study
Gear mesh	Constant	Constant	Variable	Constant (sliced model)
Bearing	Rigid	Constant axial, radial, tilt (no damping)	Variable axial, radial, tilt (stiffness and damping)	Variable axial, radial, tilt (stiffness), constant damping
Shaft	Discrete torsional	Discrete torsional, Equivalent bending	FEA representation	Discrete torsional, Equivalent bending
Splined connection	Torsional spline connection	Torsional spline connection	Discrete torsional, Discrete bending, Discrete tilting	Torsional spline connection
Structural components	Rigid	Rigid	FEA representation	Rigid

Outputs

Torque time history	✓	✓	✓	✓
Detailed reaction forces		✓	✓	✓
Internal stresses and strains			✓	✓ (bearings only)

Table 3-1: Comparison of model types 1-3 to proposed gearbox model (adapted from [19])

The coordinate system used in this study is shown in Figure 3-2 along with the WT drivetrain schematic. The gearbox schematic shown in Figure 2-3, displays the layout and components used in the modelled gearbox. All components shown in the figure were modelled, with the exception of the bedplate, which was assumed to be rigid, and the main shaft bearings, as it was assumed that no off-axis loads were transmitted from the rotor to the gearbox, an

acceptable assumption for WTGB modelling [16, 160]. Gearbox components were modelled in 6 DOFs, while the hub and connected blades as well as the generator rotor were modelled as point inertias, free to rotate in the Z' direction. The modelling of all components at each timestep of the dynamic process using *VALDYN*, is expressed in 6 DOFs by equation 2.15. An image of the model in the *VALDYN* user interface is provided in Appendix B. The method of modelling each component in the gearbox is discussed in section 3.1 and the development of a 750 kW gearbox model, in section 3.2.

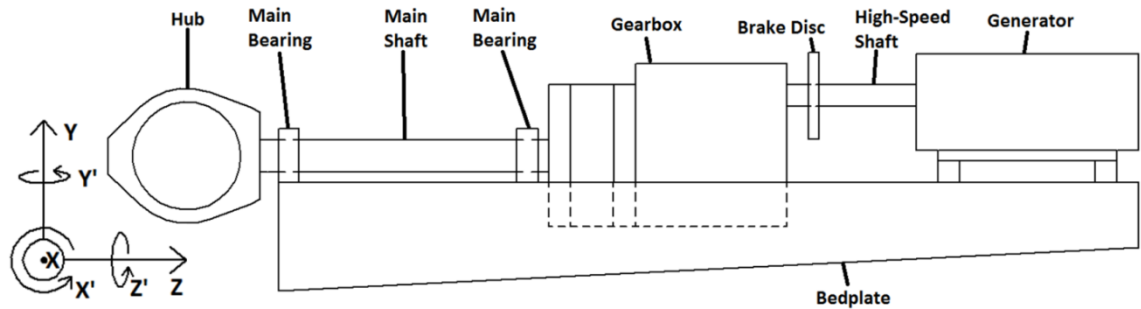


Figure 3-2: Wind turbine drivetrain schematic and coordinate system used in dynamic model

3.1.1. Mass and inertias of gearbox components

The mass and inertia of each gearbox component were calculated in 6-DOFs, described by the mass matrix in equation 3.1, where M is the mass of the component and I_x , I_y and I_z represent the inertia of the component in the X' , Y' and Z' directions respectively. Component masses and inertias were taken from component data sheets if possible, or alternatively, determined using CAD models. The rotor inertia, I_{rotor} , was approximated using the method presented in [166], using equations 3.2 and 3.3, where M_{blade} and L_{blade} are the mass and length of one blade respectively. Masses and inertias of the in the gearbox model developed in section 3.2 are shown in Table 9-1.

$$\begin{vmatrix} M & 0 & 0 & 0 & 0 & 0 \\ 0 & M & 0 & 0 & 0 & 0 \\ 0 & 0 & M & 0 & 0 & 0 \\ 0 & 0 & 0 & I_x & 0 & 0 \\ 0 & 0 & 0 & 0 & I_y & 0 \\ 0 & 0 & 0 & 0 & 0 & I_z \end{vmatrix} \quad (3.1)$$

$$M_{blade} = 2.95 \cdot L_{blade}^{2.13} \quad (3.2)$$

$$I_{rotor} = 0.636 \cdot M_{blade} \cdot L_{blade}^2 \quad (3.3)$$

3.1.2. Displacement of gearbox components

The matrices representing the displacement $[X]$, velocity $[\dot{X}]$ and acceleration $[\ddot{X}]$ of each 6-DOF component are calculated at each time step at the its centre of mass of each component in the form shown in equations 3.4, 3.5 and 3.6.

$$[X] = |x \ y \ z \ \theta_x \ \theta_y \ \theta_z|^T \quad (3.4)$$

$$[\dot{X}] = |\dot{x} \ \dot{y} \ \dot{z} \ \dot{\theta}_x \ \dot{\theta}_y \ \dot{\theta}_z|^T \quad (3.5)$$

$$[\ddot{X}] = |\ddot{x} \ \ddot{y} \ \ddot{z} \ \ddot{\theta}_x \ \ddot{\theta}_y \ \ddot{\theta}_z|^T \quad (3.6)$$

where x , y and z represent linear motion in the directions of their respective axis and θ_x , θ_y and θ_z represent rotational motion in the directions of their respective axis.

3.1.3. Bearings

6 DOF bearing stiffness is described by the stiffness matrix shown in equation 3.7 [162]. Note in this case, the value for $k_{z'z'}$ is zero, because this is the DOF representing rotation along the shaft axis (axial friction will be considered later). Constant values for the diagonal terms (shown in bold) assume linearly varying stiffness with bearing displacement, which are used in standard type 2 models [158]. The modified model in this study uses varying stiffness values, calculated within VALDYN from the bearing geometry, which was input into bearing models for each bearing in the gearbox. This simulation method takes into account the off-diagonal terms, which link the 6 degrees of freedom. VALDYN is able to model both CRBs and TRBs in this way, using the theory presented in [167].

$$\begin{pmatrix} k_{XX} & k_{XY} & k_{XZ} & k_{XX'} & k_{XY'} & 0 \\ & k_{YY} & k_{YZ} & k_{YX'} & k_{YY'} & 0 \\ & & k_{ZZ} & k_{ZX'} & k_{ZY'} & 0 \\ & & & k_{X'X'} & k_{X'Y'} & 0 \\ & \text{Symmetric} & & & k_{Y'Y'} & 0 \\ & & & & & k_{Z'Z'} \end{pmatrix} \quad (3.7)$$

The bearing loads, F_x , F_y and F_z , and tilting moments, M_x , M_y , are computed at each time step as functions of the relative displacements expressed by the displacement components (listed in equation 3.4) of the outer and inner raceways, i and j respectively. Initial displacements must be zero. o_i and o_j are the initial axial inner and outer race offsets; i.e. the distance from the common centre of mass of the outer race and inner race respectively in the z direction [168]:

$$x = x_i - x_j \quad (3.8)$$

$$y = y_i - y_j \quad (3.9)$$

$$z = (z_i + o_i) - (z_j + o_j) \quad (3.10)$$

$$\theta_x = \theta_{xi} - \theta_{xj} \quad (3.11)$$

$$\theta_y = \theta_{yi} - \theta_{yj} \quad (3.12)$$

Values for acceleration and velocity are calculated over each timestep, using these displacement results. VALDYN then calculates the forces, F_x , and F_y , in the x and y directions respectively and R_I , the radius at which the force acts. The loads F and moments M acting on each of the raceways are calculated as shown in equations 3.13-3.16 [168]:

$$F_i = (F_x, F_y, F_z) \quad (3.13)$$

$$F_j = -F_i \quad (3.14)$$

$$M_i = ((M_x - F_y \cdot o_i), (M_y + F_x \cdot o_i), M_z) \quad (3.15)$$

$$M_j = (-(M_x - F_y \cdot o_j), -(M_y + F_x \cdot o_j), -M_z) \quad (3.16)$$

The axial moment caused by bearing friction is calculated by equation 3.17, considering the coefficient of rotational friction μ_F . Assumed values of μ_F are 0.0011 and 0.0018 for standard cylindrical roller bearings and tapered roller bearings respectively [169].

$$M_z = \pm \mu_F R_I \sqrt{F_x^2 + F_y^2} \quad (3.17)$$

The most difficult bearing parameter to estimate accurately is its damping coefficient c . One method is to consider bearing damping as a fraction of its critical damping. Critical damping was calculated using equation 3.18 where k is the bearing stiffness and I is the inertia of the rolling elements rather than that of the inertia of the system attached to the raceways [58].

$$c = 2\sqrt{Ik} \quad (3.18)$$

Introducing the fraction of the critical damping ζ allowed the level of the damping to be set.

$$c = 2\zeta\sqrt{Ik} \quad (3.19)$$

Bearing stiffness values at rated torque were used to calculate constant damping coefficients in the 5 restrained DOFs. These constant bearing stiffness values were provided by NREL and are presented in Table 9-2 of Appendix C. Three damping coefficients were required; axial c_{ax} , radial c_{rad} and tilt c_t . The axial damping was calculated using the axial stiffness; the radial damping, using the mean radial stiffness in the x and y directions; and the tilt damping, using the mean tilt stiffness in the X' and Y' directions. The axial, radial and tilt damping were calculated as shown in equations 3.20-3.22, allowing a damping matrix to be formed in

equation 3.23. Calculated damping values for each bearing in the gearbox model developed in section 3.2 are shown in Table 9-2 of Appendix C.

$$c_{ax} = 2\zeta\sqrt{Ik_{zz}} \quad (3.20)$$

$$c_{rad} = 2\zeta\sqrt{I\left(\frac{k_{xx}+k_{yy}}{2}\right)} \quad (3.21)$$

$$c_t = 2\zeta\sqrt{I\left(\frac{k_{x'x'}+k_{y'y'}}{2}\right)} \quad (3.22)$$

$$\begin{vmatrix} c_{rad} & 0 & 0 & 0 & 0 & 0 \\ 0 & c_{rad} & 0 & 0 & 0 & 0 \\ 0 & 0 & c_{ax} & 0 & 0 & 0 \\ 0 & 0 & 0 & c_t & 0 & 0 \\ 0 & 0 & 0 & 0 & c_t & 0 \\ 0 & 0 & 0 & 0 & 0 & 0 \end{vmatrix} \quad (3.23)$$

3.1.4. Gears

Meshing gears can be modelled in VALDYN, using simple, sliced and FEA models. It was found that FEA modelling was too computationally expensive for this investigation. The simple model, which models gear contact as a sinusoidally varying force was trialled, but results were found to be too noisy. The sliced model, which takes a user-specified number of slices through a gear-tooth contact, was therefore selected, and was found to provide accurate results. The number of slices chosen has an effect on result accuracy, with a higher number of slices providing more accurate results at a cost of computational effort. A previous study found that the optimum number of slices is 35 [162], so this number was tested and found to be a good compromise between computational cost and accuracy. Tooth mesh stiffnesses were assumed because the effective tooth stiffness of a pair of spur gears is relatively independent of the tooth and gear size when standard involute tooth profiles are used [170]. For spur gears, $k_T = 14 \text{ N}/(\text{mm}\cdot\mu\text{m})$ and for helical gears (helix angle, $\beta = 20^\circ$): $c' = k_T = 13.1 \text{ N}/(\text{mm}\cdot\mu\text{m})$. These values were adjusted using linear interpolation for different helix angles. Tooth damping C_T was approximated, using an appropriate critical damping ratio of 10 % of the critical damping based on the inertia ($I_{Z,A}$ and $I_{Z,B}$) of the gears and the stiffness coupling them [168]:

$$C_T = 0.1 \times 2\sqrt{k_T(I_{Z,A} + I_{Z,B})} \quad (3.24)$$

For this model, it has been assumed that gear contact friction is zero, as it is anticipated that it will have little effect on bearing loading. Table 9-3 in Appendix C shows the gear tooth stiffness and damping properties used in the gearbox model developed in section 3.2.

3.1.5. Shafts

The VALDYN shaft element, used in conjunction with two mass elements, models the three-dimensional motion of a rotating shaft between two components. To model a shaft connected to more than two components, more than one shaft element must be used in series, back to back. Each length of shaft between gearbox components requires one shaft element as shown in Figure 9-1 in Appendix B. Forces and moments at both shaft ends are calculated from the bending, torsional and axial deformations. The user specifies mass, inertia and bending and torsional damping values. VALDYN is capable of modelling shafts using FEA models, however, it was found that again, this was too computationally expensive. It is also possible to model the shafts as rigid components, but modelling the damping provided by the axles is vital in order to accurately capture the system dynamics [160]. The VALDYN 'shaft' element provided the best compromise. The following calculations were required by the 'shaft' element in VALDYN:

- 2nd moment of inertia about the x and y axes, denoted I_{xx} and I_{yy} respectively. Shaft cross sectional areas are symmetric about the x and y axis so their 2nd moments of inertia are identical and found by using equation 3.25, where D_o and D_i are the outer and inner diameter of the shaft, respectively [157]:

$$I_{xx} = I_{yy} = \frac{\pi}{64}(D_o^4 - D_i^4) \quad (3.25)$$

- The polar moment of inertia, I_p along the Z axis was found using equation 3.26 [157]:

$$I_p = \frac{\pi}{32}(D_o^4 - D_i^4) \quad (3.26)$$

- The bending damping about the x and y axes were found using equation 3.27 [168]:

$$C_x = C_y = 2\zeta \sqrt{\frac{3EI_x M}{L^3}} = 2\zeta \sqrt{\frac{3EI_y M}{L^3}} \quad (3.27)$$

- The axial damping was found using equation 3.28 [168]:

$$C_z = 2\zeta \sqrt{\frac{EA m}{L}} \quad (3.28)$$

- The torsional damping was found using equation 3.29 [168]:

$$C_t = 2\zeta \sqrt{GI_p \frac{I_z}{L}} \quad (3.29)$$

where ζ is the fraction of critical damping, M is the mass of the shaft and I_z is the mass moment of inertia of the shaft [157], G is the shear modulus (which is approximately 80 GPa for steel) and L is the length of shaft between the two components that that section of shaft connects[162].

As ζ was unknown, a logarithmic decrement method was used to find the axial damping values by way of a dynamic response test using FEA, shown in equation 3.30. The logarithmic decrement, δ , was used to approximate the damping of an underdamped system, which is

defined as the natural logarithm of the ratio of two successive amplitudes; $B(t)$, $B(t + P)$, and was obtained from equation 3.30 [17].

$$\delta = \ln\left(\frac{B(t)}{B(t+P)}\right) \quad (3.30)$$

where P is the period and B is the amplitude of the oscillation. If the characteristic roots of an underdamped system are substituted into equation 3.31 and the resulting expression is solved for ζ , equation 3.32 can be formed [17]:

$$\zeta = \left(\frac{\delta}{\sqrt{4\pi^2 - \delta^2}}\right) \quad (3.31)$$

where:

$$\delta = \frac{1}{n} \ln\left(\frac{B_n}{B_{n+1}}\right) \quad (3.32)$$

Since the results from the dynamic test were over too long a time step to fit to a curve which oscillation magnitudes could easily be read from, the results were used to create a decaying sine curve, of the form:

$$y(t) = A \cdot e^{-\lambda_d t} (\cos \omega t + \varphi) \quad (3.33)$$

where:

- A is the amplitude of the first oscillation
- ω is the time taken to complete one oscillation
- φ is the phase, equal to the time taken for the signal to first cross the x axis
- λ_d is the decay constant, found using equation 3.34

$$\lambda_d = \frac{0.693}{L_{0.5}} \quad (3.34)$$

where $L_{0.5}$ is the half-life of the signal.

Equations 3.27-3.29 were then used to calculate the damping coefficients.

This process for shaft "ISS2" from the gearbox modelled in section 3.2 is provided in Appendix D. It has been assumed that the fraction of critical damping will be similar for each shaft, as they are of similar dimensions and are made from the same material, so these values have been calculated based on the properties of the high speed intermediate shaft. It has also been assumed that the fraction of critical damping for axial deformations is the same as the radial value. As shaft damping is very high in comparison to other components, this is assumed to be a non-critical model input. All shaft properties used in the model developed in section 3.2 are shown in Table 9-4 in Appendix C.

3.1.6. Planetary carrier

The planetary carrier was assumed to be a rigid body as the computational cost of using a FEA model was too high. This assumption is valid, provided that modelling unequal load sharing between upwind and downwind planetary gear bearings is not required. The magnitude of the sum of the upwind and downwind bearing forces for each planetary gear is correct. It was decided that an investigation into unequal load sharing was not required because previously calculated scaling factors for unequal load sharing are later introduced to approximate maximum load magnitudes.

3.1.7. Splined sun shaft connection

Many WT gearboxes use a splined connection to allow the planetary stage sun gear to ‘float’. A floating sun gear centres itself within its planets, encouraging load sharing. The splined connection has been modelled as a rigid connection in the X, Y, Z and Z' DOFs, while the X' and Y' degrees of freedom are unrestrained, so the sun gear is able to move freely in these directions. As the sun gear is partially restrained in the X' and Y' by the three planets, its displacements in these directions are small, thus the unrestrained X' and Y' DOF assumption is valid. The stiffness and damping of the splined shaft is modelled by two separate shaft elements, connected as described in section 3.2.

3.1.8. Generator resistance torque

A simple induction generator model as described in section 2.4.4, was used to model the generator resistance torque for the modelled gearbox, since it was capable of accurately calculating generator resistance torque, for the operational conditions used in this model. The resistance torque at different generator speeds used in the model developed in section 3.2 is shown in Figure 9-2 of Appendix C.

3.1.9. Gearbox casing and elastomer supports

The gearbox casing was modelled under the assumption that it is rigid, using a series of zero-mass “connection points” that are linked by rigid arms to a mass positioned at the centroid of the casing. The positions of these “connection points” corresponded to the location of each bearing. The casing was allowed to move in six degrees of freedom and is supported by two rubber mounts. Testing of the rubber mounts used for this gearbox model was undertaken by Romax [171], using a test rig at the The Tun Abdul Razak Research Centre (TARRC), a unit of the Malaysian Rubber Board. The rig was used to measure the dynamic and static responses of a rubber mount at two temperatures (-20°C and 21°C) and stiffness values were determined. The readings at 21°C are closer to typical operating conditions, so a measured dynamic stiffness value of 80 kN/mm was selected for the VALDYN model. This is assuming linearly varying stiffness with displacement, which is a valid assumption if displacements are small [16]. The elastomer mounts are modelled as three linear springs representing the X, Y and

Z DOFs. Rubber torsional stiffness values were not provided, however, as the gearbox is pinned in two locations separated by a relatively large distance, rotational displacements will be very small and are therefore assumed to be negligible. No information was available for elastomer mount damping c_{EM} , so the same method was used as for bearing damping calculations. The same critical damping ratio ($\zeta = 0.075$) was used, allowing equation 3.35 to be formed, where m is the gearbox mass and n is the number of rubber mounts, which in this case is two. The calculated stiffness used in the model developed in section 3.2 is presented in Appendix C.

$$c_{EM} = 0.15 \sqrt{\frac{m}{n}} k \quad (3.35)$$

3.1.10. Disc braking

A trial and error process was utilised, by applying different contact loads (simulating the brake pads) to a brake disc, created using a braking element in VALDYN, which applied a frictional retarding force to the brake disc. The contact loads were altered until the time take to bring the gearbox model to a stop from 10 rpm was the same as that taken in a real shut down event for the gearbox to be modelled, measured in the 750 kW NREL drivetrain test facility.

3.1.11. Maximum Hertzian contact stress calculation

After simulation results of bearing dynamic loading were obtained, the maximum contact stress on the inner raceway of each bearing in the gearbox was calculated. First, the maximum load experienced by the most heavily loaded roller raceway contact Q_{max} was approximated using equation 3.36 [172], where W is the maximum load experienced perpendicular to the bearing roller/raceway contact and z is the number of rolling elements. This calculation was completed under the following assumptions: that the internal clearance of a bearing is greater than zero, that the elastic deformation of a rolling element is never negative and that the bearing roller is a perfect cylinder. These assumptions will lead to conservative estimations of bearing contact stresses as they do not take into account stress concentrations due to edge loading and roller profile. The standard Hertzian equation for line contact loading (discussed in section 2.1.3.1, equation 3.37 was used to calculate maximum contact pressure P_{max} [29, 30].

$$Q_{max} = 5 \frac{W}{z} \quad (3.36)$$

$$P_{max} = 2 \frac{Q_{max}}{\pi A} \quad (3.37)$$

3.2. Application to the NREL750 kW WTG

The NREL 750 kW gearbox was modelled in this study, using the method discussed in section 3.1. All the input values for the various properties of each component required to create the gearbox model are summarised in Table 3-2. The values used in the model that can be shared (with permission from NREL) are presented in Appendix C.

Rotor	Planet carrier	Gears	Shafts	Bearings	Brake	Casing	Generator																					
Mass	Dimensions	No. of teeth	Dimensions	Axial damping	Peak normal force	Mass and inertia (6 DOFs)	Mass and inertia of generator rotor (Z')																					
Blade length	Mass and inertia (6 DOFs)	Gear module	Young's modulus	Radial damping	Inner radius of disc contact area	Casing dimensions	Synchronous generator speed																					
Moment of inertia (Z' DOF)		Addendum modification	Shear modulus	Tilt damping				Coefficient of rotational friction	Outer radius of disc contact area	Elastomer mount stiffness (X, Y, Z DOFs)	HSS rated speed																	
		Normal pressure angle	Mass and inertia (6 DOFs)	Number of rolling elements								Rolling element diameter	Mass and inertia of disc (6 DOFs)	Elastomer mount stiffness and damping (X, Y, Z DOFs)	HSS Rated torque													
		Helix angle	Bending damping about X													Bearing bore diameter	Rolling element contact length	Radial and tilt clearance	Pullout torque									
		True involute form diameter	Bending damping about Y																	Bearing outer diameter	Contact angle							
		Tip diameter	Axial damping																			Rolling element contact length	Bearing stiffness matrix at rated torque (6 DOFs)					
		Tooth face width	Torsional damping																					Contact angle				
		Normal backlash allowance	Damping coefficient																						Radial and tilt clearance			
		Contact stiffness																								Bearing stiffness matrix at rated torque (6 DOFs)		
		Damping coefficient																									Bearing stiffness matrix at rated torque (6 DOFs)	
		Mass and inertia (6 DOFs)																										Bearing stiffness matrix at rated torque (6 DOFs)

Table 3-2: Parameters of VALDYN model of NREL 750 kW wind turbine gearbox

The NREL 750 kW gearbox is a conventional three-stage design (shown in Figure 2-3), with a low speed planetary stage that has three planetary gears, followed by two parallel stages. The gearbox overall ratio is 1:81.49, with a planetary stage ratio of 1:5.71, and two parallel ratios of 1:3.57 and 1:4.00 respectively. The sun gear is attached to the intermediate stage gear, via a shaft with a splined connection, which allows some movement in the X' and Y' rotational directions. The WT is able to generate power at two rated speeds, using either four or six generator poles, although only the higher speed, six pole mode is modelled in this study.

DYNAMIC MODELLING OF WIND TURBINE GEARBOX BEARING LOADING DURING TRANSIENT EVENTS

As previously mentioned, it has been found that WTGB failures experienced by small-scale WTs (500 – 1000 kW) are also found in modern larger turbines. This confirms that findings from a study based on the 750 kW test-turbine, can be extrapolated to larger WTGs [7], despite their larger size, using updated design standards and different control systems. This is highly advantageous because working with smaller turbine test facilities reduces the cost and increases the availability of relevant experimental research. Additionally field and laboratory measurements are widely available for older turbines, whereas many modern designs are still protected by industry and so cannot be modelled by external researchers.

The appearance of the model on the VALDYN user interface is presented in Appendix B, with the various gearbox stages, the rotor, the generator and the gearbox casing labelled. When viewed in the VALDYN kinematic simulation interface, that allows the motion of the model to be viewed, the gearbox appears as shown in Figure 3-3.

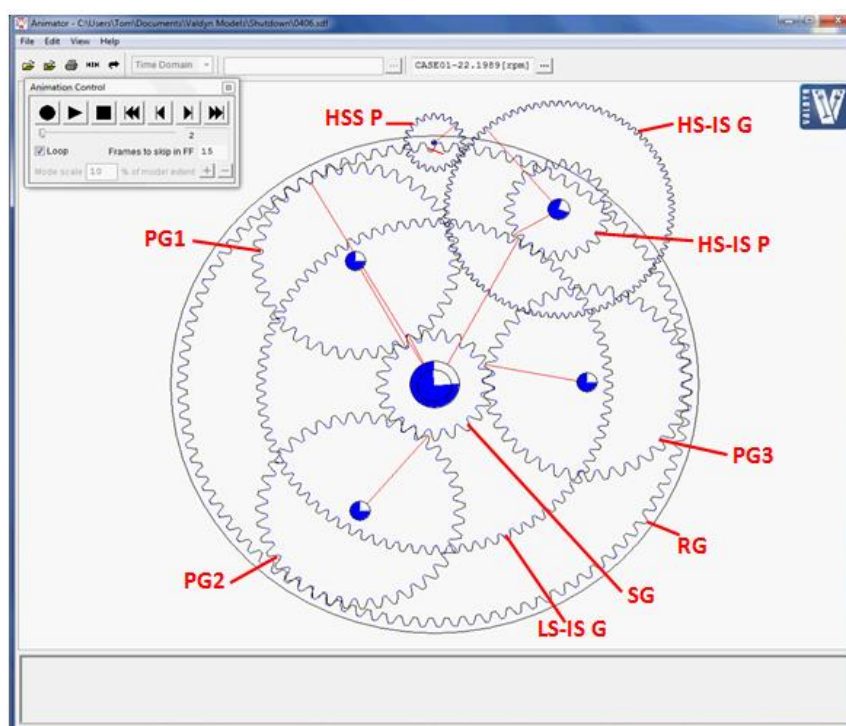


Figure 3-3: Gearbox model viewed in VALDYN kinetic simulation interface

3.2.1. Model validation

Before being used to simulate WT operation, the model was validated to evaluate the assumptions made during its development. This process was limited to the results that were available for comparison and is described in this section. The first step was to compare torque distribution throughout the gearbox with that obtained by the anonymous GRC contributors involved in the round-robin project [161]. The modelling method used by each of the partners involved different software packages, by which the studies were independently performed. The VALDYN model was loaded at rated torque and the torque distribution throughout the

gearbox was calculated. The results showed good agreement with the GRC round-robin results, as shown in Figure 3-4a, with torque levels that were close to all GRC partners, the maximum error from the mean result being 1.8 % for the ISS2 torque level. The small differences were likely to be due to the inaccuracy of one or more of the assumptions made when developing the gearbox model. The GRC mean result is possibly skewed by result D, which is slightly different from all other results in the case of the LSS and ISS2. This comparison validates the models ability to calculate torque distribution, proving that gearbox ratios and component dimensions have been setup correctly.

The second stage of validation was to examine loading levels in the sun/planet gear contact, in order to check that the gear mesh model was valid. The VALDYN model was run at rated torque until all vibrations, caused by initial system unbalance had dissipated. At this point, the contact load was calculated and as Figure 3-4b shows, there was excellent agreement between this study and GRC results. The largest percentage difference from the mean GRC result was 2.4 % for the radial contact load and is again, probably due to the use of different modelling methods and assumptions made.

The final part of validation, involved examining the bending of the main shaft under rated load, in order to check that the assumptions used for modelling shaft bending was valid and bearing stiffness values were correct. A model was created, in which the shaft was split into four lengths, separated by five masses, with mass matrices representing the section of shaft they represented in 6-DOF. This allowed the deflection to be calculated in three locations along the shaft section between its supporting bearings (PC-A and the main shaft bearing approximately 446 mm along the shaft, towards the rotor). Main shaft bearing geometry was input into the VALDYN model, allowing the program to calculate bearing stiffness values. Rated rotor torque was input into the model, as was the corresponding generator resistance torque. The relative displacements in comparison to the main shaft at zero load, compared to NREL results displayed in Figure 3-4c shows that the results from the GRC round-robin were inconsistent. Reading maximum displacement values from the figure allows the mean GRC result to be calculated to be approximately 7.3 μm . The calculated maximum value in this study; 8.2 μm , is around 11 % higher than the mean magnitude and only the GRC result D is closer to this mean. This suggests that assumptions made were reasonable and validates the method used to model shafts and their support (bearing stiffness) in VALDYN.

DYNAMIC MODELLING OF WIND TURBINE GEARBOX BEARING LOADING DURING TRANSIENT EVENTS

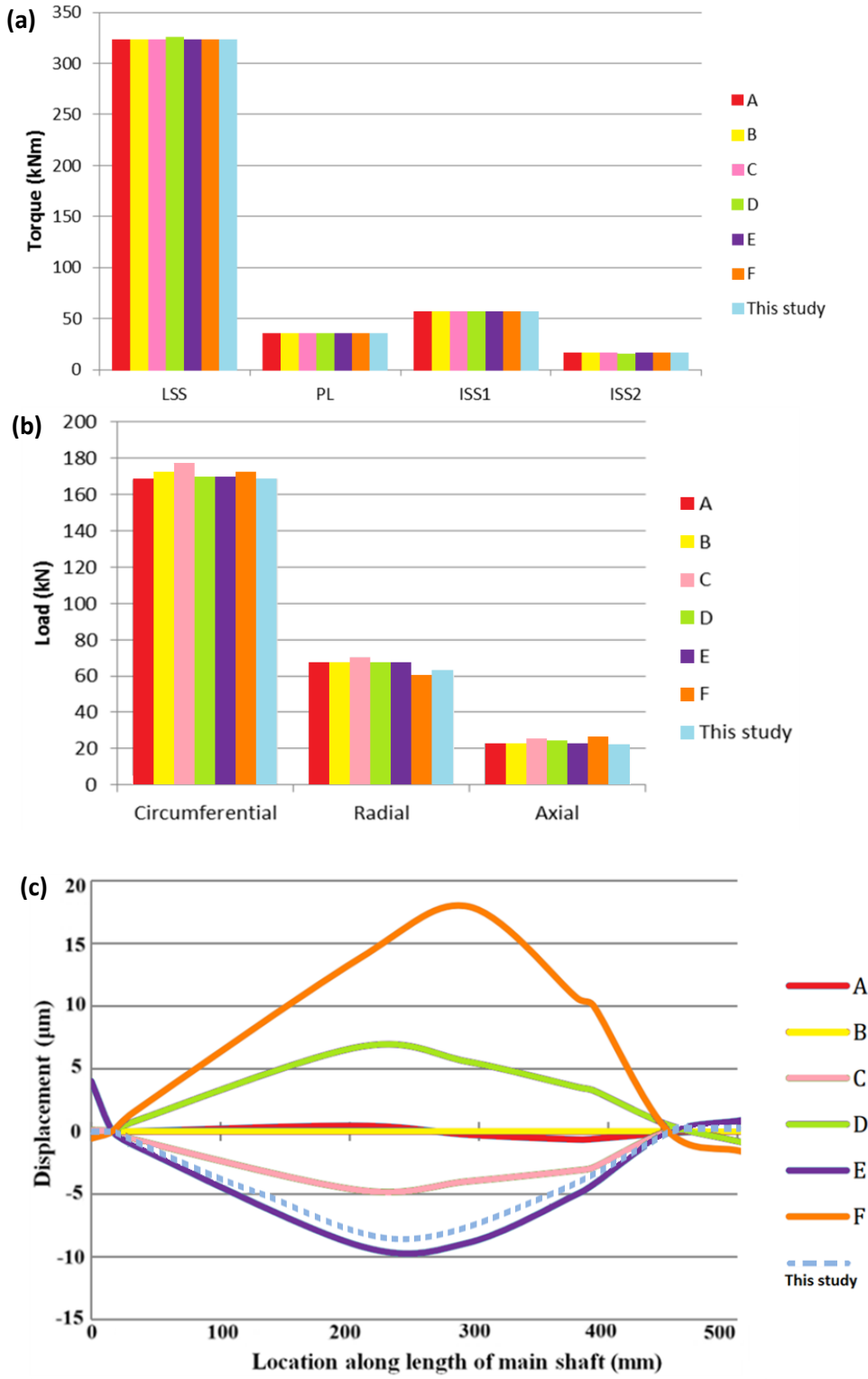


Figure 3-4: Validation of model in comparison to partners A-F (20) (a) Shaft torque levels (b) Planet-sun gear contact load levels (c) Main shaft bending displacement

3.2.2. Torque loading

Input torque and rotor speed data were provided by NREL for the following operating conditions:

1. **Normal Operation:** 90 seconds of continuous operation at six-pole rated speed.
2. **Shut-down:** the rotor begins at six-pole rated speed, then the generator is disconnected and aerodynamic braking is initiated, until the rotor reaches 10 rpm, at which point the disc brake is engaged, bringing the rotor to a halt.

Figure 3-5 shows the LSS input torque for the two operating conditions that were investigated further by the developed dynamic model.

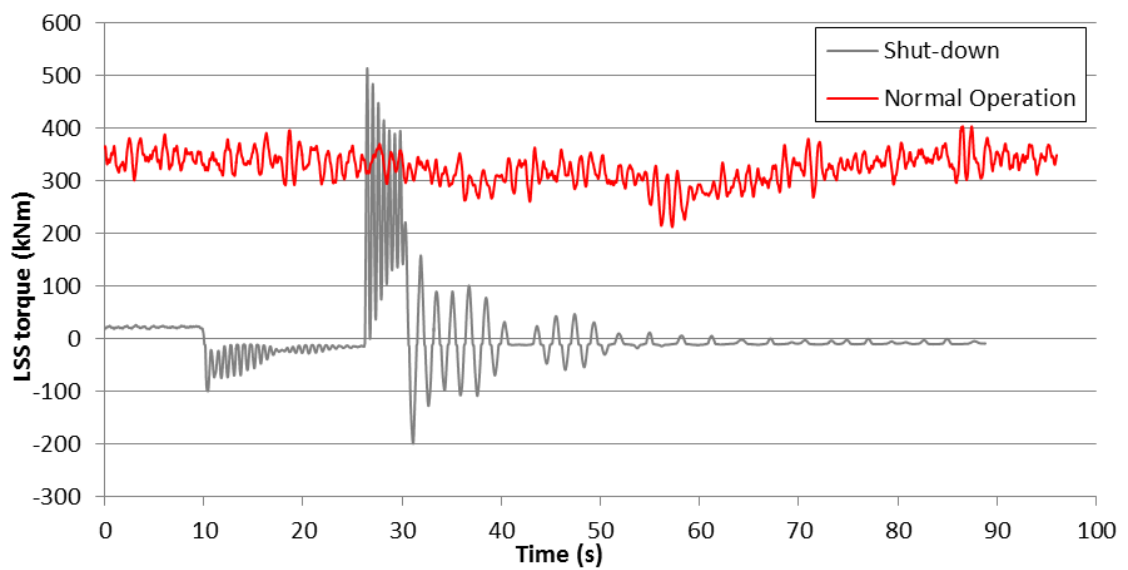


Figure 3-5: Input torque for normal operation and shutdown events

3.3. Results from simulated model and analysis

Although the dynamic model has the capability of calculating dynamic bearing loading for any of the bearings in the gearbox, planetary gear bearings and HSS bearings have historically been the most problematic in wind turbines, so have been selected to be analysed in detail in this study.

3.3.1. Normal operation

Figure 3-6 displays the LSS and HSS velocities over the 96 second simulation period. Ignoring oscillations caused by initial system unbalance in the first 5 seconds, LSS speed oscillation magnitudes of approximately 0.8 rpm compare well with NREL measured data, and the average velocity of the simulated LSS signal was 0.13 % different from NREL measured data. No comparison data was available for the HSS velocity, which oscillates either side of the generator rated speed of 1809 rpm by approximately +/-5 rpm.

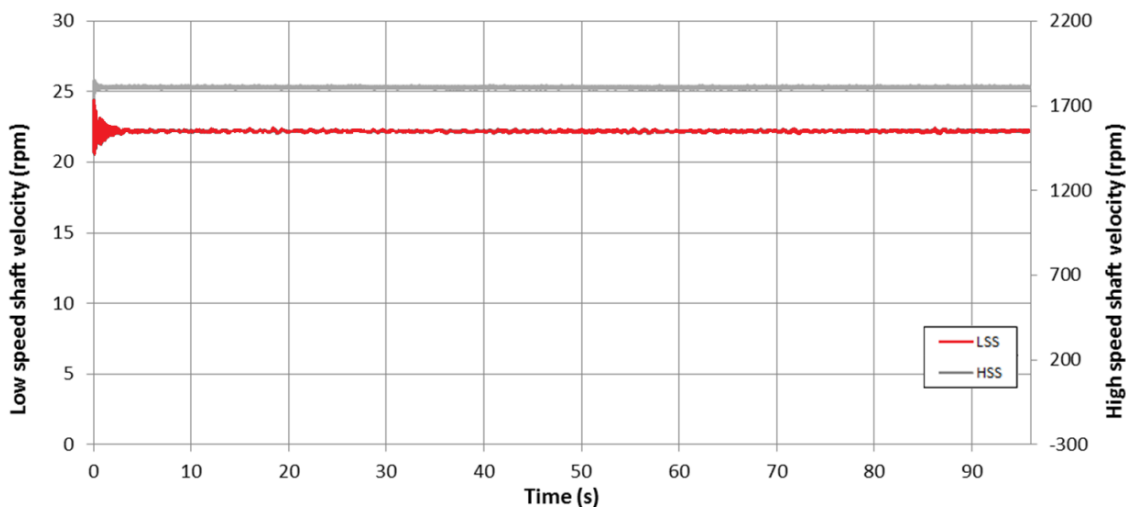


Figure 3-6: LSS and HSS velocity during normal operation

Figure 3-7a shows the resultant force acting on both of the planetary bearings, *PL-A* and *PL-B*, supporting each planet gear 1, 2 and 3. Note that, the resultant force on these cylindrical roller bearings is purely radial. The maximum resultant force experienced was 250 kN. Figure 3-7b shows the resultant forces acting on the HSS bearings, which in the case of *HSS-B* and *HSS-C* include both axial and radial elements, as they are tapered roller bearings, able to support axial loads with maximum values of 63 kN, 79 kN and 15 kN for bearings *HSS-A*, *HSS-B* and *HSS-C* respectively.

Analysis of the Premature Failure of Wind Turbine Gearbox Bearings

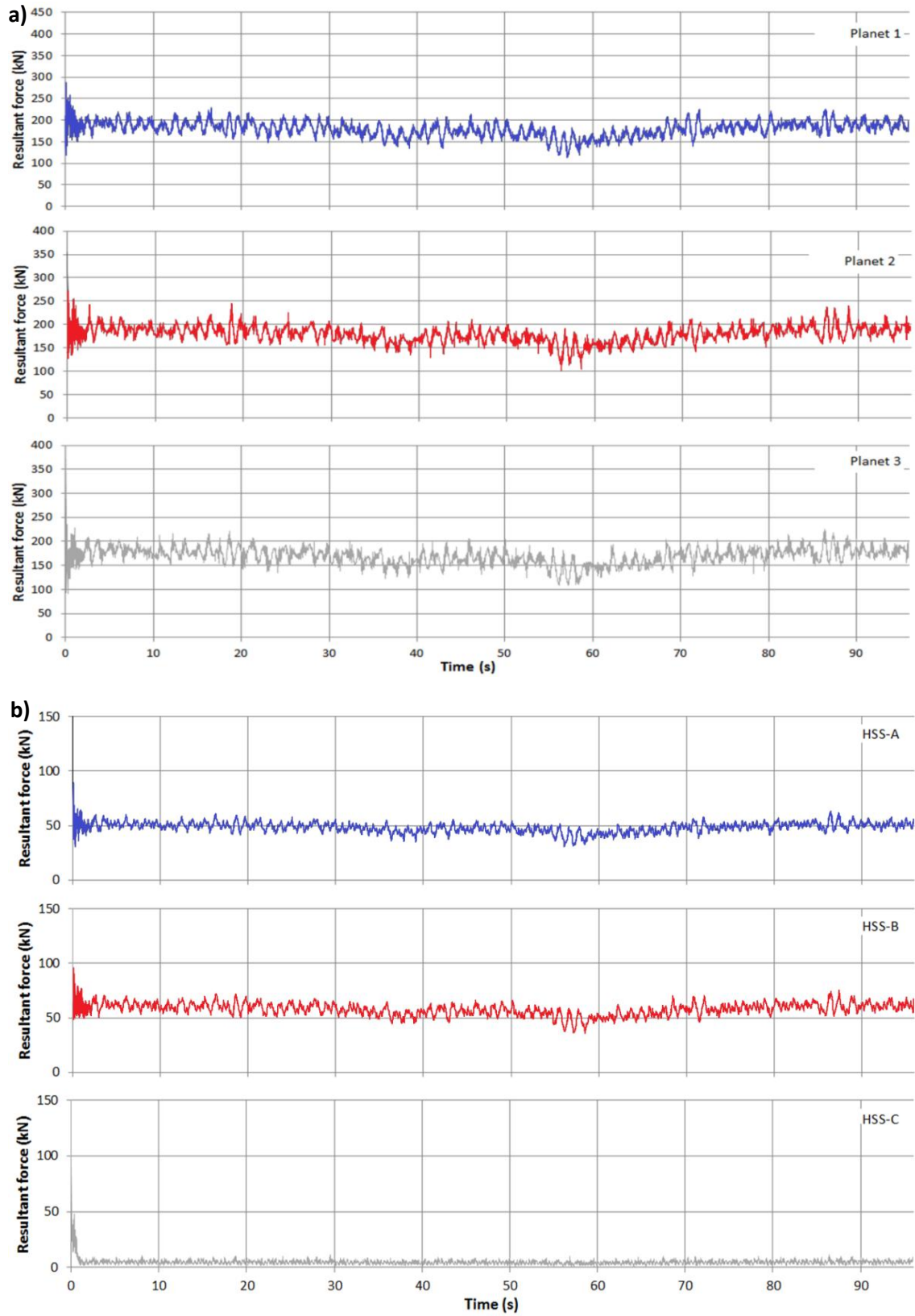


Figure 3-7: Resultant forces acting on bearings roller/raceway contacts during normal operation for: (a) Planetary bearings (b) High speed shaft bearings

3.3.2. Shut-down

The LSS and HSS velocities during the shut-down event are shown in Figure 3-8. The simulation was stopped after 36 seconds as the rotor velocity was oscillating either side of zero and maximum bearing loading had been experienced. Figure 3-9a shows the planetary bearing loading in the X and Y directions. The resultant load peaks after 10 seconds, when the generator is switched offline, then a higher loading peak of 358 kN is experienced when the disc brake is engaged at 26 seconds. Figure 3-9b shows that the HSS bearings experience maximum resultant force magnitudes of 110 kN for *HSS-A*, 102 kN for *HSS-B* and 63 kN for *HSS-C* under braking.

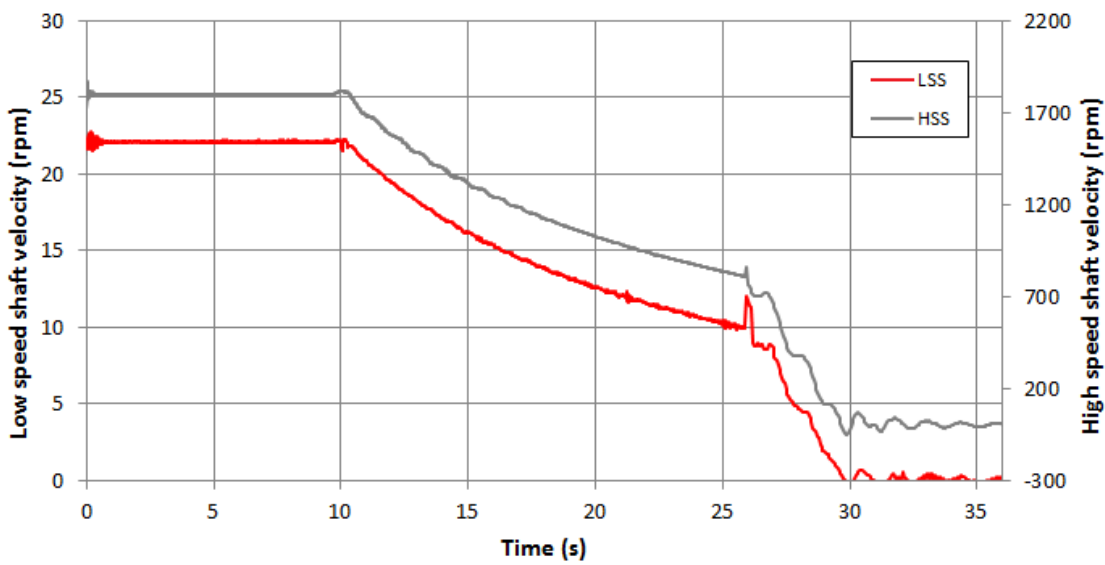


Figure 3-8: LSS and HSS velocity during shut-down

Analysis of the Premature Failure of Wind Turbine Gearbox Bearings

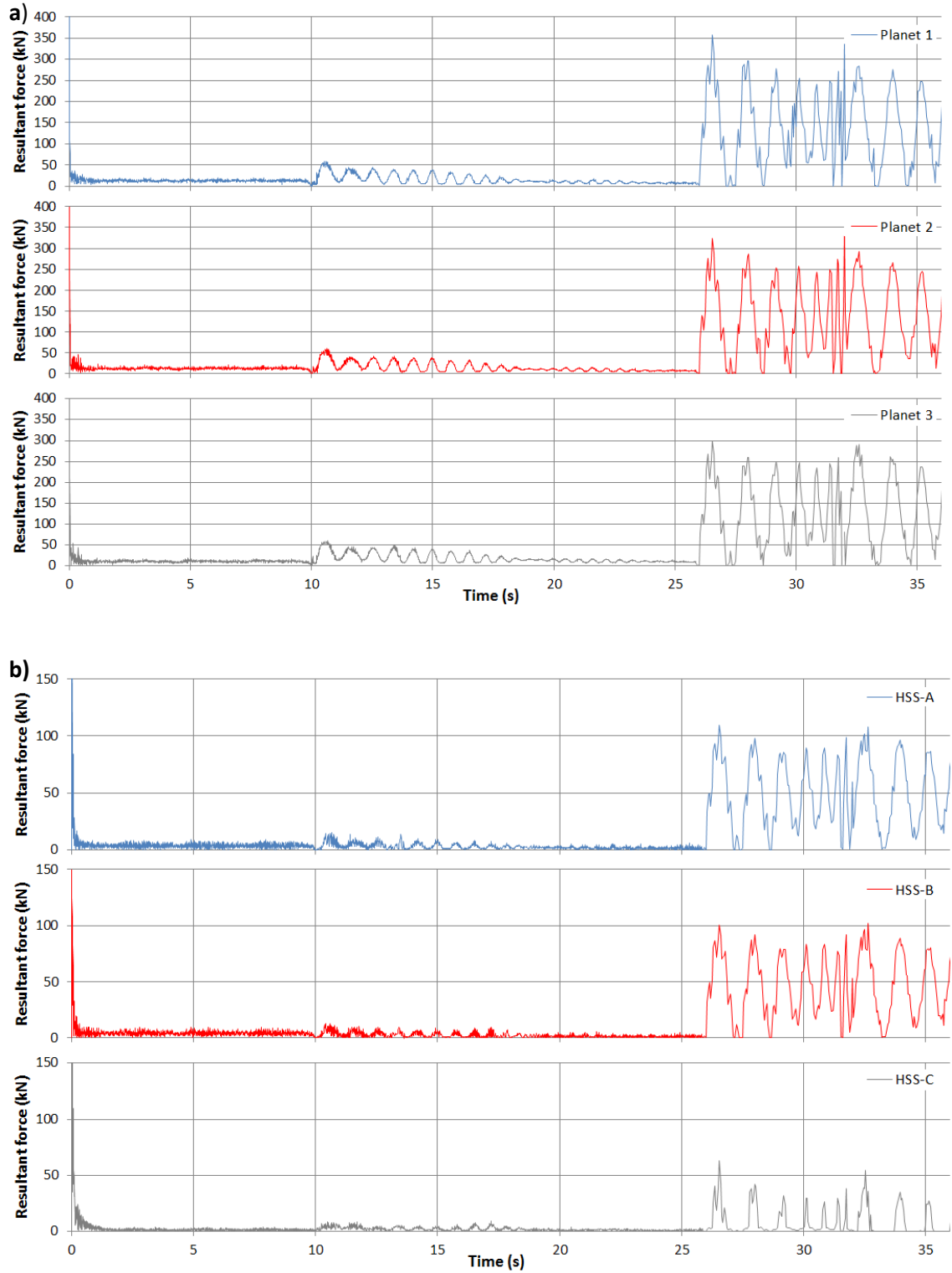


Figure 3-9: Resultant forces acting on planetary bearings roller/raceway contacts during shut-down for: (a) Planetary bearings (b) High speed shaft bearings

3.3.3. Maximum Hertzian contact stresses

The maximum contact pressures between the inner race and rolling elements, experienced by each bearing in the gearbox, were calculated. The inner raceway was investigated rather than the outer as most WTGBs fail on the inner race (as discussed in section 2.1.2). As previously mentioned, the developed dynamic model in this study has not yet taken into account unequal load sharing between the upwind and downwind planetary bearings. Previous studies [162, 173, 174] have found that the upwind planetary bearings experience considerably higher load than the downwind bearings. It is reported in [173] that maximum upwind planet bearing load sometimes reaches 1.3 times that of the downwind bearing. This factor is taken into account for the maximum planetary bearing contact stresses listed in Tables 3-3 and 3-4 below.

Tables 3-3 and 3-4 show calculated values for maximum Hertzian stress experienced for normal operation and shut-down respectively at each bearing location. This maximum stress level is presented as a percentage of the recommended allowable maximum contact stress (P_{rec}) as listed in current wind turbine design standards, which is 1,500 MPa for low speed planetary bearings and 1,300 MPa for HSS bearings [18].

	PLA	PLB	PLC	HSSA	HSSB	HSSC
P (kN)	277	322	278	63	78	15
P_{max} (MPa)	1410	1520	1410	1170	688	305
% of P_{rec} reached	94	101	74	90	83	20

Table 3-3: Maximum bearing contact stresses during normal operation

	PLA	PLB	PLC	HSSA	HSSB	HSSC
P (kN)	412	408	345	110	102	63
P_{max} (MPa)	1720	1710	1570	1540	788	618
% of P_{rec} reached	115	114	105	118	61	48

Table 3-4: Maximum bearing contact stresses during shut-down

3.4. Discussion

A gearbox model has been successfully created and validated in this study. Bearing loading results can be assumed to be accurate, taking into account the following limitations of the model:

- Inability to directly model load sharing differences between planet gear bearing pairs.
- Inability to model off-axis loads from the rotor and generator.
- Inability to model bedplate, planetary carrier and casing deflections.

It can be seen that planetary loading is fairly evenly shared between the three planetary gears, which have similar maximum load levels, for both shutdown and normal operation conditions. This suggests that the splined shaft connection does, as designed, promote load sharing in the planetary stage.

The planetary bearings are loaded to higher magnitudes than the high speed shaft bearings during both operating regimes and exceed the maximum recommended contact stress during manual shutdown (by 15 %) and normal operation (by 1 %). Bearing *HSS-A* on the *HSS* is also loaded to a surprisingly high percentage of recommended contact stress during normal operation (90 %) and significantly exceeds recommended levels during manual shutdown (by 18 %). It is anticipated that extreme operating conditions, such as emergency shutdown, would increase contact stresses even further. As a result, bearing inner raceways will accumulate fatigue damage and will possibly suffer localised plastic deformation under such operational conditions.

The tapered roller bearing pair, *HSS-B* and *HSS-C* do not come close to exceeding maximum allowable contact stress. This could be due to the fact that the tapered roller bearings are designed to withstand high levels of axial loading, which were not experienced during these simulations. The radial loading is shared between the two tapered bearings, whereas the axial load is only supported by one of the two, as *HSS-B* is positioned to take a positive axial load, while *HSS-C* is positioned to take a negative axial load. In addition to this, it is interesting to observe that during both events, loading on *HSS-B* is considerably higher than *HSS-C*. This is likely to be because *HSS-B* is supporting the shaft in the radial direction, to a greater extent than *HSS-C*, due to the fact that it is closer to the meshing gears thus taking a greater load.

During normal operation, the input torque was fairly steady however it is initially higher than that during shutdown, since the turbine is operating at rated power. During shutdown, maximum bearing loading conditions are experienced during the braking event, showing that a normal shutdown event induces greater transient bearing loading than that during normal operation. The shutdown event also produces large torque reversals in the gearbox, visible by the highly fluctuating bearing loading during braking. Hammering impact between the roller and raceway can therefore be expected during shutdown. It is expected that during emergency stop events, this will be experienced at higher levels.

Another consideration is that material defects in the bearing steel microstructure act as stress raisers. At sub-surface level, these defects will multiply the stress that the material experiences and are likely to cause plastic deformation in their close proximity during normal operation. This is investigated in detail in Chapters 5-7. Additionally, this study has assumed that all rolling elements are identically sized. In reality this is not the case and any variation in rolling element diameter can have large implications on load sharing [175]. Bearing misalignment and resulting roller edge loading has not been considered in this study. It is anticipated that a small misalignment angle between rolling element and raceway would lead to a considerably reduced contact area and therefore a considerably increased contact pressure. As previously mentioned, rollers and raceways have been assumed to be perfect cylinders under ideal Hertzian line contact, which equally distributes loading over the length of the line contact, the small increase in contact pressure caused by roller profiling has not been considered.

3.5. Summary

This chapter has shown that under normal operating conditions such as shutdown, the bearing loading exceeds recommended values both on the high speed shaft and the planetary stage, using a simulation model that likely underpredicts contact stresses. During extreme events such as emergency shutdown or grid disconnection due to grid faults, the bearing loading is very likely to be higher. As a result the bearings used in this gearbox are thought to be undersized and unable to deal with operating at rated torque and during manual shutdown events for their design lifetime. The results from this section show that bearings are frequently exposed to high contact pressures during operation and validate the tests designed in Chapter 4, which investigate the effect of exposure to many load cycles at the high contact pressures found in this Chapter (~1.7 GPa) as well as the higher contact pressures cited in the literature review (up to around 3.1 GPa [10]), that occur during extreme loading events. It should be noted that the confidence in the accuracy of the results presented in this chapter could be increased by undertaking a sensitivity analysis of the various assumptions made in constructing the gearbox model.

4. PROCEDURE FOR EXPERIMENTAL AND METALLURGICAL INVESTIGATIONS

This chapter outlines the methodology used to prepare and observe the specimens examined in Chapters 5 - 7 before discussing the test procedure design and testing methods used to recreate damage experienced by WTGBs in bearing steel test specimens. Figure 4-1 shows the Thesis work flow chart.

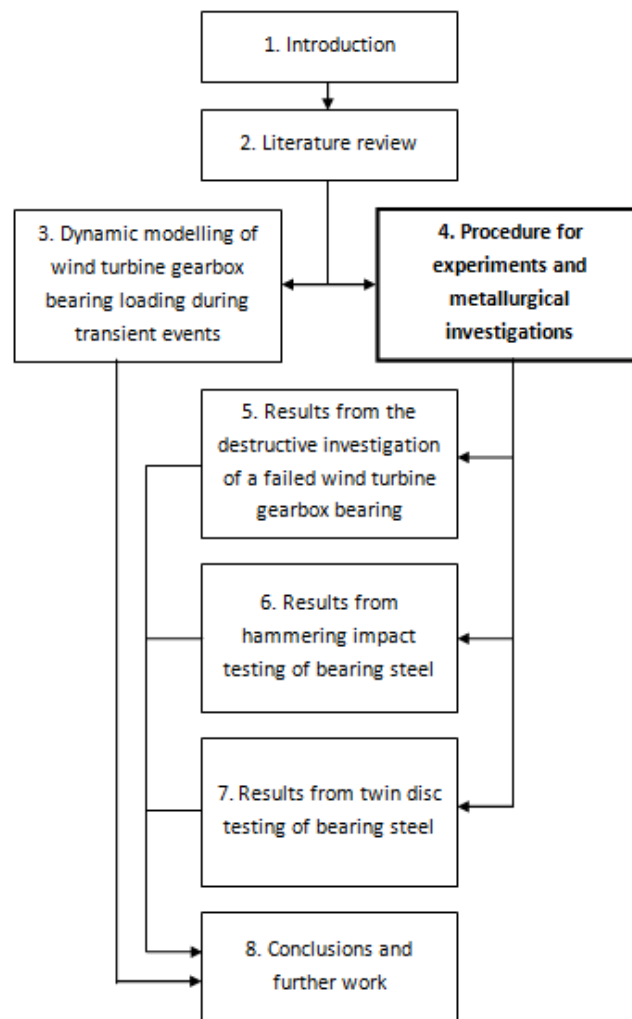


Figure 4-1: Thesis work flow chart

The chapter is split into five sections:

- Section 4.1 presents the specimen preparation methods.
- Section 4.2 presents the specimen observation methods.
- Section 4.3 presents the method used to examine the features formed in a failed WTGB.
- Section 4.4 presents the experimental design of reciprocating hammering impact testing of bearing steel.
- Section 4.5 presents the experimental design of twin disc RCF testing of bearing steel on the Sheffield University Rolling Sliding (SUROS) Specimen test rig.

4.1. Specimen metallurgical preparation

A five stage process to prepare specimens for observation throughout this study. This process is summarised in Figure 4-2 and described in detail below:

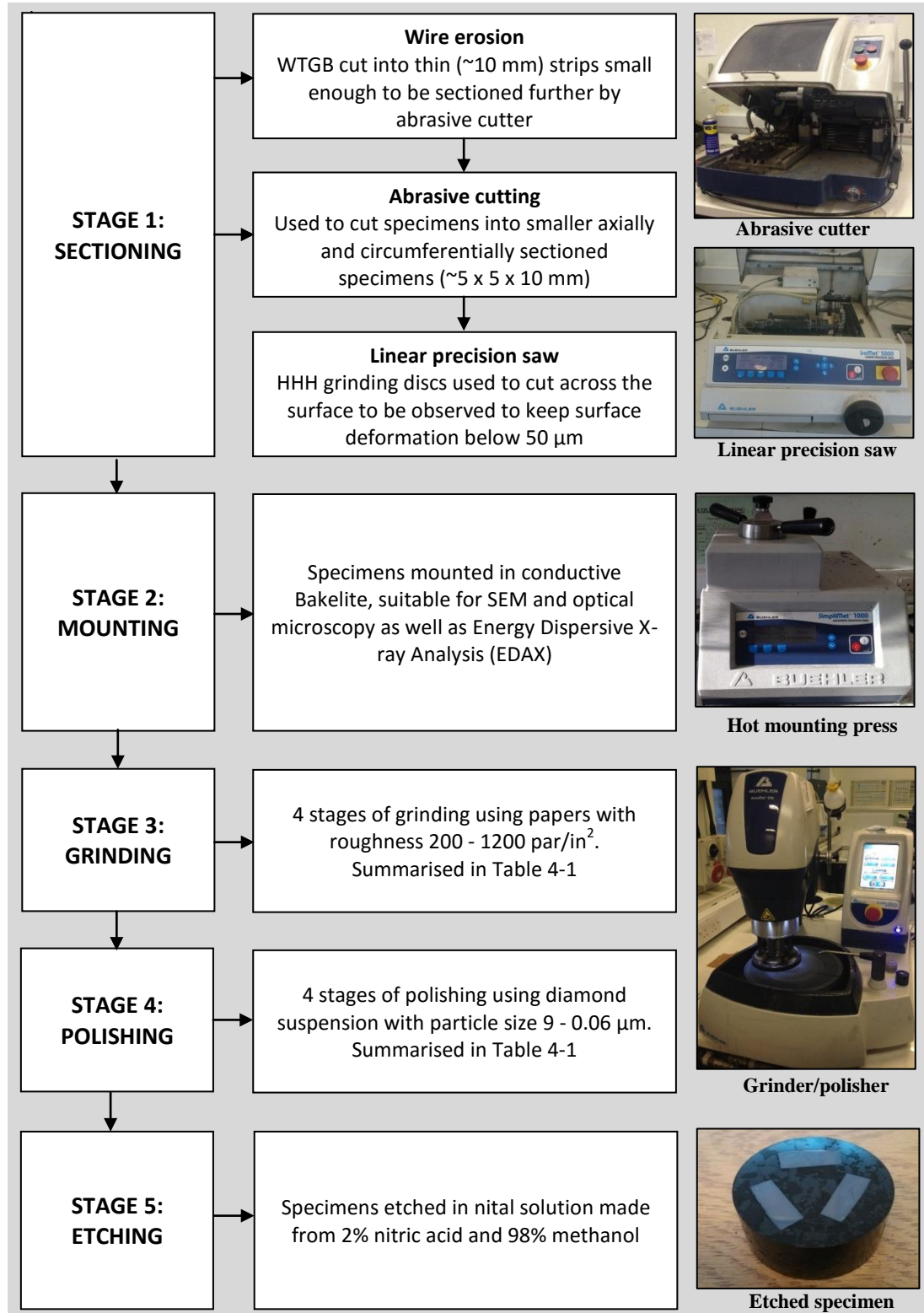


Figure 4-2: Specimen preparation summary

The first stage of specimen preparation was to section the specimens into small enough pieces to be mounted into cylindrical moulds using the hot mounting press. Since the failed WTGB was too large to fit into the abrasive cutting tool used to further section specimens, it was first cut into smaller strips using a wire eroder. These strips were then cut along their length to remove material deeper than ~5 mm from the raceway surface, since most damage features were expected to be found close to the depths of maximum stress concentrations (discussed in section 4.3), at depths much less than 5 mm. The thinner strips were small enough that up to three specimens could be mounted in one mould, as discussed in the following paragraph. This is advantageous since it reduces the time taken to hot-mount specimens, reduces the amount of material preparation equipment required and ensures that specimens can be efficiently observed in the SEM, as three can be viewed without the need to change the cylindrical mount. Strips of the WTGB were then cut into smaller sections using the abrasive cutter. Wedges from the hammering impact and twin disc specimens could be cut directly from the discs using the abrasive cutter with a *MetPrep™ type 3H* abrasive cutting disc, ensuring that axial cuts were made normal to the raceway surface tangent. Since these wedges tended to be wider than the sectioned WTGB specimens, only two could fit into each cylindrical mount. Cuts across the specimen face that was to be observed were made using the linear precision saw, which uses a much slower cutting speed and precision blade to minimise damage to the surface. 40 specimens were prepared for observation from the failed WTGB, 24 from hammering impact tests and 48 from SUROS specimens.

After sectioning, specimens were ready for hot mounting. Since steel is not adversely affected by the pressures and temperatures experienced in a *Beuller® SimpliMET® 1000* hot mounting press, they were compression-moulded using *Beuller® Konductomet™* graphite and mineral (SiO_2) thermosetting resin, which allows electrons to escape during SEM observations. For WTGB specimens, three were mounted in each mould, whereas for hammering impact and SUROS, only two could fit as shown in Figure 4-3. During mounting, specimens were heated to a temperature of 180 °C at a pressure of 250 bar for a period of 150 seconds, then cooled for a period of 240 seconds, before they were ready to be ground and polished.

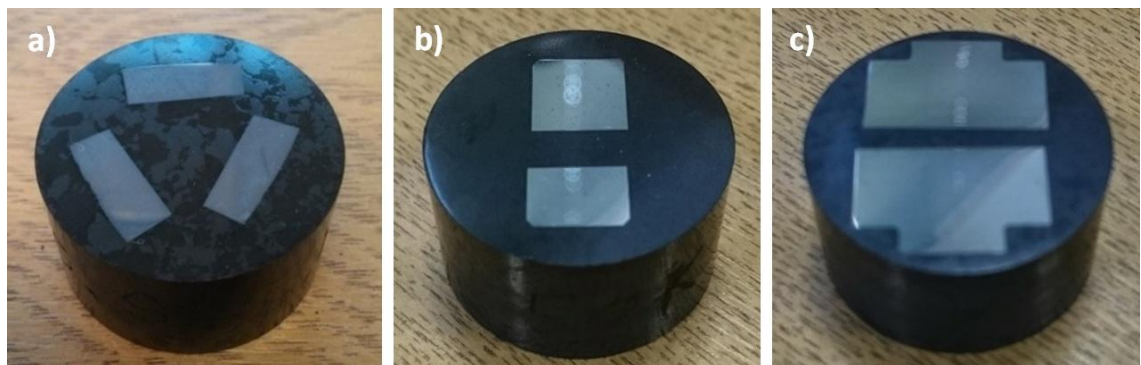


Figure 4-3: Examples of prepared specimens: a) WTGB b) hammering impact c) twin disc

Grinding and polishing was used to remove any surface damage caused during the cutting process and to produce a high quality, smooth, mirror-like finish, in order to provide high-quality images of the steel microstructure. An *AutoMETTM* automatic grinding and polishing machine was used to obtain this surface finish. Four grinding stages were required, using *MetprepTM* silicon carbide grit papers of decreasing grit size, which introduces progressively finer scratches, until the surface was smooth enough to be polished. Four polishing stages, using progressively smaller diamond particles (up to 0.06 μm in diameter) in *MetprepTM* suspension fluid on compatible polishing discs achieved the mirror-like finish required to obtain high quality images of the microstructure at high magnifications. In all stages, a force of 25 N was applied to the specimens to push them against the grinding/polishing discs. The rotational speed of the specimen holder, or “head”, was always set to 51 rpm and the grinding/polishing disc, or “base”, to 150 rpm with the exception of the final polishing stage, which was set to 200 rpm, since it was found to deliver a higher quality surface finish. The reason that the head speed was set at 51 rpm rather than 50 rpm, is that if the speed of the base divided by that of the head is a whole number, the same part of the grinding/polishing disc contacts the same part of each specimen over a number of rotations, which produces a poorer surface finish, since the full area of the disc is not used. The direction of rotation of the base and head was the same (anticlockwise) for all stages other than the final polishing stage, in which the head direction was reversed as this was also found to improve the surface finish. The process is described in full in Table 4-2. All grinding stages were carried out for 180 seconds, with the exception of the first which was continued until the specimen was level and all visible surface damage from cutting had been removed. All polishing stages were carried out for 300 seconds.

Preparation step	Grade (par/in ² μm)	Time (s)	Force (N)	Head speed (rpm)	Base speed (rpm)	Rotational direction (base/head)	
Grind	1	200	Until level	25	51	150	Same
	2	400	180	25	51	150	Same
	3	800	180	25	51	150	Same
	4	1200	180	25	51	150	Same
Polish	1	9	300	25	51	150	Same
	2	3	300	25	51	150	Same
	3	1	300	25	51	150	Same
	4	0.06	300	25	51	200	Opposite

Table 4-1: Preparation process for specimen observation

Finally, the samples were etched in nital made from a mixture of 2 % nitric acid and 98 % methanol, found to be ideal to reveal white etching features in previous studies [12, 13, 26, 50, 52, 53, 54, 55]. As well as revealing WEAs, the process highlights grain boundaries and carbides by selectively chemically attacking the polished surface. Microstructural grains orientated at different angles are etched to different levels and grain boundaries are more susceptible to etching. Consequently, different grains reflect light differently and contrast is added to the

image [176]. The etching process took around 10 seconds per specimen with a variance of approximately plus or minus three seconds, depending on the exact strength of the solution. This varied slightly due to small errors in measurements of the nitric acid. Specimens were visually inspected during etching until the surfaces appeared slightly clouded, at which point they were washed in water, rinsed with ethanol then dried. At this point they etched to the correct level to highlight ground boundaries, carbides and the white etching microstructure. After etching, observation of the microstructure could take place.

4.2. Observation of specimens

A number of different methods were used to inspect the specimens' visual appearance as well as their properties. These are summarised below.

4.2.1. Optical Microscopy

Optical images were taken using a *Nikon Eclipse LV150* microscope (shown in Figure 4-4a), linked to a computer controlled digital camera. Lenses with magnification levels of 50-1000 times allowed detailed observation of the specimen microstructure to be undertaken. Measurements could be made using the computer at the different magnification levels, including scale bars, length of features and angle measurements, which were used to determine the depth and orientation angles of the inclusions analysed in Chapters 5-7.

4.2.2. Scanning Electron Microscopy

Two scanning electron microscopes were used throughout this study. The *JEOL 6400* microscope was used first but was found to be unable to take high quality focussed images of small (~10 µm length) inclusions. Most images presented in this study were taken using the *FEI Inspect F* microscope, which was able to take well-focussed images at over 30,000 times magnification when used to observe well-prepared samples. Images were taken in secondary electron mode using accelerating voltages between 10-20 kV. Like the optical microscope, both SEMs user interface programmes were able to measure distances and orientation angles of features.

Energy dispersive X-ray analysis (EDAX) was used to determine the composition of specimen bulk material and contained inclusions, carbides and other features. The SEMs described above both had EDAX capability were used to find vol% and wt% of the elements present in specific areas or at points within the specimens, allowing, for example, the type of inclusion or carbide being observed to be identified.

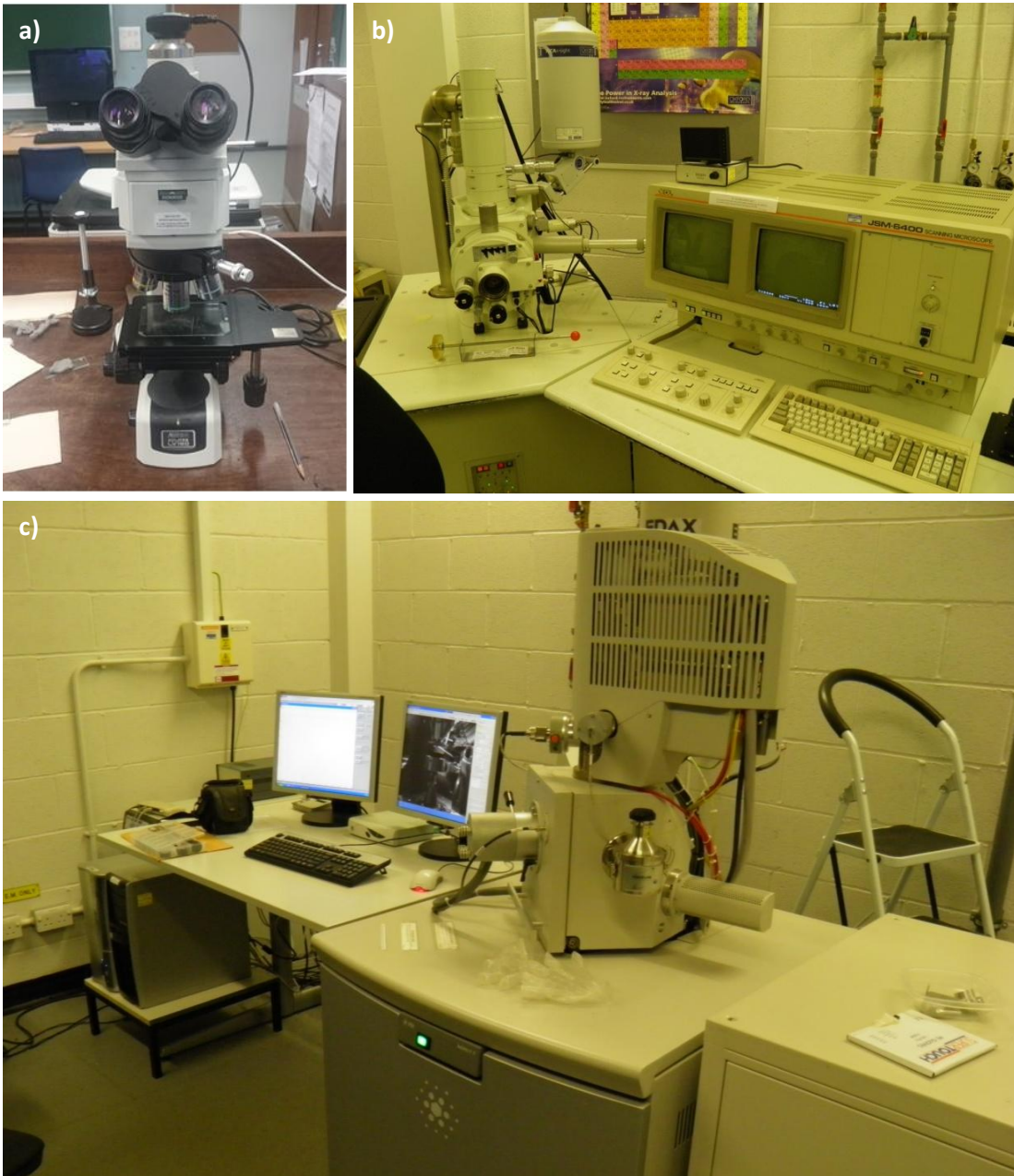


Figure 4-4: Microscopes used in this study a) Nikon Eclipse LV150 optical microscope b) JEOL 6400 SEM c) FEI Inspect F SEM

4.2.3. Surface profile measurements

The surface roughness of specimens was determined using a *Mitutoyo Surftest SV-600* 2D linear profilometer, which drags a stylus across the surface, plotting surface elevation against distance scanned in millimetres. From the resulting profile, surface roughness values including R_a and R_q could be found. Each surface roughness value stated in this report is a mean value from at least three measurements, which were taken in specimen axial directions.

4.2.4. Nano-hardness measurements

A nano-hardness indenter with a Berkovich tip was used to measure the hardness of WEAs found in specimens from the failed WTGB. The Oliver and Pharr method [177] was used to process the experimental data. In order to determine hardness H , the peak load W_{max} and depth at peak load d_{max} were required. The contact area A , could be found from d_{max} , which allowed the hardness to be calculated using equation 4.1. At least nine indentations were made at each feature tested for hardness and a mean taken, in order to increase the accuracy of results [1].

$$H = \frac{W_{max}}{A} \quad (4.1)$$

4.3. Destructive investigation of a failed planetary bearing

A failed upwind bearing from the low speed planetary stage of an onshore wind turbine that was operated in the EU was destructively investigated in order to examine subsurface material damage. The bearing is a CRB *SKF Explorer* model; an exploded schematic of which is shown in Figure 4-5. The wind turbine gearbox had been operating without major incident for five years. A routine oil analysis was carried out 10 days prior to failure, the subsequent report concluding that wear levels were satisfactory and the routine sampling interval should be maintained. The turbine was taken out of service 10 days later when the supervisory control and data acquisition (SCADA) control system received the low gear oil pressure alarm. After inspection, it was found that the bearing had catastrophically failed. The information about the failure was provided by the wind farm operator who must remain anonymous for confidentiality reasons.

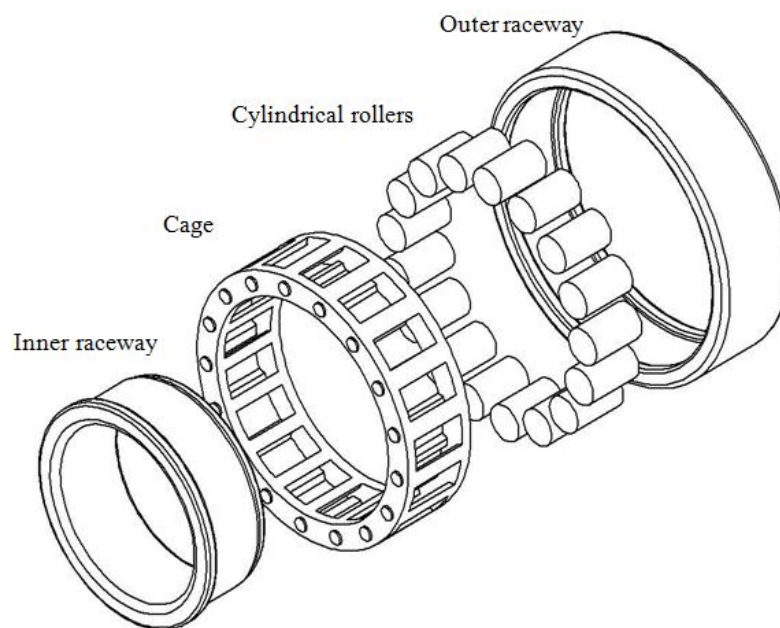


Figure 4-5: Sectioned planetary bearing exploded schematic (adapted from [1]).

The operating conditions for the bearing are summarised in Table 4-2. Approximate depths of maximum Hertzian stresses τ_{max} , $\tau_{O,max}$ and σ_v,max have been calculated using equations 2.1-2.3 followed by the approximations listed in section 2.1.3.2 and are presented in Table 4-2 based on the bearing dimensions (presented in Figure 9-7 in Appendix E) and the recommended maximum contact pressure for planetary WTGBs (1,500 MPa) listed in the wind turbine design standard IEC 61400-4 [18] and confirmed in Chapter 3 and [98]. Photographs of the bearing and other components from the same gearbox are presented for interest in Figure 9-8 - Figure 9-17 in Appendix E.

Motion	Nominally rolling contact. Inner ring stationary with rotational motion of outer ring and cylindrical rollers. Rotational speed of outer ring: 38 rpm. Sliding of rolling elements in unloaded zone likely.
Loading	Repeated loading of same inner raceway arc. Torque reversals and impact loads known to occur. Misalignment possible. Bearing contact pressures expected to be approximately 1,500 MPa during normal operation [18, 98, 173], but may exceed 1,700 MPa during WT shutdown (see chapter 3 and [98]).
Depths of maximum stresses	τ_{max} depth: 233 μm $\tau_{O,max}$ depth: 150 μm σ_v depth: 209 μm

Table 4-2: Operating conditions of sectioned bearing

4.3.1. Inspection of surface damage and location of prepared specimens

Wear was evident for approximately 55 % of the inner raceway circumference, but within this region the coverage and type of damage changed. Outside this region there was little to no evidence of wear. The transition from damaged zone to non-damaged zone was immediate and distinct, at a line that is likely to have been positioned at the entry to the loaded zone of the bearing raceway (as discussed in section 2.1.2). The variation in damage has been described by three distinct zones as illustrated in Figure 4-6.

- Zone 1: Non-damaged zone. Over the remaining 45 % of the raceway circumference there was very little evidence of damage detectable by eye.
- Zone 2: There was a transition to the area of damage coverage. Damage was mainly evident on one side of the raceway towards the non-flanged side of the raceway. The wear damage was intermittent but well defined at a width of around 20 mm for approximately 35% of the bearing circumference. Within the main 20 mm band of damage there was severe spalling. There were also smaller wear scars outside of this band around the centre of the raceway.
- Zone 3: Damage covered most of the raceway width for approximately 20 % of the circumference. There was severe spalling with evidence of material removal from the surface.

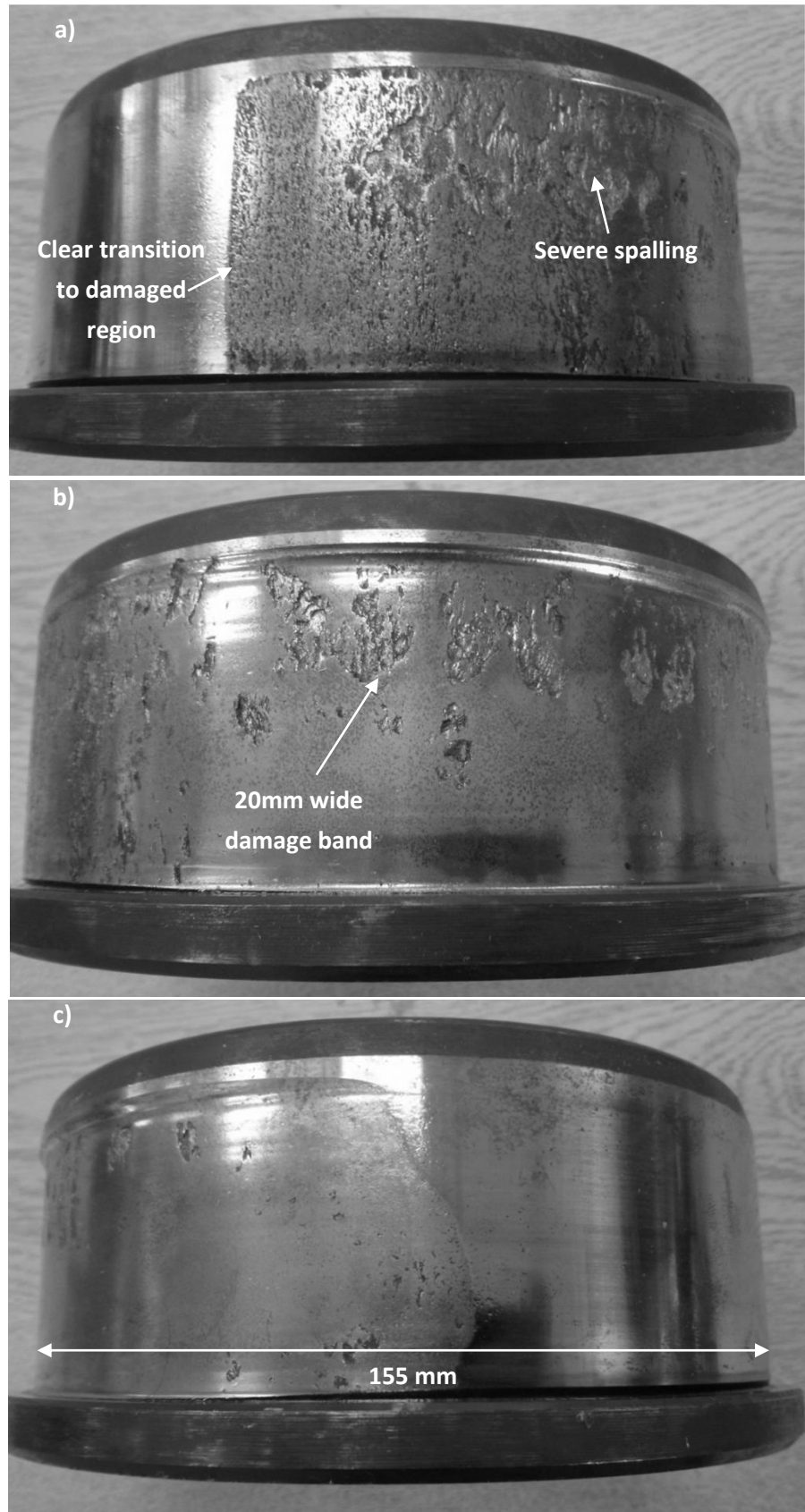


Figure 4-6: Photographs of raceway damage a) Zone 3 b) Zone 2 c) Zone 1

From the initial observation of the bearing, it was clear that the failure occurred at some point within the inner raceway, as the outer raceway was relatively undamaged. The inner raceway was therefore selected for investigation. A total of 40 specimens from the three zones were prepared for inspection using the method described in section 4.1. As has been previously highlighted, it is important to consider damage on both axial and circumferential sections of the bearing, since inclusion orientation may be critical to the level of damage caused. As a result, it was necessary to prepare specimens sectioned both axially and circumferentially, in order to determine whether cracks form preferentially in either direction.

Section details	Specimen Nos.
Section 1a - Circumferential section. Zone 3 damaged region.	1-6
Section 1b - Axial section. Zone 3 damaged region.	6-12
Section 2a - Circumferential section. Zone 1/Zone 2 boundary.	13-18
Section 2b - Axial section. Zone 1/Zone 2 boundary.	19-24
Section 3a - Circumferential section. Zone 2 damaged region.	25-30
Section 3b - Axial section. Zone 2 damaged region.	31-36
Section 4a - Circumferential section. Zone 1 non-damaged region.	37-40

Table 4-3: WTGB specimens prepared for metallographic observation

4.3.2. Observation of WTGB microstructure

As discussed in section 2.2.2, typical bearing steel is produced by rapid quenching from above the eutectoid temperature, before tempering at around 160 °C [26]. The general microstructure of the steel is shown in Table 4-4 which was found using EDAX analysis as described in section 4.2.2 and confirmed to be the 100CrMo7-3 grade (see section 2.2) due to the increased levels of Molybdeum (Mo) compared to the 100Cr6 steel grade. Note that the value for carbon in the table is approximate since EDAX cannot be assumed to be accurate when measuring elements with small atomic numbers, such as carbon. From analysing several SEM images such as Figure 4-7 it has been observed that the microstructure of the sectioned bearing is interspersed with spheroidal iron-chromium (M_3C) carbides, identified as such by their high levels of carbon (C) and chromium (Cr) EDAX tests. The average chemical compositions from a sample of five cementite M_3C carbides with similar appearance to those in Figure 4-7 were: C 18.1 wt%, Cr 5.3 wt%, Fe 73.3 wt%. Damage inducing MnS inclusions were present throughout the microstructure and their chemical composition was confirmed with EDAX as shown in Figure 4-8.

Steel grade	C%	Si%	Mn%	Cr%	Mo%	Fe%
100CrMo7-3	~1*	0.21	0.37	1.71	0.20	Balance

Table 4-4: Elements present in WTGB from EDAX analysis. *Carbon value approximate

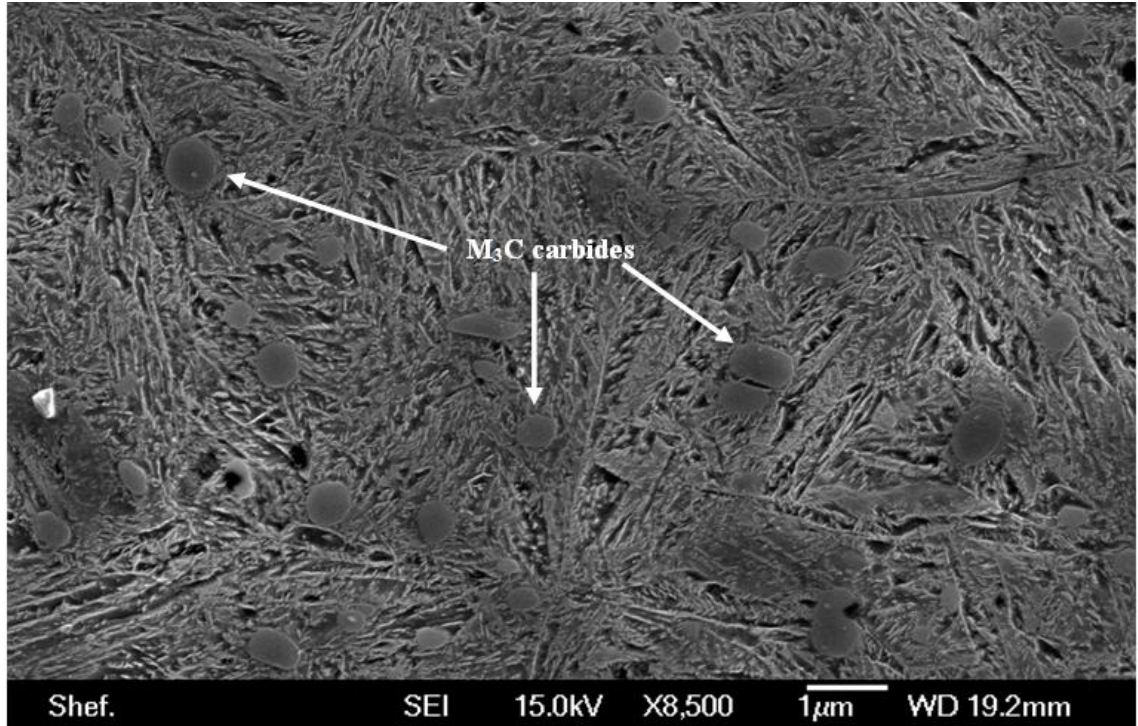


Figure 4-7: Bearing steel microstructure highlighting spheroidal iron-chromium (M_3C) carbides

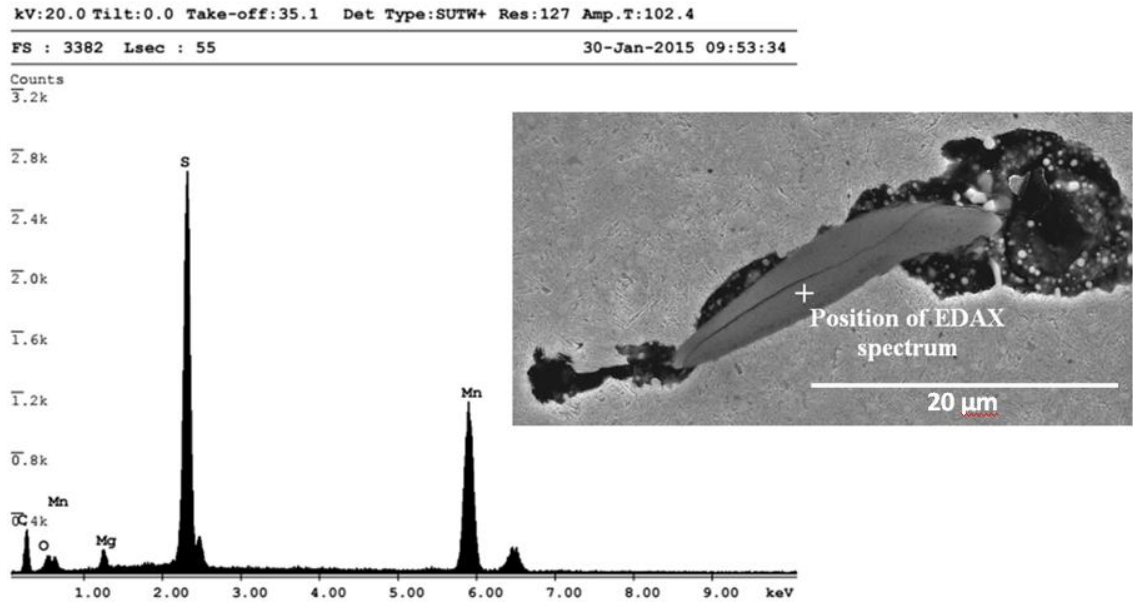


Figure 4-8: EDAX spectrum showing chemical composition of MnS inclusion

4.3.3. Illustration of undamaged inclusions

Ten MnS inclusions at depths of greater than 5 mm from the contact surface (assumed to be deep enough to be unaffected by the Hertzian stress field) were identified using the *Inspect F* SEM. These inclusions were found at random within Zone 3 damaged region of the bearing raceway, being the first 10 that were encountered. It was important to do this in order to make distinctions between the damaged inclusions and undamaged inclusions and to ensure that none of the damage was caused by the sectioning process or during manufacturing. Observing the inclusions in Figure 4-9 confirms that almost no damage was caused to these deep inclusions, although some black marks are present at the boundary between steel matrix and inclusion. These marks could be small voids caused by separation of the MnS inclusion from the steel matrix during quenching.

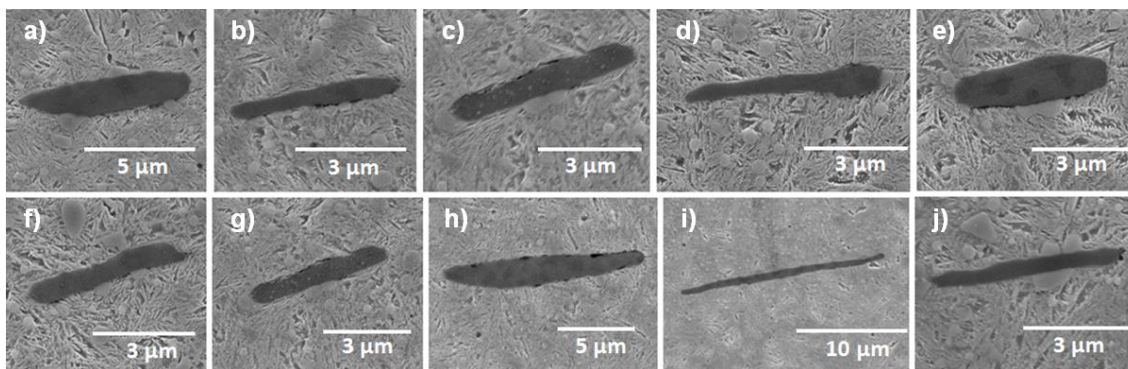


Figure 4-9: Examples of undamaged inclusions at depths of greater than 5 mm (specimen 31)

4.3.4. Damage initiating MnS inclusion database

During observation of the specimens, it became apparent that the vast majority of subsurface cracking and WECs were connected to MnS inclusions. It was decided therefore, to create a database of all inclusions found to have initiated some form of damage. The following data was recorded, with the aim of finding trends between the damage types found:

1. Inclusion length
2. Total length of WEC initiated from inclusion
3. Total length of crack initiated from inclusion
4. Inclusion depth from surface
5. Angle of inclusion from horizontal (parallel to surface)
6. Whether the inclusion was internally cracked
7. Whether the inclusion was separated from the surrounding steel matrix

As discussed in section 4.2, it was possible to use the control software for the optical microscope to measure distances and angles. The measurements made for each inclusion in the database are summarised in Figure 4-10. The results from analysing the data collected are discussed in Chapter 5.

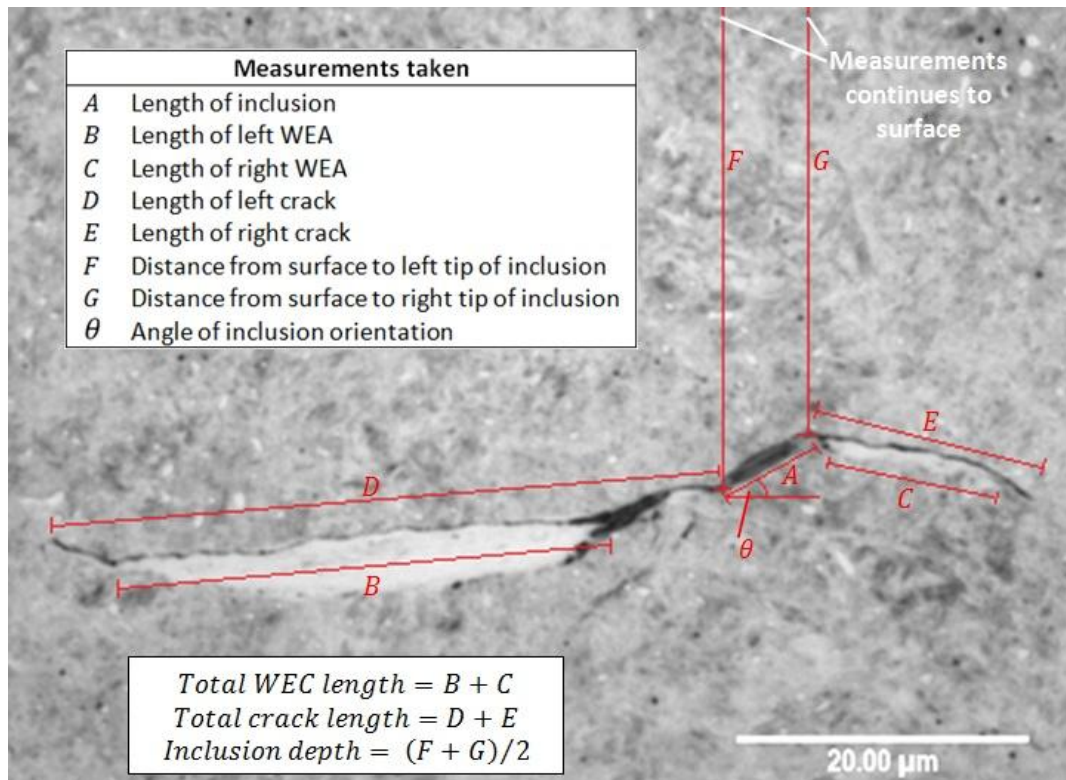


Figure 4-10: Measurements made for each damage initiating inclusion in the database

4.4. Hammering impact testing of 100CrMo7-3 bearing steel

Hammering impact testing was designed in order to investigate the effects caused by repeatedly exposing bearing steel to high contact stresses in a controlled environment. Testing to investigate the following was undertaken:

1. Whether repetitive impacts alone cause WEA and butterfly crack formation in bearing steel.
2. The effect on the extent of damage caused by varying the number of impacts (loading cycles).
3. The effect on the extent of damage caused by varying the level of contact stress.
4. The importance of the impacting object sliding along the surface during impact.

4.4.1. Apparatus

In order to carry out the testing, a test rig that was developed by Slatter and used extensively for previous work of material surface wear [178, 179, 180] at the University of Sheffield was modified for use in this study. The simple rig used in this study uses a motor-driven cam to lift an oscillating lever arm, which is kept in contact with the cam surface by a spring. At the end of the arm is a striker that holds a steel ball, which makes contact with the specimen. The rig provided a repeatable way to apply a set impact force to a specimen, at a set impact angle, at

set time intervals for a set number of impact cycles. The modified rig is shown in Figure 4-11, the main modifications from that described in [180] being:

1. The development of a new specimen holder that operates like a vice, to clamp cylindrical test specimens (45 mm diameter, by 10 mm width) in position under the striker component as shown in Figure 4-11. Note that the position of the specimen is such that the ball bearing hits the specimen in a radial direction.
2. The attachment of the “mass holder” plate onto the “pivot block”, allowing for counterweights to be attached to the arm, altering the effective mass of the “striker”.

Surface sliding was introduced by using an angled striker component, allowing the impacting ball to hit the specimen at an angle of 45° to the surface tangent. As a result, the ball slips along the specimen surface during impact as described in Figure 4-12, introducing surface traction.

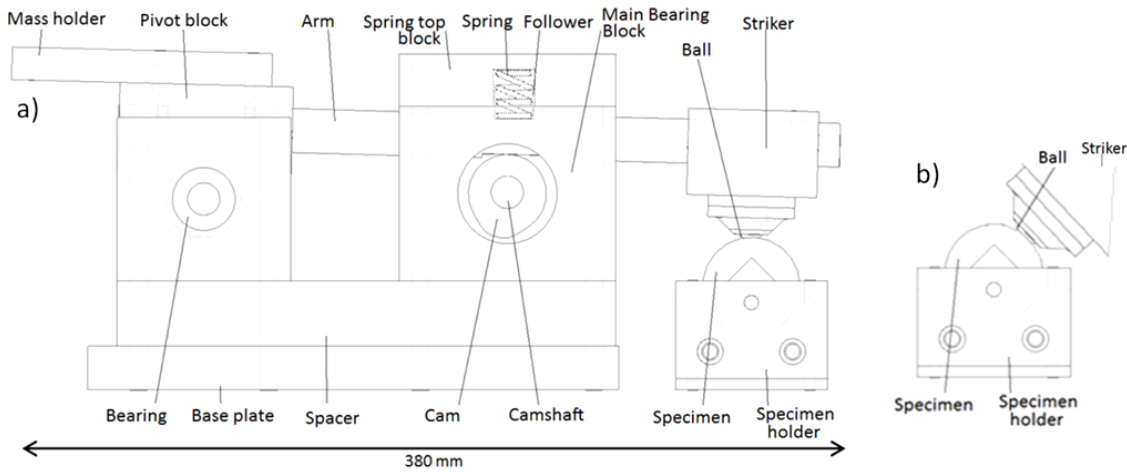


Figure 4-11: Modified impact test rig a) standard setup b) angled striker setup for compound impact testing

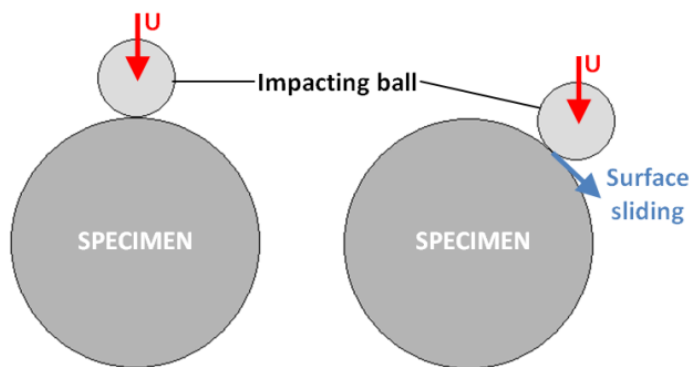


Figure 4-12: Illustration of surface sliding induced by angled contact

4.4.2. Technical analysis of rig

A full technical analysis of the test rig was undertaken by Slatter [180]. The velocity at the point of impact U , measured to be 0.45 m/s at an impact frequency of 10 Hz, using high speed video footage. With various spring stiffnesses and counterweights, the rig was found to operate well at a frequency range of 2-11 Hz. The impact velocity at 10 Hz can be linearly scaled (as shown in Figure 4-13) to give the impact velocity at different impact frequencies under the following assumptions:

1. The components used to make the rig are perfectly stiff (excluding the spring), so deflections and vibrations can be neglected. In reality, multiple impacts per rotation will take place, as the arm vibrates. Analysis of high speed video footage allowed the actual rig performance to be determined, showing that four impacts took place per cycle for typical conditions used. Since the first impact was of significantly greater energy than the subsequent, it was assumed that the other impacts had no effect on the test specimen.
2. The cam and arm are always in contact (i.e. the inertia of the arm and striker are ignored). In reality the arm will leave the cam for a moment, when the cam lift is at a maximum.
3. The cam was assumed to be identical to that in the design state and it had not worn. In reality, the cam profile will be slightly altered.

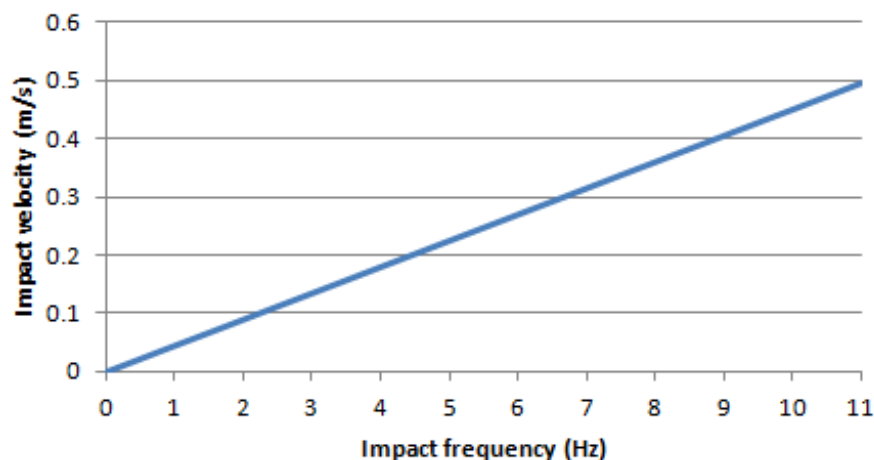


Figure 4-13: Impact velocity (U) at different impact frequencies (0-11 Hz) for the impact test rig

The effective mass of the striker could be altered in order to change the impact energy, by changing the spring stiffness, the mass of the striker, or by bolting counterweights onto the back of the rig. Moments were taken around the pivot, to work out the effective mass of the striker, taking into account the force applied by the springs used as shown in Figure 4-14. The weight of the counterweight is denoted W_1 and other components, W_{2-5} as shown in Figure 4-14. The force applied by each of the two springs at the point of impact F_{s1} and F_{s2} respectively were multiplied by their respective distances in the X-direction from the pivot. Distances of each force from the pivot are denoted d_{1-6} as shown in Figure 4-14. The spring

force was calculated by multiplying the stiffness of each spring by the extension at the point of impact. The addition of moments divided by the distance of the point of impact (d_6) gave the effective weight of the striker for each test.

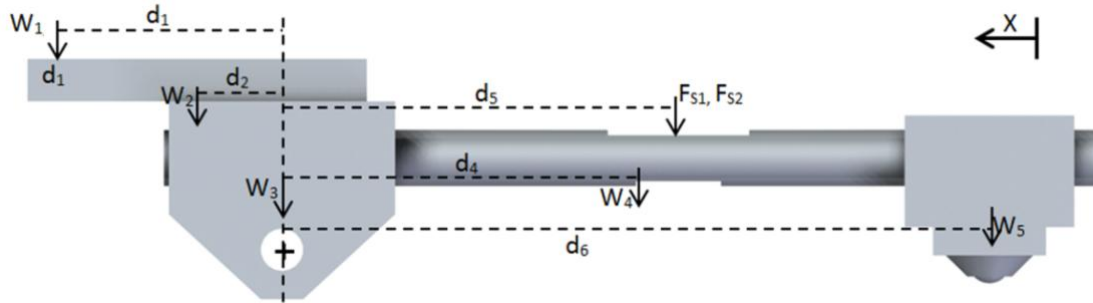


Figure 4-14: Moments taken about impact rig pivot

Equation 4.2 was used to find the effective mass (M_e) in kg of each striker, where g is the acceleration due to gravity, equal to 9.81 ms^{-2} :

$$M_e = \left(\frac{W_1 d_1 + W_2 d_2 - W_4 d_4 - F_{s1} d_5 - W_5 d_6}{d_6 \times g} \right) \quad (4.2)$$

Using a combination of different springs and counterweights, a wide range of effective striker masses were available for testing. The different spring stiffnesses that were available for use are shown in Table 4-5. An initial feasibility study found that the rig operated best with the two stiffer springs (part numbers 2270 and 2323) at the frequency range and masses required; hence these springs were used in the tests presented in this report. Using the calculated values for effective mass M_e , and impact velocity U , for each test condition used, allowed the contact pressure during the test to be estimated using FEA (as discussed in section 4.4.4).

Part Number	Outside diameter (mm)	Free length (mm)	Solid length (mm)	Wire diameter (mm)	Stiffness (N/mm)
2230	17.25	40.5	6.90	1.25	1.44
2250	17.60	34.00	11.00	1.60	3.87
2270	18.00	30.00	12.50	2.00	9.26
2323	20.00	27.20	16.40	2.80	29.25

Table 4-5: Spring stiffnesses used in hammering impact testing. Springs 2230 and 2250 (shown in *italic*) were tested for use but rejected. Springs 2270 and 2323 were used in to damage specimens that are presented in this study (Chapter 6).

4.4.3. Specimens

Through-hardened 100CrMo7-3 bearing steel specimens were tested using the hammering impact rig. Before testing, the specimens were quenched then tempered at $260 \text{ }^\circ\text{C}$, to achieve a hardness of around 60 HRC. The surface was ground to give a maximum roughness, R_a , of less than $1 \text{ } \mu\text{m}$ (measured using method described in section 4.2.3). The specimens were

chosen for their yield strength and hardness properties, which were suited to the capabilities of the test rig so that subsurface damage could be caused, without significant surface damage. Additionally, the steel was of the same type as the sectioned WTGB (as described in section 4.3), with MnS inclusions of similar size and axial orientation as shown in Figure 4-15. The steel balls used to impact the specimens were slightly harder than the specimens, so that damage was first experienced on the specimens. The steel balls were changed between tests. The approximate chemical composition of the specimens is shown in Table 4-6, provided by the manufacturer [66] and the mechanical properties of both the specimens [66] and the impact steel ball, in Table 4-7.

C%	Si%	Mn%	S%	Cr%	Ni %	Mo%	Fe
0.99	0.30	0.70	0.015	1.80	0.13	0.25	Balance

Table 4-6: Chemical composition of 100CrMo7-3 specimens used in testing

	100CrMo7 (specimen)	100Cr6 (ball)
Young's modulus (GPa)	210	210
Hardness (HRC)	59-61	60-67 [180]
Yield strength (GPa)	1.7	~2
Tensile strength (GPa)	2.4	~2.3
Poisson's ratio	0.3	0.3
Density (kg/m ³)	7800	~7800
Diameter (mm)	45	15
Surface roughness (max) (µm)	1	0.125 [180]

Table 4-7: Mechanical properties of specimens [26] and impact steel balls used in testing (Approximate 100Cr6 properties from [26])

As previously discussed, the orientation of MnS inclusions in bearing raceways could be critical for the formation of WECs. Inclusions were orientated with their longest dimension parallel to the specimen central axis, as shown in Figure 4-15, as was the case in the sectioned WTGB shown in Figure 4-6. Since through hardened WTGBs are frequently found to fail due to axial cracking [13], it was decided that specimens would be sectioned in the axial direction. Any MnS inclusions lying on the observed plane would be sectioned along the xy plane shown in Figure 4-15. All inclusions within the section made through the impact zone were observed and photographs were taken of those that had initiated damage. All measurement of inclusion lengths and their depths from the contact surface were made using the measurement tool built into the control software of the microscopes used. Six examples of MnS inclusions in an undamaged specimen are displayed in Figure 4-16 for comparison to damaged inclusions discussed in Chapter 6. The inclusions in the undamaged specimen display no damage from the heat treatment or sectioning processes. Although other inclusion types were found within the specimens, only MnS-type inclusions were found to have initiated damage.

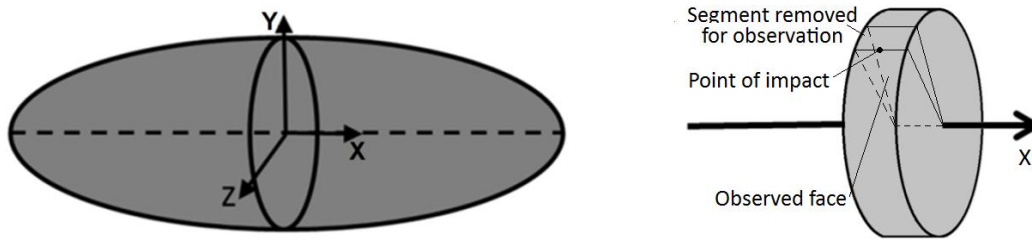


Figure 4-15: Orientation of MnS inclusions in specimens

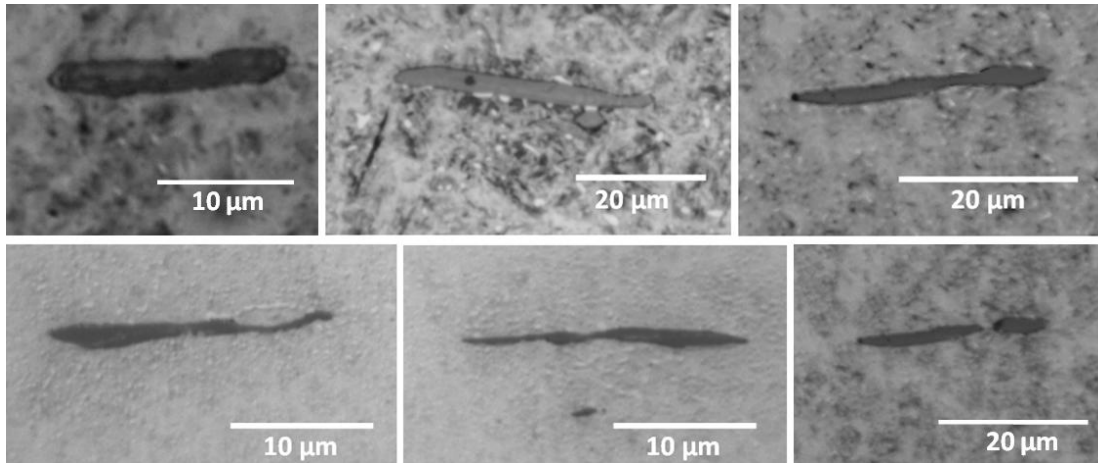


Figure 4-16: Typical MnS inclusions in undamaged specimen

The chemical composition of 10 MnS inclusions from the specimens was tested to verify their composition. Figure 4-17 shows an example MnS inclusion from a specimen, with the area scanned in the EDAX analyses highlighted. These inclusions sometimes contained oxide parts, (typically aluminas) as shown in the figure, which are analysed in detail in Chapter 5. Average element weight and atomic percentages of the 10 MnS inclusions are shown in Figure 4-17b, which clearly shows that the inclusions are of MnS-type. Since WECs are only visible as white when viewed in optical light, inclusions had to be identified by their appearance. This analysis identifies grey “sausage shaped” inclusions as MnS in the hammering impact specimens.

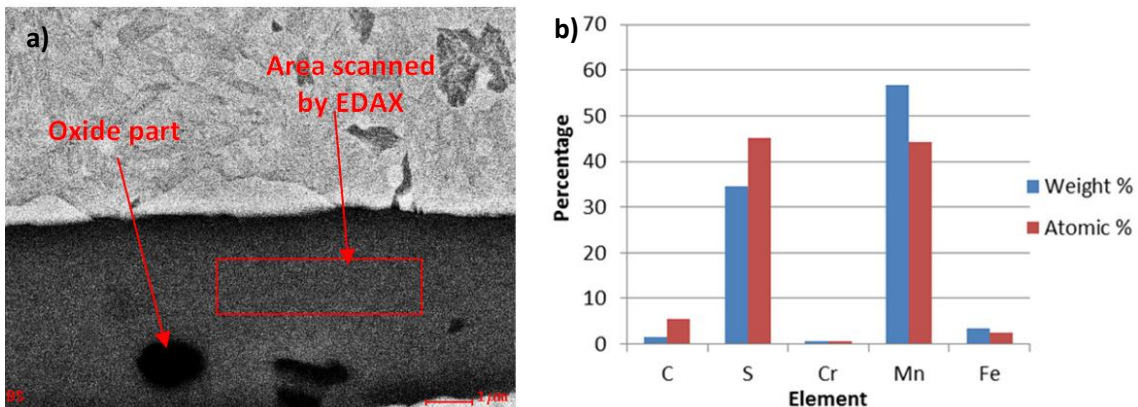


Figure 4-17: Identification of MnS-type inclusions: a) example area scanned b) mean weight and atomic percentages of 10 MnS inclusions from hammering impact specimens

4.4.4. Test design using FEA

Since WEC damage is known to initiate at subsurface inclusions, it seemed logical to design experiments that caused the subsurface stress to exceed the material yield strength, but remaining below the yield strength on the surface. *Abaqus* was used to create a FEA model simulating the impact between the ball and specimen. As with any FEA model, results should not be assumed to be completely accurate without validation. Since it was not possible to measure specimen surface deformation during impact, there was no way of theoretically calculating the contact pressures, taking into account the energy transferred during impact. An FEA model was therefore deemed to be the best way to approximate contact pressures.

Explicit analysis was used to model the contact stresses caused by the impact of a correctly dimensioned steel ball, with the effective mass M_e of the striker, upon a specimen. The material properties listed in Table 4-7 along with its plastic strain behaviour in Figure 4-18, were used to define the material stress-strain curve. Elastic behaviour modelled material strain up to its yield strength and plastic strain using an isotropic hardening model beyond this. Plastic strain data was obtained from the results of tensile test [181] of through hardened 100Cr6 bearing steel (also tempered at 260 °C), which has very similar strain behaviour to 100CrMo7 bearing steel [182]. Compressive stress-strain data was not available and although tensile behaviour cannot accurately model compressive behaviour close to the material's ultimate strength, it has been assumed that the results are accurate enough to approximate the surface stress (the key result from the simulations), which is below the yield strength of the material for all tests. Maximum stress levels on the surface and subsurface were recorded from the equivalent stress distribution calculated using FEA.

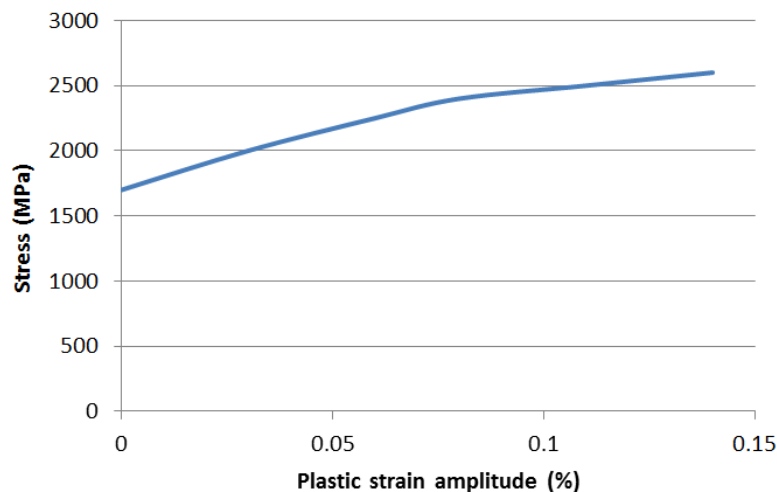


Figure 4-18: Plastic strain amplitude vs. stress for 100Cr6 steel (adapted from [181])

Contact was modelled using “hard” contact with default constraint enforcement; normal behaviour and tangential behaviour was assumed to frictionless; a fair assumption since the impact was perpendicular to the surface and there was no surface sliding. Surfaces were

assumed to be smooth. Since contact between the two bodies is symmetrical around the centre of contact when sectioned axially (along the specimen axis) and circumferentially (through the circumference of the specimen), modelling a quarter of the lower half of the impacting ball and upper half of the specimen provided a more efficient way of obtaining results. Consequently, the effective mass of the ball was divided by four, since only a quarter of the contact area was available to absorb the impact energy. Each plane that intersected the centre of contact was restrained from moving perpendicularly, or rotating in any off-plane direction as shown in Figure 4-19, where X , Y and Z refer to linear displacements along, and X' , Y' and Z' refer to rotational displacements around, the x , y and z axis respectively (axis convention is indicated on the figure). The ball component was given an initial velocity in the negative direction on the y axis, equal to that of the test it was representing (see Figure 4-13). Since the model was designed to simulate symmetric contact about the centre of impact, it could not be used to accurately simulate sliding contact, which effectively has a moving point of impact. For this reason the simple assumption was made that the contact pressures were equal to that of a normal impact with an impact velocity equal to the radial velocity component of the sliding impact, found using equation 4.3. From this, the contact pressure could be found using the normal impact FEA model.

$$U_{radial} = \frac{U_{sliding}}{\sqrt{2}} \quad (4.3)$$

A coarse mesh with elements $\sim 5 - 10$ mm in width was used for the majority of the model, but a finer mesh with elements of width 0.1 mm was used in volume of 1.5 mm radius around the point of impact as shown in Figure 4-20. The 1.5 mm radius volumes in both the specimen (cylindrical shape) and ball (spherical shape) were found to contain the point of maximum contact stress and the majority of the surrounding stress field caused by impact loading. The fine mesh was controlled by edge seeds along the y axis and the contact surface intersected by the xy and yz planes that are defined in Figure 4-19. Refinement of the mesh was trailed using mesh element widths of 0.05 mm, which had very little effect on results, so the mesh size was assumed to be fine enough for stress fields to be accurately calculated.

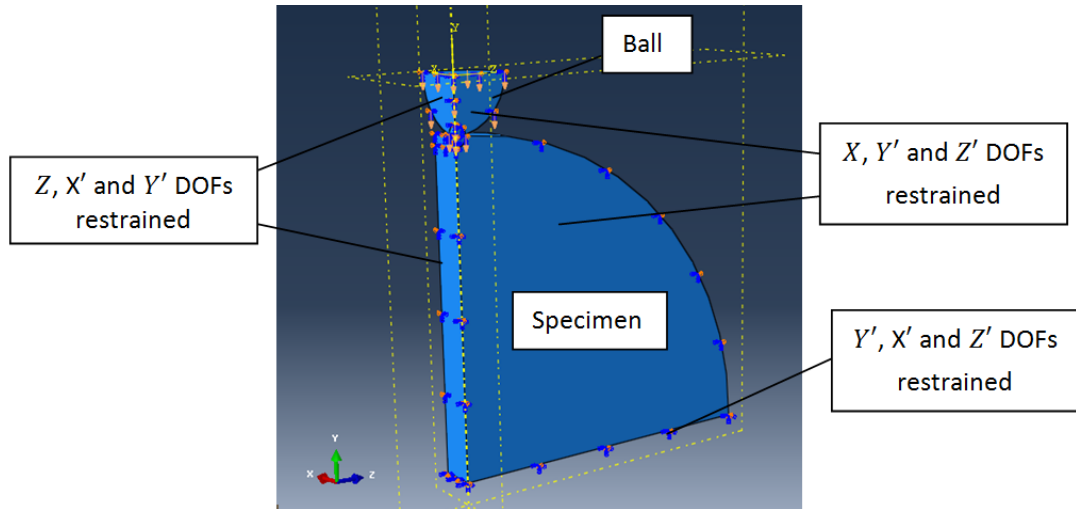


Figure 4-19: Boundary conditions restraining model

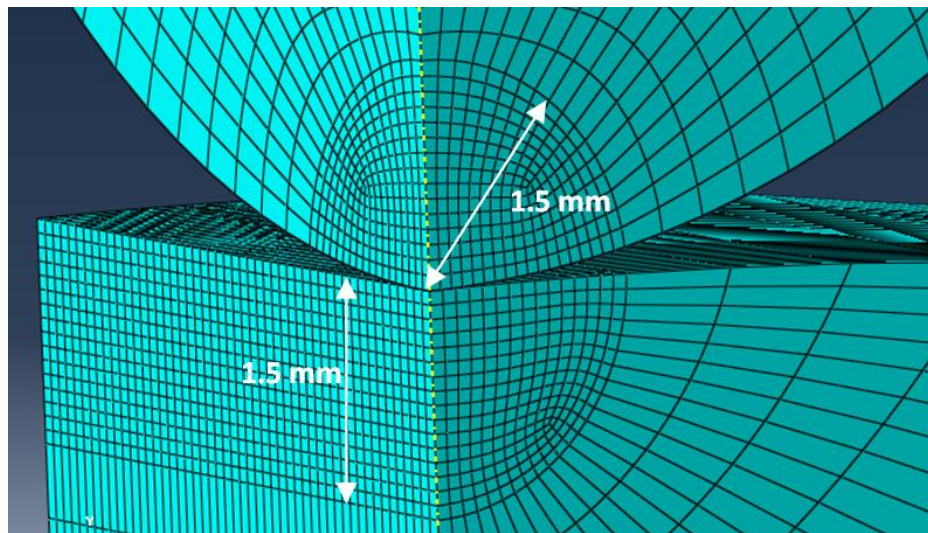


Figure 4-20: Mesh around the point of impact

Figure 4-21a shows the initial stress distribution under impact loading and Figure 4-21b, the stress distribution at the point of maximum equivalent stress (when the surface displacement caused by impact is maximum), which is directly beneath the centre of the impact zone. The maximum surface stress however, was found to be at two symmetric zones either side of the centre of impact as shown in Figure 4-21b. This shows that the area around the point of impact is of interest and any features found in the microstructure away from its direct vicinity may also be linked to the hammering impact loading. For consistency between specimens it was decided to study stress distribution around the spherical volume with a 1 mm radius around the point of impact. This "impact zone" was observed in detail for all sectioned specimens. Table 4-8 shows the calculated maximum surface contact stresses and subsurface equivalent stresses for all investigated impact conditions. Although surface roughness will have a localised effect on the stress field, it is assumed that as it is relatively low (of the order of 1 μm), it will have little effect on the stress distribution around relatively large MnS inclusions (of the order

of 10 μm) that are some distance away from the surface (of the order of 100 μm). This seems like a fair assumption since surface contact investigations have shown that the subsurface stress field was almost unchanged below 100 μm in a rail-wheel application, with surface roughness, R_a , of 0.4 μm under a contact stress of around 1 GPa. In this example, subsurface principal shear stress variation was minimal below 50 μm [183]. Although this is not a direct comparison, it is clear that at sufficient depths, the subsurface stress field is unaffected by surface roughness. As a result, it has been assumed that the effects of surface roughness are low enough in these tests, that the overall mechanisms leading to cracking and separation damage at subsurface inclusions are not affected.

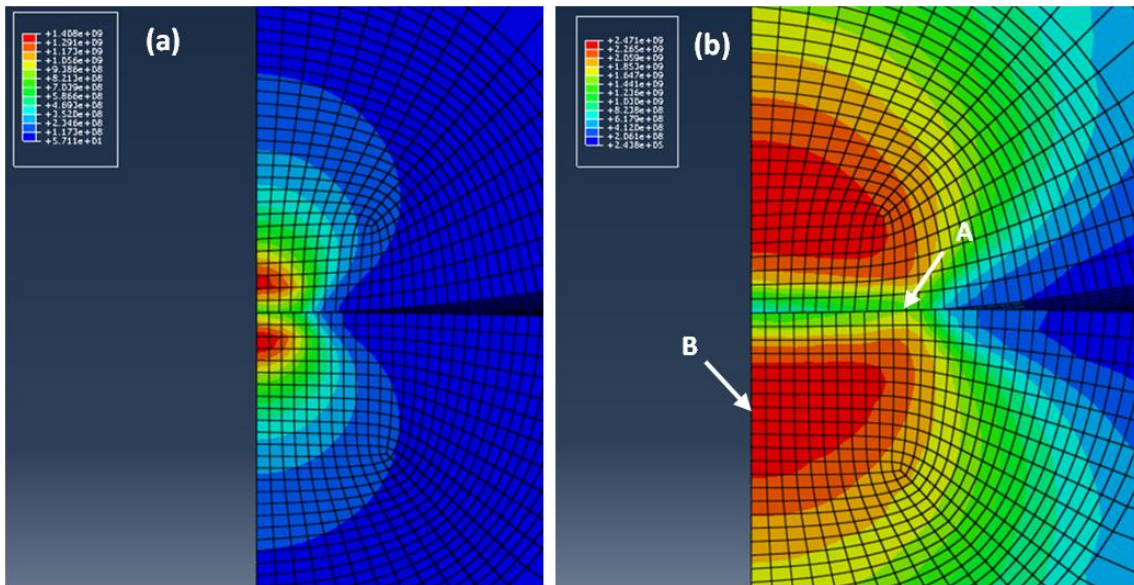


Figure 4-21: Equivalent stress distribution for 0.4 m/s impact velocity at (a) initial contact (b) max loading showing the approximate positions of maximum surface equivalent stress (A) and subsurface equivalent stress (B)

4.4.5. Testing procedure

A combination of the test rig dynamic analysis and FEA modelling described above allowed the following testing schedule to be designed. It should be noted that due to the assumptions discussed in the previous section, the listed stress values are approximations only. It is clear from the results presented in Chapter 6 however, that damage was caused in the subsurface region, while the surface appeared to be relatively undamaged so the test design can be assumed to be accurate. The full test schedule is described in Table 4-8. The results from testing are described in Chapter 6.

Analysis of the Premature Failure of Wind Turbine Gearbox Bearings

	Specimen number	Impact freq. (Hz)	Impact velocity (m/s)	Surface stress max (GPa)	Subsurface stress max (GPa)	Striker angle (°)	Test time (min)	No. of cycles (1000s)
Initial testing	1	10	0.45	1.67	2.58	90	166.7	100
	2	10	0.45	1.67	2.58	90	166.7	100
	3	10	0.45	1.67	2.58	90	166.7	100
TEST 1: Varying number of impacts (1)	4	11	0.50	1.69	2.60	90	18.9	12.5
	5	11	0.50	1.69	2.60	90	37.9	25
	6	11	0.50	1.69	2.60	90	75.8	50
	7	11	0.50	1.69	2.60	90	151.5	100
	8	11	0.50	1.69	2.60	90	227.3	150
	9	11	0.50	1.69	2.60	90	303.0	200
TEST 2: Varying impact energy	10	3	0.14	1.54	2.15	90	277.8	50
	11	5	0.23	1.58	2.36	90	166.7	50
	12	7	0.32	1.65	2.48	90	199.0	50
	13	9	0.41	1.68	2.56	90	92.6	50
	14	11	0.50	1.69	2.60	90	75.8	50
TEST 3: Varying number of impacts (2)	15	7	0.32	1.65	2.48	90	29.8	12.5
	16	7	0.32	1.65	2.48	90	59.5	25
	17	7	0.32	1.65	2.48	90	119.0	50
	18	7	0.32	1.65	2.48	90	238.1	100
	19	7	0.32	1.65	2.48	90	357.2	150
	20	7	0.32	1.65	2.48	90	476.2	200
TEST 4: Long term tests	21-22	11	0.50	1.69	2.60	90	1515.2	1,000
	23-24	11	0.35*	1.66*	2.51*	45	1515.2	1,000
	25-26	11	0.35*	1.66*	2.51*	45	1515.2	1,000

Table 4-8: Procedure for normal hammering impact testing (*for sliding 45 degree impact tests, the radial components of the impact velocities are displayed for comparison and the stresses calculated for an equivalent radial velocity used to estimate stress levels).

4.5. Twin disc testing of 100Cr6 bearing steel

Twin disc testing was undertaken to investigate the effect of Rolling Contact Fatigue (RCF) on bearing steel test specimens. Since the equipment available was unable to rotate at the high speeds that more modern test rigs are capable of and needed to be supervised at all times, test lengths were limited in comparison to that of some other studies [23, 56, 109] that are discussed in section 2.3.6. Consequently, it was decided that the effects of early stage damage after comparatively few load cycles, would be investigated in detail, which has not, to the author's knowledge, been done before. All twin disc tests were carried out using line contact geometry, since most REBs in WTGBs are CRBs. The testing was designed to fulfill a number of objectives:

1. To determine whether WECs or subsurface cracking could be initiated by RCF alone.
2. To determine whether pre-seeding specimens with impact damage accelerated the time taken for subsurface damage to initiate.
3. To determine thresholds of contact pressure and slip ratios at which different forms of damage occurred.
4. To investigate the effect of different inclusion types on subsurface crack initiation.
5. To investigate the depths at which damage initiated and compare that to the theoretical depths of τ_{max} , $\tau_{0,max}$ and σ_v .

4.5.1. Equipment

The Sheffield University Rolling Sliding (SUROS) twin disc machine is based around a Colchester Mascot 1600 lathe, which was originally modified by Garnham and Beynon [184] and then further by Fletcher and Beynon [185]. The machine is used to drive two discs that are rolled against one another, the upper of which is driven by the lathe and the lower, by an additional AC motor; the main modification. A normal load of up to 29 kN can be applied to the lower disc by a hydraulic piston, which lifts the pivoted drive shaft that is driven by the AC motor. The two discs central axes are parallel, ensuring a line contact between the two discs. A schematic of the SUROS test rig is shown in Figure 4-22. The machine has been used extensively for rail wheel testing, including [131, 156, 186, 187, 188].

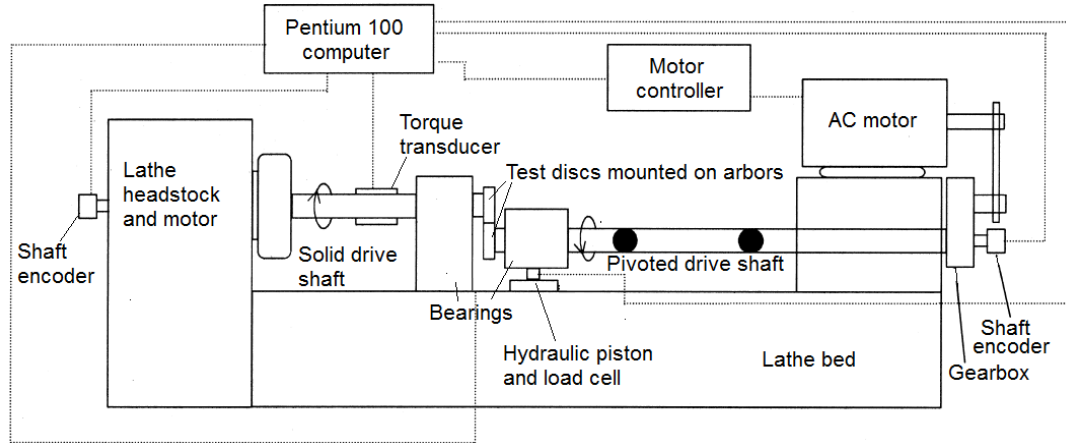


Figure 4-22: SUROS test rig schematic (modified from [185])

National Instruments® Labview® version 4 run on a Pentium 100 computer is used to control the machine and to data log the speed, number of revolutions, shaft torque and applied load. The lower disc can be controlled to spin faster than the upper in order to introduce slip. Slip is controlled by the computer and instantaneous slip S_i , is calculated as a percentage using equation 4.4.

$$S_i(\%) = 200 \left(\frac{R_T U_T - R_B U_B}{R_T U_T + R_B U_B} \right) \quad (4.4)$$

where R_T and R_B are the disc radii in millimetres and U_T and U_B are the rotational velocities of the discs in revolutions per minute.

The hydraulically applied load is controlled manually during testing based on a load cell read-out of the measured load applied to the test specimens by the hydraulic piston [185]. The maximum Hertzian contact pressure P_{max} between the two discs is given by the following equation; relevant for two elastically identical steel cylinders in line contact [185, 189], where P is the load per unit length of the contact and E is the Young's modulus of the test specimens.

$$P_{max} = 0.418 \sqrt{PE \left(\frac{1}{R_T} + \frac{1}{R_B} \right)} \quad (4.5)$$

For two identically sized cylinders, equations 4.4 and 4.5 respectively become:

$$S_i(\%) = 200 \left(\frac{U_T - U_B}{U_T + U_B} \right) \quad (4.6)$$

$$P_{max} = 0.591 \sqrt{\frac{PE}{R}} \quad (4.7)$$

4.5.2. Operation of SUROS rig

The standard procedure for SUROS rig operation was followed. First, test specimens were cleaned in an ultrasonic bath of acetone for a period of five minutes immediately before testing. After cleaning and being left for a period of time for the acetone residue to evaporate, specimens were weighed, so that the mass before and after testing could be compared and any mass loss recorded. Specimens were then mounted and bolted onto the arbors as shown in Figure 4-22. This configuration is shown in more detail in Figure 4-23a. The position of the lower disc could be moved along the pivoted drive shaft central axis by using a telescopic connection, allowing the position of the discs to be staggered while keeping their axes parallel. The specimen position was locked by securing the bearing housing to the lathe bed via a mounting bolt. This allowed the contact pressure to be varied as shown in Figure 4-23b and c, since the same contact load was distributed over different line contact lengths. Three specimen positions were implemented for the tests designed; their nominal contact widths were 10, 5.5 and 3.5 mm respectively. Although the setup in Figure 4-23c introduced edge loading stress concentrations in comparison to the setup shown in Figure 4-23b, it was interesting to investigate such conditions, as edge loading occurs to some extent in real wind turbine bearings, as discussed in Chapter 2.

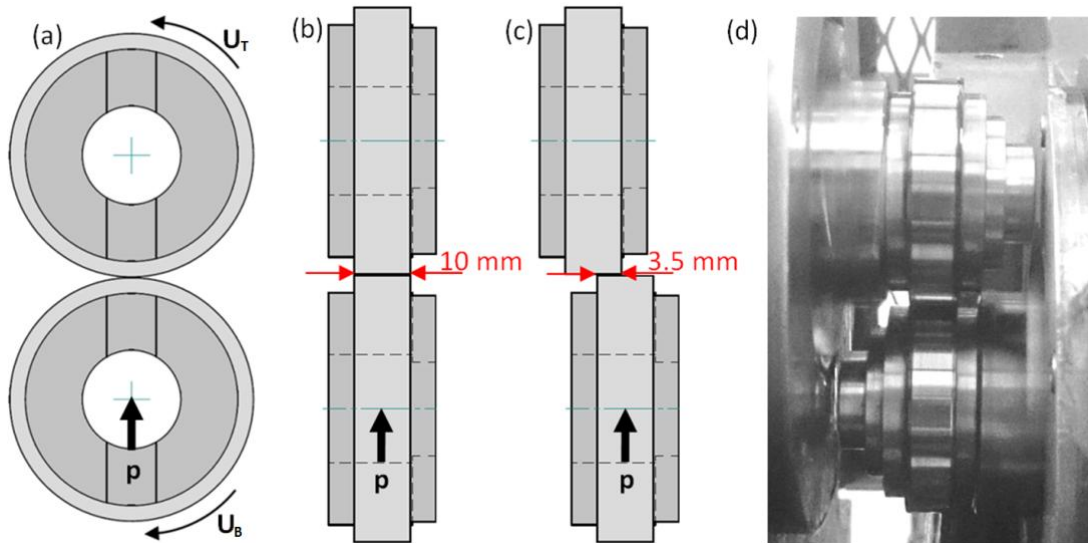


Figure 4-23: Twin disc testing specimen position (a) standard test (b) 10mm line contact (c) 3.5 mm line contact (d) 10 mm SUROS test. U_T = top disc velocity, U_B = bottom disc velocity, p = hydraulic load pushing up bottom disc.

After specimens were mounted, test conditions were input into the control system, namely: lathe shaft speed U_T (rpm), required maximum contact pressure P_{max} (MPa), required slip S (%), specimen radii R (mm) and line contact width (mm). At this point, the rig was calibrated for testing. The lathe shaft speed was manually set and the AC motor shaft automatically accelerated to the correct speed, calculated by the computer using equation (4.4). A restraining bolt was used to stop the discs contacting, allowing the hydraulic piston to be

actuated, and the hydraulic load to be set to the required level by the operator. The required load was calculated by the computer and the hydraulic pressure manually adjusted until the load cell readout matched the required load. The torque readout was also calibrated to zero at this point. The load was then released, allowing the restraining bolt to be removed and the measured slip level and shaft speed readouts checked. If everything was in order, the load was re-applied without the restraining bolt and the test started.

During the tests, the computer recorded shaft torque, contact load, speed and slip level data and automatically controlled the shaft speed and slip levels. Typically 75 % of the total number of cycles were within ± 0.08 of the nominal percentage value, but over a test, these are cancelled out, which results in a difference within a range of ± 0.02 for the cumulative slip [156]. All slip values during testing were negative, indicated a driving AC shaft disc. A readout of the hydraulic load was provided on the user interface screen allowing manual control of the contact pressure, which is typically maintained to within an error of $\pm 2\%$ of the required value [185], which was the case for the testing described in this study. Oil lubricant (discussed in section 4.5.5) was manually dripped onto the rotating discs during testing. Fresh lubricant was regularly applied at least once every five minutes and live shaft torque readout on the user interface was monitored to ensure lubrication remained consistent. Post-test analysis of the coefficient of traction history during testing confirmed that tests were consistently lubricated throughout, with the exception of some very short time periods when the lubricant dried up before the five minute period and had to be re-lubricated early. This is discussed in section 4.5.5. Once the required number of cycles had taken place, the test was stopped and the discs removed, cleaned for five minutes in the acetone ultrasonic bath, and re-weighed before observation of the surface and subsurface took place.

4.5.3. Specimens

Fifteen identical discs made from 100Cr6 bearing steel were used for testing, twelve of which represented bearing raceways, and were sectioned for metallographic investigation. The other three represented rollers and were used to roll against the raceway specimens, allowing twelve tests (tests 1-12) at different operating conditions to be undertaken. Roller specimens 1, 2 and 3 were each used for four tests (1-4, 4-8 and 9-12 respectively) (see section 4.5.4 for details of each test operating conditions) in order to reduce the cost of testing and were visually examined between tests in order to confirm that no serious surface damage had taken place, although the surface roughness will likely have changed slightly during tests. Specimens representing raceways were positioned on the lathe shaft that rotates at speed U_T and those representing the rollers, on the AC motor shaft that rotates at speed U_B , where $U_T < U_B$. The reason for this orientation is explained in Figure 2-10, which shows that the slower moving surface is more susceptible to surface damage since surface linked cracks are pulled open by the traction force. This meant that damage to the raceway specimens would be accelerated

compared to that of the rollers which was beneficial for both observing damage caused and for prolonging roller specimen life over the four tests that they were each used for.

Discs were sawn into blanks from a 50 mm diameter annealed rolled bar, before being ground down to a diameter of 47 mm, with a central bore of 22 mm and a keyway cut into one face to allow for mounting on the twin disc machine arbors. The discs underwent a through hardening heat treatment process, which involved a stress relieving annealing stage, martensitic hardening, quenching in a salt bath, before tempering at around 240 °C to achieve a hardness value of 61 HRC (confirmed by the manufacturer). Following heat treatment, the surface was ground to a maximum arithmetic mean surface roughness R_a of 0.39 μm and a maximum root mean squared surface roughness R_q of 0.50 μm which was determined using the method discussed in 4.2.3. Surface profile measurements were made across the 10 mm width of the test discs, perpendicular to the direction of travel. Disc dimensions are shown in Figure 4-24 and typical physical properties of 100Cr6 steel in Table 2-5. The chemical composition was checked using EDAX using the method discussed in 4.2.2 and the steel grade was confirmed to be 100Cr6 as shown in Table 4-9. As previously discussed the carbon value is approximate since EDAX analysis is not accurate for elements with small atomic numbers.

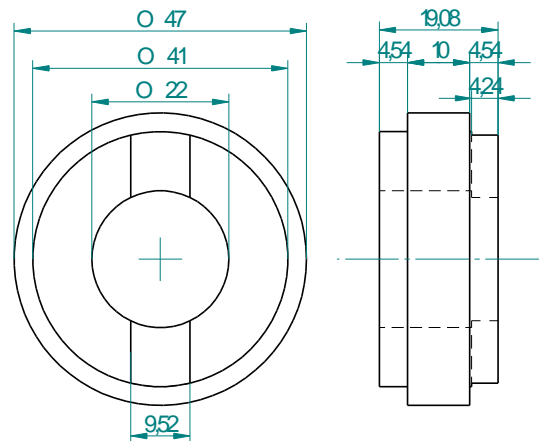


Figure 4-24: Twin disc testing specimen dimensions

Steel grade	C%	Si%	Mn%	Cr%	Mo%	Fe%
100Cr6	~1%*	0.20	0.43	1.59	0.03	Balance

Table 4-9: Chemical composition of twin disc specimens. *Carbon value approximate.

The hammering impact test rig described in section 4.4 was used to seed damage in the SUROS test specimens at two opposite locations on the circumference of each of the 12 discs representing bearing raceways. 50,000 sliding impact samples causing a maximum Hertzian stress value of approximately 2.51 GPa at an impact angle of 45 degrees were applied to the impact locations. This level of impact loading was found to be a condition that created subsurface cracking at MnS inclusions in the specimens described in section 4.4. Each of the 12

discs representing raceways in the twin disc testing were damaged in this manner before SUROS testing commenced in order to initiate subsurface microcracks, which were expected to propagate under RCF. The locations of impact were investigated by destructive sectioning after SUROS testing, one of which was sectioned axially and one, circumferentially. Any location further than a few millimetres from the point of impact was assumed to be unaffected by hammering impact loading and so the effects of RCF without pre-seeded impact damage, could be investigated and compared to the pre-damaged impact zone.

Examination of the impact zones on the surface of each of the specimens after twin disc testing showed no sign of the wear scar, which was obscured entirely by the wear tracks caused by RCF. The position of the impact zones was known before twin disc testing commenced so that they would not be lost during the test. The position of the impact zone was measured with Vernier callipers (± 0.01 mm accuracy) before each impact test to ensure it was in the middle of the specimen line contact, which were 5.00 mm, 2.75 mm and 1.75 mm from the specimen edges of specimens 1-4, 5-8 and 9-12 respectively. The centre of each impact zone was aligned as closely as possible with the leading arbor keyway, as shown in Figure 4-25. Once mounted in the hammering impact rig, the position of the IZ was checked by applying ink from a marker pen to the impacting ball and manually making contact with the specimen. This left a small ink mark on the specimen surface at the point of impact, the position of which could then be measured and adjusted if necessary.

When sectioning the tested specimens, cuts were made approximately 0.5 mm away from the arbor keyway for axial sections and from the centre of the line contact for circumferential. After cuts were made, the exact distance between the keyway edge (axial) or the specimen surface edge (circumferential) and the surface of the cut were measured and the specimen width was reduced by the required amount for the exposed surface to be as close to the impact zone centre as possible. All measurements were made with a Vernier calliper (± 0.01 mm accuracy).

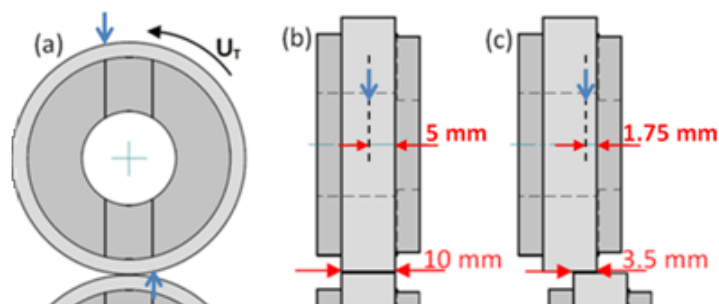


Figure 4-25: Positions of pre-seeded impact damage (indicated by blue arrows): a) viewed along shaft axial direction b) viewed from in front of rig for 10 mm contact width tests (1-4) c) viewed from in front of rig for 3.5 mm contact width tests (9-12).

4.5.4. Testing procedure

Since the tests were operated on the limit of the SUROS rig capabilities in terms of contact load applied, test cycles were limited to 2×10^5 cycles to minimise damage to the test rig and to limit the test length to reasonable operation times. Although these tests are shorter than many that have taken place in previous studies [23, 56, 190]; 2×10^5 stress cycles is above the threshold found to be required for butterfly initiation as shown in Figure 2-18. Logically, it is by examining very early stage damage that the best insight into the location of the initiation point of that damage can be achieved. As a result, the limited test length did not adversely affect experiment design. From previous experience [185], the maximum contact pressure that the rig could safely be used with lubricated conditions was 1,800 MPa over a line contact of 10 mm width. This corresponded to a hydraulic load of 10.28 kN (calculated using Hertzian contact theory as described in section 2.1.3.1), which is the limit of the machine. Applying the same load over shorter line contacts allowed the pressure to be increased to a maximum value of 3.03 GPa, over a 3.5 mm contact width. All contact pressures and the depths of the corresponding maximum stress concentrations, $\sigma_{v,max}$, τ_{max} and $\tau_{O,max}$ were calculated as per the method presented in section 2.1.3.1.

This contact pressure was deemed to be great enough to investigate the initial stages of butterfly formation, since higher contact pressures are not expected to occur frequently in wind turbine gearbox bearings. An intermediate contact pressure of 2.41 GPa, was also tested, in order to compare results to a value in the middle of the loading range. Slip ratios were also changed, in order to investigate the effect of changing the level of surface traction on subsurface damage. The maximum allowable slip level was 10 %, again from previous experience of using the SUROS rig under lubricated conditions [185]. A range of slip levels from 0.2-10 % was selected to investigate the effects of changing the slip from low to high levels, which provided similar slip levels to those in previous twin disc bearing RCF experiments [23, 56] (see section 2.3.6). All other variables were held constant, including the pre-seeded impact damage, as shown in Table 4-10. Details of the changed slip and contact pressure levels in each of the 12 tests are shown in Table 4-11. These contact pressures are presented for illustrative purposes and are approximate since the effect of surface traction on the position of maximum shear and equivalent stress (as discussed in section 2.1.3.3) is not considered in the calculation to determine these values.

Fixed variable	Condition
Number of pre-seeded impacts	50,000
Angle of impact	45°
P_{max} during impact	2.58 GPa
Impact test time	83 minutes
Number of cycles on SUROS	200,000
SUROS test speed	400 rpm
SUROS test time	500 minutes
Hydraulic load applied	10.28 kN

Table 4-10: Fixed test conditions

Disc no.	1	2	3	4	5	6	7	8	9	10	11	12
Slip (%)	0.2	2	5	10	0.2	2	5	10	0.2	2	5	10
Contact width (mm)	10.0	10.0	10.0	10.0	5.5	5.5	5.5	5.5	3.5	3.5	3.5	3.5
P_{max} (GPa)	1.79	1.79	1.79	1.79	2.41	2.41	2.41	2.41	3.03	3.03	3.03	3.03
Depth of $\sigma_{v,max}$ (μm)	258	258	258	258	347	347	347	347	435	435	435	435
τ_{max} (MPa)	538	538	538	538	726	726	726	726	910	910	910	910
Depth of τ_{max} (μm)	287	287	287	287	387	387	387	387	485	485	485	485
$\tau_{O,max}$ (MPa)	448	448	448	448	603	603	603	603	758	758	758	758
Depth of $\tau_{O,max}$ (μm)	184	184	184	184	248	248	248	248	311	311	311	311

Table 4-11: Variable test conditions showing positions of maximum shear τ_{max} , $\tau_{O,max}$ and equivalent stress $\sigma_{v,max}$

4.5.5. Lubrication of specimens

The Hamrock-Dowsen visous-elastic method for calculating the thickness of a lubricant film separating two bodies was used in this section as follows [191]:

$$\frac{h_0}{R} = 1.714 \left(\frac{\eta_0 U}{E' R'} \right)^{0.694} (\alpha E')^{0.568} \left(\frac{W'}{E' R'} \right)^{-0.128} \quad (4.8)$$

Where:

U is the entraining surface velocity (m/s)

$$U = (U_T + U_B)/2 \quad (4.9)$$

where the subscripts T and B refer to velocities of the top and bottom discs respectively;

η_0 Dynamic viscosity of the lubricant at atmospheric pressure (Pa.s)

E' is the reduced Young's modulus:

$$\frac{1}{E'} = \frac{1}{2} \left[\frac{1-\nu_A^2}{E_A} + \frac{1-\nu_B^2}{E_B} \right] \quad (4.10)$$

which for two bodies of the same material becomes:

$$\frac{1}{E'} = \left[\frac{1-\nu^2}{E} \right] \quad (4.11)$$

R' is the reduced radius of curvature:

$$\frac{1}{R'} = \left[\frac{1}{R_T} + \frac{1}{R_B} \right] \quad (4.12)$$

which for two identically sized discs becomes:

$$\frac{1}{R'} = \frac{2}{R} \quad (4.13)$$

α is the pressure-viscosity coefficient (m^2/N), which can be approximated by the following equation, derived by Wooster and quoted in [19] as:

$$\alpha = (0.6 + 0.965 \log_{10}(\eta_0 \times 10^3)) \times 10^{-8} \quad (4.14)$$

W' is the contact load per unit length (N)

Texaco Meropa 320 oil was used for all tests, which has kinematic viscosity values of 304 cSt and 23.2 cSt at 40 °C and 100 °C respectively and a density of 856 kg/m^3 (specified at 15 °C) [192]. The lubricant contained a sulphur-phosphorus additive, designed to increase wear resistance including micropitting in heavily loaded situations. This helped protect the specimen surface, which was important since surface damage can spread downwards and mask subsurface initiated damage. The pressure-viscosity coefficient α , was approximated using equation 4.14. Using the method presented in ASTM D341 [193], the viscosity value at room temperature (21 °C) was calculated to be 0.994 Pa.s and the pressure-viscosity coefficient was approximated as $\sim 35 \times 10^{-9} \text{ Pa}^{-1}$ using equation 3.14. The Young's modulus of the steel was assumed to be 200 GPa and the Poisson's ratio, 0.3 (properties are presented in Table 2-5).

Initial lambda ratios at the very beginning of each test were calculated using equation 4.8 and 2.12, with the properties of lubricant at room temperature. Since the lubricant film thickness is dependent on W' and U , lubrication conditions for tests were varied caused by altering the level of slip and the width of the line contact. Lambda ratios at room temperature were calculated to range from 4.8 – 5.6, depending on test conditions, so all tests began in the hydrodynamic lubrication regime. Since the lubricant was heated up during testing, its viscosity dropped, which corresponded to a decrease in the lambda ratio and a shift to the left on the Stribeck curve, as shown in Figure 4-26, and consequently into the mixed lubrication regime. As described in section 2.1.6, when the lambda ratio is less to 1 (i.e. the fluid film thickness and equivalent surface roughness are equal), lubrication enters the boundary regime and at lambda ratio of 1 – 1.5 lubrication is in the mixed regime. Using equations 4.8 – 4.14 and the method in ASTM D341 [193], it was calculated that a lambda ratio of 1.5 occurred at lubricant temperatures of approximately 43 – 46 °C depending on the test conditions. Similarly, a lambda ratio of 1 occurred at approximately 54 – 58 °C. Fresh lubricant at room temperature was applied regularly throughout the testing, which altered the lubricant temperature. Additionally tests took at least two days to complete, meaning that there were periods throughout a single test where the specimens and test rig cooled. There was no way to measure the temperature of the lubricant and since the specimen surface roughness will have reduced during testing due to surface wear it is not possible to accurately determine the lubricant regime. It is estimated that typical tests were mainly in the mixed regime, with periods of boundary lubrication and short periods after start-up, of EHL/hydrodynamic conditions. Since the temperature of WTGB lubricant alters significantly during operating, these conditions were deemed to be an appropriate simulation of planetary bearing operating conditions.

Traction coefficients μ_T , calculated using equation 2.9, were measured during testing and typically changed similarly to the example illustrated in Figure 4-27, which displays the traction coefficient data collected from one of the tests. Initially the μ_T was high, but over time it decreased, presumably as surface wear increased and surface roughness decreased. The test was undertaken over two days, indicated by the drop in traction coefficient at 100,000 cycles, when the contact load was removed and the subsequent increase after the resumed the following day. A number of short term increases in μ_T (indicated on the figure) occurred when the contact started to become dry, which was instantly rectified by dripping lubricant on the rotating discs and as a result, assumed to not have caused any noticeable damage. Mean values of μ_T were found for each test, as shown in Table 4-12, which allowed the approximate lubrication conditions to be estimated. Comparing these values to a Stribeck curve with values of friction (traction) coefficient indicated on the y axis, shows that the all tests were theoretically in the mixed regime. This may not necessarily be the case because this does not take into account lubricant additives, which reduce traction in boundary/mixed lubrication conditions, but it does confirm that tests were in either the mixed or the boundary regime, as is the case for planetary WTGBs in operation as discussed in 2.1.6. μ_T range (0.021 – 0.082) is similar to that used in other twin disc testing that had been used to create inclusion initiated WEAs [51, 56].

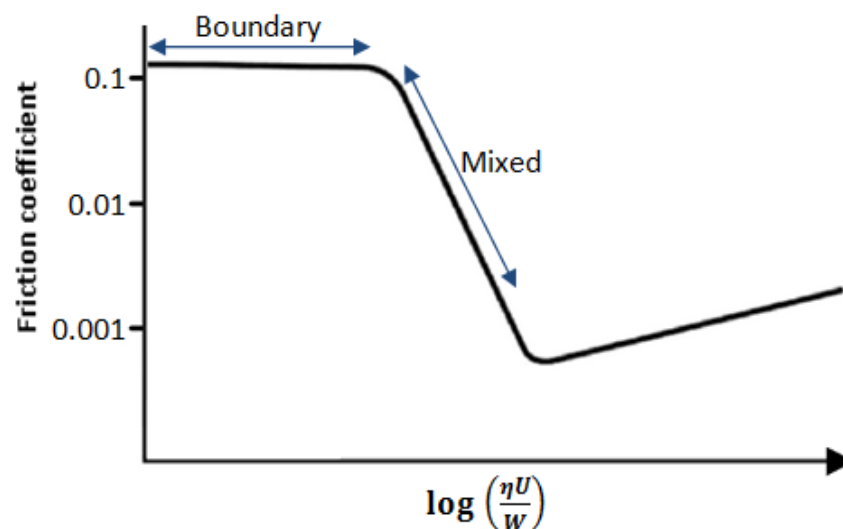


Figure 4-26: Stribeck curve showing approximate friction (traction) coefficient during boundary and mixed lubrication regimes (adapted from [194]) where: η is dynamic viscosity, U is sliding speed, W is normal force.

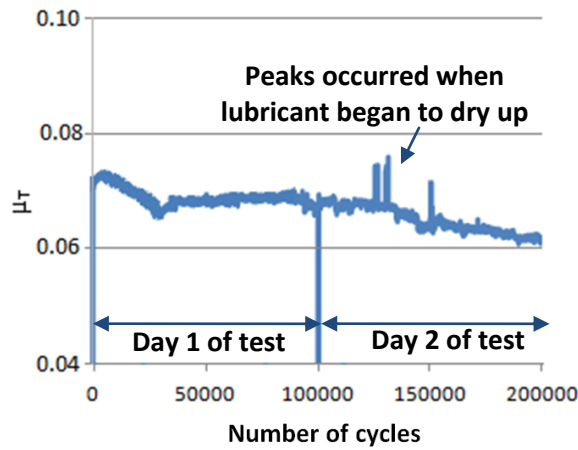


Figure 4-27: Example traction coefficient (μ_T) readout from SUROS rig (data from 2 % slip, 2.48 GPa contact pressure)

Contact pressure (GPa)	Mean traction coefficient at slip % levels			
	0.2 %	2 %	5 %	10 %
1.79	0.029	0.064	0.078	0.079
2.48	0.021	0.067	0.080	0.083
3.03	0.029	0.070	0.079	0.082

Table 4-12: Mean traction coefficients during each test

4.6. Summary

This chapter first presented the methods used to prepare bearing steel specimens and observe the microstructure and the damage caused to them. The method of sectioning a failed WTGB is presented before the development of experimental tests using hammering impact and twin disc test rig is presented. The following Chapters 5, 6 and 7, present the results of the experimental methods presented in this chapter.

5. RESULTS FROM THE DESTRUCTIVE INVESTIGATION OF A FAILED WIND TURBINE GEARBOX BEARING

This section presents the results from the metallurgical investigations of the failed planetary WTGB inner raceway described in section 4.3. Figure 5-1 shows the Thesis work flow chart.

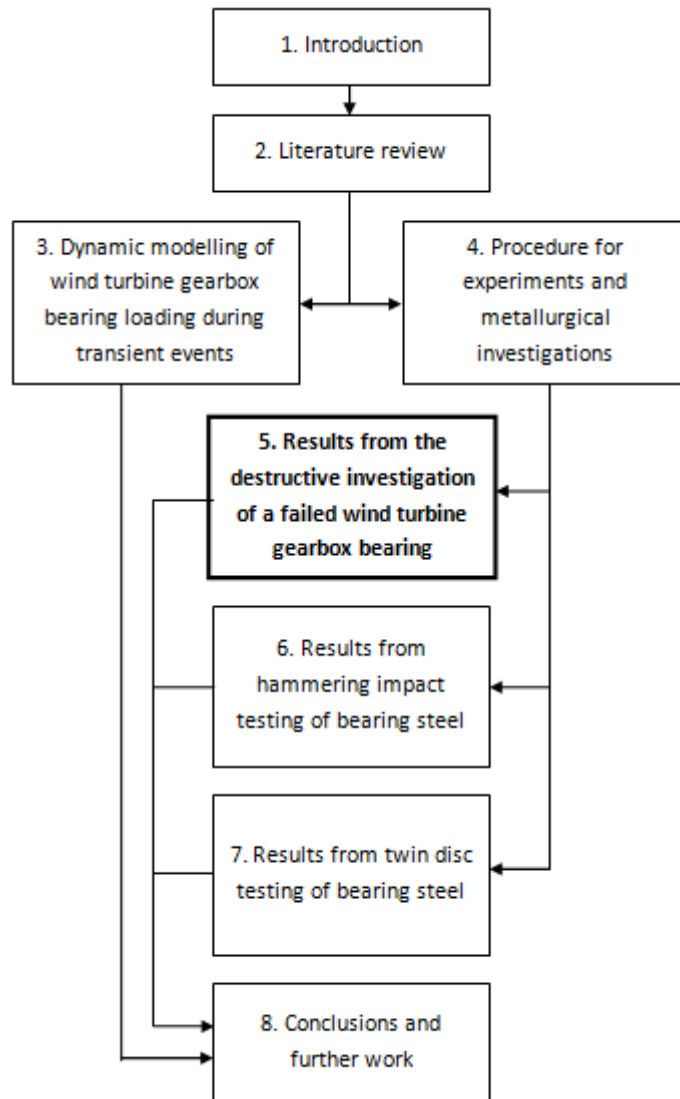


Figure 5-1: Thesis work flow chart

This chapter is split into three sections:

- Section 5.1 recaps the surface damage features discussed in Section 4.3.
- Section 5.2 describes the damage features found in the failed inner raceway subsurface.
- Section 5.3 presents the results of the database of damage initiating MnS inclusions
- Section 5.4 summarises the finding of this chapter.

5.1. Observed surface damage

As previously discussed and shown in Figure 4-6, approximately 55 % of the raceway circumference was worn. Three zones of damage were identified in Section 4.3.1, namely:

- Zone 1: Non-damaged zone. Over the remaining 45 % of the raceway circumference there was very little evidence of damage detectable by eye.
- Zone 2: Wear damage was intermittent but well defined at a width of around 20 mm for approximately 35% of the bearing circumference. Within the main 20 mm band of damage there was severe spalling.
- Zone 3: Severe spalling covered most of the raceway width for approximately 20 % of the circumference.

An example of the spalling damage within the Zone 2 damage band is presented in Figure 5-2.



Figure 5-2: Spalling on the raceway surface in Zone 2

5.2. Observed subsurface damage

A summary of the specimens investigated and the damage found at each location is provided in Table 5-1. As discussed in section 4.3, MnS inclusions were quickly identified to have initiated the majority of the damage features found in the raceway. As previously mentioned, the processes used during the manufacture of bearing raceways, determine the orientation of the MnS inclusions in the steel. In this bearing, inclusions were elongated and orientated with their major axis close to parallel with the bearing surface when viewed in an axial cross section as shown in Figure 5-3a. They were also elongated to a lesser extent when observed in circumferential sections and were generally angled at approximately 30 degrees from the surface tangent as shown in Figure 5-3b. MnS inclusions were consistently orientated in this manner, regardless of their location in the bearing raceway. Four main types of damage were found at MnS inclusions, which can be classified as: (1) separation from the matrix, (2) internal cracking of the inclusion, (3) crack initiation and (4) WEC initiation.

Section details	Sample Nos.	Observations/Features
Section 1a - Circumferential section. Phase 3 damaged region.	1-6	WEA interacting inclusions Crack initiating inclusions Separation of matrix from inclusions Butterfly cracks in near surface zone.
Section 1b - Axial section. Phase 3 damaged region.	6-12	
Section 2a - Circumferential section. Phase 1/Phase 2 boundary.	13-18	WEA interacting inclusions Crack initiating inclusions Separation of matrix from inclusions Butterfly cracks in near surface zone. Significant subsurface crack parallel to the raceway. Substantial WEC orientated normal to the raceway surface Surface initiated RCF cracks
Section 2b - Axial section. Phase 1/Phase 2 boundary.	19-24	
Section 3a - Circumferential section. Phase 2 damaged region.	25-30	WEA interacting inclusions Crack initiating inclusions Separation of matrix from inclusions Small butterfly initiated WEC Large butterfly crack with WEC propagating to surface Surface initiated RCF cracks Plastically deformed region
Section 3b - Axial section. Phase 2 damaged region.	31-36	
Section 4a - Circumferential section. Phase 1 non-damaged region.	37-40	No evidence of damage

Table 5-1: Summary of sectioned specimens and damage found

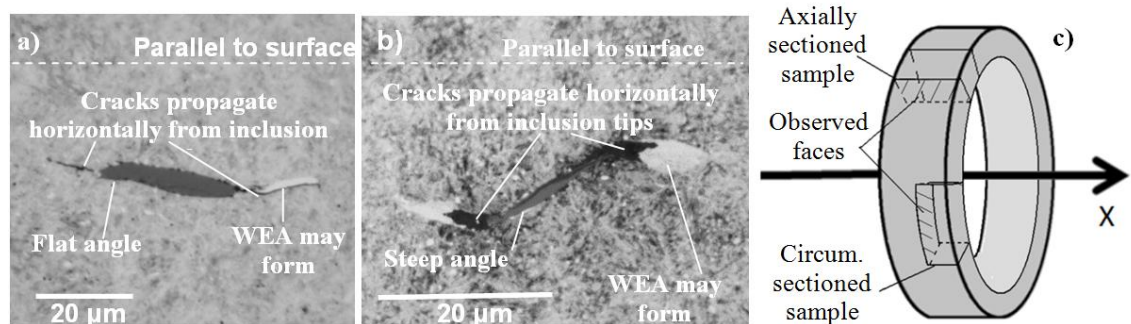


Figure 5-3: Inclusion orientation in inner raceway a) Typically MnS inclusion viewed axially b) Typical MnS inclusion viewed circumferentially c) Specimen orientation (not to scale)

5.2.1. Distinction of “butterfly” and WEC initiating inclusions

It has become apparent that there has been some confusion over the definition of the term “butterfly” in the literature. The term has been used by many, in order to describe both two and four winged features with cracks propagating at 30-50° and 130-150° (close to the angle of maximum unidirectional shear stress) from a central initiating point, which is usually a void or defect [12, 26]. It has also been used to describe short WECs initiated at much shallower or even horizontal angles, which, in the opinion of the author, are not the same feature. For the remainder of this thesis, the term butterfly crack will be used to identify a feature with “wings” propagating at the angles mentioned above and the term “WEC initiating inclusion”, to describe an inclusion with WECs propagating at shallower angles.

RESULTS FROM THE DESTRUCTIVE INVESTIGATION OF A FAILED WIND TURBINE GEARBOX BEARING

Figure 5-4a presents an example of a series of large butterflies and connected WECs that propagate to the raceway surface. Highly magnified SEM images of the main butterfly feature are presented showing the severe elongation of M_3C carbides near to the boundary between WEA and the normal steel microstructure. Since there was no obvious inclusion initiating any of the WEC features observed in Figure 5-4a, approximately 20 μm material layer was ground from the specimen surface (the exact amount removed was not critical and the thickness of the specimen was measured with a Vernier calliper to an accuracy of $\pm 10 \mu\text{m}$) before it was polished and etched for observation again. Figure 5-4b shows two MnS inclusions that interact with this WEC network, confirming that damage may spread between MnS inclusions and offering evidence that the crack network may have been initiated by MnS inclusions. Figure 5-4 is believed to show a late-stage WEC network that may have contributed to the failure of the bearing. This section will now look in detail at earlier stages of damage, specifically that which initiated at MnS inclusions.

To confirm reports [12, 109, 53] that WEAs are harder than the surrounding steel matrix, nano-hardness indentation was used to compare hardness values as described in section 4.2.4. Nine values were used to find the average hardness of the steel matrix and 16, to find that of the WEC. WEA hardness measurements were taken from areas of the butterfly wings shown in Figure 5-4. Table 5-2 shows the results from the tests, confirming that the WEA microstructure was considerably harder (30.4 % average) than the steel matrix [1, 195].

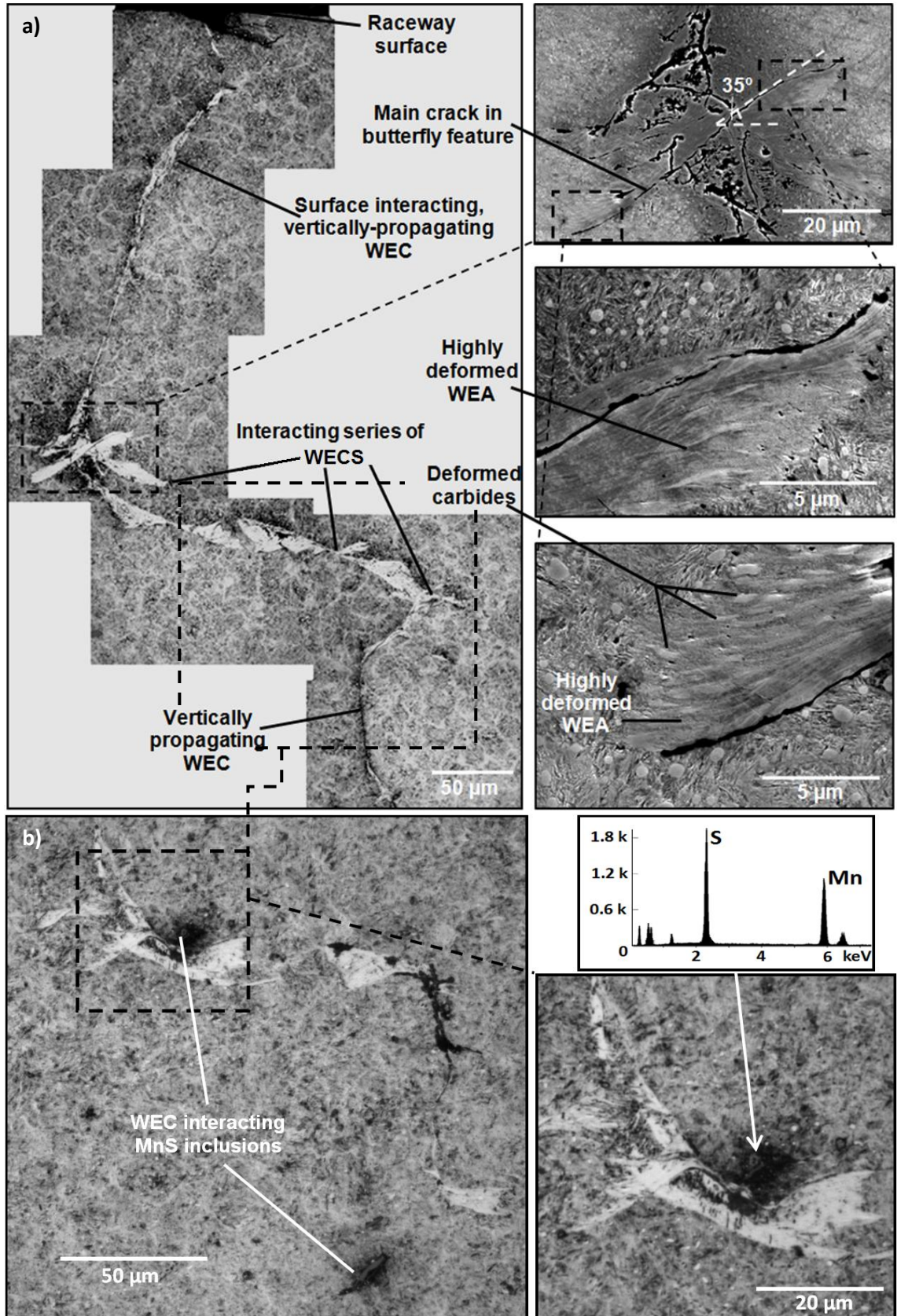


Figure 5-4: Series of butterflies and connected WECs in circumferential section a) first section observed b) second section observed approximately 20 μm below first section.

RESULTS FROM THE DESTRUCTIVE INVESTIGATION OF A FAILED WIND TURBINE GEARBOX BEARING

Region	Minimum hardness recorded: GPa (HRC)	Maximum hardness recorded GPa (HRC)	Average Hardness GPa (HRC)
Non- damaged matrix	6.37 (58)	7.99 (65)	7.23 (62)
WEC	8.51 (66)	10.77 (70)	9.43 (68)

Table 5-2: Nano hardness results for steel matrix and WEC

Of the 112 catalogued inclusions found in the failed bearing inner raceway, 89 inclusions (79.5%) were connected to WECs that appeared to have propagated from the inclusion tips. Each of these 89 inclusions had either one or two WECs that tended to propagate at much shallower angles than traditional “butterfly wings”; the vast majority at less than 30 degrees from horizontal. It is suggested that these MnS inclusion initiated WECs may not be caused by a concentration of unidirectional shear stress as “butterfly wings” are thought to be [12, 23, 26, 52, 56], but are initiated due to Mode I loading of the inclusion tips at locations near to the maximum equivalent stress, which would explain their near parallel-to-surface propagation. Examples of these inclusion-initiated WECs are shown in Figure 5-5, which were taken from circumferentially sectioned specimens. Figure 5-5a-b are SEM images thus it cannot be proved from the images that the highlighted WEA regions are indeed white in colour. It seems however, that given the evidence presented in Figure 5-5c-w, that it can be ascertained that these regions are WEAs. It can be clearly seen that the angle of WEC propagation in all example images (with the possible exception of Figure 5-5l and q) is lower than the angle of butterfly wing propagation presented in Figure 5-4a. This finding is in line with the findings presented in [196], which states that the most common angle of WEC propagation in bearing steel is between –10 and +20 degrees from the horizontal, where the negative sign indicates an angle below the horizontal.

Further evidence is presented in Figure 5-6a-c, which show relatively long MnS-initiated microcracks around 20 µm in length that are clearly propagating close to horizontally. These cracks appear to have no attached WEA, suggesting that crack formation may precede the formation of the WEA. Figure 5-6d-f show long WECs found in axially sectioned specimens that are clearly propagating close to horizontally. Since the WEC is not attached to the crack along its full length in Figure 5-6e, it again seems likely that the crack formation precedes the formation of the WEA rather than the other way round. A relatively long (~50 µm) WEC was found at a depth of around 500 µm, as shown in Figure 5-7. The evidence presented in this chapter suggests that it is highly likely that the WEC was initiated by an off-plane MnS inclusion, although this was not confirmed. Figure 5-7 shows a highly magnified image of the WEC, with the WEA microstructurally changed region forming on the lower side of a clear crack through the material. Figure 5-7b shows that the microstructure within the WEA is not uniform, showing areas that may be elongated carbides closer to the bottom WEA/steel matrix boundary.

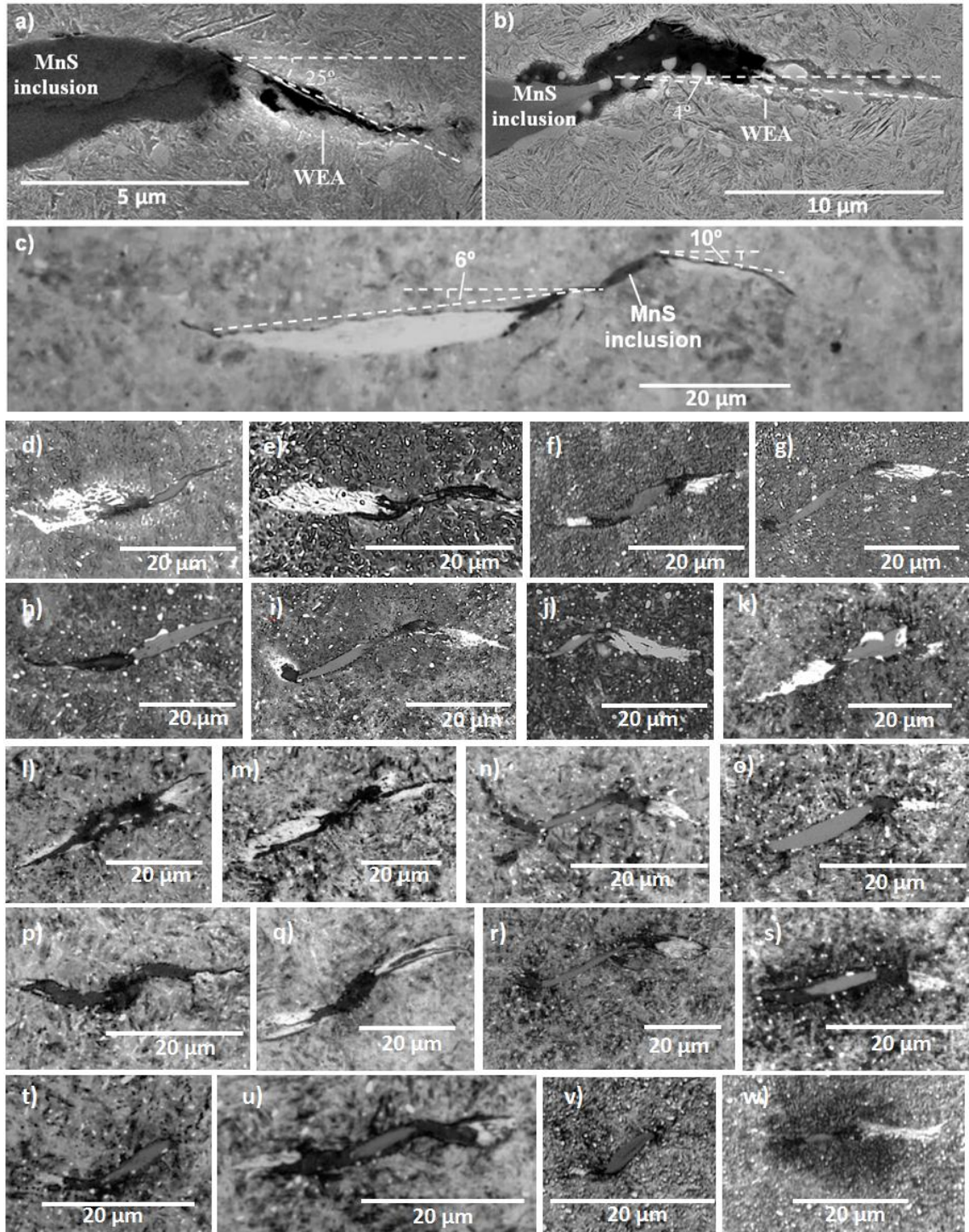


Figure 5-5: Examples of WEA-interacting MnS inclusions (circumferentially sectioned specimens)

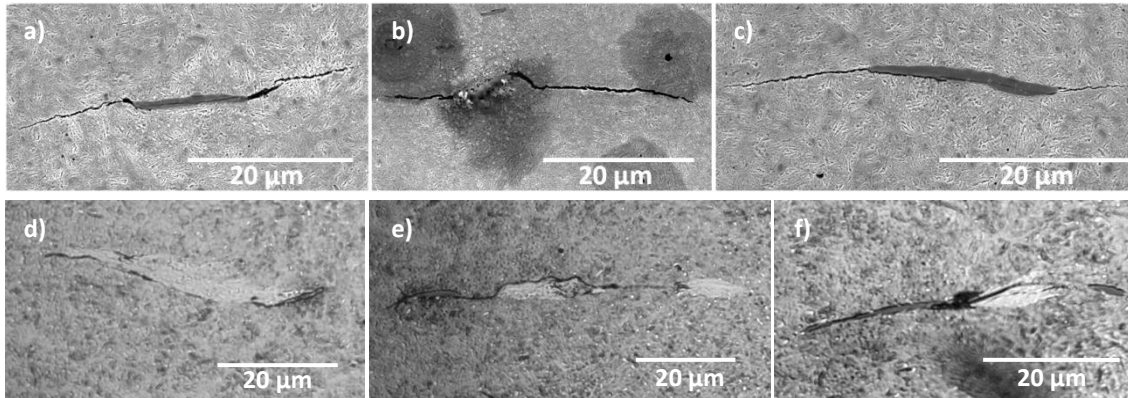


Figure 5-6: Damage linked to MnS inclusions in axially sectioned specimens: a-c) SEM images of microcracks, with no visible in-plane WEC d-f) optical images of WECs.

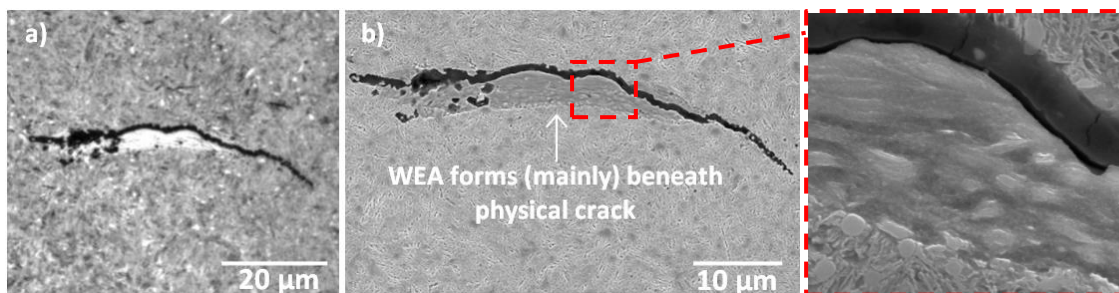


Figure 5-7: Standalone WEC: a) optical microscope image b) SEM image showing WEA microstructure

5.2.2. Subsurface inclusion-initiated WEC formation

There is debate regarding the location of WEC initiation; broadly there are two arguments:

1. WECs initiate subsurface and propagate up to the surface, leading to failure, either by WSF or axial cracking [12, 26, 36, 52, 53, 123, 197]
2. WECs initiate on the surface and propagate downwards [109], meaning that they are a result of surface failure rather than its cause.

Argument 1 and 2 are not necessarily mutually exclusive, however, evidence found in this study certainly suggests that point 1 is correct and that cracks and WECs are initiated subsurface, most commonly at MnS inclusions. The evidence presented in Figure 5-5 and Figure 5-6 supports argument 1, while Figure 5-8 and Figure 5-9 present further evidence that subsurface cracks and WECs are initiated at MnS inclusions. Figure 5-4 shows that MnS inclusions and butterflies interact with WECs, which supports argument 1, although does not offer proof that the damage was initiated from the butterfly or from the inclusions. Figure 5-8 offers evidence that Mode I tensile loading occurs at the tips of MnS inclusions, since the cracks formed at the inclusion tips are clearly wider near the inclusion, suggesting Mode I loading is pulling the crack apart. It is suggested that residual tensile stress concentrations above and below MnS inclusions, acting along their length, may cause this Mode I loading (see Figure 2-17 for illustration of residual stresses at inclusions).

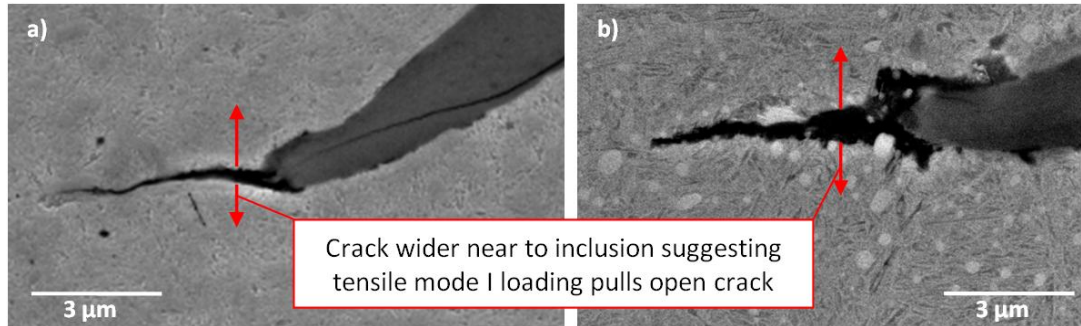


Figure 5-8: Evidence supporting theory that Mode I loading caused crack initiation/propagation (circumferentially sectioned inclusions)

Figure 5-9a shows three nearby inclusions, which have each independently initiated cracking. They are not part of an extended crack network and no other cracks are visible on this plane, therefore crack initiation must have begun at the inclusions. Figure 5-9b shows a typical WEA, initiated at an inclusion at around 150 μm below the raceway surface. Again the feature does not appear to be linked to any extended crack network. Since all 112 catalogued damage initiating inclusions did not appear to be part of a larger crack network, the evidence that the damage was initiated at the inclusions is conclusive. Figure 5-9c-k (optical) show typical separation and cracks formed at the ends of damaged inclusions. The SEM image shows an EDAX reading of a darker part of the inclusion near to the cracks, revealing it to be an area of Al_2O_3 alumina, which may have influenced crack initiation. Studies have found that MnS inclusions containing oxide parts are more damaging than those that do not [50, 106] (as discussed in section 2.3.5.6), however no evidence suggesting that oxide parts are required for WECs initiation was found in this study. Every WEC found in this study appeared to have initiated at the inclusion tips (the lowest radius of curvature), coinciding with the location of maximum stress concentration around the inclusion [90, 97, 198].

It could be the case that WECs remain close to the initiating inclusion and never propagate to significant distances through the material. Figure 5-4 provides evidence that WECs may propagate between MnS inclusions and affect greater areas, although it cannot be considered conclusive because there is a chance that the WECs may have approached the vicinity of the highlighted inclusions randomly. It should also be noted that it is possible that any separation around inclusions shown in the Figures may have been exaggerated in some images due to the etching process; since etchant may not be washed out completely from the small voids/separated regions between inclusion and matrix, causing acid damage.

RESULTS FROM THE DESTRUCTIVE INVESTIGATION OF A FAILED WIND TURBINE GEARBOX BEARING

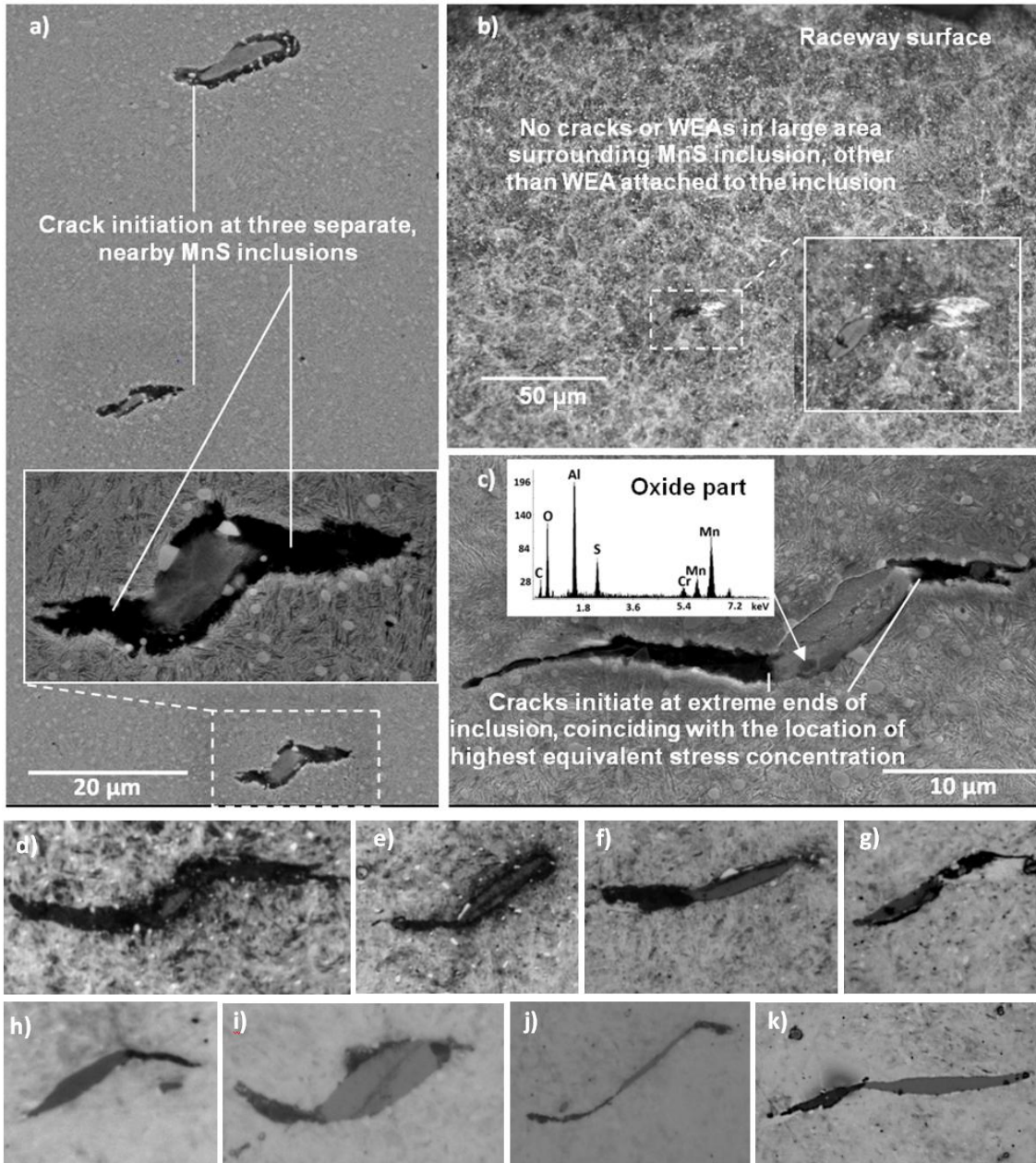


Figure 5-9: Evidence supporting subsurface crack and WEA initiation at MnS inclusions

5.2.3. Oxide parts within MnS inclusions

As has been previously highlighted, it is the opinion of some authors [50, 106] that oxide parts (particularly Al_2O_3) within MnS inclusions that are in contact with the steel matrix, lead to the necessary tensile residual stress concentrations required to create Mode I loading and are the reason that cracks are initiated adjacent to the inclusions. A detailed SEM/EDAX analysis was undertaken to examine the effect of oxide parts that are often, but not always, present inside MnS inclusions. The crack that has been initiated on the left side of the inclusion shown in Figure 5-10 has clearly spread from the inclusion tip. EDAX spectrums are shown in the Figure showing:

1. That the inclusion body is MnS-type
2. That the black area has high levels of carbon, silicon and oxygen, which suggests it is a void/separated region that is full of the *KonductoMET™* bakelite used to mount the specimen, which contains carbon, oxygen and silicon elements [199] (discussed further below).
3. That the white area connected to the inclusion is a temper carbide (M_3C type) (discussed in section 2.2.2).
4. That there are a number of alumina oxide parts within the inclusion, that don't appear to influence on the internal or external crack propagation.

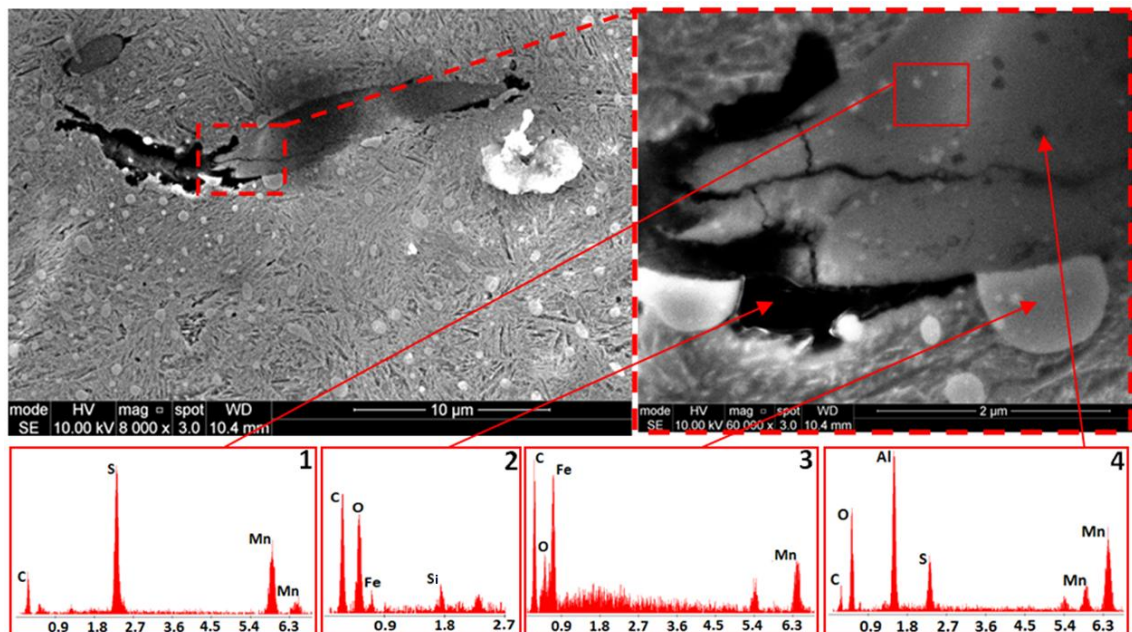


Figure 5-10: MnS inclusion and adjacent separation from the steel matrix with EDAX of features: 1. MnS inclusion main body; 2. Void at point of separation; 3. Temper carbide (M_3C) adjacent to inclusion; 4) Alumina part of inclusion

RESULTS FROM THE DESTRUCTIVE INVESTIGATION OF A FAILED WIND TURBINE GEARBOX BEARING

Further evidence that oxide parts at inclusion tips are not necessary to initiate cracks is presented in Figure 5-11 and Figure 5-12. Each of the inclusion tips were carefully examined with both high magnification SEM imagery and EDAX analysis, with no evidence of any oxide parts. Figure 5-11 shows internally cracked inclusions that have initiated cracks and Figure 5-12 shows inclusions without internal cracks that have also initiated damage.

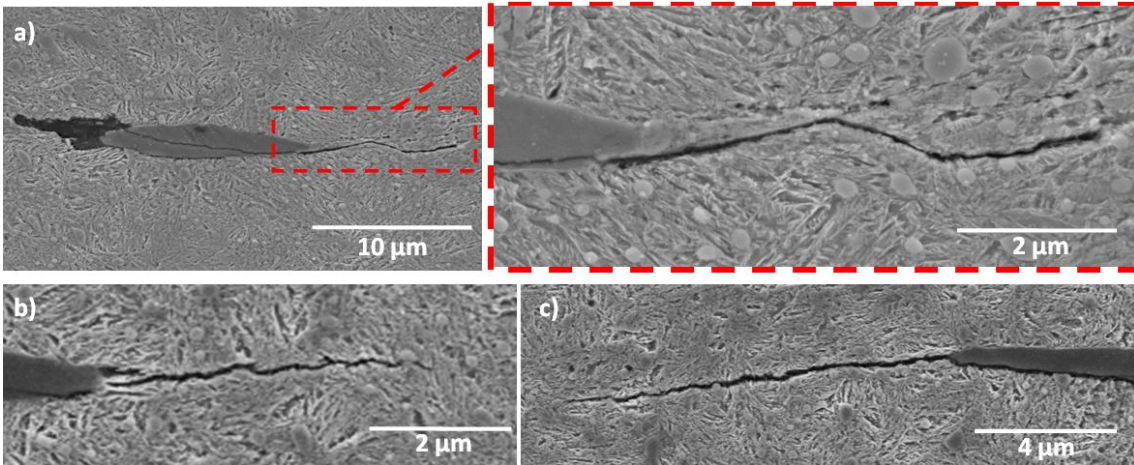


Figure 5-11: Internally cracked MnS inclusion initiated cracks with no interacting oxide part at inclusion tip (axially sectioned inclusions)

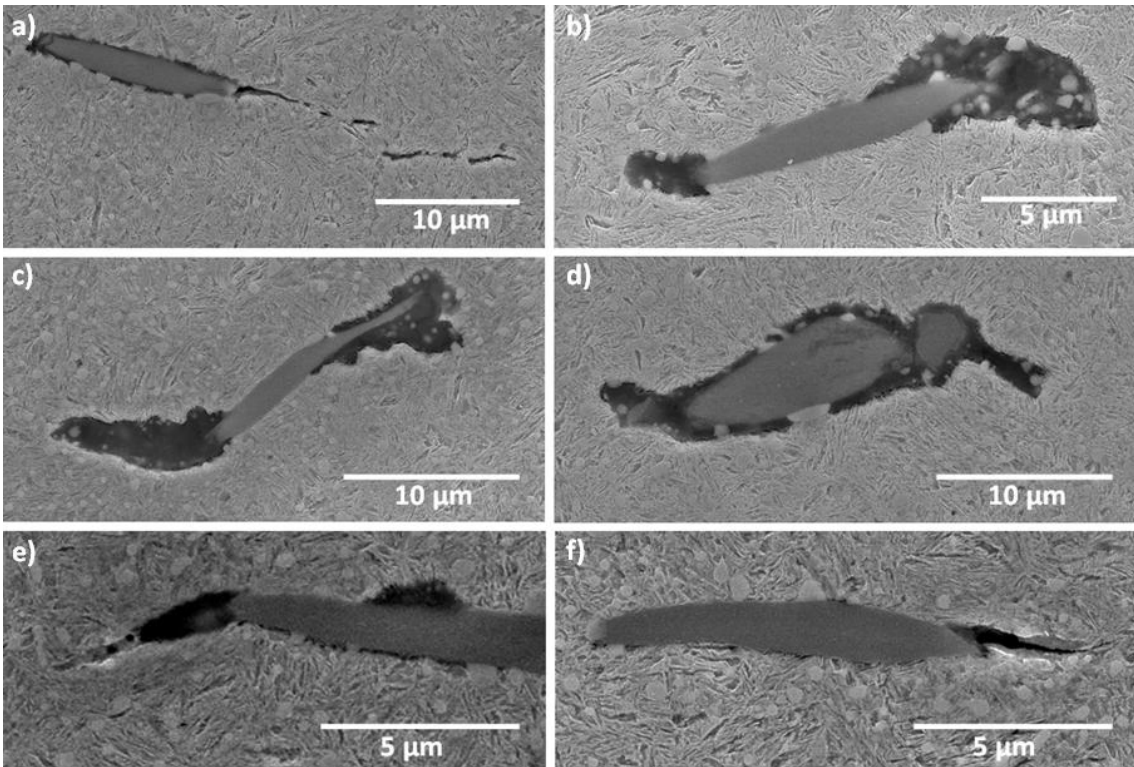


Figure 5-12: Evidence suggesting internal cracking of MnS inclusions is not necessary (inclusions do not appear to have oxide parts near inclusion tips).

Further analysis of the separated region in Figure 5-12c was carried out and the results are presented in Figure 5-13. It is thought that the separated region is relatively thin, meaning that

the *KonductoMET™* bakelite trapped in the void is only a thin layer. Since carbon is a small element, it is difficult to detect using EDAX which may be the reason that only small amounts are detected in the analysis. The fact that the levels of iron (Fe) are relatively high also suggests that the layer of *KonductoMET™* is thin and that the iron underneath is being detected. The evidence that the area is a void (separated region) filled with *KonductoMET™* is apparent when comparing the results of the analysis to the elemental composition of *KonductoMET™*. Five areas of a specimen made from only *KonductoMET™* with an area of one square millimeter were scanned and a mean composition was found, as shown in Table 5-3. When compared to the steel composition, the Bakelite clearly had high levels of silicon (Si) and oxygen (O). This is the case for all five positions indicated on Figure 5-13. The high levels of manganese (Mn) and sulphur (S) are due to the proximity of the MnS inclusion.

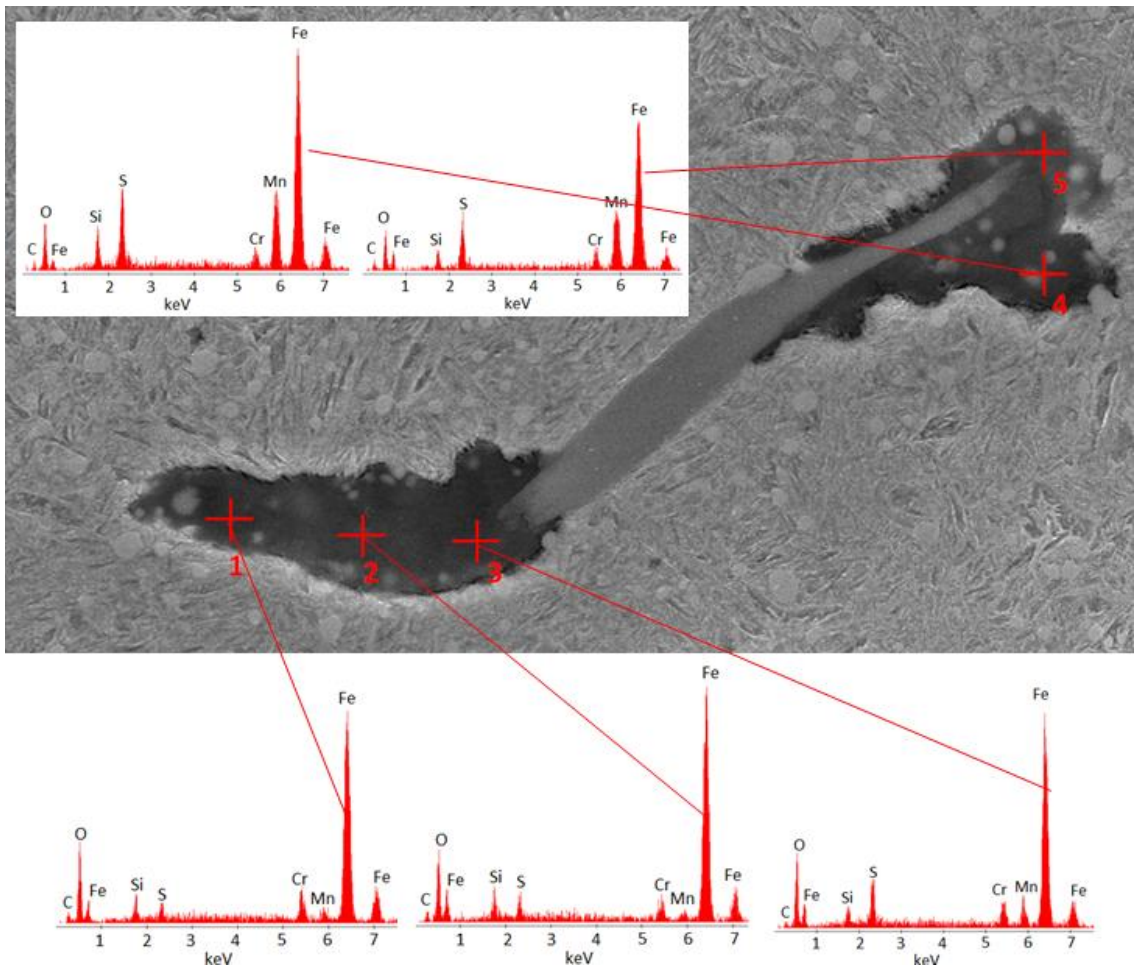


Figure 5-13: EDAX analysis of separated areas adjacent to inclusion

Element	C	O	Al	Si	Ca
Vol%	80.4	12.8	1.3	3.6	1.2

Table 5-3: Mean volume percentage of major detected elements in Bakelite EDAX scan

5.2.4. Detailed examination of inclusion initiated WEC

A high magnification image of a WEC linked to an axially sectioned MnS inclusion is presented in Figure 5-14. The nanograin WEC containing no carbides is clearly displayed in the highly magnified area. There is a clear distinct boundary between the underside of the WEA and the steel matrix, whereas to the right of the WEA, the boundary is much less clear, possibly suggesting that the microstructure is in the process of changing from the steel matrix into the WEA.

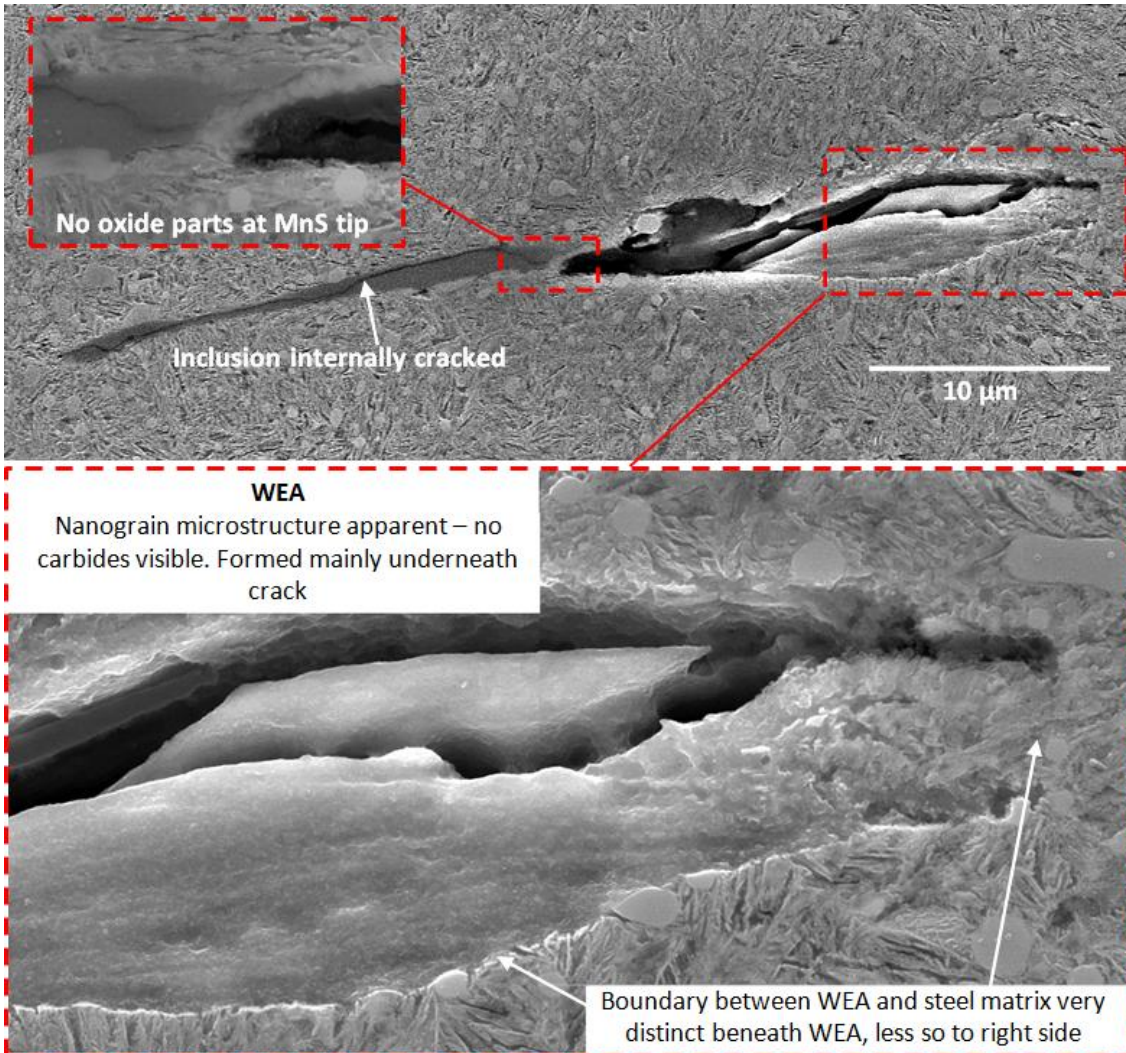


Figure 5-14: MnS inclusion initiated WEA detail

5.2.5. Additional extended WEC networks

A number of large WEC networks were found in the zone 2 damaged region. Figure 5-4 has previously presented one such network. Figure 5-15 and Figure 5-16 present two more, both of which appear to be vertically propagating cracks, which may have been initiated subsurface or at the surface. Highly magnified SEM images reveal details at the WECs. Figure 5-15 shows the degree of damage in the vicinity of the WEC. The main crack is linked to a network of smaller cracks within the attached WEC. Figure 5-16 shows the WEC interacting with the surface, where there is a large WEA. Within this WEA there are severely deformed carbides, voids and a crack between the WEA and steel matrix.

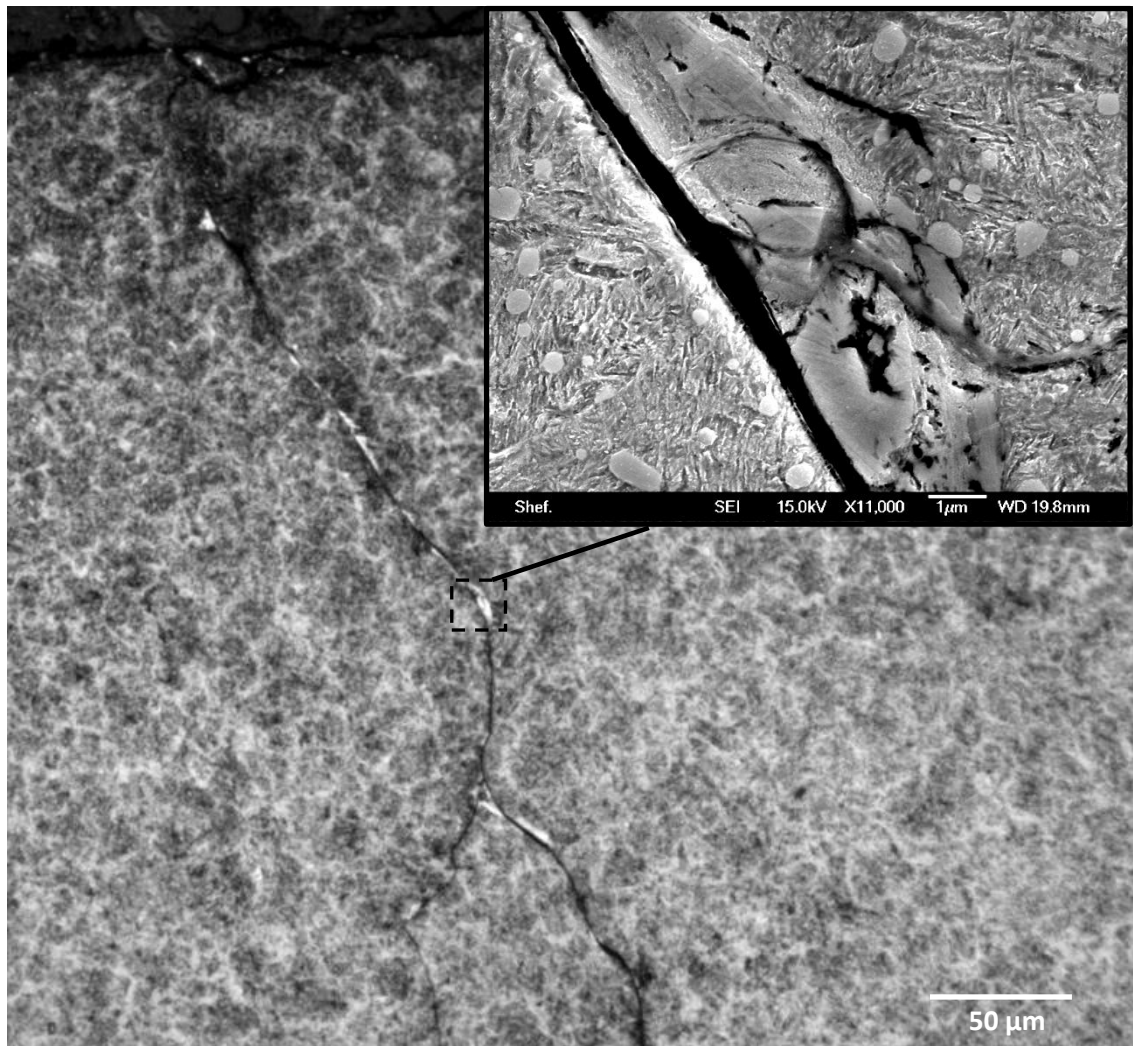


Figure 5-15: Extended surface breaking WEC network (circumferential section, phase 2 damage)

RESULTS FROM THE DESTRUCTIVE INVESTIGATION OF A FAILED WIND TURBINE GEARBOX BEARING

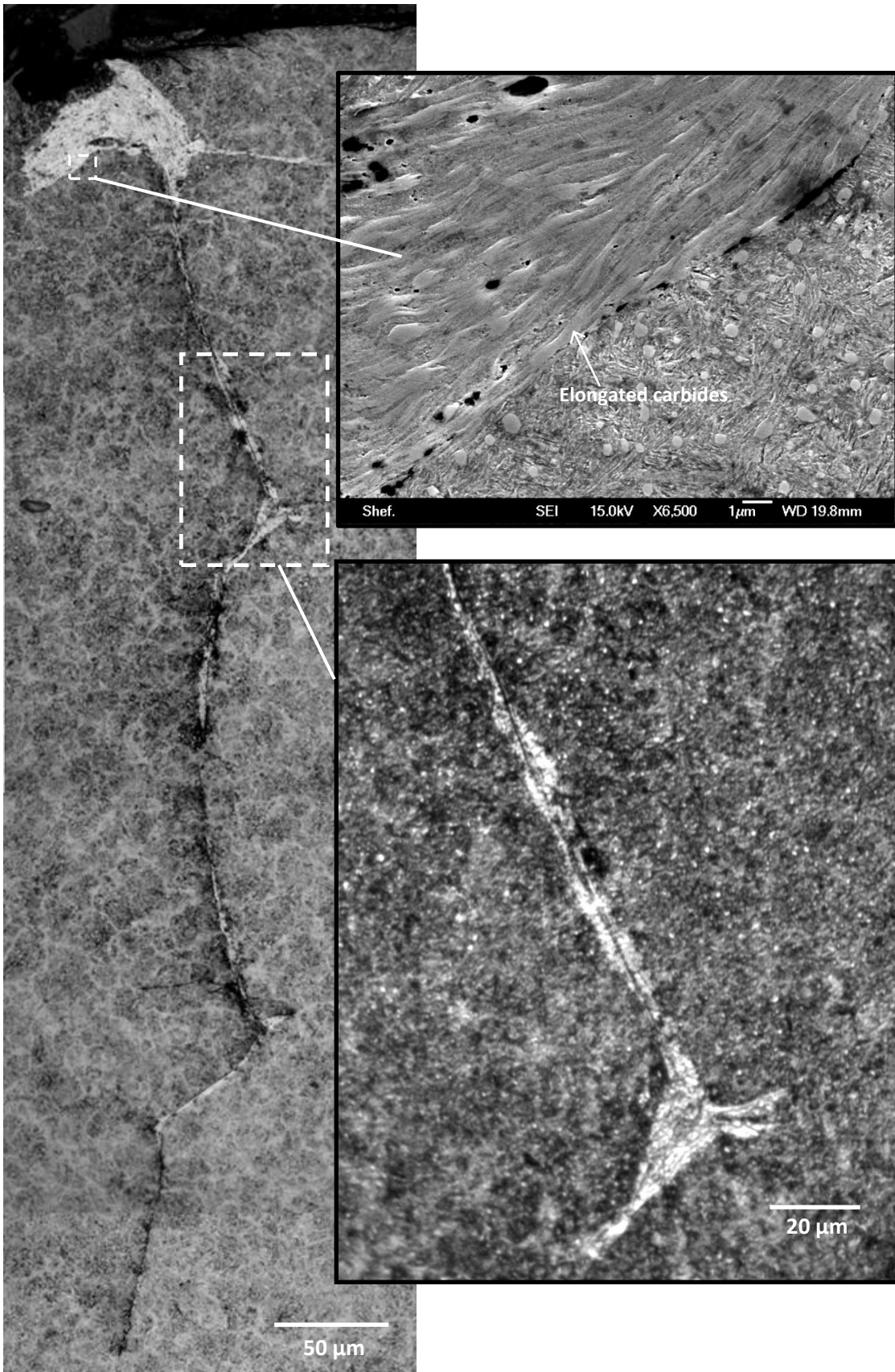


Figure 5-16: Large surface breaking, vertically propagating WEC (circumferential section, phase 2 damage)

5.2.6. Other interesting damage features

It has been reported that MnS inclusions may act as “virtual cracks” [200], which, due to their low strength, may propagate actual cracks through the steel matrix. Examples of MnS inclusions acting as virtual cracks are presented in Figure 5-17 and Figure 5-18, where the inclusion that are intersected by a larger crack network (assumed to be surface initiated and with no apparent attached WEA), divert cracks by a distance of approximately 10 μm and 2 μm respectively. The finding supports the theory that cracks preferentially propagate along MnS inclusions, rather than the surrounding matrix and shows that they are a "weak spot" within the steel microstructure. Figure 5-17 and Figure 5-18 show MnS inclusions that are linked to surface breaking cracks propagating in the axial and vertical directions respectively. It cannot be proved whether the crack began at the surface and propagated downwards, intersecting the inclusion, or whether the crack initiated at the inclusion and propagated upwards until it reached the surface. Since the crack changes direction within the MnS inclusions, it is clear that the inclusion has influenced crack propagation direction, possibly due to the influence of a residual stress concentration. The fact that the cracks change direction to propagate along the length of the inclusion supports the theory that there is a strong influence from the tensile residual stress that exists acting along the length of the top and bottom boundaries of the inclusion.

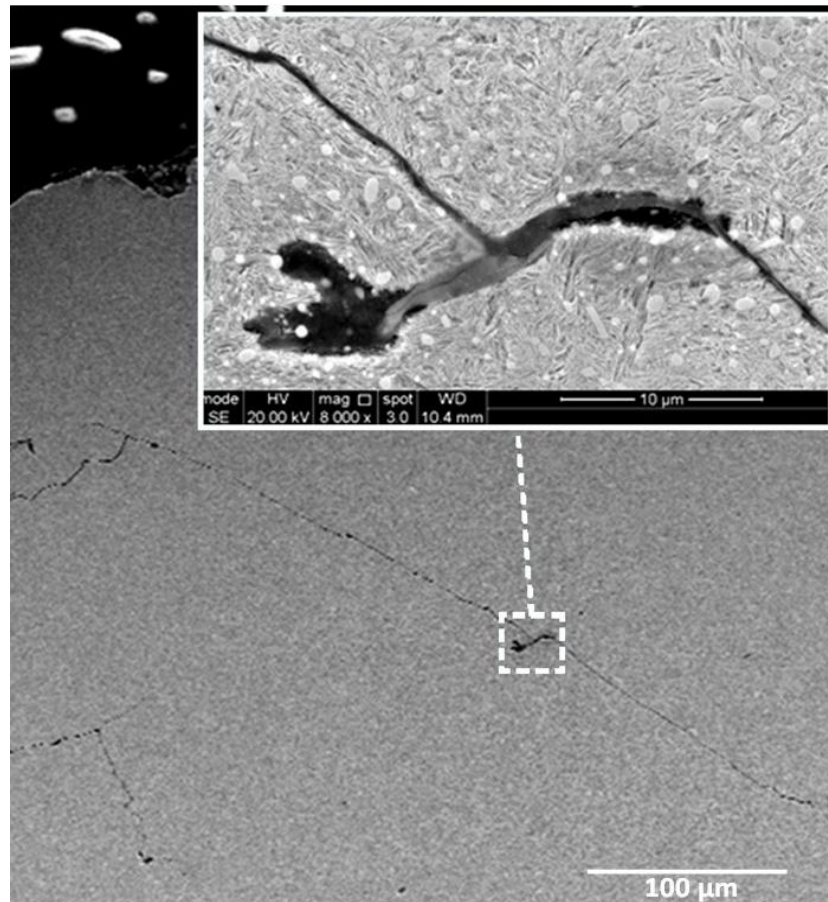


Figure 5-17: Axially propagating crack surface linked crack deflection by MnS inclusion

RESULTS FROM THE DESTRUCTIVE INVESTIGATION OF A FAILED WIND TURBINE GEARBOX BEARING

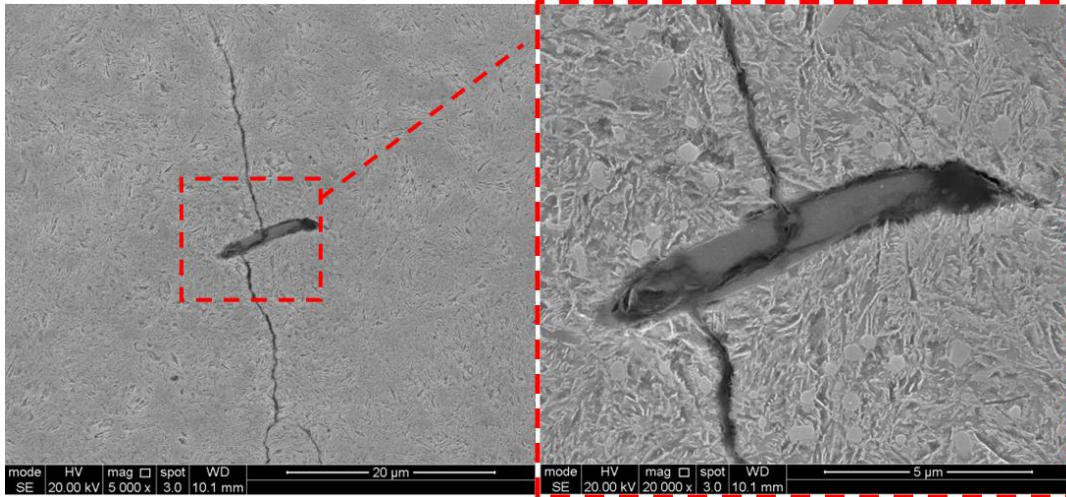


Figure 5-18: Vertically propagating surface linked crack deflection by MnS inclusion

Figure 5-19 shows an interesting image of a MnS inclusion initiated crack propagating through the middle of an M_3C carbide. Such carbides are therefore not obstructions to crack growth and indeed can be split apart themselves by subsurface cracking. Figure 5-20 shows a partial white etching layer (WEL), which may have been more extensive before material was removed from the raceway surface. The presence of a WEL indicates high levels of slip (investigated in detail in section 7.2.5). This finding suggests that a high level of slip was experienced by this bearing at some point during operation.

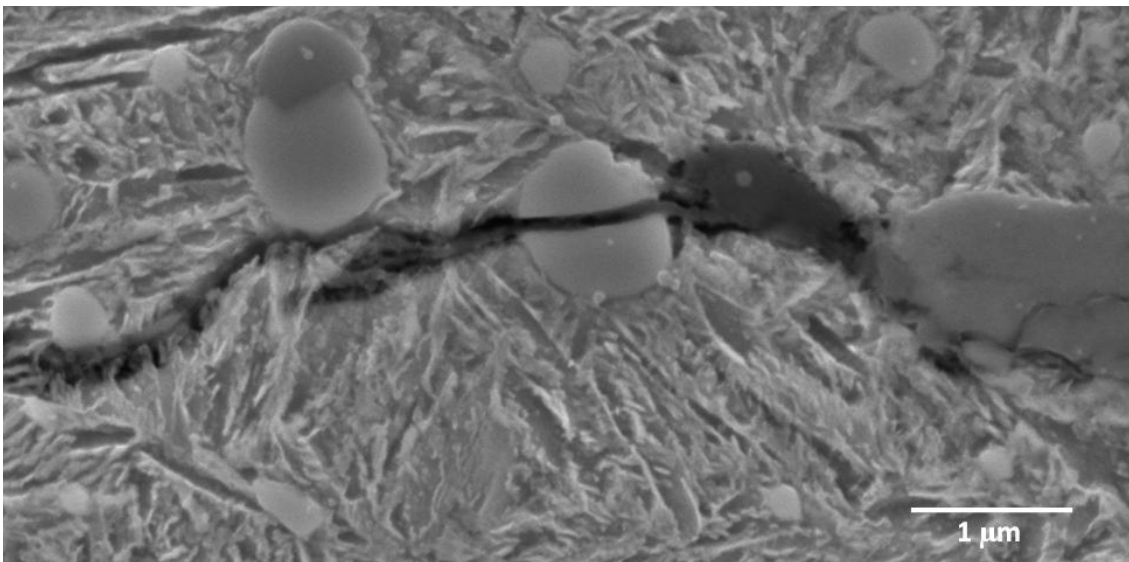


Figure 5-19: Crack propagation through an M_3C carbide

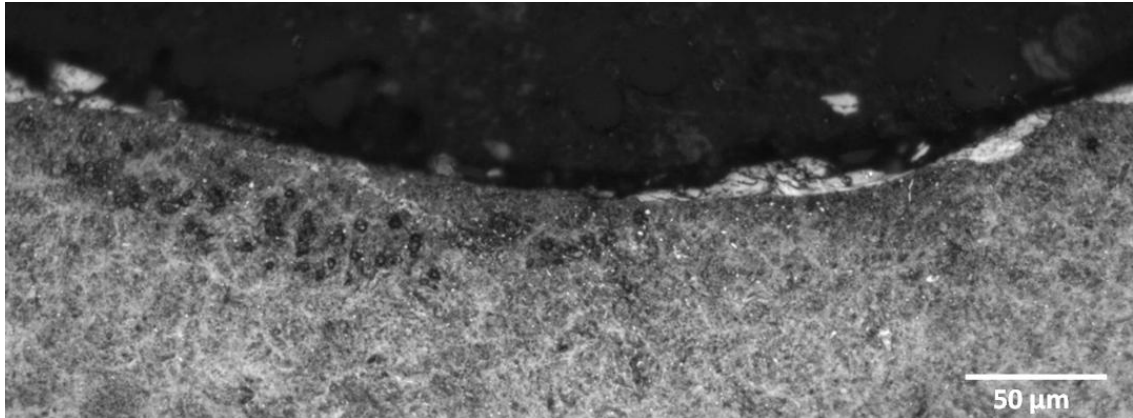


Figure 5-20: White etching layer attached to raceway surface

5.2.7. Damage initiation and propagation at MnS inclusions

From the observed damage at MnS inclusions found during sectioning, a hypothesis of damage initiation and propagation is summarised in detail in Figure 5-21. Inclusions are initially undamaged and well-bonded to the matrix (stage 0). The first sign of damage may be internal cracking of the inclusion (stage 1a) and/or separation of the inclusion from the steel matrix (stage 1b). Cracking may be initiated into the steel matrix (stage 2), possibly from propagation of the stage 1a internal crack, from stage 1b type separation, or from the inclusion tip that may act as a stress concentration point. WEAs then form at stage 1b separation (stage 3a) or, at stage 2 type propagated cracks (stage 3b). Further propagation of cracks and sometimes, of their attached WEAs, may then take place (stage 4), leading to the propagation of what has been termed white etching cracks (WECs), far away from the MnS inclusions. The likelihood of each damage type occurring and the possible relationships between each are investigated in section 5.3. Note that the findings here are different from those in [23, 33], which state that an inclusion must be internally cracked in order to initiate a WEC.

RESULTS FROM THE DESTRUCTIVE INVESTIGATION OF A FAILED WIND TURBINE GEARBOX BEARING

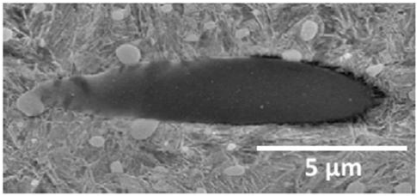
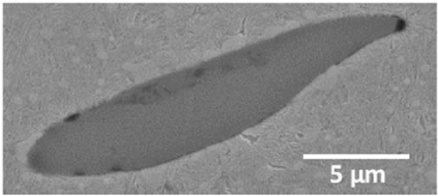
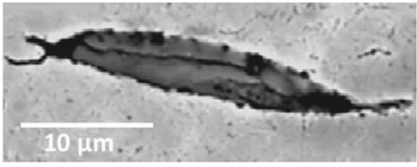
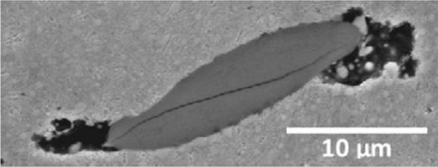
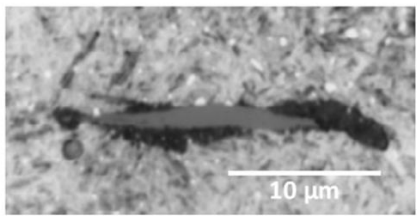
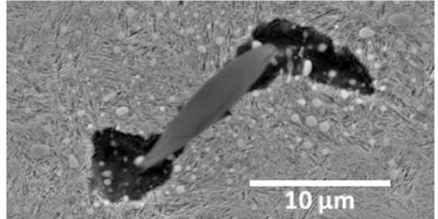
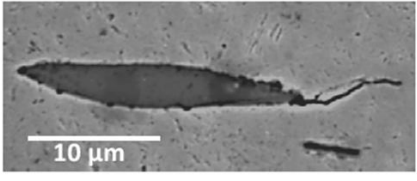
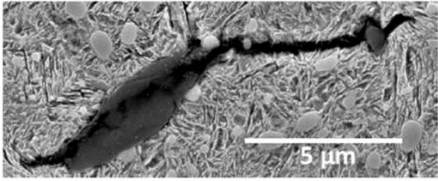
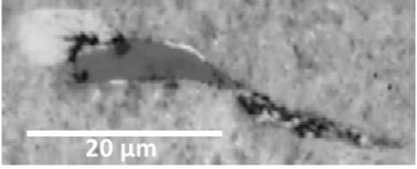
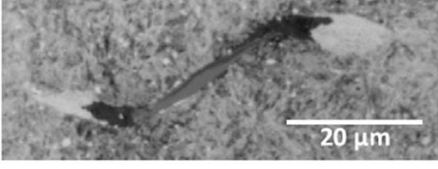
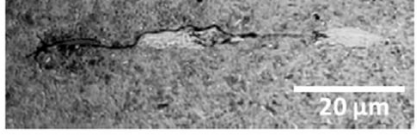
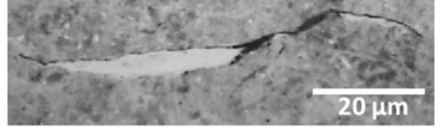
	Axial cross-section shape	Circumferential cross-section
Stage 0 Undamaged inclusion		
Stage 1a Inclusion internal cracking		
Stage 1b Separation of inclusion from matrix		
Stage 2 Crack propagation into matrix from inclusion tip		
Stage 3a WEC propagates from separation at inclusion tips		
Stage 3b WEA develops adjacent to cracks		
Stage 4 Further propagation of crack and WEA into bulk material		

Figure 5-21: Damage initiation and propagation at MnS inclusions

5.3. Analysis of inclusion database

112 damage initiating inclusions from circumferentially and axially sectioned samples were identified and catalogued. The following data was recorded, with the aim of finding trends between the damage types found, as summarised in Figure 4-10:

- Depth from surface
- Angle of inclusion
- Whether the inclusion is internally cracked
- Whether the inclusion is separated from the surrounding steel matrix
- Total length of crack initiated from inclusion (left side crack length + right side crack length)
- Total length of WEC initiated from inclusion (left side crack length + right side crack length)

5.3.1. Relationship between damage types at MnS inclusions

Figure 5-22 shows the relationship between three types of damage at MnS inclusions: internal cracking, separation from the bulk material and WECs linked to the inclusions. Figure 5-22a shows that 29 % of damaged inclusions were both internally cracked and WEC initiating, while, 50 % had initiated WECs without being internally cracked. This result clearly demonstrates that an inclusion does not necessarily need to be internally cracked in order to initiate a WEC. Similar percentages in Figure 5-22b show that separation from the bulk material has a similar link to the probability of the inclusion interacting with a WEC, with 28 % of separated inclusions being linked to WECs, and 51 % of non-separated being also linked. This shows that an inclusion that does not separate from the steel matrix is more likely to initiate a WEC than one that does, perhaps because some stress is relieved by the separation. Figure 5-22c appears to show no strong prevalence of damage occurring at inclusions that are internally cracked or that are separated from the bulk material, or those that are both internally cracked and separated.

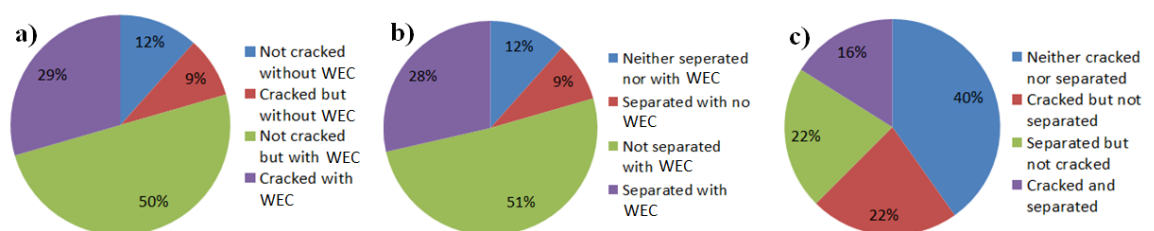


Figure 5-22: Relationship between damage types: a) internal cracking and WEC formation b) separation from bulk material and WEC formation c) internal cracking and separation from bulk material

5.3.2. Variation of MnS inclusion initiated damage with depth

No trends were found when comparing the angle and the size of inclusions with their depth from the raceway surface, thus it is clear that inclusion distribution is random in the sample bearings and that the effects of over-rolling during service have little influence on the size and orientation of the inclusions. In addition, WECs were found on many of the deepest damaged inclusions, to a depth of approximately 600 μm from the raceway surface (corresponding to a contact stress of around 2.6 GPa if τ_{max} occurred at that depth, possibly suggesting that the bearing may have experienced extremely high loading). It was interesting, however, that no internally cracked or separated inclusions were found deeper than 430 μm . In fact the mean depths for inclusions that were internally cracked and for those that had separated from the surrounding bulk material were just 3 μm different (mean values of 219.5 μm and 216.2 μm respectively). This suggests that damage in the form of inclusion cracking and inclusion separation may both be affected by similar loading mechanisms. These results are outlined in Figure 5-23.

The mean depths of damaged inclusions that were cracked, separated, or had initiated WECs, were all very close to the calculated values of τ_{max} and $\sigma_{v,max}$ (see Table 4-2). This finding is similar to that of Grabulov [18] as discussed in section 2.3.6. The mean values did not correspond as closely to the depth of $\tau_{0,max}$, which suggests that it may not be as critical as τ_{max} and $\sigma_{v,max}$ for WEC initiation at MnS inclusions. Grabulov found that $\tau_{0,max}$ was critical for butterflies to form at Al_2O_3 inclusions, again suggesting that these features are not the same. Figure 5-24 displays the mean and maximum crack lengths at inclusions within different ranges of depths in: a) circumferentially and b) axially sectioned specimens. It can be seen that the mean value of WEC lengths is relatively constant at about 10 μm , in the circumferentially sectioned specimens, up to a depth of 500 μm . While WEC length is greatest between 200-300 μm in depth in axially sectioned specimens (with the exception of the one inclusion found in the range 400-500 μm), which corresponded with the depths of τ_{max} and $\sigma_{v,max}$.

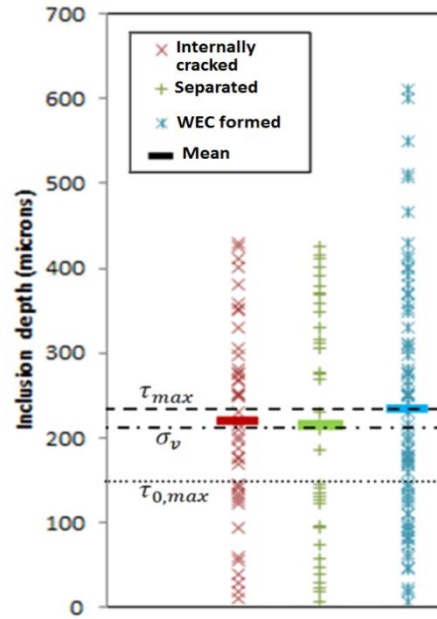


Figure 5-23: Variation of inclusion initiated damage with inclusion depth and depths of maximum stresses τ_{max} , $\tau_{0,max}$ and $\sigma_{v,max}$

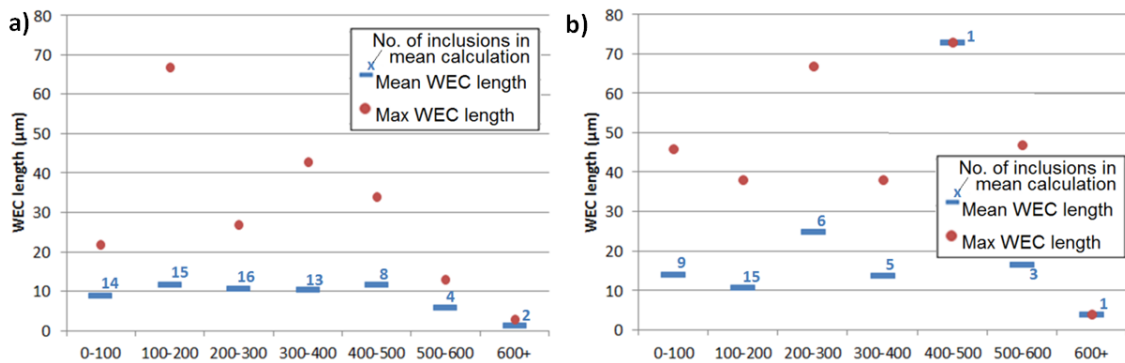


Figure 5-24: Variation of mean and max WEC length with MnS inclusion depth in: a) circumferentially sectioned specimens, b) axially sectioned specimens

5.3.3. Variation of WEC length with MnS inclusion orientation angle

No trends were found when WEC lengths were compared to inclusion orientation in the circumferential sectioned samples, however Figure 5-25a shows that mean WEC lengths were generally shorter at the extreme ends of the orientation angle range (i.e. angles $> 10^\circ$ and $< 60^\circ$). Figure 5-25b shows that the length of cracks propagating in the axial direction were generally longer in “flatter” axially sectioned inclusions. That is to say that it appears that the closer the inclusion’s major axis is to being parallel with the bearing raceway surface, the longer the initiated propagated crack is likely to be. The direction of the inclusion orientation from parallel (anticlockwise or clockwise) is not considered since the stress field is symmetric when viewed on the axial section (assuming no misalignment).

RESULTS FROM THE DESTRUCTIVE INVESTIGATION OF A FAILED WIND TURBINE GEARBOX BEARING

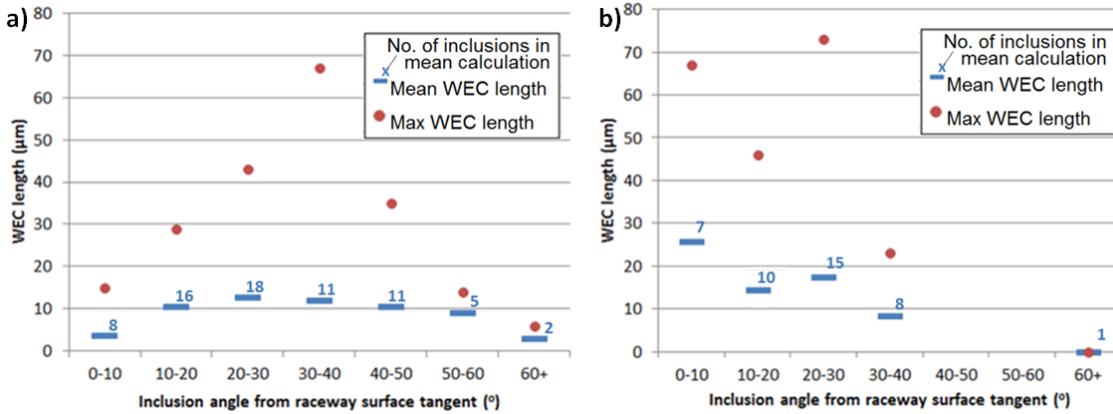


Figure 5-25: Variation of mean and max WEC length with MnS inclusion orientation angle in: a) circumferentially sectioned specimens, b) axially sectioned specimens

5.3.4. Variation of WEC length with MnS inclusion length

Clear trends were found between the length of WECs propagating into the bulk material and the length of the initiating MnS inclusions. As shown in Figure 5-26, crack length tended to be longer at smaller inclusions for both axially and circumferentially sectioned samples (ignoring the single inclusion found that was less than 8 µm in length). A study at the University of Southampton in which a WTGB was similarly sectioned found that smaller inclusions (average length less than 20 µm) were the most likely to initiate WECs [6, 25], although this contradicts the findings presented in [54], which states that coarser inclusion sizes, in general, have a larger local stress-concentration factor. The highest mean value of WEC lengths for both circumferentially and axially sectioned specimens was initiated by inclusions of lengths between 8-16 µm. The downward trend is clear in both Figure 5-26a and Figure 5-26b. The results also show that WECs tended to be longer in axially sectioned inclusions than circumferentially, suggesting that WECs preferentially propagate in the axial direction, perhaps explaining why through-hardened bearings have been found to fail via axial cracking [5].

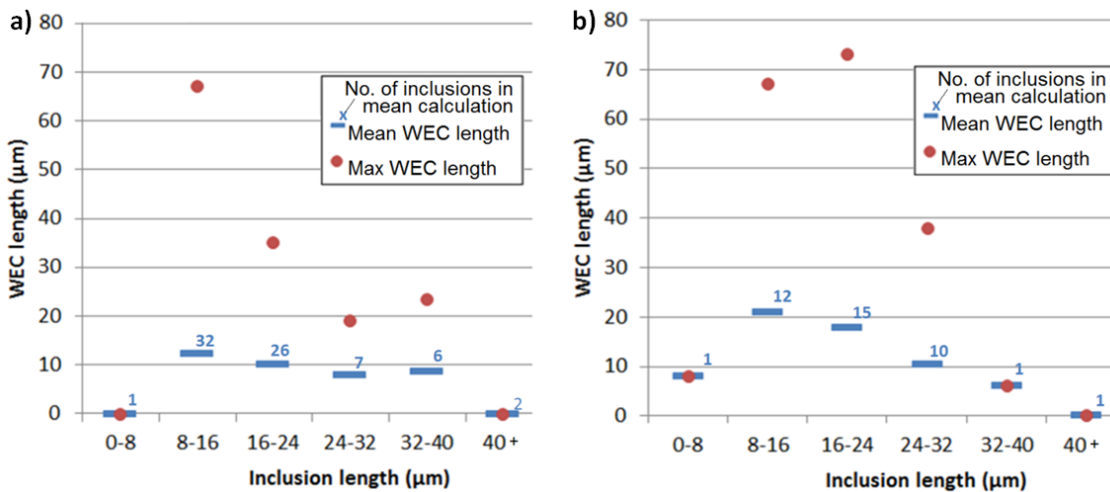


Figure 5-26: Variation of mean and max WEC length with MnS inclusion length in: a) circumferentially sectioned specimens, b) axially sectioned specimens

5.4. Summary

This chapter reports the results of an investigation by destructively sectioning of the inner raceway from a failed low speed planetary stage WTGB and the damage found at manganese sulphide (MnS) inclusions within the bearing steel. The bearing inner raceway was sectioned through its circumferential and axial directions in order to compare the damage around inclusions in different directions. 112 damage initiating inclusions were catalogued and their properties investigated. WECs were found attached to MnS inclusions of lengths 3-45 μm at depths of up to 630 μm from the bearing raceway surface and at a wide range of angles of orientation. Damage at MnS inclusions included internal cracking of the inclusions, separation from the surrounding steel matrix, crack initiation and WEC initiation. Evidence has been found to support the theory that WECs are initiated subsurface, by MnS inclusions, but that butterfly cracks with wings propagating at 30-50° from parallel to the raceway surface, are not necessarily the same features as MnS inclusion-initiated WECs. Shorter inclusions were found to initiate longer WECs, as were inclusions that were closer to parallel to the raceway surface in axially sectioned samples. The conclusions from this chapter will be summarised in section 8.1.2.

6. RESULTS FROM HAMMERING IMPACT TESTING OF 100CrMo7-3 BEARING STEEL

The hammering impact tests described in section 4.4 were designed in order to investigate the effect of repetitive impact loading on MnS inclusions in bearing steel since findings from the literature review suggested that impact loading is likely to frequently occur during WT operation. To the author's knowledge, no other similar study has been undertaken so no previous results were available to compare results to, although damage found could be compared to that found in the failed planetary WTGB in Chapter 5. The effect of normal impact loading, perpendicular to the specimen surface tangent was first investigated, to examine the effect of Mode I loading conditions. The effects of changing both the number of impact cycles (12,500 – 200,000) and the contact pressure (2.153 - 2.603 GPa) experienced during impact loading were investigated, in order to find thresholds at which damage initiation started. Next, longer term tests were undertaken where specimens were exposed to 1,000,000 impact cycles. The effects of normal impact loading were compared to that of compound impact loading; where the impacting ball hit the specimen surface at an angle, in order to introduce surface traction. Figure 6-1 shows the Thesis work flow chart.

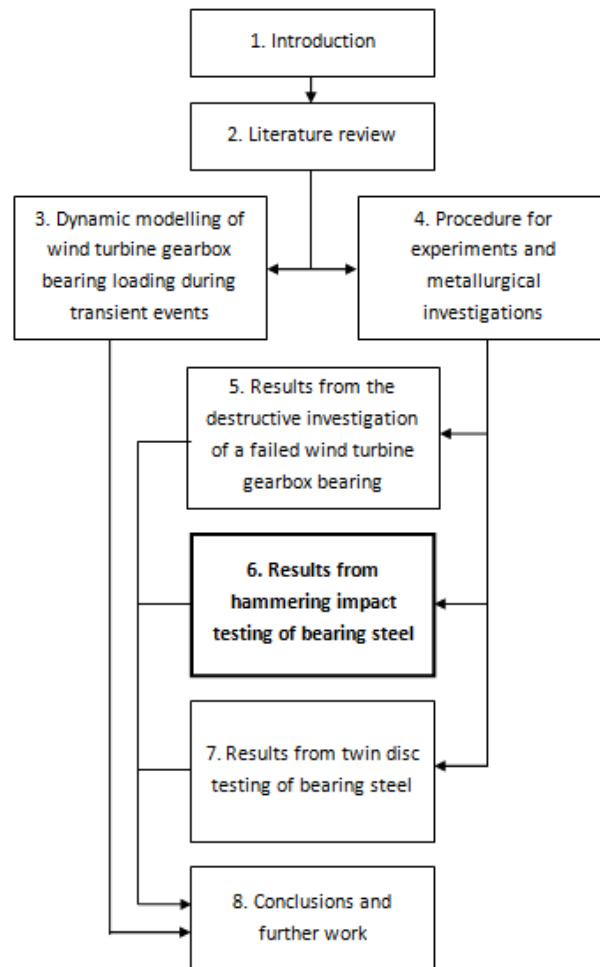


Figure 6-1: Thesis work flow chart

This chapter is split up into the following sections:

- Section 6.1 describes the results of initial testing, which was undertaken to confirm that the test rig was capable of producing subsurface damage at MnS inclusions in the bearing steel.
- Section 6.2 investigates the effect of changing the number of impacts on the damage caused at the highest contact stress level (2.603 GPa) that the rig could produce.
- Section 6.3 investigates the effect of changing the contact stress caused by impact testing on the damage caused over 50,000 cycles, a number determined to be above the threshold for damage initiation from the results of section 6.2.
- Section 6.4 investigates the effects of changing the number of impacts on the damage caused at a lower contact stress level (2.477 GPa), a stress determined to be above the threshold for damage initiation from the results of section 6.3.
- Section 6.5 summarises the results from the sections 6.1-6.4 and hypothesises thresholds for damage initiation in terms of number of impacts and contact stress levels.
- Section 6.6 summarises the damage found during longer term tests and compares the effects of normal and compound impact loading.
- Section 6.7 summarises the findings of this chapter.

6.1. Initial observations

After testing had taken place, surface inspection of the impact zone (IZ) revealed that there was almost no visible surface damage on any of the specimens, although a small “smoothed” mark was left where the surface oxide layer had been removed. This mark was useful to determine the exact point of impact, which was carefully marked before sectioning. It is unclear whether this small mark was caused by very low levels of plastic deformation of the surface or the removal of an oxide layer. However, as bearing contact stress in WTGs sometimes exceeds bearing steel yield strength by significantly higher percentages than those experienced during these tests [10], surface plastic deformation may also occur in WTGBs. As damage was found as deep as 300 μm below the contact surface, it is assumed that damage at inclusions was not affected by this small mark. As previously noted, some damage may be exaggerated in the images presented in this chapter, since when specimens are etched, the etchant may work its way into gaps created by separation damage or cracks. When the specimens are rinsed some etchant may remain in these gaps and cause acid burn damage. Although the damage may be exaggerated, some separation or cracking must take place for the etchant to flow into and avoid being rinsed off. Inclusions in an undamaged section of a specimen are displayed in Figure 4-16.

Initial tests were carried out on specimens 1-3, which were each impacted 100,000 times, experiencing a maximum subsurface equivalent stress, $\sigma_{v,max}$, of 2.58 GPa. After sectioning, 12 MnS inclusions in the three specimens had been found to have initiated separation damage, mainly at what appeared to be the tips of inclusions. Since the images are two-dimensional

sections through inclusions, Figure 6-2a (that appears to contain two nearby MnS inclusions), for example, may show damage in the centre of a longer inclusion, that is linked away from the sectioning plane. Figure 6-2 presents examples of the damage observed at five of the damaged MnS inclusions. Most inclusions found showed signs of separation from the matrix, although it is possible that a microcrack was initiated in the inclusion shown in Figure 6-2e (this cannot be confirmed since the image is not of high enough resolution). The depths of each of the 12 damage initiating inclusions are presented in Figure 6-3, as well as their mean depth, which was found to be 186 μm .

These findings prove that damage was being caused under the above stated impact conditions and that further testing could be designed to find thresholds of the level of contact stress and number of impact cycles at which the damage first appears. The damage found was not dissimilar to separation damage found in Chapter 5 (see Figure 5-9). Since the damage was not particularly extensive in the tested specimens, it seemed logical to expose specimens to higher impact numbers and contact pressures, to generate higher levels of subsurface damage.

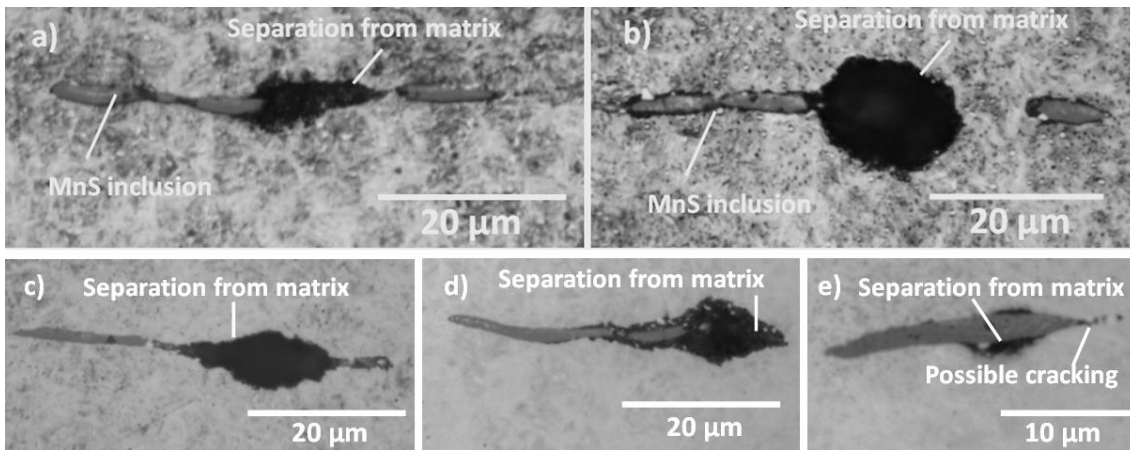


Figure 6-2: Examples of damage initiation at MnS inclusions during initial tests: a-b) specimen 1, c-d) specimen 2, e) specimen 3

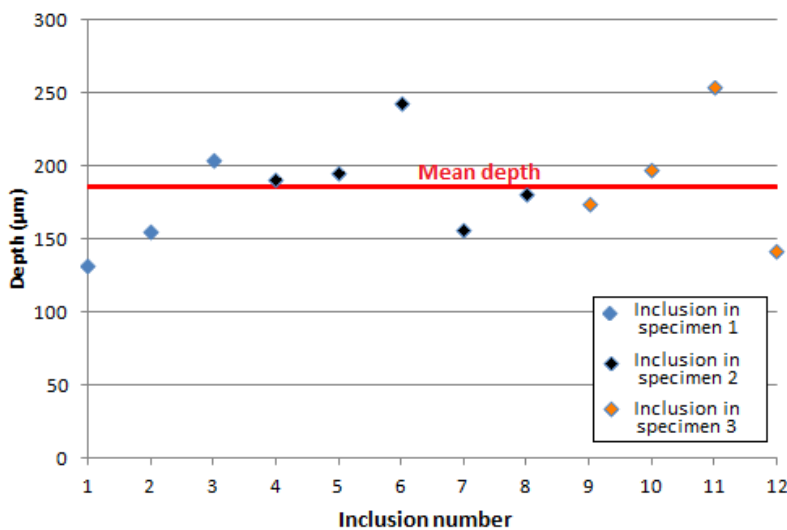


Figure 6-3: Depths of damage initiating inclusions found in initial impact tests

6.2. Test 1: Varying number of impacts at contact stress of 2.60 GPa

Specimens 4-9 were exposed to a maximum subsurface equivalent stress of 2.603 GPa; the maximum that the rig was capable of inflicting. The number of impacts was increased from 12,500 to 200,000 with higher impact numbers applied each time; test details are given in Table 4-8. The purpose was to observe what effect the number of impacts had on the quantity of damaged inclusions within the specimens. After observation, it was clear that damage at MnS inclusions was sensitive to the number of impacts experienced. Many inclusions were found to have separated from the steel matrix, examples of which are shown in Figure 6-4. Figure 6-4e clearly shows crack initiation from the inclusion tips. Figure 6-4c shows an inclusion that appears to have internally cracked along its length, which may be affected by the presence of a possible oxide part (only identified by its visual appearance since it could not be found with the SEM after sample had been repolished). Damage was considerably more common in the specimens that had been exposed to higher numbers of impacts. At least four inclusions had initiated damage for samples that had been exposed to over 50,000 impacts. One damage initiating inclusion was found in the specimen that had been impacted 25,000 times and none were found on the sample with 12,500 impacts. These results, along with the depths that inclusions were found at are summarised in Figure 6-5 and suggest that separation of inclusions from the matrix is very much dependent on the number of impacts experienced.

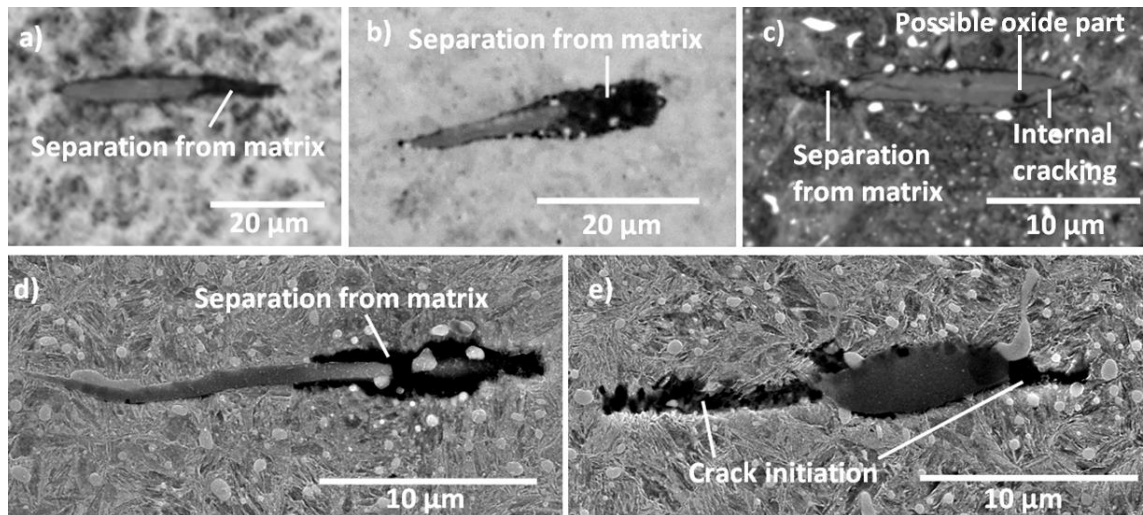


Figure 6-4: Examples of damage at MnS inclusions during varying number of impact tests a) 50,000 b-c) 100,000 d-e) 200,000

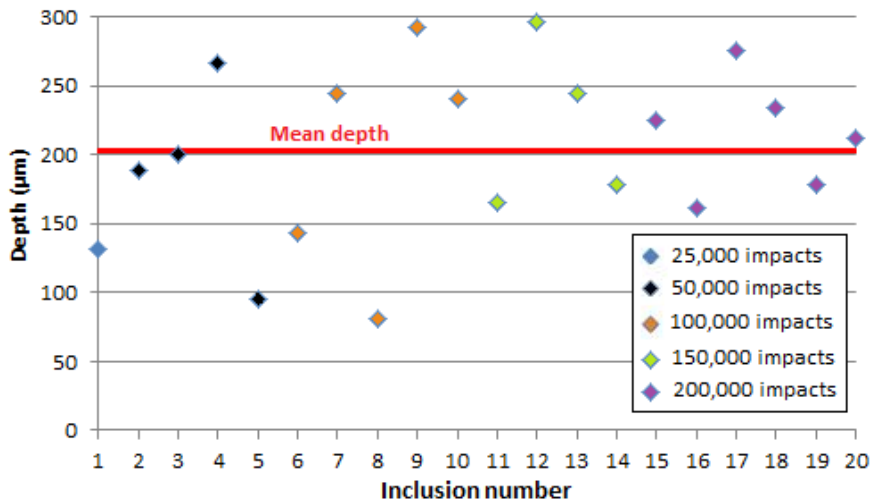


Figure 6-5: Depths of damage initiating inclusions found in varying number of impacts testing at 2.603 GPa (25,000 – specimen 5, 50,000 – specimen 6, 100,000 – specimen 7, 150,000 – specimen 8, 200,000 – specimen 9).

6.3. Test 2: Varying level of contact stress

Specimens 10-14 were impacted 50,000 times, a quantity that was determined to be above the threshold required for subsurface damage to initiate by observing the damaged samples from Test 1. The maximum subsurface equivalent stress was changed from 2.15 GPa to 2.60 GPa by altering the impact velocity (test conditions are presented in Table 4-8), to investigate the effect that changing this factor had on the resulting damage. Five examples of damaged inclusions found during varying contact stress tests are presented in Figure 6-6. The most common form of damage was, again, separation from the steel matrix. However, short cracks were initiated on some inclusions, as shown in Figure 6-6a and d, and that the inclusion in Figure 6-6d appears to be internally cracked. Figure 6-7 shows the depths at which each damaged inclusion was found, as well as their mean depth of 193 µm. There seems to be a threshold for damage initiation above subsurface equivalent stresses of 2.48 GPa, since no damaged inclusions were found at lower contact stresses. This is investigated in more detail in section 6.5.

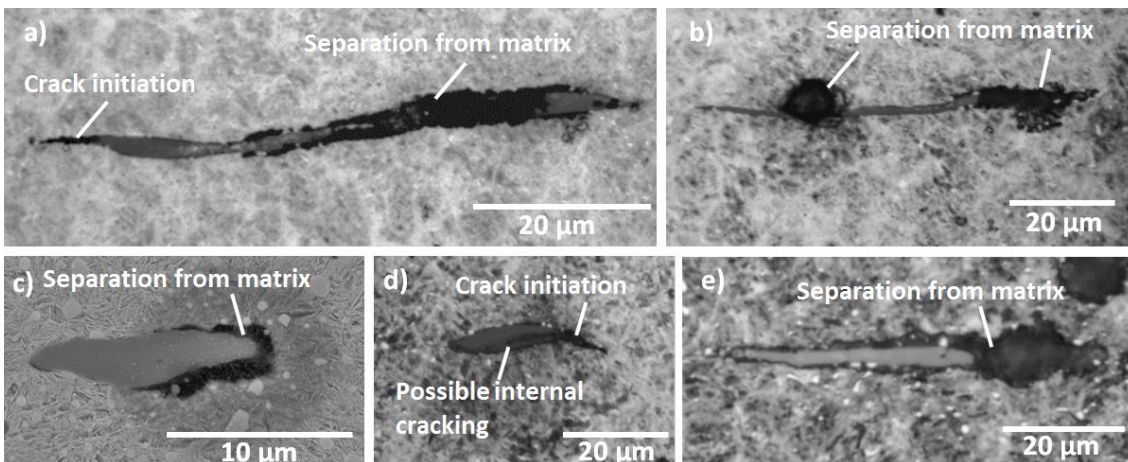


Figure 6-6: Example of damage at MnS inclusions during tests when subsurface stress was altered (a) 2.48 GPa (b) 2.60 GPa. c-e) 2.56 GPa

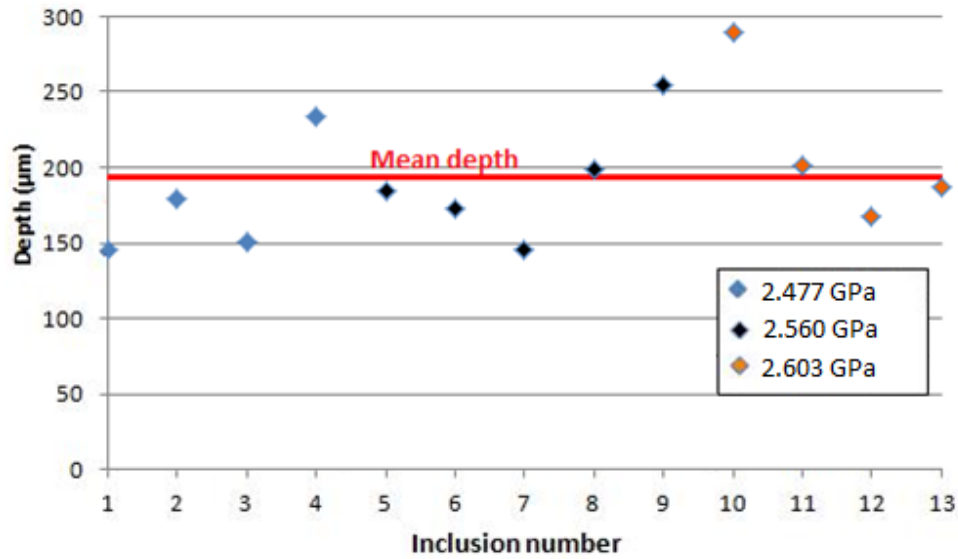


Figure 6-7: Depths of damage initiating inclusions found in varying contact pressure impact tests (specimen 12 - 2.477 GPa, specimen 13 - 2.560 GPa, specimen 14 - 2.603 GPa).

6.4. Test 3: Varying number of impacts at contract stress 2.48 GPa

The results from test 2 showed that levels of equivalent stress above 2.477 GPa caused damage at MnS inclusions. It was decided to run another set of tests with varying numbers of impact, to see the effect at lower contact stresses. The same range of impact cycle numbers as test 1 was used, at contact stresses of 2.477 GPa. Similar damage as the previous tests was identified at inclusions, although it appeared that in general, the separated area may have been smaller than at higher contact stresses. Examples of the damage found are presented in Figure 6-8 and the depths of the damaged inclusions, in Figure 6-9. It is clear that at this lower contact stress level, that after 50,000 impacts, the inclusions that are likely to initiate damage will probably have done so, since there did not seem to be an increase in the number of damaged inclusions when the number of impact cycles increased. This threshold appears also to be true for the results from test 1, since although a single damaged inclusion was found in the 25,000 impact cycle test, at least four damaged inclusions were found in each of the tests exposed to at least 50,000 cycles. Damage thresholds are discussed in more detail in the following section.

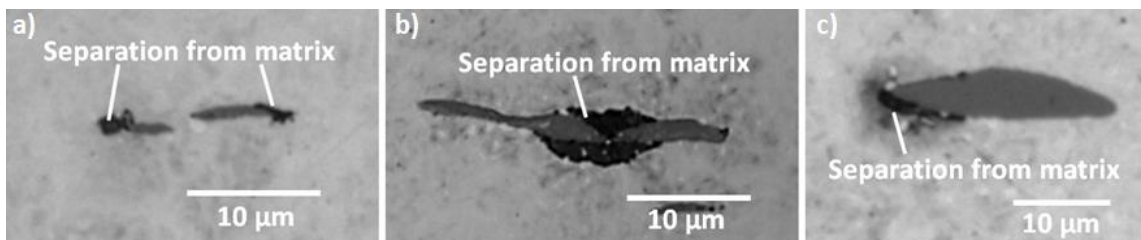


Figure 6-8: Examples of damage at MnS inclusions during varying number of impact tests a) 50,000 b) 100,000 c) 200,000

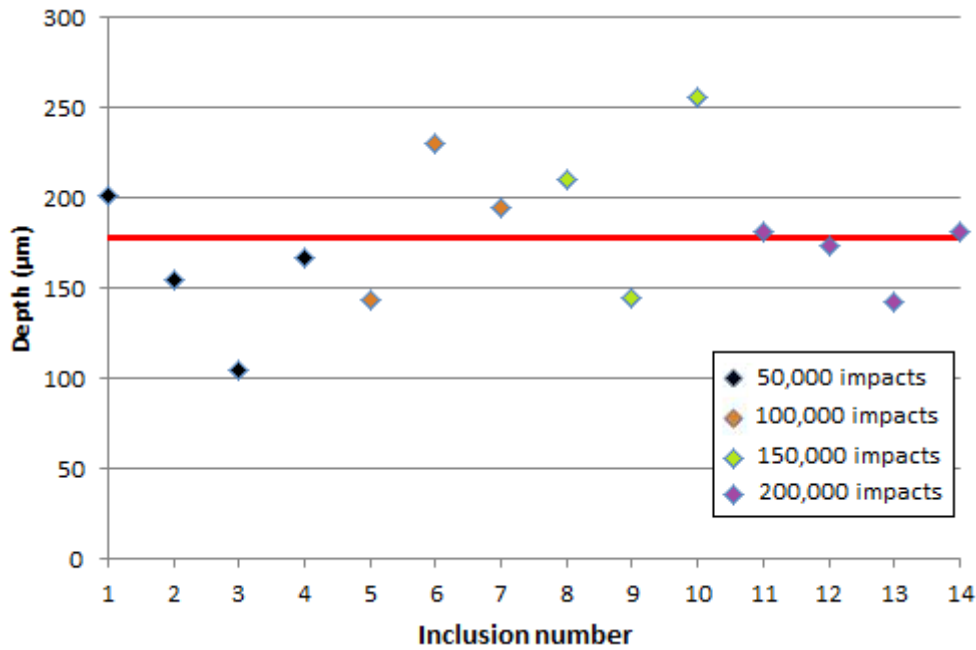


Figure 6-9: Depths of damage initiating inclusions found in varying number of impacts testing at 2.477 GPa (50,000 – specimen 17, 100,000 – specimen 18, 150,000 – specimen 19, 200,000 – specimen 20).

6.5. Identification of damage thresholds

The results from the initial tests and tests 1-3 allowed the identification of approximate damage thresholds. Although these results should be treated with caution since they are based on a relatively small batch of sample data, they do begin to show levels at which damage can be expected to be found at MnS inclusion in bearing steel. Figure 6-10 displays the number of damaged inclusions identified at each tested condition. The shaded area highlights conditions in terms of the number of impacts and maximum equivalent stress from impact loading, at which damage was found. The damage found was mainly separation of the inclusion from the steel matrix; however some inclusions had also cracked internally and/or initiated cracking of the adjacent steel matrix. It can be concluded with confidence (since multiple damage initiating inclusions were found at each data point) that if the 100CrMo7-3 bearing steel specimens experienced at least 50,000 impact cycles causing a maximum equivalent stress of at least 2.477 GPa; then subsurface damage could be expected to occur adjacent to MnS inclusions. Since the average depths of the inclusions found were similar, no trends were obvious when comparing maximum stress experienced, with the depth of damaged inclusion. However, it can be stated that all inclusions found to initiate damage in the initial tests and tests 1-3 were found within a range of depths of 81-297 µm.

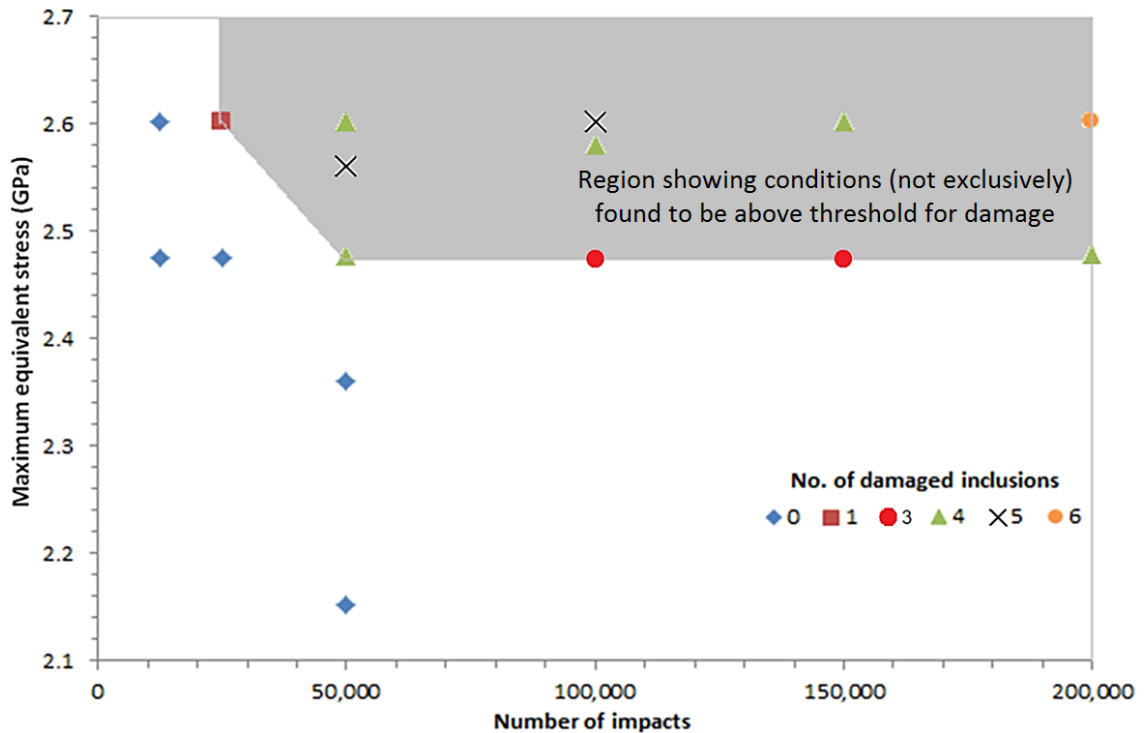
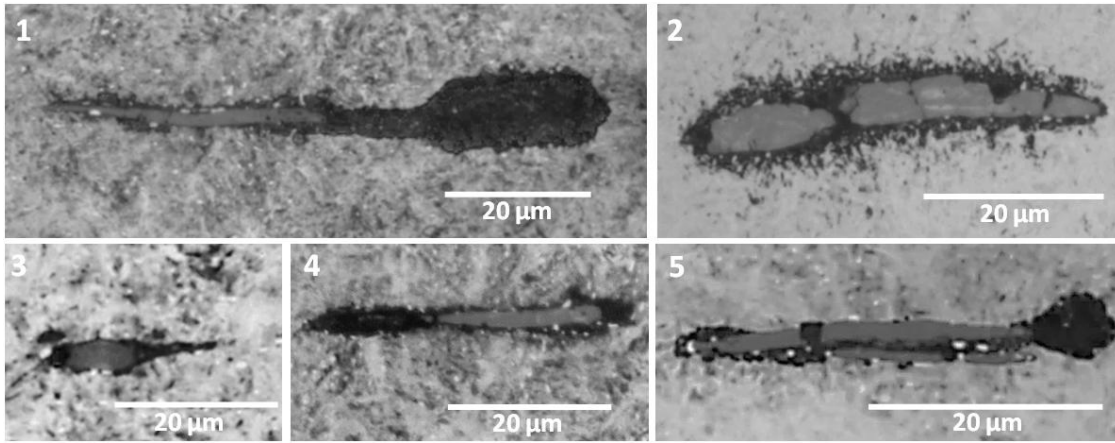


Figure 6-10: Number of damaged inclusions for each test when subjected to various testing conditions (note value of 4 damaged inclusions for initial tests is a mean of the 12 damaged inclusions from three specimens – plotted at 100,000 impacts and 2.560 GPa)

6.6. Test 3: Long term tests

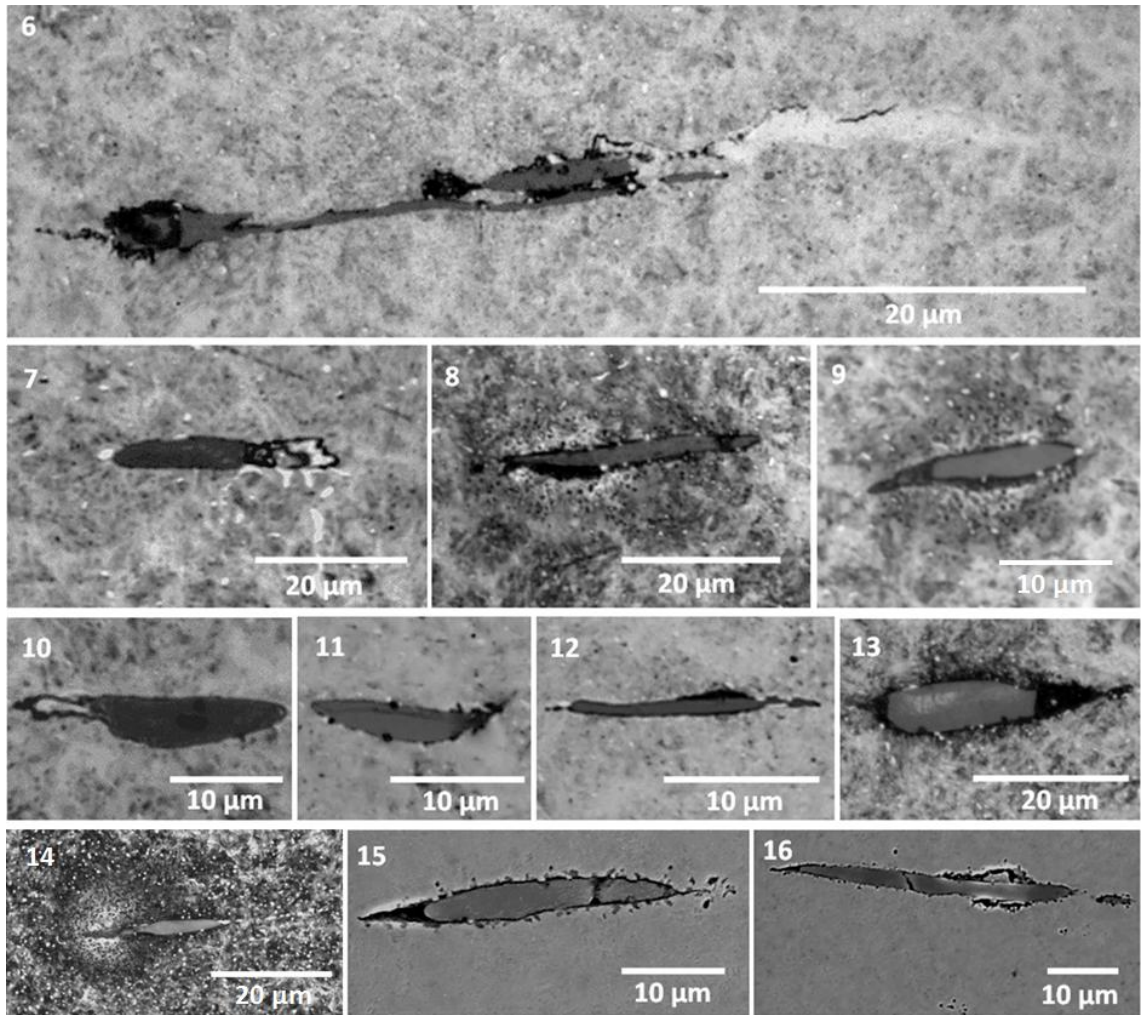
Six specimens were subjected to long term impact tests. Each was hit one million times at the maximum impact energy that the test rig could provide. Two specimens were impacted normally, perpendicular to specimen surface, and four, at an angle of 45 degrees from the raceway surface tangent in order to introduce surface traction. Table 4-8 summarises the described test schedule. Figure 6-11 displays images of damaged inclusions found at depths of up to 285 μm beneath the surface in samples 1 and 2. Major separation, cracking of inclusions and crack initiation has been observed. The table presented in Figure 6-11 describes the damage in more detail. In summary, although the damage in specimens 21-22 is fairly extensive, the location of the damage is fairly local to the inclusions and crack propagation has not occurred to any great extent. This is in agreement with the theory that Mode I loading may cause crack initiation and short growth, but some shear loading is required for further propagation.



Inclusion no.	Inclusion depth (µm)	Inclusion length (µm)	Comments
1	89	31	Major separation to right side. Possible that the inclusion continues off-plane through the centre of the separated area
2	130	37	Major break and cracking within inclusion, separation from surrounding matrix
3	144	8	Separation on left and right, crack propagation on right side
4	285	20	Separation and possible crack propagation on left side
5	95	32	Inclusion internally cracked, separation to left and right, significantly to right side

Figure 6-11: Example inclusions damaged under normal impact loading (specimens 21-22)

Figure 6-12 displays that significantly more damage was caused by sliding impact testing. Damage found in specimens 21-22 was found to a greater extent in specimens 23-26. A WEC was found on inclusion 6 and possible WEAs on a number of others. Inclusion 6 was situated directly below the impact site at a depth of 98 µm. It appears to have been internally cracked and broken up as well as initiating cracking in the bulk material from its tips and WEC formation from its right hand end. The WEA seems to have formed beneath a crack that has propagated from the right hand side. It is hypothesised that the increased levels of Mode II/III shear loading caused by the surface traction force were necessary to propagate the crack. The free surfaces created by the crack may then have rubbed against one another over thousands of shear loading cycles and caused the formation of the WEA.



Inclusion no.	Inclusion depth (μm)	Inclusion length (μm)	Comments
6	98	38	Break up of inclusion, separation, cracking to left and right, major WEC to right
7	93	19	Cracking and possible small WEA to right
8	243	29	Separation on left bottom of inclusion, WEA surrounding left side
9	201	13	Separation below, separation and possible crack initiation to left, WEA surrounding inclusion
10	290	17	Cracking and possible small WEA to left
11	111	12	Inclusion split along length, crack from right side
12	220	18	Small crack to left and possibly right, separation to top right of inclusion
13	106	18	Separation to left and right, crack initiation to right
14	194	18	Possible crack initiation to left, WEA to left
15	176	24	Inclusion split vertically, separation to left, crack initiation and possible WEA to left and crack initiation to right
16	178	67	Inclusion split vertically, separation above and below, crack initiation to left, possible WEA to top and bottom

Figure 6-12: Example inclusions damaged under sliding impact testing (specimens 23-26)

Crack initiation was found at a number of inclusions, examples can be seen on inclusion 6, 11, 15 and 16. Inclusion 11 is cracked along its length, similarly to many of the inclusions found in the sectioned failed planetary WTGB in Chapter 5. WECs and WEAs were only found adjacent to inclusions that had been exposed to compound tests, which suggests that the Mode II/III shear loading caused by surface traction is required for the propagation of WECs. Comparing the sizes of damaged inclusions showed no trend of damage with inclusion size. It appears that cracking can occur on inclusions of differing lengths (from 8 to 67 μm). It is the case that damaged inclusions of shorter lengths (around 20 μm) were more common than damaged longer inclusions (between 30 to 70 μm), however this is likely to be because shorter inclusions are more populous than longer inclusions in general. It is likely that proximity to the point of subsurface maximum equivalent stress is a more important factor than inclusion length itself. The importance of these factors will be thoroughly investigated by twin disc testing, described in Chapter 7.

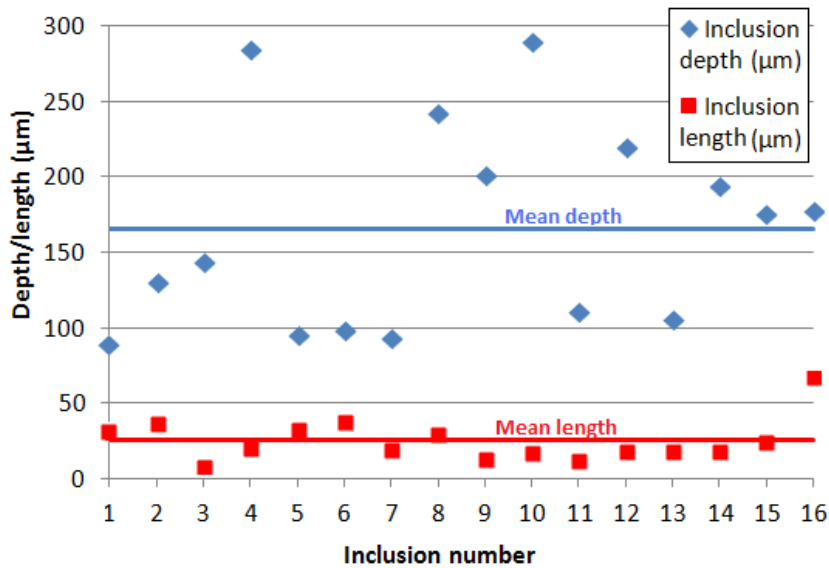


Figure 6-13: Long term impact test damage initiating inclusion lengths and depths (inclusions 1-5 from normal impact tests, inclusions 6-16 from compound impact tests)

6.7. Summary

A number of tests were carried out using a reciprocating hammer type impact rig, which was set up in order to induce subsurface yielding at stress concentrating manganese sulphide (MnS) inclusions. The effects of increasing surface contact stress and number of impact cycles, with and without surface traction, were investigated. Damage in the form of: internal cracking of MnS inclusions, separation of inclusions from the surrounding material, crack propagation from inclusions into the steel matrix and formation of WECs were recreated on bearing steel test specimens. It has been found that increasing the subsurface equivalent stresses and the number of impact cycles both led to increased damage levels. Damage was observed at subsurface equivalent stresses of above 2.48 GPa after at least 50,000 impact cycles. WECs were recreated during tests that applied surface traction for 1,000,000 impact cycles. Findings of this chapter support the hypothesis that hammering impact loading is one cause of premature WTGBs failure. The conclusions from this chapter will be summarised in section 8.1.3.

7. RESULTS FROM TWIN DISC ROLLING CONTACT FATIGUE TESTING OF 100Cr6 BEARING STEEL

Twin disc testing was undertaken using the Sheffield University SUROS rig, as described in section 4.5. Test length was limited to 200,000 cycles to investigate the effects of RCF at an early stage of the lifetime of a bearing. Specimens were pre-seeded with hammering impact damage in two locations, in order to investigate whether the damage propagated under RCF conditions. A number of other studies have been undertaken to investigate the effects of RCF on WTGBs using a twin disc machine, but to the author's knowledge, no study focussing on early stages of damage initiation, or investigating pre-seeded subsurface damage due to impact loading, has been undertaken. Discs were destructively sectioned, as described in section 4.1, then observed and the types of damage found were identified. Thresholds at which the tested discs first become damaged are identified before examining the depths at which damage occurred. Figure 7-1 shows the Thesis work flow chart.

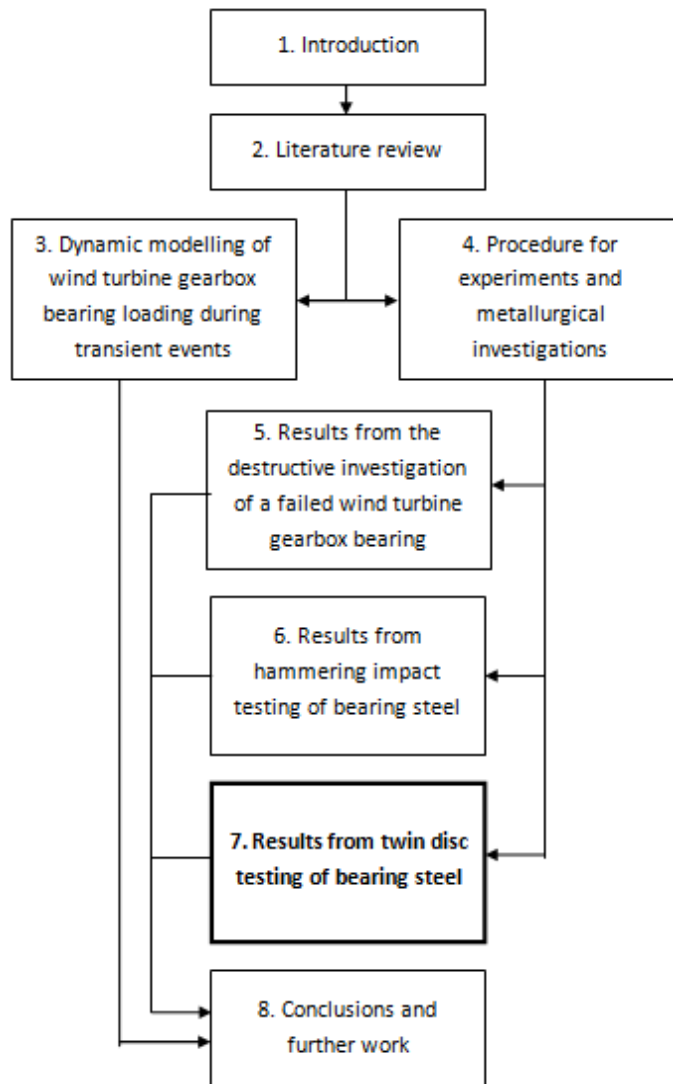


Figure 7-1: Thesis work flow chart

The chapter is split into the following sections:

- Section 7.1 describes the non-destructive examination of the tested discs, including their mass loss, surface profile and surface appearance.
- Section 7.2 describes the subsurface damage found after the tested discs were destructively sectioned.
- Section 7.3 identifies thresholds at which the damage first occurs, in terms of contact pressure and surface sliding levels.
- Section 7.4 examines the depth at which white etching areas were formed.
- Section 7.5 summarises the findings of this chapter.

7.1. Non-destructive examination of the specimens

Before and after testing, discs were weighed on a self-calibrating top pan balance ($\pm 0.0001\text{g}$ accuracy) in order to determine whether material had been removed during testing. Discs were cleaned in an acetone ultrasonic bath for ten minutes to remove any dirt or lubricant. Results showed that there was very little material removed during any of the tests and that the amount removed did not seem to vary much over the different testing conditions. The maximum amount of material removed was 8 mg and the minimum, was 2 mg. These low levels of mass loss suggest wear levels were low and that the tests were lubricated well.

Disc no.	1	2	3	4	5	6	7	8	9	10	11	12
Mass difference (mg)	-5	-4	-6	-8	-3	-4	-2	-5	-3	-4	-5	-7

Table 7-1: Mass loss from disc specimens representing bearing raceways during twin disc testing

After testing, the wear tracks left on the surfaces of the 12 disc representing raceways were examined using the optical microscope described in section 4.2.1. The images of the wear tracks are presented in Appendix F, Figure 9-18 - Figure 9-21. No signs of surface spall were observed so it can be said that the bearing steel had not "failed" by the definition in ISO 281:2007 [40]. No major surface damage was found, although small "strips" around the circumference showing signs of scuffing were apparent in the specimens exposed to the highest slip levels (5 and 10 %) at higher contact pressure levels (2.41 and 3.03 GPa) as shown in Figure 9-19 - Figure 9-20 in Appendix F. From these observations, it is assumed that if the steel surfaces examined were from operating bearings in the field, they would still be in operation and that any subsurface damage found would likely be at an early stage and unlikely to be surface-linked (as was the case for many of the crack networks found in the failed bearing in Chapter 5. As previously mentioned in section 4.5.3, there was no sign of the mark left by impact testing on the specimen surface.

7.2. Summary of types of damage found

The different types of damage found in the tested specimens are presented in this section independently of the testing conditions, which are summarised in Table 4-11. Links between the damage found and the testing conditions are discussed in section 7.3. All images in this section have been denoted by a lower case letter in the top right corner if from a circumferential section [c] or from an axial section [a]. In the following sections, it is indicated in the captions of Figures, whether or not the images are taken in the impact zone of specimens.

Under investigation, it soon became clear that the test specimens were significantly “cleaner” than the specimens used for hammering impact testing in Chapter 6 and the material in the failed WTGB sectioned in Chapter 5. MnS inclusions were orientated similarly in axial and circumferential sections, being close to parallel with the surface in axial sections, but at steeper angles, in the same direction in the circumferential. However, the variation was less obvious since inclusions were smaller and in general, less elongated and less steeply angled in the circumferential direction than those in the WTGB sectioned in Chapter 5. The fact that the tested steel was cleaner, with less non-metallic inclusions in its microstructure, meant that it was more difficult to find damage at inclusions, simply because there were less of them. Although this did prove the logical assumption that fewer inclusions in the steel results in lower levels of subsurface damage, it also meant that there was less chance of a specific location in the steel subsurface, containing damage initiation sites. As a result, fewer inclusions were found at hammering impact zones, and finding damage initiating inclusions at other points in the specimen was more difficult, since each specimen was prepared a number of times, in order to view different sections through the specimen and intersect more inclusions. This required the use of more material preparation equipment and was therefore more expensive and time consuming than preparing the specimens used in other tests as results presented in Chapter 5 and 6. Despite this difficulty, many damage initiating inclusions were found, although investigations would have been more efficient if steel with a higher inclusion density had been sourced for testing.

7.2.1. Subsurface initiated cracks

Subsurface cracks, which did not appear to have any link to the surface, were found in many of the specimens. Since sections are two-dimensional slices through the specimen, it cannot be confirmed that any of the presented cracks initiated subsurface or at the surface, but due to the horizontal direction and position under the point of impact of the crack propagation in Figure 7-2, the depth of the microcracks presented in Figure 7-3 and the presence of a likely initiating inclusion in Figure 7-4, these images are thought to show subsurface initiated cracking.

Figure 7-2 shows three nearby subsurface cracks, a few hundred micrometres in length, directly under the impact zone found in disc 11. The approximate position of the impact ball

has been superimposed onto the photograph to illustrate the scale of the ball in comparison to the cracks. Since the cracks are near to the surface, it seems likely that surface traction played a role in their initiation or propagation. These cracks were much longer than any found away from the point of hammering impact, the longest of which were of the order of tens of micrometres in length. The figure also displays a damage initiating pair of MnS inclusions at a depth of 668 μm , the depths of $\sigma_{v,max}$ and τ_{max} during RCF (435 μm and 485 μm respectively). This was the deepest damage initiating inclusion found in the twin disc specimens, which correlates with the deepest found in the sectioned wind turbine bearing (see Chapter 5), found at a depth of 625 μm .

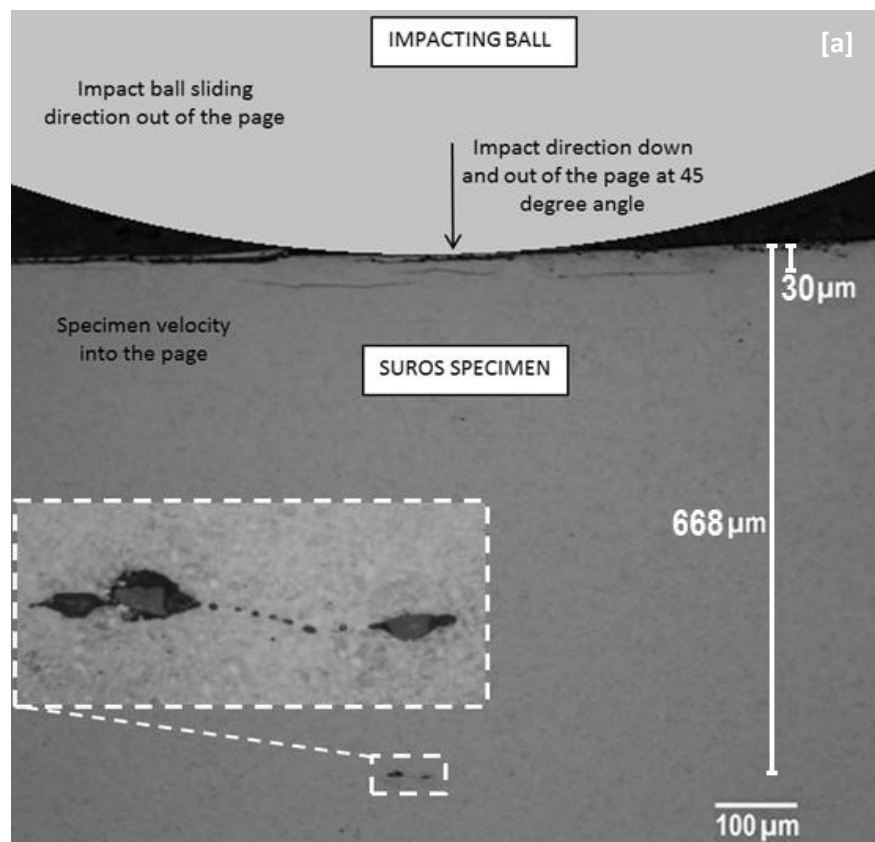


Figure 7-2: Subsurface cracks beneath impact zone of specimen 11, with approximate position of impacting ball superimposed

Figure 7-3 shows two small microcracks. Similar cracks were found in many of the specimens, above certain thresholds of surface sliding and contact pressure (discussed in detail in section 7.3). Figure 7-3a shows a short crack that appears to interact with a carbide on its left side, which may have contributed to its initiation. Figure 7-3b shows a possible WEA linked to a subsurface microcrack that was found in specimen 10 (2 % slip, 3.03 GPa contact pressure). It is possible that the crack and WEA may be linked to an MnS inclusion on another plane, however further sectioning did not reveal this, possibly because too much material was removed during the process. Both cracks were found at depths correlating strongly with that

of $\sigma_{v,max}$, at depths of 317 μm and 405 μm respectively. This compares to maximum stress depths in disc 7 of 347 μm , and in disc 12 of 435 μm .

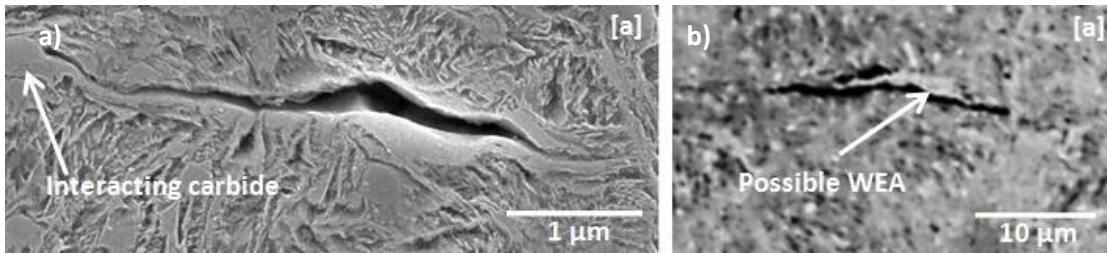


Figure 7-3: Subsurface microcracks: a) In specimen 7 at depth of 317 μm (not affected by impact) b) Suspected WEC in specimen 10 at depth of 405 μm (within impact zone).

MnS inclusions connected to extended cracks were found from a number of specimens, examples of which are given in Figure 7-4. Figure 7-4a shows a near surface MnS inclusion away from the impact zone, that appears to have initiated an extended crack from its left tip in the axial direction. Figure 7-4b shows a small MnS inclusion that was close (within 300 μm) to the centre of the impact zone, which is attached to a surface breaking crack from its left tip and a shorter crack from its right. It is not clear that whether the crack initiated at the inclusion, but it has certainly been affected by the inclusion, as the crack direction changes markedly in its vicinity.. It should be noted that the inclusion in Figure 7-4a was not confirmed as MnS by EDAX, since it could not be found again once the specimens were polished and etched for observation with the SEM after optical microscopy had taken place.

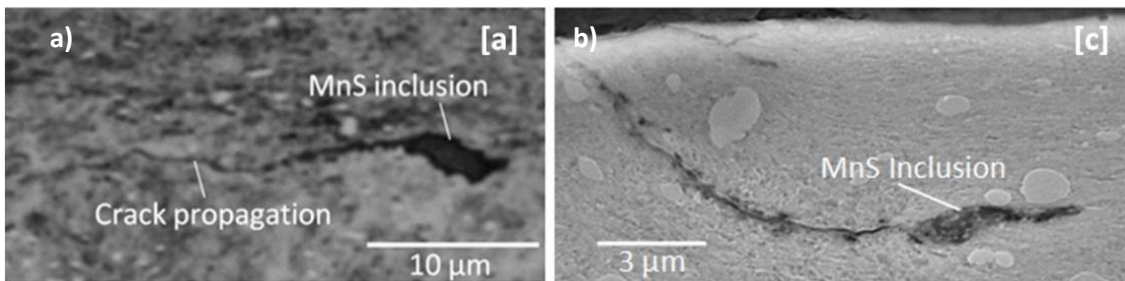


Figure 7-4: Extended cracking in: a) disc 4 (depth ~ 20 μm not affected by impact loading) (b) disc 10 (within impact zone)

7.2.2. Surface initiated cracks

Cracks that were linked to the surface were found in specimens that had been subjected to high slip and high contact pressure conditions. It is most likely that these cracks were initiated at the surface due to high levels of traction, although it is possible that initiation of some cracks may have occurred subsurface and propagated upwards. An example of such damage is displayed in Figure 7-5, from specimen 11, which experienced the highest contact pressure (3.03 GPa) and 5% slip.

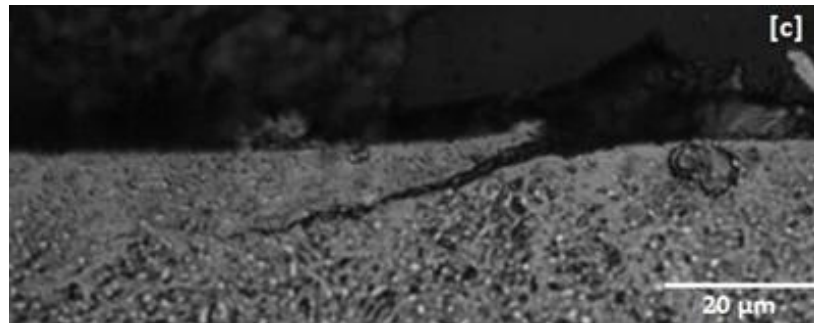


Figure 7-5: Surface cracking in specimen 11 (not within impact zone).

7.2.3. Separation and cracking at manganese sulphide inclusions

The creation of a free surface by separation of MnS inclusions from the surrounding steel matrix has been identified as an initiation mechanism for WECS. SUROS testing found that separation occurs to varying degrees at a wide of range of slip levels and contact pressures. Separated inclusions were populous at depths, under the impact zone of the specimens, near to the location of $\sigma_{v,max}$ and τ_{max} , which are shown in Table 4-11 and investigated further in section 7.3. Separation was found at MnS inclusion tips, above and below inclusions as well as completely surrounding inclusions, examples of which are shown in Figure 7-6. As previously discussed, it should be noted that etching can sometimes exaggerate separation damage, since etchant that gets stuck in the small void may cause acid damage to the specimen. It is thought, however, that no major damage was caused by the etchant in the figures presented below, since specimens were carefully washed after etching.

Separation from the tips of inclusions that spread into the surrounding material was found in specimens that had experienced high contact pressure and high slip, as shown in Figure 7-7. This wide separation that appears to spread from the inclusion tips into the steel matrix, may or may not be the same feature as the thinner cracks that have initiated from the inclusion tips shown in Figure 7-8. Figure 7-8 is believed to show the very first stages of cracking damage at MnS inclusions. This evidence backs up previous evidence that suggests cracking precedes the formation of WEAs at MnS inclusions. Similarly to the failed planetary WTGB in Chapter 5, many of the damaged inclusions were internally cracked, as shown in Figure 7-9. No clear differences between the impact damaged specimens and non-impact damage specimens exists, but in general, the damage does perhaps appear to be more extensive in impact damaged specimens.

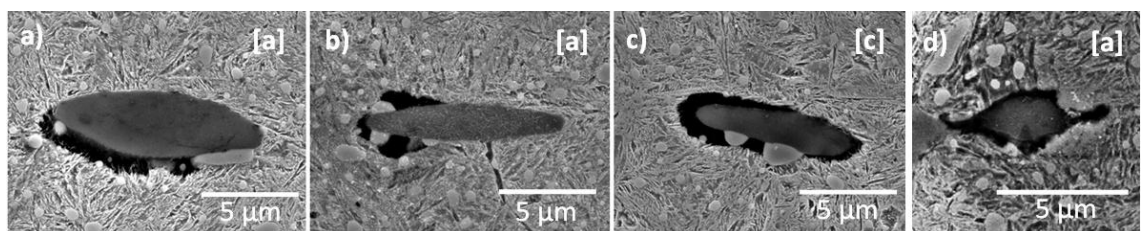


Figure 7-6: Separation around MnS inclusions in (a) disc 11* (b) disc 7 (c) disc 8 d) disc 12*. *specimens affected by impact loading

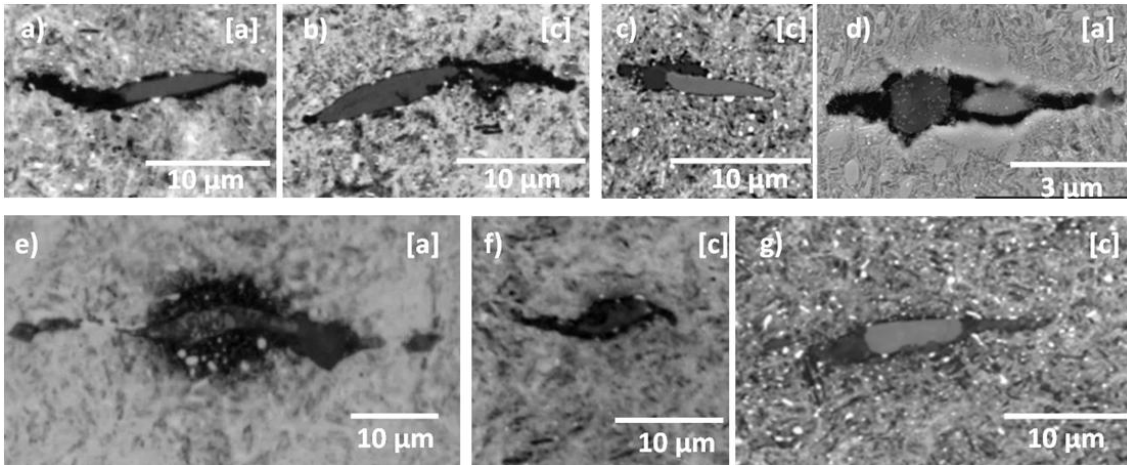


Figure 7-7: Separation from inclusion tips spreading into surrounding material in: a-b) specimen 10* c) specimen 11 d) specimen 7* e-f) specimen 8* g) specimen 4*. *specimens affected by impact loading.

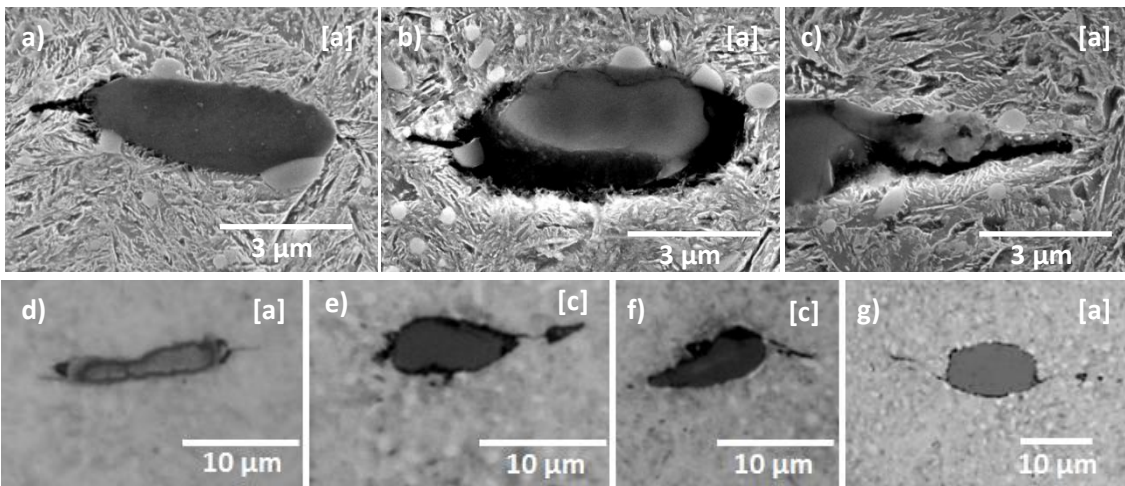


Figure 7-8: Cracking from MnS inclusion tips in: a-b) disc 11* c) disc 10* d-e) disc 7 f) disc 8 g) disc 12. *specimens affected by impact loading.

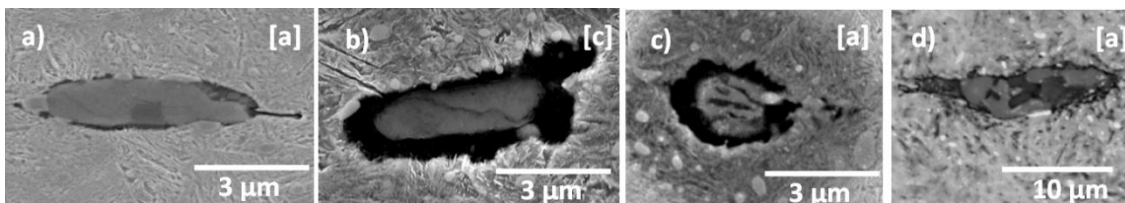


Figure 7-9: Internally cracked MnS inclusions in a) disc 7* b) disc 10* c) disc 8 d) disc 11. *specimens affected by impact loading.

7.2.4. WEAs and WECs at manganese sulphide inclusions

White etching areas were found adjacent to many inclusions in the higher slip and higher contact pressure specimens (slip and contact pressure thresholds are discussed in section 7.3). Many inclusions had initiated WEAs in their near vicinity as shown in Figure 7-10. In Figure 7-10h, the inclusion, which was closer to the surface and under the point of hammering impact in disc 12, appears to be separated from the matrix to the right of the inclusion, and linked to a surface breaking crack. A WEA has developed adjacent to the crack. It is not possible to state whether the crack was initiated at the surface or at the inclusion, although it seems very likely that it is inclusion initiated given the evidence presented in previous chapters. It is likely that more cycles would have initiated further damage here and led to material spall from the surface. Figure 7-10i shows a much deeper MnS inclusion, with an attached WEA, at just over 300 μm from the contact surface. There appears to be a horizontally propagating crack close by, which spreads to distances of as far as 70 μm from the inclusion. Other damage linked to the WEAs including internal crack, separation and crack propagation is displayed in the figure.

The damage presented in this section further proves that MnS inclusions are points at which white etching areas may initiate. Figure 7-10j, l and n, show WEAs attached to tips of internally cracked MnS inclusions, which are similar in appearance to many found in the failed WTGB discussed in Chapter 5. However, most inclusions appear to be significantly less damaged than those investigated in the failed WTGB and it is thought that the damage found in the twin disc specimens are at an earlier stage of failure. Again, the inclusions that are underneath the point of impact appear, in general, to show more extensive damage, particularly shown in Figure 7-1 h, i and j.

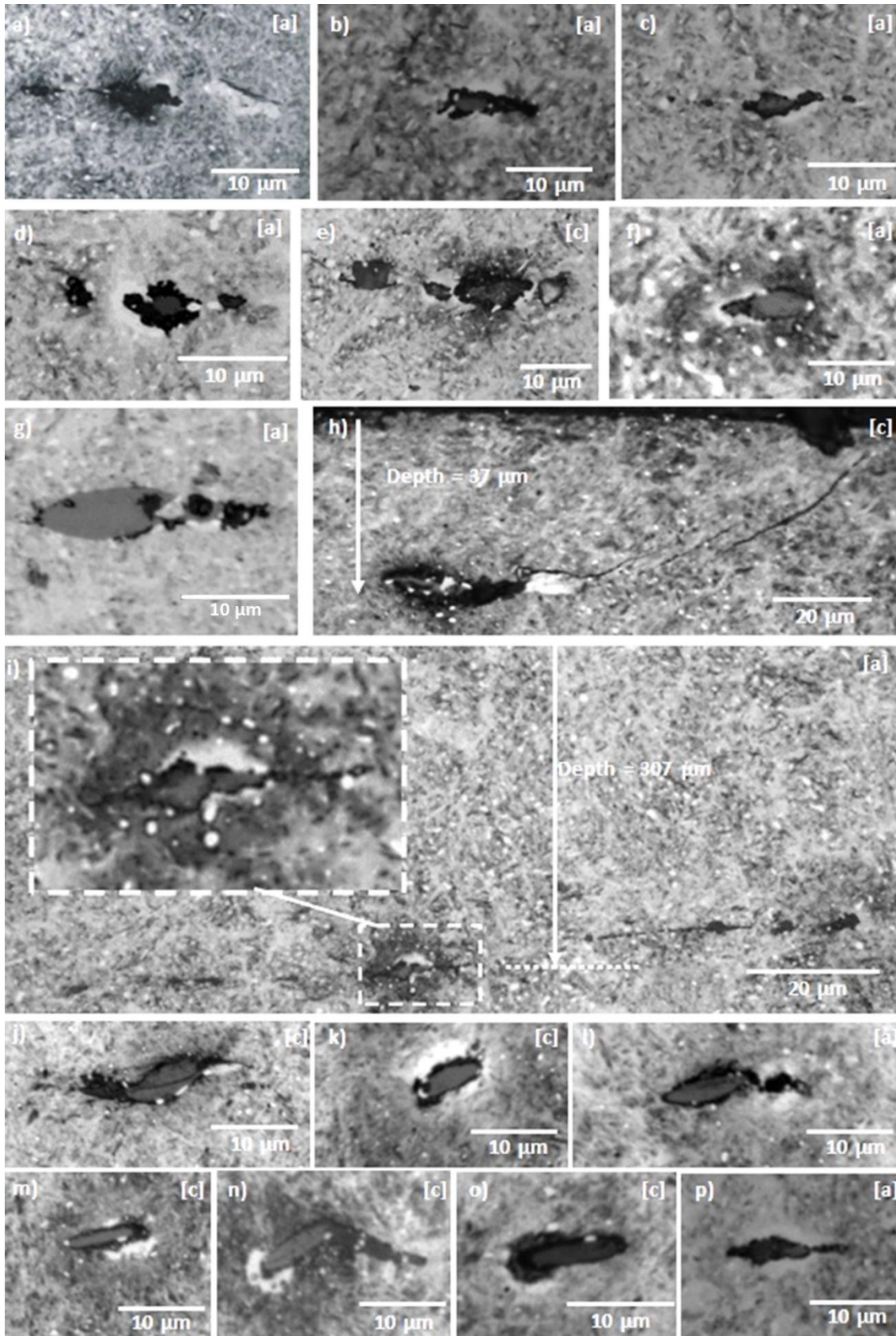


Figure 7-10: WEAs initiated at MnS inclusions in: a-b) disc 7*, c) disc 8, d) disc 7, e) disc 8*, f) disc 9*, g) disc 10*, h) disc 12*, i-k) disc 10 l-m) disc 11 n) disc 10* o) disc 12 p) disc 11*. *specimens affected by impact.

7.2.4.1. Damage at other inclusions types

Damage was found to a lesser extent at other inclusion types as presented in Figure 7-11. Image a shows the internal cracking of an alumina inclusion, which had not propagated into the bulk material. Image b shows what appears to be a very short microcrack propagating from the right side of a titanium inclusion. Image c shows what appears to be a small area of microstructural change and possible separation to the left of a second alumina inclusion. Image d shows microcracks propagating either side of a third alumina inclusion. These images show the most extreme damage found at non-MnS inclusions and it can therefore be stated that under the RCF conditions experienced, MnS inclusions were the most damaging.

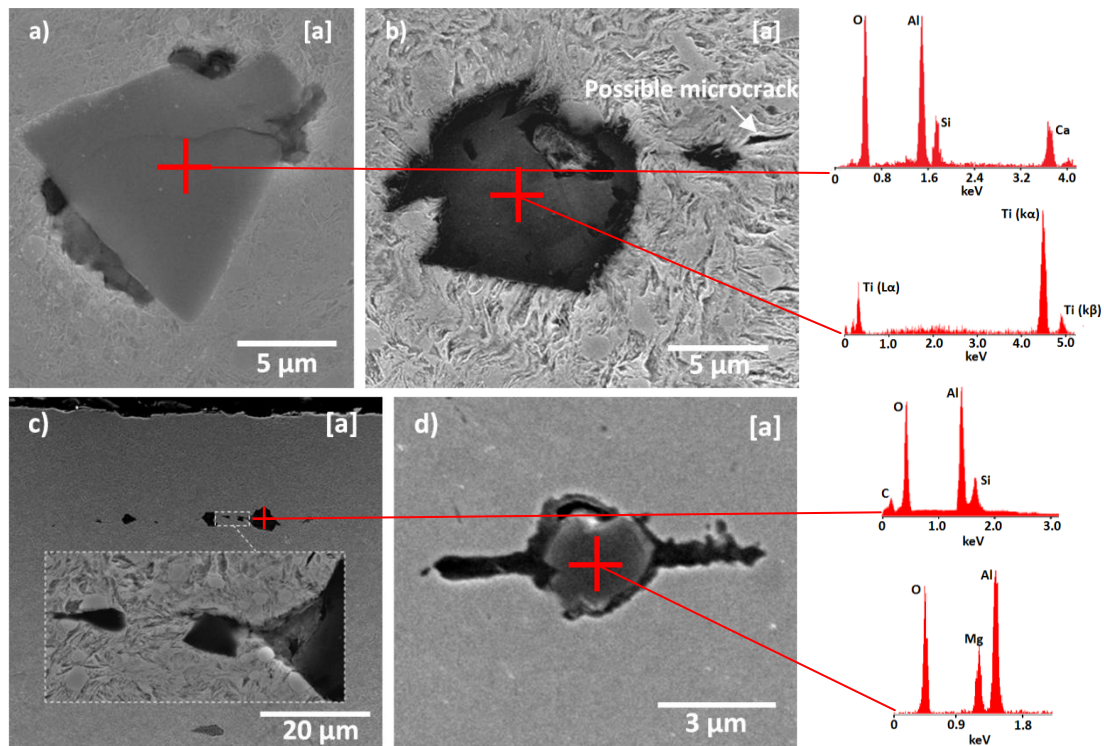


Figure 7-11: Damage at other inclusion types: a) internal cracking of alumina inclusion b) external microcrack connected to titanium inclusion* c) possible damage at alumina inclusion d) microcracks either side of alumina inclusion. *specimen affected by hammering impact.

7.2.4.2. Carbide elongation, break-up and crack initiation at carbides

As has been apparent with damage in the near vicinity of inclusions found in the sectioned WTGB, carbide accumulation was observed in the near vicinity of damaged inclusions. Figure 7-12 shows a very small (~3 μm in length) axially sectioned crack initiating inclusion, with an accumulation of carbides around 5 μm to its left. The image is taken underneath the point of impact on disc 8, which experienced the highest slip level (10%) at the second highest contact stress level (2.41 GPa). At this high level of magnification (20,000 times), it can be seen that carbides themselves may act as crack initiators. Carbides that have initiated cracking or have separated from the steel matrix are pointed out by white arrows in Figure 7-12. EDAX analysis

was used to identify the chemical composition of the labelled carbides in the figure. Four readings were taken; at position 1, an area of the bulk material was scanned, while at positions 2-4, point readings were taken at suspected carbides. Carbon, chromium and iron weight percentages at each location are displayed in the table included in the figure. The high wt% of carbon and chromium at positions 2-4 in comparison to that of the bulk material at position 1 identifies the carbides as iron-chromium (M_3C) type. M_3C carbides are normally spherical in shape, so it appears that a number of the carbides have been elongated in the direction parallel with the specimen surface, which is horizontal as viewed in the figure.

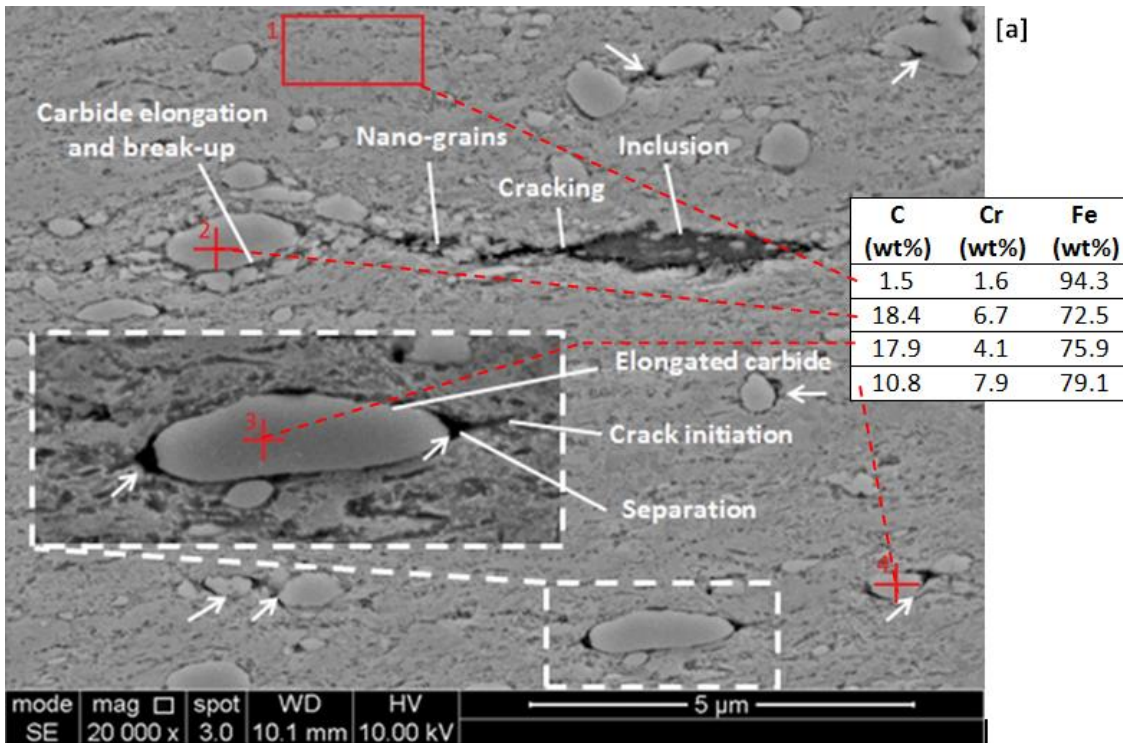


Figure 7-12: Damage at carbides in specimen 8

Further evidence of carbide related damage was found in many of the specimens as shown in Figure 7-13. Figure 7-13a appears to show cracking to the left and right of a relatively large carbide. Whether crack propagation has occurred or not, the image certainly shows an area of microstructural change at the location of maximum equivalent stress concentration around the carbide. Figure 7-13b shows a significantly elongated carbide just beneath the surface, with a small area of separation above it. Figure 7-13c shows the changes to carbides in an area of deformed material in the near vicinity of a stress concentrating inclusion. Carbides within the area of deformation are noticeably smaller in size, possibly due to the breakup of larger carbides under stress. Figure 7-14 displays how the interface between carbides and MnS inclusions can act as initiation points for crack formation, possibly due to their different strain behaviour from the bulk material under deformation. Further examples of elongated carbides are shown in Figure 7-15 and Figure 7-16, the latter showing significant separation along the top boundary.

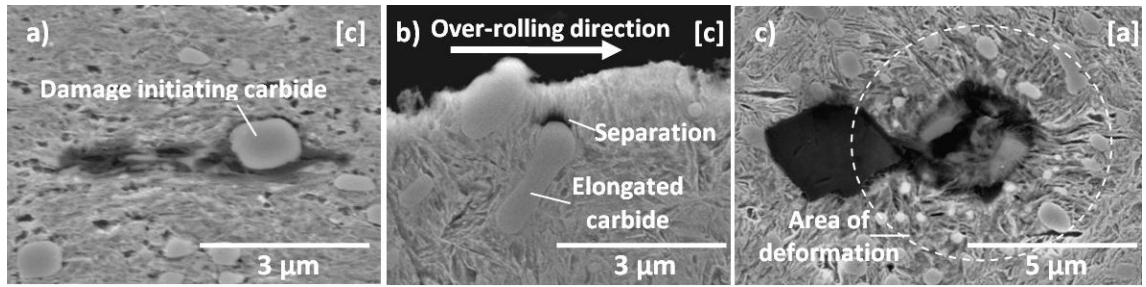


Figure 7-13: Carbide related damage in SUROS specimens: a) Possible cracking at spherical M_3C carbide in specimen 8, b) Separation at near-surface elongated M_3C carbide in specimen 12, c) Apparent dissolution of M_3C carbides at damaged area in close vicinity of stress concentrating inclusion in specimen 11.

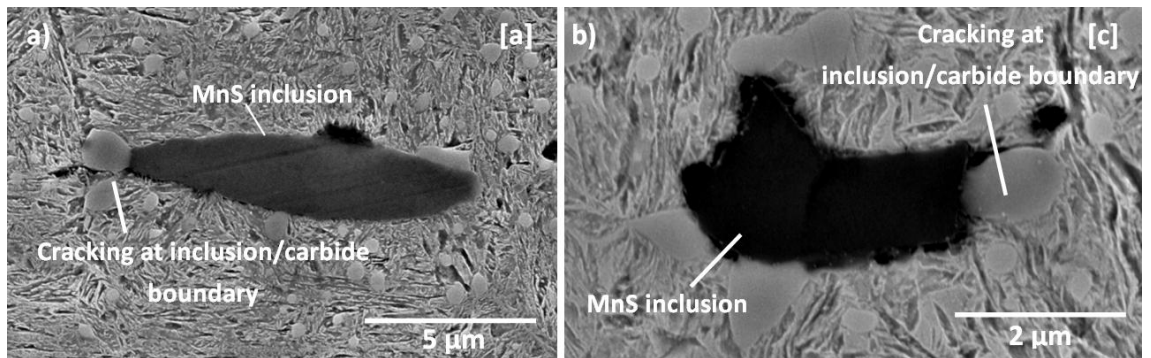


Figure 7-14: Separation around carbides adjacent to MnS inclusions in SUROS specimens: a) 8, b) 11

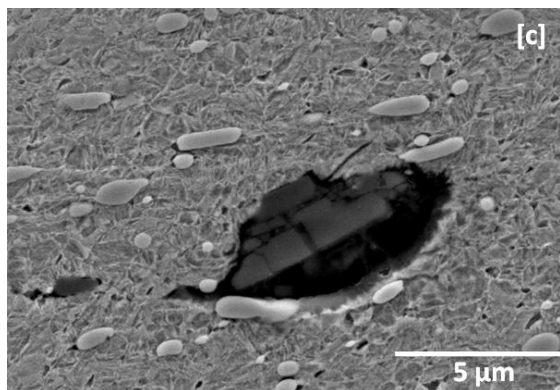


Figure 7-15: Elongated carbides around separated and cracked MnS inclusion in specimen 12

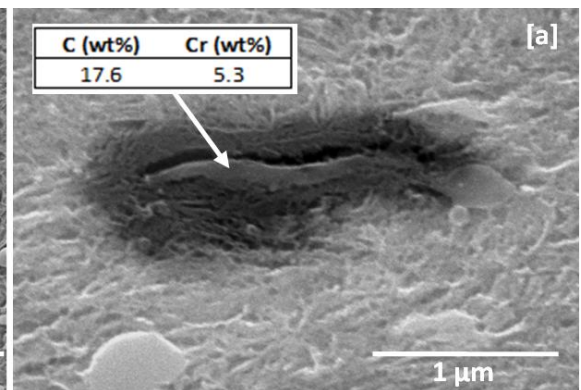


Figure 7-16: Severely elongated separated carbide under impact zone in specimen 11

7.2.5. White etching layer in failed test

Two specimens that were used as the leading discs (representing rollers) in tests 1-12 were tested again with the aim of exposing them to further fatigue cycles and longer term testing. After around 100,000 cycles, a bolt sheared and caused the keys holding the arbor on to the lower driveshaft to move out of place. The key began to rub against the bearing housing and caused the rig to heat up. When a small amount of smoke became visible, the fault was noticed and the rig was instantly shutdown but due to operator error the lathe was stopped a couple of seconds before the contact pressure was released, creating a short term application

of extremely high surface sliding. No lasting damage was caused to the rig and the results from this test were discounted for comparison to other tests since the specimen surface was significantly damaged. One of the specimens was, however, sectioned in order to examine the effects of short term high levels of surface sliding. This allowed analysis of the changed microstructure in the significant white etching layer that had formed. An optical image of the WEL as well as highly magnified images of inclusions and the WEL structure is shown Figure 7-17a. Figure 7-17b shows a circumferential section through the same WEL at a different location in the sample. Figure 7-17c and d display the difference between the martensite and the nanograin WEA microstructure. An SEM image of the same WEL at a different circumferentially sectioned location revealed significant cracking within the layer, as shown in Figure 7-18. The presence of the WEL under high slip confirms that high levels of sliding creates this WEA microstructure, supporting the hypothesis that sliding between free surfaces at subsurface cracks and at the separated inclusion/steel matrix boundary may be one cause of WEC formation. A larger area of the WEL was examined using the SEM and was found to be a chaotic, severely deformed region, with significant cracking, carbide dissolution and elongation, with major plastic deformation. An image of the damaged surface of the specimen is presented in Figure 9-21 in Appendix F.

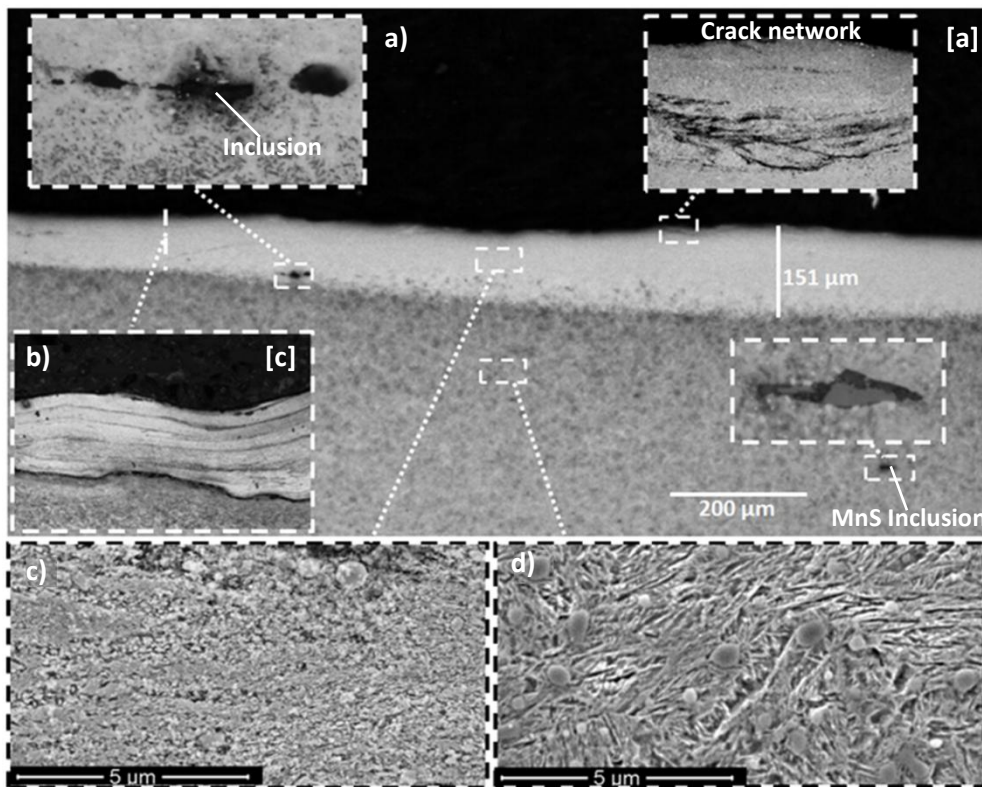


Figure 7-17: WEL formed in failed test showing a) axial section through disc b) circumferential section through disc (location in relation to axial section not accurate - only shown for illustrative purposes) c) WEA microstructure d) martensitic 100Cr6 steel microstructure

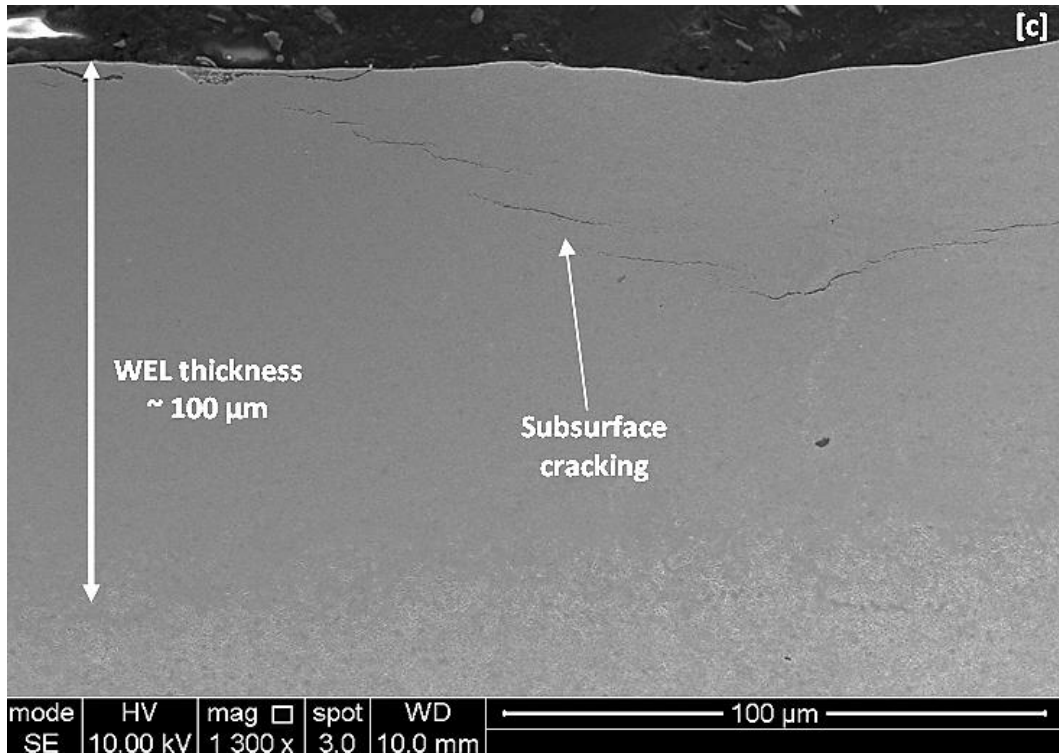


Figure 7-18: Cracking within WEL

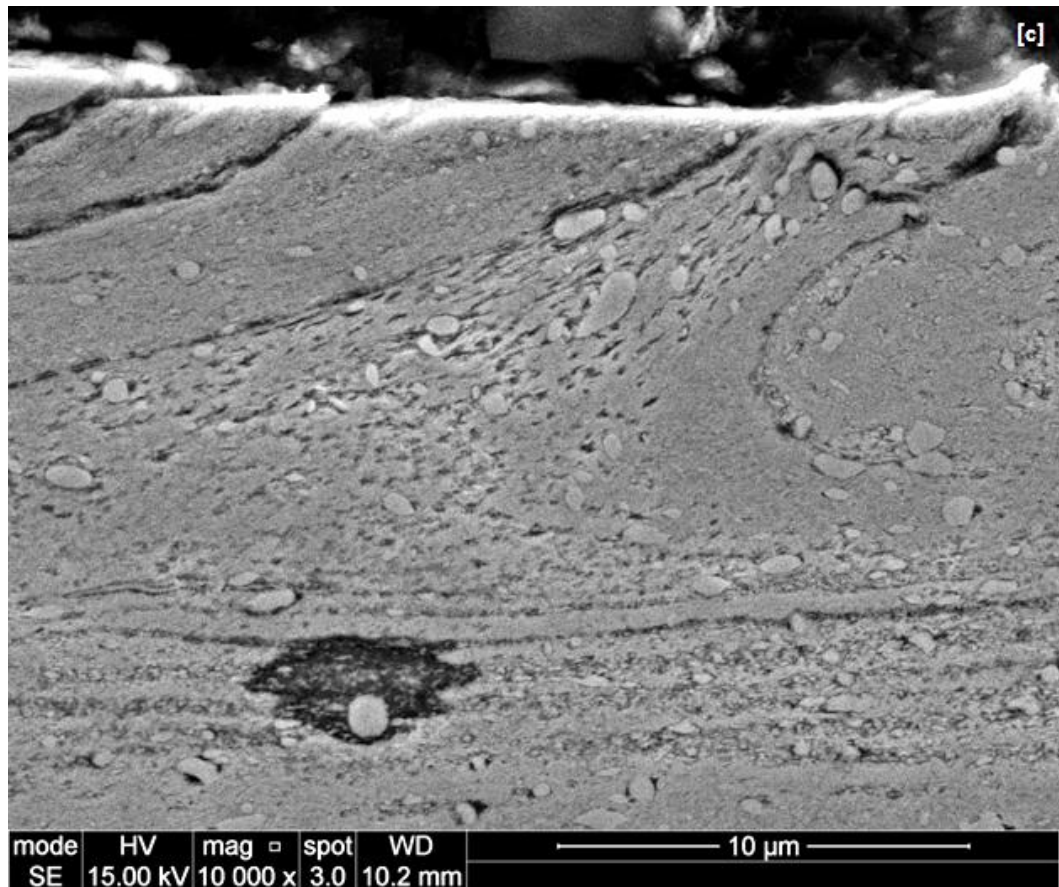


Figure 7-19: Variation of carbide size within WEL

7.3. Identification of damage initiating condition thresholds

Threshold levels of surface sliding and contact pressure have been identified at which the different types of damage were found to initiate at both: points where impact loading was used to pre-damage specimens; points away from impact damage zones. Figure 7-20 displays these thresholds by showing the lowest contact pressures and slip levels at which the damage was found. Figure 7-21 plots the thresholds in terms of contact pressure and traction coefficient rather than slip. Comparing results in this way allows the minimum required levels of different damage initiating factors, taking into account their combined effects, to be estimated. Mean traction coefficients at different slip levels and contact pressures are displayed in Table 4-12. It is proposed that any point to the right or above the plotted lines is above the threshold required to initiate damage. It is clear that increasing contact pressure, slip or traction coefficient within the ranges investigated, caused increasing levels of damage, so it is assumed that if a specimen has experienced damage at a lower contact pressure and slip level/traction coefficient, then it will do so at higher levels, even if that damage was not directly observed from the results of this study. Clearly, this figure should be used with caution as it cannot accurately predict the thresholds between data points and contact pressures below 1.79 GPa, which were not investigated in this study. Figure 7-20a and Figure 7-21a display the results for specimens that had been pre-seeded with impact damage, Figure 7-20b and Figure 7-21b displays results for those with no pre-seeded damage. Both figures show clearly that all forms of damage at MnS inclusions are sensitive to increased levels of contact pressure, slip or traction coefficient as well as to pre-seeded hammering impact damage.

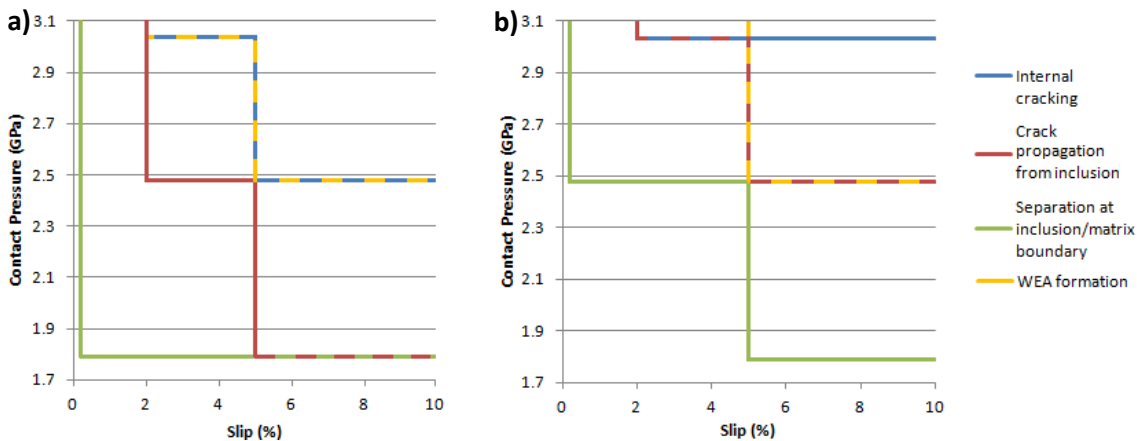


Figure 7-20: Contact pressure and slip (%) threshold identification for different forms of MnS inclusion initiated damage for: a) specimens pre-damaged with hammering impact loading b) specimens with no pre-seeded damage (overlapping thresholds indicated by dashed two-colour lines).

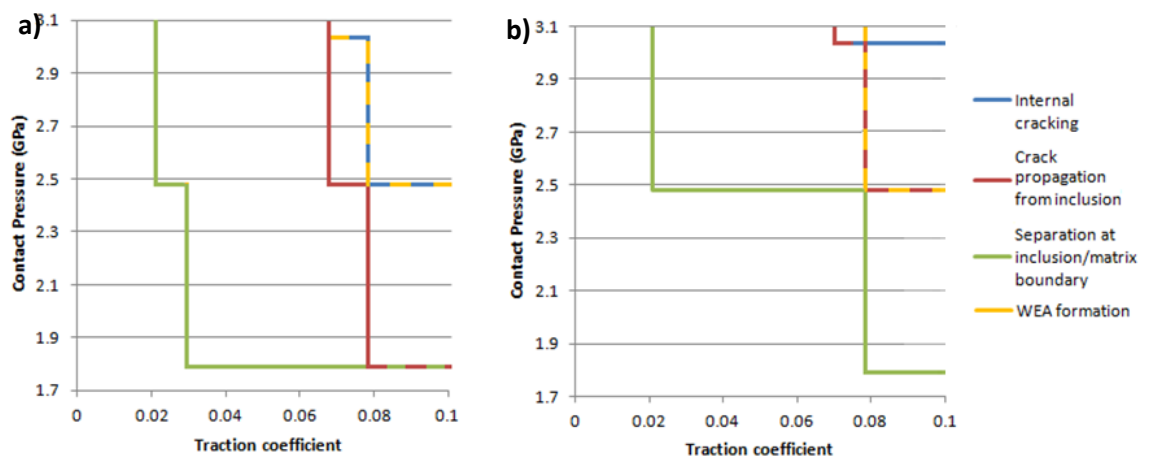


Figure 7-21: Contact pressure and traction coefficient threshold identification for different forms of MnS inclusion initiated damage for: a) specimens pre-damaged with hammering impact loading b) specimens with no pre-seeded damage (overlapping thresholds indicated by dashed two-colour lines).

All damage types were more extensive under higher contact pressures and higher traction coefficients (and slip percentages). Separation at inclusions occurred in all specimens, other than the non-impact damaged specimens in disc 1 (defined in Table 4-11), which experienced the lowest slip level and lowest contact pressure of all tested specimens. However, increased levels of traction above certain contact pressure levels were required for the separation to spread away from inclusion tips into the steel matrix as shown in Figure 7-7. This occurred at the lowest contact pressure (1.79 GPa), when the traction coefficient was above 0.079, as shown in Figure 7-2.

Inclusions that were internally cracked were not found at lower levels of contact pressure/slip so it is clear that the pre-seeded hammering impact damage was not extensive enough to directly lead to this form of damage. However, since internally cracked inclusions appeared at lower contact pressures of 2.48 GPa in the pre-damaged areas of discs rather than 3.03 GPa in the areas of no pre-seeded damage, it appears that hammering impact damage did perhaps weaken the inclusions within the impact zone. It is clear that this damage mode is affected by surface traction, since in both specimens that were pre-damaged and in those that were not, a traction coefficient threshold of around 0.07 appeared to exist, below which, no internally cracked inclusions were found.

Crack propagation from inclusion tips occurred at lower contact pressures and slip levels than inclusion internal cracking, which offers further evidence that the latter is not required to initiate the former. It was clear that the pre-damaged specimens had lower contact pressure and traction coefficient threshold for this damage mechanism, further backing up the hypothesis that hammering impact damage may accelerate damage of WTGBs.

As with the other forms of damage, WEA formation at inclusions only occurred above certain contact pressures and traction coefficients. WEA formation appeared to be less affected by the

hammering impact pre-damage, although at the highest contact pressure, it did appear at a slightly lower traction coefficient (0.070 compared to 0.079). Since only 16 WEAs were found at inclusions however (as shown in Figure 7-10), this result cannot be considered conclusive. It is possible that if further RCF load cycles had been applied to the specimens, the separated/crack initiating inclusions discussed above may have gone on to initiating WECs at the created free surfaces. In which case, it is likely that WEAs may have occurred at lower slip/contact pressure thresholds if the number of load cycles was higher. Evidence to support this hypothesis is presented in Chapter 6, since WEAs were only found in the long term hammering impact tests. WEAs were found at a variety of depths from the contact surface and the variation in the location that they formed is discussed in the following section.

Subsurface cracking appeared above contact pressures of 2.4 GPa and at lower contact pressures when the slip was increased to 10 %. Subsurface cracks were found to be slightly longer under the impact zone, although this result was not conclusive and may have been due to chance as well as over-analysis of IZ sites compared to non-IZ sites. Hammering impact damage seeding did not seem to affect the probability of a subsurface crack initiating in these samples. Surface cracking, perhaps unsurprisingly, was strongly affected by both the level of surface sliding and the contact pressure. All specimens that were exposed to 5 % slip or higher experienced surface cracking, which occurred at lower slip levels when the contact pressure was higher than 2.48 GPa.

7.4. Depth of WEA damage

The depth of each of the WEA initiating inclusions was investigated. Five were found in discs 7 and 8, which were exposed to the second highest contact stress (2.41 GPa), and 11 in discs 9-12, which experienced the highest contact stress (3.03 GPa). The depths of each of the WEA initiating inclusions are presented in Figure 7-22, together with the depths of the maximum shear stress concentrations, τ_{max} and $\tau_{0,max}$, as well as that of the maximum tensile equivalent stress, $\sigma_{v,max}$. As was previously discussed, one WEA initiating inclusion (Figure 7-10h) was very close to the surface, in comparison to the rest and was linked to a surface breaking crack. Since it cannot be proved whether the crack was initiated in the material subsurface or on the surface, it was decided to treat it as an anomalous result and to ignore it when calculating the mean depth of WEA inclusions in discs 9-12. The mean depths calculated from the other 15 WEA initiating inclusions are plotted in Figure 7-22. For both datasets; disc 7-8 and discs 9-12, the mean depth corresponded most closely with the maximum equivalent tensile stress, $\sigma_{v,max}$.

The limitations of these results include: that the depths of maximum stress are estimates, that do not take into account surface traction, and that the test sample sizes are fairly small, since only 16 WEA initiating inclusions were found. Nevertheless, the results are thought to be accurate enough to back up the hypothesis that was reached in previous chapters: that the

maximum equivalent tensile stress $\sigma_{v,max}$ is a key factor when considering the initiation of subsurface WEAs at MnS inclusions.

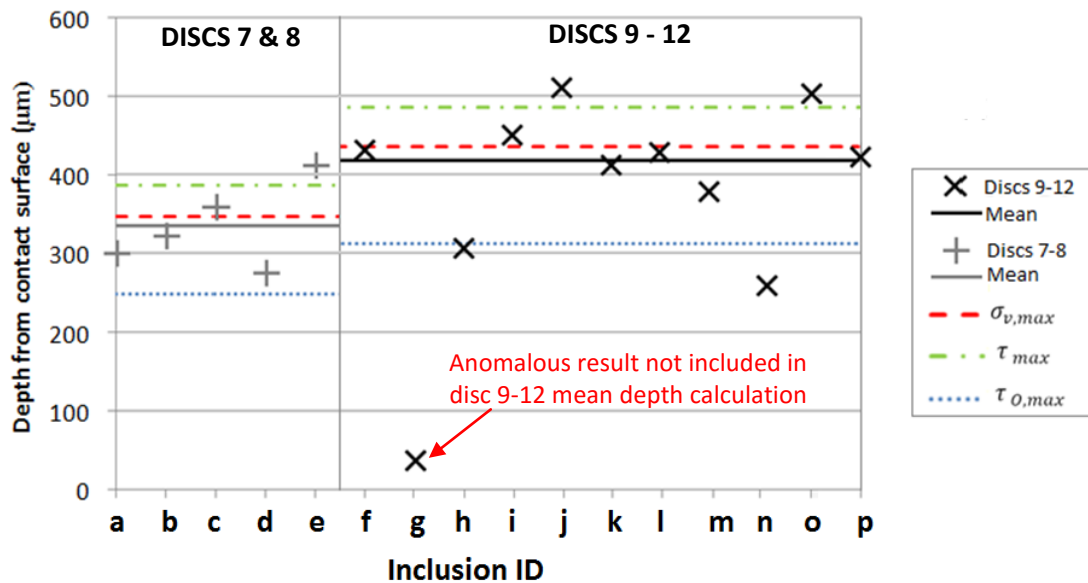


Figure 7-22: Depths of WEA initiated in twin disc testing with comparison to depths of maximum stress concentrations (inclusion ID letters correspond with image labels in Figure 7-10).

7.5. Summary

In summary, a significant number of sites where damage had been initiated were found within test specimens. Once again MnS inclusions were found to be the primary damage initiator in the bearing steel. In general, the main forms of damage at MnS inclusions were similar to those found in both failed WTGB discussed in Chapter 5 and hammering tested specimens in Chapter 6, namely:

- Separation of MnS inclusions from the matrix
- Internal cracking of inclusions
- Cracking propagating from the inclusion
- Development of WEAs in the near vicinity of inclusions

Other forms of damage included: surface linked cracking; subsurface cracking without any attached inclusion; carbide elongation and possible crack initiation at carbides; internal cracking and external cracking at other inclusion types. Damage was found both underneath points that specimens had been pre-damaged by impact loading and at points where they had experienced only RCF and surface traction. No major differences were found when observing circumferentially sectioned specimens compared to those that were axially sectioned. This may be because the damage found was at an earlier stage than that found in the failed WTGB and/or because the inclusion geometry varied less in the SUROS specimens. Additionally, a WEL was inadvertently created in a failed test at extremely high slip levels, showing that the

WEA microstructure is formed by high slip in 100Cr6 bearing steel and therefore supporting the hypothesis that subsurface rubbing of free surfaces may lead to the creation of WEAs/WECs.

All forms of damage occurred were more likely to occur in specimens that had been exposed to higher contact pressures and surface traction. Pre-seeding the specimens with impact loading, in general, accelerated the damage, allowing separation, internal cracking and crack propagation to occur at lower loads and slip levels. WEA damage was recreated by twin disc testing but was believed to be at a much earlier stage than in the WTGB. The depths at which the WEA damage was created corresponded strongly with the depth of maximum equivalent stress. Conclusions from this chapter are presented in section 8.1.4.

8. CONCLUSIONS AND FURTHER WORK

This chapter firstly summarises the contribution of this study to research. This will be followed by discussion of the main conclusions and findings from the work in this study before suggesting ways that the work could be expanded to achieve further understanding of the subject. Figure 8-1 shows the Thesis work flow chart:

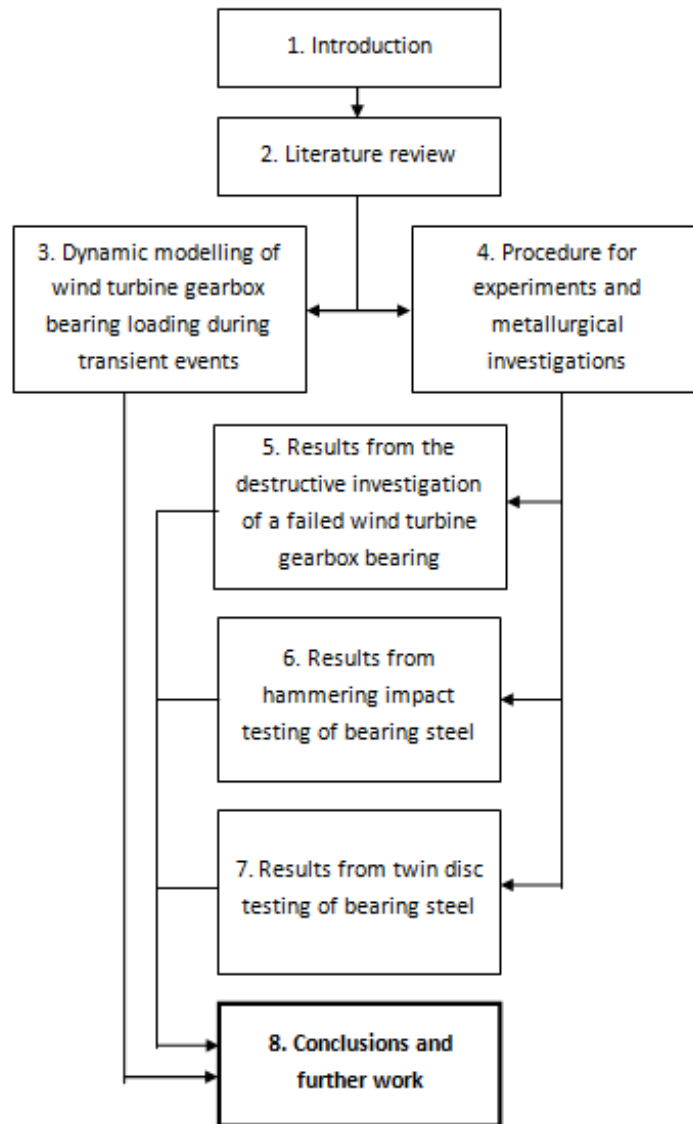


Figure 8-1: Thesis work flow chart

This chapter is split into three sections:

- Section 8.1 presents the key findings and contributions made by this study.
- Section 8.2 presents the main conclusions from the four main bodies of work completed.
- Section 8.3 suggests future work that could be carried out.

8.1. Conclusions

When starting this research project, the initial aim of analysing WTGB failure modes was fairly quickly focussed on the WEC failure mode, which, as was made clear from the literature review (Chapter 2), is generally thought to be the failure mode causing premature failure of WTGBs. The early stages of the work summarised in Chapter 5 (sectioning the failed WTGB) confirmed this and led to the study further focussing on WEC initiation and propagation from MnS inclusions. Dynamic modelling of a WTG (Chapter 3) highlighted that loading higher than designed levels is frequently experienced by WTGBs, which suggested that these loads were what is causing the premature failure of WTGBs. Testing was designed in order to prove this hypothesis, using a hammering impact rig and a twin disc machine to investigate the effects of changing contact pressure, surface traction and cycle numbers on the damage sustained at MnS inclusions in bearing steel. The main conclusions from this study are now discussed from the four main sections of investigations completed, as listed below. Finally, key research novelty and contributions arising from this study are summarised, from the combined conclusions of the four main work sections:

1. The creation of a multibody dynamic model of a wind turbine gearbox to calculate loading of the gearbox bearings (Chapter 3), published in [98].
2. The destructive sectioning investigation of a failed, low speed stage, upwind planetary wind turbine gearbox bearing leading to the creation of a database of damage initiating manganese sulphide inclusions (Chapter 5), published in [195].
3. Hammering impact testing of 100CrMo7-3 bearing steel specimens (Chapter 6), published in [196]
4. Twin disc testing of 100Cr6 bearing steel specimens (Chapter 7).

8.1.1. Conclusions from the dynamic modelling of a 750 kW wind turbine gearbox

A multibody dynamic model of a 750 kW wind turbine gearbox has been successfully developed, validated and used to simulate bearing loading under normal operation and manual shutdown conditions. Bearing loading variations in the time domain have been calculated and analysed. The model found that the gearbox bearings are undersized and recommended contact stresses were exceeded on four of the six analysed bearings:

1. It was found that during normal operation, the maximum contact stress on one of the planetary bearing inner raceways exceeded the maximum recommended level of 1,500 MPa by 1 %.
2. During the braking event in the wind turbine shutdown procedure, contact stresses in the planetary bearings exceeded the maximum recommended level of 1,500 MPa in all bearings and by a maximum of 15% in one of the bearings.

3. The upwind high speed shaft bearing *HSS-A*, experienced contact stresses 18% higher than recommended levels of 1,300 MPa during manual shutdown.

8.1.2. Conclusions from the destructive sectioning of a failed planetary bearing

Investigations of the subsurface damage in a failed wind turbine gearbox bearing found that MnS inclusions had initiated significant levels of damage. By observing and cataloguing the damage, the following conclusions were reached:

1. In the investigated failed WTGB, WECs were preferentially initiated at MnS inclusions ahead of other inclusion types. Four main forms of damage were found at MnS inclusions: internal cracking, crack propagation into the bulk material without an attached WEA, separation from the surrounding material, and WEC initiation and propagation.
2. The mean depth of MnS inclusions that had initiated WECs in the subsurface of the analysed WTGBs interrelated very strongly with the positions of maximum equivalent stress and maximum unidirectional shear stress. Since the majority of the 89 WEC initiating MnS inclusions (79.5% of catalogued inclusions) had WECs that propagate at shallower angles than traditional “butterfly wings”, it is hypothesized that the WECs have been initiated due to stress concentrations at inclusion tips at locations near to the maximum equivalent stress.
3. It was found to be more likely for a WEC to form at an inclusion that was not internally cracked (50% of catalogued inclusions), than one that was (29% of catalogued inclusions). It was found to be more likely for a WEC to form at an inclusion that was not separated from the surrounding material (51% of catalogued inclusions), than one that was (28% of catalogued inclusion). It should be noted that these results are from a small sample size of 112 MnS inclusions.
4. Neither internal cracking of inclusions nor separation of inclusions from the surrounding material occurred at inclusions deeper than $\sim 420 \mu\text{m}$ from the raceway surface, although WECs were found at inclusions as deep as $\sim 630 \mu\text{m}$.
5. Cracks propagating from inclusions tended to be longest when initiated by smaller inclusions of around 8-16 μm in length. This result is consistent with the findings of Evans et al. [23]. When viewed in an axial cross-section, longer WECs were found to have initiated from inclusions that were closer to being parallel with the raceway surface, than those that were more steeply angled. In general, cracking was more extensive in the axial direction than circumferentially, although damage propagated significantly in both directions.

8.1.3. Conclusions from the hammering impact testing of 100CrMo7-3 bearing steel

Having investigated factors affecting damage initiation caused by hammering impact loading at MnS inclusions in bearing steel and recreated white etching cracking at MnS inclusions, the following conclusions may be drawn. It should be noted that the conclusions were reached from a relatively small sample size and a limited study.

1. Damage was created at subsurface MnS inclusions in bearing steel by using a reciprocating hammering impact test rig at depths of up to 290 μm from the impact surface. Damaged inclusions were between 8 – 67 μm in length, but were most commonly around 20 μm long. Damage in the form of cracking of the bulk material and/or separation of the inclusion from the bulk material appears to preferentially occur at the point of lowest radius of curvature at the ends of the inclusion.
2. Increasing the number of loading cycles increased the level of damage caused, with increasing cycle numbers causing damage at a higher number of inclusions. Tests of over 50,000 impact cycles created damage at four or more inclusions in each tested sample and seemed to be a threshold for damage initiation.
3. The level of subsurface equivalent stresses correlated with the amount of damage caused, with higher stress levels causing damage at a higher number of inclusions. Tests of above 2.48 GPa consistently created damage at more inclusions and seemed to be a threshold for damage initiation.
4. Commonly observed damage features in wind turbine gearbox bearings, including the cracking of MnS inclusions along their length, the propagation of the cracks from MnS inclusions into the bulk material and the separation of MnS inclusions from the steel matrix, can be created by exposing bearing steel to many cycles (over 50,000) of normal hammering impact loading. The initiation and propagation of WECs; can be replicated by exposing bearing steel to many cycles (of the order of 1 million) of simultaneous hammering impact and surface sliding (compound impact) at subsurface equivalent stresses of approximately 2.5 GPa. It is hypothesised that surface traction is necessary for the formation of WECs due to increased cycles of Mode II/III shear loading.

8.1.4. Conclusions from the twin disc testing of 100Cr6 bearing steel

Having investigated subsurface damage in bearing steel specimens that had been exposed to twin disc RCF tests at a range of slip levels and contact pressures, some of which had been pre-damaged with 50,000 impact loading cycles, it can be concluded that all forms of damage increased with increased levels of surface traction, contact pressure and impact loading. More specifically, the following conclusions can be reached:

1. WEAs are formed adjacent to MnS inclusions in bearing steel that is exposed to RCF loading. WEAs were created in specimens that had experienced contact pressures above 2.48 GPa and at traction coefficients of above around 0.07. WEA initiation was more likely at higher contact pressures and levels of surface traction. 16 MnS inclusions were found to interact with WEAs, while no other inclusion type was found to have initiated any significant damage. The depth of inclusions that were attached to WEAs corresponded strongly with the depth of maximum equivalent stress ($\sigma_{v,max}$).
2. Three other forms of damage were also observed at MnS inclusions, namely; separation at the inclusion/steel matrix boundary, internal cracking of the inclusion and propagation of cracks from the inclusion tips. All three damage forms were more likely to occur at higher contact pressures and slip levels and were all accelerated by hammering impact loading.
3. A large WEL was formed under extremely high slip levels created in a failed test. This suggests that high levels traction between surfaces creates WEAs. It is hypothesised that subsurface rubbing of two free surfaces, either at a crack or at an area of separation between MnS inclusions and the steel matrix, may be one method of WEA/WEC formation.
4. Carbides were also found to have initiated cracking and created free surfaces at their boundary with the steel matrix. Carbides within the WEA creating in a large WEL were found to have been severely elongated, broken up and dissolved, supporting evidence that carbide dissolution occurs in WEAs.

8.2. Summary of research novelty and key contributions

Key finding from Chapters 5-7 are new to the field and allow the following novel conclusions to be reached. These conclusions are believed to be relevant to all WTGBs and WTGs that are similar to the "typical" designs discussed throughout this thesis.

1. It has been confirmed that WEC damage is more likely at higher contact pressures, load cycles number and surface traction. Findings suggest that there is a threshold based on a combination of all three that will determine whether a WEC will form or not. This threshold is also affected by the depth of MnS inclusions. Reciprocating hammering impact loading and twin disc RCF testing were used to investigate these thresholds and minimum levels at which different damage types at MnS inclusions were found are discussed in the previous section.
2. It has been shown that surface traction accelerates WECs formation in bearing steel and possibly is required for them to form. The results from both Chapters 6 and 7 confirm this, since WECs were only produced in tests with surface sliding on the hammering impact rig and at high slip levels on the twin disc rig. No WECs were found in specimens that had not experienced high surface traction. Although hydrogen has previously been found to accelerate damage, the results from this study prove that the presence of unusually high levels of hydrogen is not necessary for WEC formation. Since WECs were created using

CONCLUSIONS AND FURTHER WORK

compound hammering impact loading (simultaneous normal loading and surface traction), it has also been found for the first time that RCF is not the only method of forming inclusion initiated WECs.

3. It has been categorically proven that MnS inclusions are the most critical damage initiating inclusion bearing steel, since the results from Chapters 5-7 all provide extensive evidence that this is the case, using three different bearing steels that had been exposed to different loading cycles. It seems that MnS inclusion initiated WECs are generally not the same as "traditional" butterfly cracks that have crack (wing) propagation angles of $\sim 45^\circ$. It is suggested for the first time, that MnS inclusion initiated WECs are **not** necessarily the same feature as butterfly cracks. It is the author's opinion that this is a **vital** observation, since much research has been completed where inclusion initiated WECs have been presented as butterflies.
4. Evidence supporting a previous claim [23] that shorter MnS inclusions create more damage than longer, is presented, as well as a new finding that inclusions that are closer to parallel with the raceway surface create more damage in the bearing axial direction. This study also proves that despite previous findings, oxide parts are not necessary for cracks to be initiated at MnS inclusions (although it is not disputed that they may contribute in some cases). It has been proven too, that steel cleanliness is vital in reducing damage. However cleanliness ratings based on maximum inclusion size will not necessarily help in attempts to reduce WECs in WTGBs since smaller inclusions appear to be more damaging. Results from this study suggest that reducing the number of inclusions, particularly in the critical near-surface zone of around 0-600 μm depth from the raceway surface, will reduce the number of WECs initiated.
5. Evidence is presented supporting the hypothesis that the key contributing stress component, in terms of the Hertzian stress field, is the maximum equivalent (von Mises) stress, rather than either the orthogonal or unidirectional shear stresses. The fact that cracks found in Chapters 5-7 tended to propagate at close to horizontal angles, and that cracks have been observed to pulled open at the inclusion end prove that tensile mode I loading is present in the vicinity of MnS inclusions, possibly influenced by the residual stress field around the inclusion. Since surface traction certainly increases WEC damage, it can be inferred that crack initiation is due to Mode I loading and that further propagation is accelerated by Mode II/III shear loading, supporting the claims in [23, 48] and conflicting with claims in [190].
6. The possible damage initiated at MnS inclusions in WTGBs, have, for the first time, been categorised into four groups; separation at the inclusion/matrix boundary; internal cracking of the inclusion; crack propagation from the inclusion into the matrix (either from a free surface created due to separation or internal cracking); WEC propagation from the inclusions (at free surfaces caused by crack propagation or separation). It has been shown for the first time, that MnS inclusions do **not** need to be internally cracked to initiate WECs, which is different to the findings of [52, 109], although the findings in this study

agree that the internal cracking of inclusions certainly does lead to the initiation of some WECs. Evidence is also presented to suggest that oxide parts within inclusions are not necessary for damage to be initiated at MnS inclusions.

8.3. Further work

The aim of this section is to use the knowledge gained by the work completed in this study to suggest future work that could be completed to further contribute to the understanding of the premature failure of WTGBs. In addition to the additional work suggested below, the confidence in the results presented in Chapter 3 could be increased by undertaking a sensitivity analysis of the various assumptions made in constructing the gearbox model.

8.3.1. Possible research in relation to improving bearing steel

Perhaps the key theme throughout the chapters presented in this study is that manganese sulphide inclusions are the critical material defect that allows subsurface WECs to initiate. The author suggests the following further work to investigate their effects on bearing life:

1. A finite element analysis study of the effect of MnS inclusion properties on the different forms of damage. This would involve the development of a detailed model of a loaded bearing in a FEA programme, which would include MnS inclusions. The inclusion depth, length, width, orientation, shape and bonding to the steel matrix could be changed and the effects of changing these properties, under impact and transient loading conditions, on the resulting stress field investigated.
2. The development of a WEC resilient test specimen, perhaps for use on the SUROS machine, or another more modern RCF test rig. The author suggests that specimens could be made to include very small amounts of manganese sulphide, to greatly reduce the number of MnS inclusions.
3. If a novel method of bearing raceway manufacture could be used to ensure that the near surface region ($\sim 0-630 \mu\text{m}$) was free of MnS inclusions, it is thought that bearing lifetime could be greatly increased. Similarly, lifetimes could be increased if bearings raceways could be coated by an extremely well bonded layer of RCF resistant material. Black oxide coating has been cited as a material that increases WTGB lifetime [201, 202] and other materials could also be investigated. On the same theme, the testing of WEC resilient full size bearings on a test rig, or better, test drivetrain, such as the setup at NREL in the USA, or the National Renewable Energy Centre (NAREC) in the UK, would allow the more accurate testing of novel life-improvement methods to be investigated.

8.3.2. Possible research relating to mechanically redesigning WTGBs

It could be suggested that following the findings of this study and others, that it is clear that current materials are not capable of operating in the conditions that WTGB are exposed to.

CONCLUSIONS AND FURTHER WORK

Therefore the useful purpose of further research to determine the exact the nature of WEC related failures could be questioned - perhaps it is enough that we can now say for certain that it does occur under the conditions discussed in this report. An alternative method to solve the problem is to accept the possible reality that the current material used to make bearings is as good as it can economically be, and to change the design standards of WTGBs. This would involve the development of more accurate life estimation models, which can accurately predict WTGB lifetime, possibly using one of the following suggested methods:

1. Testing a large number of WTGBs to failure on test rigs that apply transient loading conditions measured from a real WT, which would be a time consuming and expensive process. This direct testing method of bearings under different loading conditions was how the current design standard was developed by Lundberg and Palmgren [41, 42]. Extensive testing could lead to the development of a new standard, specifically designed for use with WTGBs.
2. If manufacturers, researchers and WT operators could come to a collaboration agreement, where the monitoring of WTs and the subsequent investigation of WTGBs could be completed on a much wider scale than the single bearing investigated in this report, perhaps a more accurate way of predicting WTGB service life could be developed based on statistical failure rates of bearings operating in different WTGs.
3. Conducting further tests on a twin disc machine, where test specimens are run to failure at a wide range of conditions representing WT transient loading. A transient loading "curve" could be developed where the load varied proportionally to measured torque data over a long period of operation time from a real wind turbine. The magnitude of the torque curve could be changed in steps (keeping load sequences the same), which would represent altering the geometry of bearing component sizes (and load bearing capacity) to change the contact pressure between raceway and roller. This could potentially find a new threshold maximum contact pressure that bearings can safely experience, to replace that presented in [18].

Alternatively, another way of solving the problem of WTGB premature failure would be to attempt to remove the transient loads that lead to bearing impact loading and overloading. One possible solution would be the development of a transient torque removing component to be included in a WT drivetrain that could remove the extreme loading and allow WTGB to operate in more typical bearing operating conditions. It may be possible to invent a torque-transducer component in the form of a "clutch" that removed loading peaks during high torque transients.

REFERENCES

1. E. Rounding, Destructive investigation of a failed wind turbine planetary gearbox bearing (Masters Dissertation), University of Sheffield, 2013.
2. European Wind Energy Agency, The European Wind Initiative 2013 [online]. Available: (<http://www.ewea.org/publications/reports/the-european-windinitiative-2013>), 2013.
3. P. J. Tavner, J. Xiang and F. Spinato, “Reliability analysis for wind turbines”, *Wind Energy*, 10(1) (2007), 1-18.
4. J. Ribrant and L. Berting, Survey of failures in wind power systems with focus on Swedish wind power plants during 1997–2005, *Trans. Energy Convers.* 22(1) (2007), 167-173.
5. Y. Feng, Y. Qiu, C. J. Crabtree, H. Long and P. J. Tavner, “Monitoring wind turbine gearboxes”, *Wind Energy*, 16 (2013), 728-740.
6. M. Wilkinson, B. Hendriks, F. Spinato, E. Gomez, H. Bulacio, J. Roca, P. Tavner, Y. Feng and H. Long, “Methodology and Results of the Reliawind Reliability Field Study”, in *Proceedings of the European Wind Energy Conference (EWEC 2010)*, Warsaw, 2010.
7. K. Smolders, H. Long, Y. Feng and P. Tavner, “Reliability Analysis and Prediction of Wind Turbine Gearboxes,” in *Proceedings of the European Wind Energy Conference (EWEC 2010)*, Warsaw, 2010.
8. L. Roberto, C. Teodora and S. Kiti, 2012 JRC wind status report, European Commission, 2012.
9. A. Greco, S. Sheng, J. Keller, A. Eridemir, Material wear and fatigue in wind turbine systems, *Wear* 302 (1–2) (2013) 1583–1591.
10. K. Stadler and A. Stubenrauch, Premature bearing failures in industrial gearboxes, Washington D.C., 2013.
11. W. Musial, S. Butterfield, B. McNiff, Improving wind turbine gearbox reliability, Conference Paper, National Renewable Energy Laboratory, NREL/CP-500- 41548, Golden, CO, 2007
12. M. -H. Evans, White structure flaking (WSF) in wind turbine gearbox bearings: effects of 'butterflies' and white etching cracks (WEC), *Mater. Sci. Technol.* 28 (1) (2012) 3–22.
13. R. Errichello, R. Budny, R. Eckert, Investigations of bearing failures associated with white etching areas (WEAs) in wind turbine gearboxes, *Tribol. Trans.* 56 (6) (2013) 1069–1076.
14. J. Luyckx, WEC failure mode on roller bearings, Presentation at Wind Turbine Tribology Seminar, Hansen Transmissions, 2011.
15. G. Doll, Current challenges in wind turbine tribology, Presentation at Wind Turbine Tribology Seminar, The University of Akron, 2011.

REFERENCES

16. H. Link, W. LaCava, J. v. Dam, B. McNiff, S. Sheng, R. Wallen, M. McDade, S. Lambert, S. Butterfield and F. Oyague, Gearbox Reliability Collaborative Project Report: Findings from Phase 1 and Phase 2 Testing, NREL/TP-5000-51885, Golden, CO, 2011.
17. F. Oyague, Gearbox Modeling and Load Simulation of a Baseline 750-kW Wind Turbine Using State-of-the-Art Simulation Codes, NREL/T P-500-41160, Golden, Co, 2009.
18. International Organisation for Standardization, IEC 61400-4:2012: Wind turbines - Part 4: Design requirements for wind turbine gearboxes, 2012.
19. G. Stachowiak and A. W. Batchelor, Engineering Tribology, 3 ed., Elsevier, Oxford 2013.
20. S. Jain and H. Hunt, A dynamic model to predict the occurrence of skidding in wind turbine gearbox bearings, *J. Phys.: Conf. Ser.* 305, Cambridge, 2011.
21. J. Wheals, P. Guern, R. Dwyer-Joyce, M. Marshall and T. Howard, "Ricardo MultiLife™ Bearing Programme for Increased Reliability of Offshore Wind Turbines," 2011. [Online]. Available: http://proceedings.ewea.org/annual2011/posters/PO.345_EWEA2011presentation.pdf.
22. T. Harris and M. Kotzalas, Rolling bearing analysis - Essential concepts of bearing technology, Taylor & Francis, Boca Raton, FL, 2007.
23. M. -H. Evans, White structure flaking failure in bearings under rolling contact fatigue (Doctoral thesis), University of Southampton, 2013.
24. NREL, 750 kW 3D gearbox drawings, National Renewable Energy Laboratory, 2012.
25. H. Boyer, Atlas of Fatigue Curves, ASM International, Materials Park, OH, 2005.
26. H. Bhadeshia, Steels for bearings, *Prog. Mater. Sci.* 57 (2012) 268–435
27. J. Hoo, Effect of Steel Manufacturing Processes on the Quality of Bearing Steels, ASTM, Baltimore, 1988.
28. R. Bayer, Wear Analysis for Engineers, HNB Publishing, New York, 2002.
29. H. Hertz, Hertz's miscellaneous papers, MacMillan, London, 1881.
30. H. Hertz, Ueber die Berührung fester elastischer Körper., *Journal für die reine und angewandte Mathematik* 1882(92) (1882), 156-171.
31. K. Johnson, Contact Mechanics, Cambridge University Press, Cambridge, UK, 1985.
32. G. Fajdiga, Computational Fatigue Analysis of Contacting Mechanical Elements, *Tehnicki Vjesnik* 22(1) (2015), 169-175.
33. M. Bruekner, J. Gegner, A. Grabulov, W. Nierlich and J. Slycke, "Alternative butterfly formation mechanisms in rolling contact fatigue," in *Proc. 5th Int.*

- Conf. on "Very High Cycle Fatigue" 131-151*, Berlin, 2011.
34. A. Olver, The Mechanism of Rolling Contact Fatigue: An Update, *P. I. Mech. Eng. J-J*. 219(5) (2005), 313-330.
 35. Y. Kang, R. Evans and G. Doll, Roller-raceway slip simulations of wind turbine gearbox bearings using dynamic bearing model, in *STLE/ASME 2010 International Joint Tribology Conference*, San Francisco, CA, 2010.
 36. M.N. Kotzalas, G.L. Doll, Tribological advancements for reliable wind turbine performance, *Philos. Trans. R. Soc. A* 368 (2010), 4829–4850.
 37. F. Oyague, Gearbox Reliability Collaborative (GRC) Description and Loading, NREL/TP-5000-4777, Golden, Co, 2011.
 38. D. Dowson, M. Priest, G. Dalmaz and A. A. Lubrecht, “Tribological Research and Design for Engineering Systems”, in *Proceedings of the 29th Leeds-Lyon Symposium*, Leeds-Lyon, 2003.
 39. K. Farhangdoost and M. Kavooosi, Effect of Lubricant on Surface Rolling Contact Fatigue Cracks, *Advanced Materials Research*, 97-101 (2010), 793-796.
 40. International Organisation for Standardization, ISO 281:2007 Rolling bearings - Dynamic load ratings and rating life, ISO, Geneva, 2007.
 41. G. Lundberg and A. Palmgren, Dynamic Capacity of Roller Bearings, *Acta Polytech. Scand., Mech. Eng. Ser.* 2 2(4) (1952), 96.
 42. G. Lundberg and A. Palmgren, “Dynamic Capacity of Rolling Bearings,” *Acta Polytech Mech Eng Ser* 1(3) (1947), 7.
 43. T. Harris and W. Yu, Lundberg-Palmgren Fatigue Theory: Considerations of Failure Stress and Stressed Volume, *J. Tribol.* 121(1) (1999), 85-89.
 44. International Organisation for Standardization, Rolling bearings - Methods for calculating the modified reference rating life for universally loaded bearings, ISO/TS16281, 2008.
 45. S. Tanaka, N. Mitamura and Y. Murakami, Influence of sliding and chromium content in the steel on the white structural change under rolling contact, in *Proceedings of the Global Powertrain Conference*, Dearborn, MI, 2004.
 46. K. Iso, A. Yokouchi and H. Takemura, Research work for clarifying the mechanism of white structure flaking and extending the life of bearings, in *SAE World Congress*, Detroit, MI, 2005.
 47. J. Luyckx, W. Broeders and J. Geertsom, Method for increasing the fatigue strength of a predominantly steel mechanical part of a wind turbine and/or for reducing the tendency to form what are called "white etching cracks" or "brittle flakes" in such steel mechanical parts, Hansen Transmissions International, US, 2009.
 48. M. Lewis and B. Tomkins, A fracture mechanics interpretation of rolling bearing fatigue, *Proc IMechE Part J* 226(5) (2012), 389-405.

REFERENCES

49. O. Zwirlein and H. Schlicht, Rolling contact fatigue mechanisms - accelerated testing vs field performance, in Rolling contact fatigue testing of bearing steels, J. Hoo, Ed., Philadelphia, PA: American, 1982, p. 358–379.
50. M. -H. Evans, J. Walker, C. Ma, L. Wang, R. Wood, FIB/TEM study of butterfly crack formation and white etching area (WEA) microstructural changes under rolling contact fatigue in 100Cr6 bearing steel, *Mater. Sci. Eng. A* 570 (2013), 127–134.
51. M. -H. Evans, A.D. Richardson, L. Wang, R. Wood, Effect of hydrogen on butterfly and white etching crack (WEC) formation under rolling contact fatigue (RCF), *Wear* 306(1–2) (2013), 226–241.
52. M. -H. Evans, A. Richardson, L. Wang, R. Wood, Serial sectioning investigation of butterfly and white etching crack (WECs) formation in wind turbine gearbox bearings, *Wear* 302 (1–2) (2013) 1573–1582.
53. A. Grabulov, U. Ziese, H. Zandbergen, TEM/SEM investigation of microstructural changes within the white etching area under rolling contact fatigue and 3-D crack reconstruction by focused ion beam, *Scr. Mater.* 57 (7) (2007), 635–638.
54. A. Ruellan, F. Ville, X. Kleber, A. Arnaudon and D. Girodin, Understanding white etching cracks in rolling element bearings: The effect of hydrogen charging on the formation mechanisms, *P. I. Mech. Eng. J.-J. Eng.* 228(11) (2014), 1252-1265.
55. T. Lund, Sub-surface initiated rolling contact fatigue – influence of nonmetallic inclusions, processing history, and operating conditions, *J. ASTM Int.* 7 (2010) JAI102559.
56. A. Ruellen, Tribological analysis of white etching crack (WEC) failures in rolling element bearings (Doctoral thesis), INSA Lyon, 2014.
57. International Organization for Standardization, Rolling bearings - Damage and failures - Terms, characteristics and causes, ISO/15243, 2004.
58. SKF Bearings, Bearing failures and their causes, SKF, 1994.
59. T. Nisbet and G. Mullett, Rolling Bearings in Service: Interpretation of Types of Damage, Hutchingson Benham, London, 1978.
60. S. Sheng, Wind Turbine Micropitting Workshop: A Recap, National Renewable Energy Laboratory, Golden, Co., 2010.
61. J. Ransselaar, The elephant in the wind turbine, Society of Tribologists and Lubrication Engineers, 2010.
62. A. Grubin, Fundamentals of the Hydrodynamic Theory of Lubrication of Heavily Loaded Cylindrical Surfaces, Chapter 2 in *Investigation of the Contact Machine Components*, Ed. F. Ketova, Central Scientific Institute for Technology and Mechanical Engineering, 1949.

63. R. Lord, Effects of slide-roll ratio and lubricant properties on elastohydrodynamic lubrication film thickness and traction, *P. I. Mech. Eng. J- J. Eng.* 215 (2001), 301-308.
64. D. Nuruzzaman and M. Sheikh, EHL oil film thickness under rolling-sliding contact, *J. Mech. Eng.* 38 (2007), 58-60.
65. International Organization of Standardization, Heat-treated steels, alloy steels and free-cutting steels - Part 17: Ball and roller bearing steels, ISO 683-17, 2014.
66. Ovako, Ovako 825 Product Specification, Technical datasheet.
67. International Organization for Standardization, Heat-treated steels, alloy steels and free-cutting steels - Part 17: Ball and roller bearing steels, ISO 683-17, 2014.
68. SNR NTN, Bearing Technology, 2008.
69. Federal–Mogul Corporation, The effect of carbide network on the life of AISI 52100 in rolling contact fatigue, Technical report, 1982.
70. K. Tsubota, T. Sato, Y. Kato, K. Hiraoka and R. Hayashi, Bearing steels in the 21st century, in *Bearing Steels: into the 21st Century*, Pennsylvania, USA, American Society for Testing of Materials, 1998, 202-215.
71. J. Beswick, Fracture and fatigue crack propagation properties of hardened 52100 steel, *Metall. Mater. Trans. A* 20 (1989), 1961-1973.
72. A. Voskamp, R. Österlund, P. Becker and O. Vingsbo, Gradual changes in residual stress and microstructure during contact fatigue in ball bearings, *Met. Technol.* 7(1) (1980), 14-21.
73. A. Stiénon, A. Fazekas, J. Buffière, A. Vincent, P. Daguier and F. Merchi, “A new methodology based on X-ray micro-tomography to estimate stress concentrations around inclusions in high strength steels, *Mater. Sci. Eng., A* 513-514 (2009), 376-383.
74. P. Voskamp and E. Mittemeijer, State of residual stress induced by cyclic rolling contact loading, *Mater. Sci. Technol.* 13(5) (1997), 430-438.
75. H. McArthur and D. Spalding, *Engineering Materials Science; Properties, Uses, Degradation, Remediation*, Woodhead Publishing, Cambridge, UK, 2004.
76. V. Ginzburg and R. Ballas, *Flat Rolling Fundamentals*, Marcel Dekker, New York, 2000.
77. J. Verhoeven, *Metallurgy for the Non-Metallurgist*, ASM International Materials Park, Ohio, 2007.
78. H. Bhadeshia and R. Honeycombe, *Steels: Microstructure and Properties*, Butterworth-Heinemann. Oxford, 2006.
79. NSK Europe, Technical Insight (TI/E/0010), NSK.

REFERENCES

80. A. Voskamp, Fatigue and Material Response in Rolling Contact, *Bearing Steels: into the 21st Century*, Pennsylvania, USA, American Society for Testing of Materials, 1998,152-166.
81. S. Turteltaub and A. Suiker, Transformation-induced plasticity in ferrous alloys, *J. Mech. Phys. Solids.* 53(8) (2005), 1747–1788.
82. R. Vegter, J. Slycke, J. Beswick and S. Dean, The role of hydrogen on rolling contact fatigue response of rolling element bearings, *J. ASTM Int.* 7(2) 2009, 1-12.
83. N. Arakere, N. Branch, G. Levesque, V. Svendsen and N. Forster, Rolling contact fatigue life and spall propagation characteristics of AISI M50, M50 NiL, and AISI 52100, Part II-Stress modeling, Air Force Research Laboratory, Ohio, 2009.
84. A. Voskamp, Microstructural Stability and Bearing Performance, in *Bearing Steel Technology*, ASTM STP 1419, 2002, 443-456.
85. A. Voskamp and E. Mittemeijer, Crystallographic preferred orientation induced by cyclic rolling contact loading, *Metall. Mater. Trans. A* 27(11) (1996), 3445-3456.
86. International Organization for Standardization, ISO 4967:2013 Steel - Determination of content of non-metallic inclusions - Micrographic method using standard diagrams, ISO, 2013.
87. H. Bohmer, A new approach to determine the effect of nonmetallic inclusions on material behaviour in rolling contact, in *Creative use of Bearing Steels*, Philadelphia, ASTM, 1993, p. 211–221.
88. N. Tsunekage, K. Hashimoto, T. Fujimatsu and K. Hiraoka, Initiation behavior of crack originated from non-metallic inclusion in rolling contact fatigue, *J. ASTM Int.* 7(2) (2010), DOI: 10.1520/JAI102612.
89. A. Melander and A. Gustavsson, An fem study of driving forces of short cracks at inclusions in hard steels, *Int. J. Fatigue* 18 (1996), 389–99.
90. Y. Murakami, *Metal Fatigue: Effects of Small Defects and Nonmetallic Inclusions*, Elsevier, Oxford, 2002.
91. C. Sims and F. Dahle, Effect of Aluminium on the Properties of Medium Carbon Cast Steel, *AFS Trans.*46 (1938), 65.
92. TWI, Why are there different types of manganese sulphide (MnS) inclusions, and how can I distinguish between them?, [Online]. Available: <http://www.twi-global.com/technical-knowledge/faqs/material-faqs/faq-why-are-there-different-types-of-manganese-sulphide-mns-inclusions-and-how-can-i-distinguish-between-them/>. [Accessed 11 09 14].
93. British Standards Institution, PD 970:2005 Wrought steels for mechanical and allied engineering purposes. Requirements for carbon, carbon manganese and

- alloy hot worked or cold finished steels, 2005.
94. L. Canale, G. Totten and R. Mesquita, Failure Analysis of Heat Treated Steel Components, ASM International, 2008.
 95. C. Liu, M. Bassim and S. Lawrence, Evaluation of fatigue-crack initiation at inclusions in fully pearlitic steels, *Mat. Sci. Eng.* 167(1-2) (1993), 108-113.
 96. A. Chard, Deformation of inclusions in rail steel due to rolling contact, University of Birmingham, Doctoral Thesis, 2011.
 97. M. Joo, D. Suh and H. Bhadeshia, Mechanical Anisotropy in Steels for Pipelines, *ISIJ Int.*, 53 (2013), 1305-1314.
 98. T. Bruce, H. Long and R. Dwyer-Joyce, Dynamic modelling of wind turbine gearbox bearing loading during transient events, *IET Renew. Power Gen.* 9(7) (2015), 821-830.
 99. A. Perez-Unzueta and J. Beynon, Microstructure and wear resistance of pearlitic rail steels, *Wear* 162-162(A) (1993), 173-182.
 100. S. Dhua, Amitava Ray, S. Sen, M. Prasad, K. Mishra and S. Jha, Influence of nonmetallic inclusion characteristics on the mechanical properties of rail steel, *J. Mater. Eng. Perf.* 9 (2000), 700-709.
 101. P. Withers and H Bhadeshia, Residual stress: Part 1. Measurement techniques, *Mater. Sci. Technol.* 17(4) (2001), 355–365.
 102. P. Withers and H Bhadeshia, Residual stress: Part 2. Nature and origins, *Mater. Sci. Technol.* 17(4) (2001), 366–75.
 103. E. Kula and V. Weiss, Residual stress and relaxation, Plenum Publishing Corporation, 1982.
 104. G. Lucas and L. Weigel, X-ray measurement of residual stresses in martensite and austenite of quenched steels, *Materialprüfung* 6 (1964), 149–56.
 105. T. Harris, M. Ragen and R. Spitzer, The effect of hoop and material residual stresses on the fatigue life of high speed, rolling bearings, *Trib. Trans.* 35(1) (1992), 194–198.
 106. M.-H. Evans, L. Wang, H. Jones, R. Wood, White etching crack (WEC) investigation by serial sectioning, focused ion beam and 3-D crack modelling, *Tribol. Int.* 65 (2013), 146–160.
 107. B. McNiff, Wind Turbine Gearbox Reliability in Sandia National Laboratories Wind Turbine Gearbox Reliability Workshop, Albuquerque, NM, 2006
 108. P. Becker, Microstructural changes around non-metallic inclusions caused by rolling contact fatigue of bearing steels, *Met. Technol.* 8(1) (1981), 234–243.
 109. J. Gegner, Tribological aspects of rolling bearing failures, in Tribology - Lubricants and Lubrication, INTECH, 2011, 33-94.
 110. A. Vincent, G. Lormand, P. Lamagnere, L. Gosset, D. Girodin, G. Dudragne,

REFERENCES

- R. Fougères, From white etching areas around inclusions to crack nucleation in bearing steels under rolling contact fatigue, in: *Bearing Steels: Into the 21st Century*, ASTM International, West Conshohocken, PA, 1998, 109–123
111. H. Harada, T. Mikami, M. Shibata, D. Sokai, A. Yamamoto and H. Tsubakino, Microstructural changes and crack initiation with white etching area formation under rolling/sliding contact in bearing steel, *ISIJ Int.*, 45(12) (2005), 1897-1902.
 112. J. Bush, W. Grube and G. Robinson, Microstructural and residual stress changes in hardened steel due to rolling contact, *Trans. ASM*, 54 (1961), 390–41.
 113. R. Oesterlund and O. Vingsbo, Phase changes in fatigued ball bearings, *Metall. Mater. Trans. A*, 11(5) (1980), 701-707.
 114. H. Swahn, P. C. Becker and O. Vingsbo, Martensite decay during rolling contact fatigue in ball bearings, *Metall. Mater. Trans. A*, 7(8) (1976), 35-39.
 115. K. Furumura, Y. Murakami and T. Abe, Development of long life bearing steel for full film lubrication and for poor and contaminated lubrication, *Motion and Control* 1 (1996), 30-36.
 116. G. Johnston, T. Andersson, E. Amerongen and A. Voskamp, Experience of element and full-bearing testing of materials over several years, in *Rolling contact fatigue testing of bearing steels*, J. Hoo, Ed., ASTM, Philadelphia, PA: American, 1982, 190–205.
 117. M. Selecka and A. Salak, Durability and failure of powder forged rolling bearing rings, *Wear* 236(1) (1999), 682–700.
 118. V. Pasarica, J. Croitoru, S. Constantinescu, E. Dobrescu and E. Cioaca, The origin and content of Al₂O₃ nonmetallic inclusions in ball bearing steel, *Metalurgia (Bucharest)*, 33 (1981), 329–349.
 119. R. Tricot, J. Monnot and M. Lluansi, How microstructural alterations affect fatigue properties of 52100 steel, *Metals Engineering Quarterly*, 12 (1972), 39–47.
 120. R. Österlund, O. Vingsbo, L. Vincent and P. Guiraldenq, Butterflies in fatigued ball bearings - formation mechanism and structure, *Jom-J. Min. Met. Mat. S.* 11(23-32), 1982.
 121. M. Freitas and D. Francois, Formation de phase blanche en fatigue de roulement, *Scripta Metall. Mater.* 17 (1983), 683-696.
 122. H. Takemura, Y. Matsumoto and Y. Murakami, Development of a new life equation for ball and roller bearings, *Motion & Control*, 11 (2001), 1-10.
 123. J. Gegner and W. Nierlich, The Bearing Axial Cracks Root Cause Hypothesis of Frictional Surface Crack Initiation and Corrosion Fatigue Driven Crack Growth, 2011. [Online]. Available:

http://www.nrel.gov/wind/pdfs/day2_sessioniv_2_skf_gegner.pdf.

124. H. Uyama, H. Yamada, H. Hidaka and N. Mitamura, The effects of hydrogen on microstructural change and surface originated flaking in rolling contact fatigue, *Tribol. Online*, 6(2) (2011), 123-132.
125. A. Grabulov, R. Petrov and H. W. Zandbergen, EBSD investigation of the crack initiation and TEM/FIB analyses of the microstructural changes around the cracks formed under Rolling Contact Fatigue (RCF), *Int. J. Fat.* 32(3) (2010), 576-583.
126. K. Hiraoka, T. Fujimatsu, K. Hashimoto, S. Fukumoto, A. Yamamoto, Crystallographic Analyses on Cracks Initiated by Rolling Contact Fatigue in High Carbon Chromium Bearing Steel, *Mater. Sci. Forum*, 561-565 (2007), 2151-2154.
127. A. Oila and S. Bull, Phase transformations associated with micropitting in rolling/sliding contacts, *J. Mater. Sci.* 40(18) (2005), 4767-4774.
128. H. Geijselaers and E. Perdahcioglu, Mechanically induced martensitic transformation as a stress-driven process, *Scripta Metall. Mater.* 60(1) (2009), 29-31.
129. I. Polonsky and L. Keer, On white etching band formation in rolling bearings, *J. Mech. Phys. Solids*, 43(4) (1995), 637-669.
130. T. Eyre and A. Baxter, The formation of white layers at rubbing surfaces, *Tribology*, 5(6) (1972), 256-261.
131. D. Fletcher, Thermal contact stress and near surface rail cracks, in *9th International Conference on Contact Mechanics and Wear of Rail/Wheel Systems*, CM, 2012, 470-479.
132. V. M. Pchelkina, Increasing the quality and properties of bearing parts by surface hardening with the use of induction heating, *Met. Sci. Heat Treat+*. 30(3) (1988), 168-172.
133. S. Sankar, M. Nataraj and V. Raja, Failure Analysis of Bearing in Wind Turbine Gearbox, *J. Inform. Syst. Comm.* 3(1) (2012), 302-309.
134. J. Rosinski and D. Smurthwaite, Troubleshooting Wind Gearbox Problems, Gear Solutions, 2010.
135. F. C. Cambell, Fatigue, in *Elements of Metallurgy and Engineering Alloys*, Ohio, ASM International, 2008, 243-262.
136. H. Okamoto and M. Oka, Isothermal martensite transformation in a 1.80 wt% C steel, *Metall. Trans. A*, 16(12) (1985), 2257-2262.
137. Y. Matsubara and H. Hamada, A novel method to evaluate the influence of hydrogen on fatigue properties of high strength steels, in *Bearing Steel Technology - Advances and State of the Art in Bearing Steel Quality Assurance*, ASTM International, West Conshohocken, PA, USA, 2007, 153-

REFERENCES

- 166.
138. P. Smith. and A. Stewart, Effect of aqueous and hydrogen environments on fatigue in 2Ni-Cr-Mo-V rotor steel, *Met. Sci.* 13(7) (1979), 429–435.
 139. Y. Murakami. and S. Matsuoka, Effect of hydrogen on fatigue crack growth of metals, *Eng. Fract. Mech.* 77(11) (2010), 1926-1940.
 140. D. Ray, L. Vincent, B. Coquillet and P. Guirandeny, Hydrogen embrittlement of a stainless ball bearing steel, *Wear*, 65(1) (1980), 103-111.
 141. C. Beachem, A new model for hydrogen-assisted cracking (hydrogen "embrittlement"), *Metall. Trans.* 3(2) (1972), 441-455.
 142. S. Fujita, S. Matsuoka, Y. Murakami and G. Marquis, Effect of hydrogen on mode II fatigue crack behavior of tempered bearing steel and microstructural changes, *Int. J. Fatigue*, 32(6) (2010), 943-951.
 143. Y. Murakami, T. Kanezaki, Y. Mine and S. Matsuoka, Hydrogen embrittlement mechanism in fatigue of austenitic stainless steels, *Metall. Mater. Trans. A.*, vol. 39(6) (2008), 1327-1339.
 144. A. Troiano, The role of hydrogen and other interstitials in the mechanical behavior of metals, *Trans. ASM*, 52 (1960), 54-80.
 145. R. Oriani and P. Josephic, Testing of the decohesion theory of hydrogen-induced crack propagation, *Scripta. Metall. Mater.* 6(8) (1972), 681-688.
 146. J. Ćwiek and A. Zieliński, Mechanism of hydrogen enhanced-cracking of high-strength steel welded joints, *J. Achievements Mater. Manuf. Eng.* 18(1-2) (2006), 207-210.
 147. A. Barnoush, Hydrogen embrittlement, Universität des Saarlandes, Saarbrücken, Germany, 2011.
 148. L. Grunberg, D. Jamieson and D. Scott, Hydrogen penetration in water-accelerated fatigue of rolling surfaces, *Phil. Mag.* 8(93) (1963), 1553-1568.
 149. S. Suresh, *Fatigue of Materials*, Cambridge University Press, Cambridge, 1991.
 150. I. Muto, J. Shinozaki, T. Omura, M. Numata and N. Hara, Microelectrochemical Investigation of Hydrogen Absorption and Dissolution Behaviour of MnS Inclusions in Carbon Steel, *ECS Trans.* 30(35) (2011), 9-20.
 151. N. Kino and K. Otani, The influence of hydrogen on rolling contact fatigue life and its improvement, *JSAE Review*, 24(3) (2003), 289-294.
 152. K. Sugino, K. Miyamoto, M. Nagumo and K. Aok, Structural alterations of bearing steels under rolling contact fatigue, *ISIJ Int.* 10 (1970), 98-111.
 153. R. Oesterlund, O. Vingsbo, L. Vincent and P. Guiraldeny, Butterflies in fatigued ball bearings – formation mechanism and structure, *Scand. J. Metall.*, 11 (1982), 23-32.
 154. R. Tricot, J. Monnot and M. Lluansi, How microstructural alterations affect fatigue properties of 52100 steel, *Met. Eng. Q.* 12(2) (1972), 39-47.

155. V. Sastri, E. Ghali and M. Elboudjaini, Corrosion Prevention and Protection; Practical Solutions, John Wiley and Sons, West Sussex, 2007.
156. R. Carroll, Surface Metallurgy and Rolling Contact Fatigue of Rail, The University of Sheffield, Doctoral Thesis, 2005.
157. M. Friswell, J. Penny, S. Garvey and A. Lees, Dynamics of Rotating Machines, Cambridge University Press, Cambridge, 2010.
158. J. Peeters, D. Vandepitte and P. Sas, Analysis of Internal Drive Train Dynamics in a Wind Turbine, *Wind Energy*, 9(1-2) (2005), 141-161.
159. J. Helsen, F. Vanhollebeke, B. Marrant, D. Vandepitte and W. Desmet, Multibody modelling of varying complexity for model behaviour analysis of wind turbine gearboxes, *Renewable Energy* 36(11) (2011), 3098-3113.
160. K. Scott, D. Infield, N. Barltrop and A. Coultate, Effects of Extreme and Transient Loads on Wind Turbine Drive Trains, American Institute of Aeronautics and Astronautics, 2011.
161. F. Oyague, Progressive Dynamical Drive Train Modeling as Part of NREL Gearbox Reliability Collaborative, NREL/ CP-500-43473, Golden, CO, 2008.
162. W. LaCava, Y. Guo, Y. Xing and T. Moan, Determining Wind Turbine Gearbox Model Complexity Using Measurement Validation and Cost Comparison, NREL/CP-5000-54545, Golden, CO, 2012.
163. M. Singh, Dynamic Models for Wind Turbines and Wind Power Plants, NREL/SR-5500-52780, Austin, Texas, 2011.
164. L. Thévenin, Extension de la loi d'Ohm aux circuits électromoteurs complexes [Extension of Ohm's law to complex electromotive circuits], *Annales T'el'graphiques*, 10 (1883), 222-224.
165. T. Yamamoto and K. M. M. Eguchi, "NASA Technical Memorandum: Stress Concentration in the Vicinity of a Hole Defect Under Conditions of Hertzian Contact", in *Joint Lubrication Conference*, New Orleans, Louisiana, 1981.
166. A. G. G. Rodriguez, A. G. Rodriguez and M. Payán, "Estimating wind turbines mechanical constants," in *Proc. Int. Conf. Renewable Energies and Power Quality (ICREPQ'07)*, Vigo, Spain, 2007.
167. L. Houbert, A Uniform Analytical Approach for Ball Bearing and Roller Bearing Calculations, *J. Trib.* 119(4) (1997), 851-858.
168. Ricardo, *VALDYN User's Manual*, Ricardo PLC, Shoreham-by-Sea, UK, 2012.
169. SKF, *General Catalogue*, SKF Group, 2003.
170. International Organization for Standardization, Calculation of load capacity of spur and helical gears, ISO6336-3, 2006.
171. Romax Technology, NREL GRC: Rubber mount testing for NREL, 2009.
172. NSK, Bearing internal load distribution and displacement, Chapter from Catalogue: Rolling Bearings, 2009.

REFERENCES

173. Y. Guo, J. Keller and W. LaCava, Combined effects of gravity, bending moment, bearing clearance, and input torque on wind turbine planetary gear load sharing, NREL/CP-5000-55968, Golden, Co, 2012.
174. W. LaCava, Y. Xing, C. Marks, Y. Guo and T. Moan, Three-dimensional bearing load share behavior in the planetary stage of a wind turbine gearbox, *Ren. Pow. Gen.* 7(4) (2013), 359-369.
175. S. Yu, D. Wang, H. Dong and B. Wang, A new method for determining load distributions among rollers of bearing with manufacturing errors, *J. Mech. Eng. Sci.*, 227(11) (2013), 2402–2415.
176. B. Gabriel, SEM: A user's manual for materials science, American Society for Metals, Ohio, 1985, 87-92.
177. W. Oliver and G. Pharr, An improved technique for determining hardness and elastic modulus using load and displacement sensing indentation experiments, *J. Mater. Res.* 7(6) (1992) 1564-1583.
178. T. Slatter, R. Lewis and A. Jones, The influence of cryogenic processing on the impact wear resistance of low carbon steel and lamellar graphite cast iron, *Wear*, 271(9-10) (2011) 1481-1489.
179. T. Slatter and R. Lewis, The influence of induction hardening on the impact wear resistance of compacted graphite cast iron (CGI), *Wear*, 270(3-4) (2010), 302-311.
180. T. Slatter, Reducing Automotive Valve Train Recession with Surface Treatment, University of Sheffield, Doctoral Thesis, 2010.
181. S. Fujita and Y. Murakami, A New Nonmetallic Inclusion Rating Method by Positive Use of Hydrogen Embrittlement Phenomenon, *Metall. Mater. Trans. A*, vol. 44(1) (2013), 303-322.
182. Ovako, Steels for bearing production from Ovako, 2008. [Online]. Available: http://www.ovako.com/Global/Downloads/Product_information/Ovako_Group/EN/Steels%20for%20Bearings%20from%20Ovako.pdf.
183. A. Kapoor, F. Franklin, S. Wong and M. Ishida, Surface roughness and plastic flow in rail wheel contact, *Wear*, 253 (2002), 257-264.
184. J. Garnham and J. Beynon, The early detection of rolling - sliding contact fatigue cracks, *Wear*, 144(1-2) (1991), 103-116.
185. D. Fletcher and J. Beynon, Development of a machine for closely controlled rolling contact fatigue and wear testing, *J. Test. Eval.* 28(4) (2000), 267-275.
186. S. Lewis, R. Lewis, P. Richards and L. Buckley-Johnstone, Investigation of the isolation and frictional properties of hydrophobic products on the rail head, when used to combat low adhesion, *Wear*, 314(1-2) (2013), 213-219.
187. S. Lewis, R. Lewis, G. Evans and L. Buckley-Johnstone, Assessment of railway curve lubricant performance using a twin-disc tester, *Wear*, 314(1)

- (2014), 205-212.
188. C. Hardwick, S. Lewis and R. Lewis, The effect of friction modifiers on wheel/rail isolation at low axle loads, *P. I. Mech. Eng. F.-J. Rai.* 228(7) (2014), 768-783.
 189. S. Timoshenko and J. Goodier, *Theory of Elasticity*, 3 ed., McGraw-Hill London, 1970, 403-420.
 190. A. Grabulov, *Fundamentals of Rolling Contact Fatigue*, University of Belgrade, Serbia, Doctoral Thesis, 2010.
 191. B. Jacobson and J. Kalker, *Rolling Contact Phenomena*, Springer, New York, 2000.
 192. Chevron, "MEROPA® datasheet 23551," 2015.
 193. ASTM international, *Standard Practice for Viscosity-Temperature Charts for Liquid Petroleum Products*, West Conshohocken, PA, 2009.
 194. D. B. Dooner, *Kinematic Geometry of Gearing*, John Wiley and Sons, Chichester, UK, 2012.
 195. T. Bruce, E. Rounding, H. Long and R. Dwyer-Joyce, Characterisation of white etching crack damage in wind turbine gearbox bearings, *Wear*, 338-339 (2015), 164-177.
 196. J.-H. Kanga, R. Vegter and P. Rivera-Diaz-del-Castillo, *Rolling contact fatigue in martensitic 100Cr6: subsurface hardening and crack formation*, SKF University Technology Centre, Cambridge, 2014.
 197. H. Uyama, *The Mechanism of White Structure Flaking in Rolling*, 2011. [Online]. Available: http://www.nrel.gov/wind/pdfs/day2_sessioniv_1_nsk_uyama.pdf.
 198. D. Radaj and M. Vormwald, *Advanced Methods of Fatigue Assessment*, Springer, Berlin, 2012.
 199. Buehler, *Material Safety Data Sheet 9101395*, Lake Bluff, IL, 2012.
 200. C. Luo, *Modeling the Behavior of Inclusions in Plastic Deformation of Steels*, Royal Institute of Technology, 2001.
 201. K. Stadler, *How black oxide-coated bearings can make an impact on cutting O&M costs for wind turbines*, SKF, Gothenburg, Sweden, 2013.
 202. G. Doll, M. Kotzalas and Y. Kang, *Life-Limiting Wear of Wind Turbine Gearbox Bearings: Origins and Solutions*, Timken, Canton, OH, USA, 2010.

9. APPENDICES

The following appendices provide supporting information for the subjects discussed in the main body of this thesis. Any sensitive data has been published with permission from our anonymous partners. In addition, all data relating to the modelled 750 kW gearbox has been published with permission from NREL.

Appendix A: Failure mode matrix (SKF field experience)

Theoretical failure mode	Field observation	Failure mechanism	Root causes of failure	Factors contributing to failure
Wear caused by abrasive particles	Small indentations around the raceways and rolling elements. Dull, worn surfaces	Wear	Small, abrasive particles that have entered the bearing by some means, cause wear of raceways, rolling elements and cage	Lack of cleanliness before and during mounting. Ineffective Seals. Lubricant contaminated by worn particles from brass cage
Wear caused by inadequate lubrication	Worn, frequently mirror-like, surfaces; at a later stage blue to brown discolouration.	Wear	Lubricant has gradually been used up or has lost its lubricating properties.	Loss or contamination of lubricant. Non-frequent re-lubrication servicing
Wear caused by vibration	Rectangular depressions in the raceways: rectangular in roller bearings and circular in ball bearings. The bottom of these depressions may be bright or dull and oxidised	Wear	When a bearing is stationary, there is no lubricant film between the rolling elements and the raceways, causing metal to metal contact and the formation of depressions in the raceways	The bearing has been exposed to vibration while stationary.
Indentations caused by faulty mounting or overloading	Indentations in the raceways of both rings with spacing equal to the distance between the rolling elements.	Indentations, smearing	In spherical roller bearings the damage originates as smearing and subsequently, if the pressure increases, develops into a dent. The same conditions apply in taper roller bearings that are unduly preloaded without being rotated.	Mounting pressure applied to the wrong ring. Excessively hard drive-up on tapered seating. Overloading while not running.
Indentations caused by foreign particles	Small indentations distributed around the raceways of both rings and in the rolling elements.	Indentations	Foreign particles, such as swarf and burrs, which have gained entry into the bearing cause indentations when rolled into the raceways by the rolling elements	Ingress of foreign particles into the bearing.
Smearing of roller ends and guide flanges	Scored and discoloured roller ends and flange faces	Smearing	In cylindrical and taper roller bearings, and in spherical roller bearings with guide flanges, smearing may occur on the guiding faces of the flanges and the ends of the rollers. This	Sliding under heavy axial loading and with inadequate lubrication

Analysis of the Premature Failure of Wind Turbine Gearbox Bearings

			smearing is due to insufficient lubricant.	
Smearing of roller and raceways	Scored and discoloured areas at the start of the load zone in raceways and on the surface of the rollers	Smearing	Roller rotation retarded in the unloaded zone, where the rollers are not driven by the rings. Consequently their speed of rotation is lower than when they are in the loaded zone. Leads to skidding and smearing	Roller acceleration on entry into the loaded zone.
Raceway smearing at intervals corresponding to the roller spacing	Transverse smear streaks – spaced at intervals equal to the distance between the rollers – in the raceways of cylindrical/spherical/tapered roller bearings.	Smearing	When cylindrical roller bearings are being mounted, the ring with the roller and cage assembly is often entered askew and isn't rotated. The rollers then scratch the raceway of the other ring, causing smearing. The rollers may be smeared too.	During the mounting operation, the ring with the roller and cage assembly has been entered askew on the other ring. Blows applied to the wrong ring or heavy preloading without rotating the bearing.
Smearing of external surfaces	Scored and discoloured ring bore or outside surface or faces	Smearing	Here, the smearing is the result of movement of the bearing ring relative to its shaft or housing. Smearing of the inner ring bore, outer ring outside surface and ring faces	Ring rotation relative to shaft or housing
Surface distress	Initially the damage is not visible to the naked eye. A more advanced stage is marked by small, shallow craters with crystalline fracture surfaces.	Surface distress	If the lubricant film between raceways and rolling elements becomes too thin, the peaks of the surface asperities will momentarily come into contact with each other. Small cracks then form in the surfaces; this is known as surface distress.	Inadequate or improper lubrication.
Deep seated rust	Greyish black streaks across the raceways, mostly coinciding with the rolling element spacing. At a later stage, pitting of raceways and other surfaces of the bearing.	Corrosion	Penetration of the thin protective oxide film on the clean steel surfaces exposed to the air by water or corrosive elements. Patches of etching from and soon lead to rust. Deep seated rust can initiate flaking and cracks. Acid liquids are most dangerous	Presence of water, moisture or corrosive substances in the bearing over a long period of time.
Fretting corrosion	Areas of rust on the outside surface of the outer ring or in the bore of the inner ring. Raceway path pattern heavily marked at corresponding positions.	Corrosion	If the thin oxide film is penetrated, oxidation will proceed deeper into the material. Often occurs when there is relative movement between bearing ring and shaft or housing, on account of the fit being too loose. Leads to uneven support of bearing rings and a detrimental effect on load distribution.	Fit too loose. Shaft or housing seating with errors of form.
	Dark brown or greyish black fluting (corrugation) or craters in raceways	Electric current damage	When an electric current passes through a bearing, i.e. proceeds from one ring to the other via the rolling elements,	Passage of electric current through rotating bearing. Passage of electric

APPENDICES

Damage caused by passage of electric current	and rollers. Balls have dark discolouration only. Sometimes zigzag burns in ball bearings raceways. Localised burns in raceways and on rolling elements.		damage will occur. At the contact surfaces the process is similar to electric arc welding. The material is heated to temperatures ranging from tempering to melting levels, re-hardening or melting the metal.	current through non-rotating bearing.
Flaking (spall) caused by preloading	Heavily marked path pattern in raceways of both rings. Flaking usually in the most heavily loaded zone.	Flaking	Preloading on account of fits being too tight. Excessive drive-up on a tapered seating. Single row angular contact ball bearings or taper roller bearings adjusted to give excessive preload. Temperature differential between inner and outer rings too great.	Incorrect fits leading to preloading of bearing
Flaking caused by oval compression	Heavily marked path pattern in raceways of both rings. Flaking usually in the most heavily loaded zone.	Flaking	Oval shaft or oval housing seating. The latter is a common defect in split housings and machine frames. The bore of plummer blocks mounted on an uneven base becomes oval when the base bolts are tightened.	Bearing crushed into oval shape
Flaking called by axial compression	Heavily marked path pattern in raceways of both rings. Flaking usually in the most heavily loaded zone.	Flaking	Incorrect mounting, which results in axial loading, e.g. excessive preloading of angular contact ball bearings and taper roller bearings. The non-locating bearing has jammed. Axial freedom of movement has not been sufficient to accommodate the thermal expansion.	An axial force has been acting on the bearing
Flaking caused by misalignment	Deep groove ball bearings: diagonal path pattern, severely marked at two diametrically opposed sections. Cylindrical roller bearings: flaking at the edge of the raceway.	Flaking	Bearing seatings out of alignment. Bearing mounted on the skew.	Misalignment
Flaking caused by indentations	Flaking in conjunction with indentations coinciding with the rolling element spacing. Flaking in conjunction with small indentations.	Flaking	Arises from indentations (see above)	Extension of indentation damage
Flaking caused by smearing	Flaking at the start of the load zone in raceways of roller bearings. Flaking, coinciding with the roller spacing, in raceways of roller bearings.	Flaking	Arises from smearing (see above)	Extent of smearing damage

Analysis of the Premature Failure of Wind Turbine Gearbox Bearings

Flaking caused by deep seated rust	Flaking originating from rust damage.	Flaking	Arises from deep seating rust (see above)	Extent of rust damage
Flaking caused by fretting corrosion	Flaking in the raceway of either the inner or outer ring. Corroded area at corresponding part of the inner bore of outside surface.	Flaking	Arises from corrosion (see above)	Extent of corrosion
Flaking caused by fluting or craters	Flaking in conjunction with bright or corroded fluting or craters. Flaking in conjunction with dark coloured or burnt fluting or craters.	Flaking	Arises from vibration wear and from electric current damage (see above)	Extension of wear resulting from vibrations and electrical current damage
Cracks caused by rough treatment	Obvious crack	Cracking	Blows, with hammer or hardened chisel, have been directed against the ring when the bearing was being mounted.	Extent of rough treatment
Cracks caused by excessive drive-up	The bearing ring has cracked right through and has lost its grip on the shaft.	Cracking	Excessive drive-up on a tapered seating or sleeve. Interference fit on cylindrical seating too heavy.	Incorrect mounting
Cracks caused by smearing	Crack or cracks in conjunction with smearing of the bearing ring. The ring may have cracked right across. Smearing cracks generally form across the smearing.	Cracking	Arises from smearing (see above)	Extent of smearing
Cracks caused by fretting corrosion	Cracks, transverse in inner rings and generally longitudinal in outer rings, in conjunction with fretting corrosion.	Cracking	Arises from fretting corrosion (see above)	Extent of fretting corrosion
Cage damage	Visible damage to cage	Wear, cracking	Cracks, transverse in inner rings and generally longitudinal in outer rings, in conjunction with examination of a failed bearing, the cage is found to be damaged, it may in many cases prove difficult to ascertain the cause. Usually other components of the bearing are damaged too and this makes it even more difficult to discover the reason for the trouble. However, there are certain main causes of cage failure, viz. vibration, excessive speed, wear and blockage.	Vibration, excessive speed, wear, blockage, other

Appendix B: VALDYN WTG model illustration

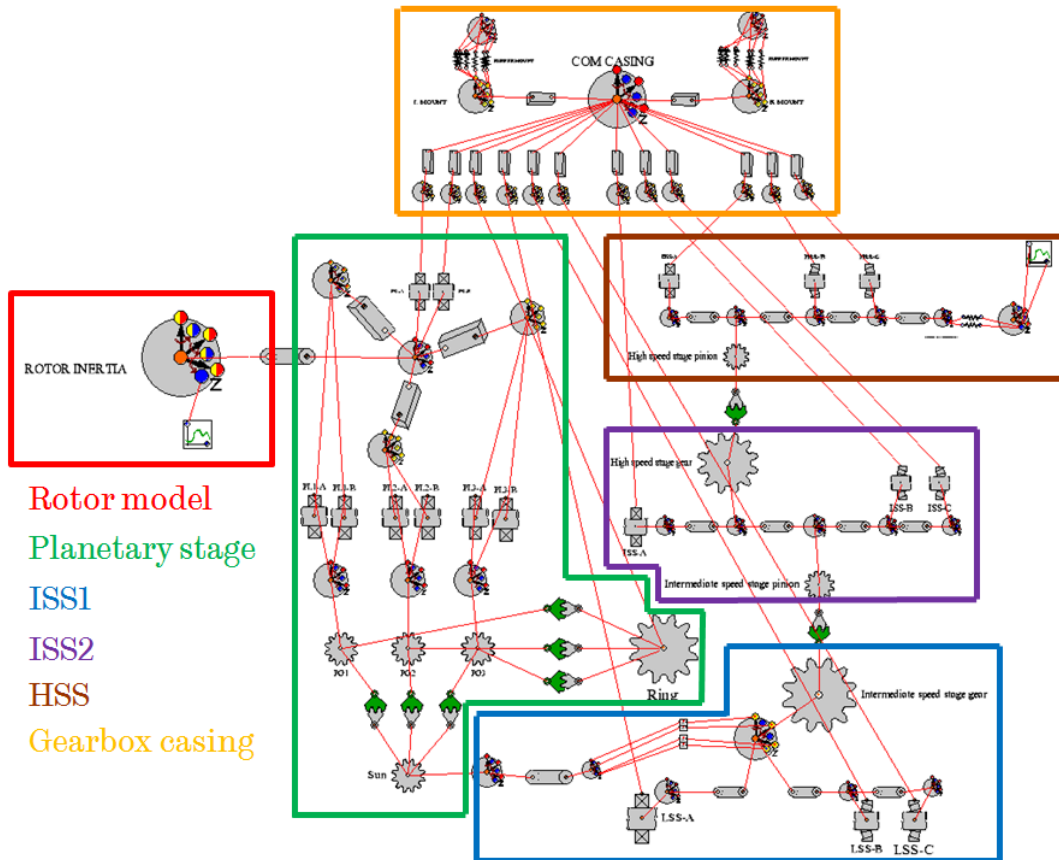


Figure 9-1: VALDYN model viewed on user interface

Appendix C: Values used to model NREL 750 kW gearbox

The following gearbox properties are shared here with permission from Dr Jonathan Keller at NREL.

Gears, shafts, rotor and generator rotor mass matrices

The four properties (M , I_x , I_y , I_m), required to create mass matrices representing the moving components in the gearbox are shown in Table 9-1 for all gearbox components.

ID	Component	M (kg)	I_x (kg.m ²)	I_y (kg.m ²)	I_z (kg.m ²)
1	Rotor (1-DOF)*	-	-	-	940,917
2	Main shaft (LSS)	2050.4	2052.0	2052.0	73.9
3	Planet carrier (PC)	835.1	272.4	272.4	65.2
4	Planet gear (PG1,2,3)	103.7	2.0	2.0	3.2
5	Sun gear and shaft (SG, SS)	180.6	21.7	21.7	1.0
6	Spline shaft (ISS1)	132.7	3.8	3.8	2.1
7	Low speed gear (ISS1G)	400.2	15.7	15.6	29.5
8	Intermediate speed pinion (ISS2P)	99.6	2.3	2.3	0.4
9	Intermediate speed gear (ISS2G)	114.6	1.8	1.8	3.4
10	High speed pinion (HSSP)	54.6	4.7	4.7	0.1
11	High speed shaft (HSS)	20.5	3.6	3.6	0.1
12	Disc brake	91.8	3.6	3.6	7.1
13	Generator rotor (1-DOF)*	-	-	-	25.2
14	Gearbox casing and ring gear (RG)	1313.4	473.7	337.5	368.1

Table 9-1: Mass and inertia properties of gearbox components. *components 1 and 13 were only modelled in 1 DOF so required only a value for I_z . Note that a combined value for the gearbox casing and ring gear is provided since they are fixed together

Bearings

Table 9-2 presents the input parameters for the bearings used in the model. The highlighted rows represent TRBs, whereas non-highlighted represent CRBs.

Bearing ID	K_{xx} (N/m)	K_{yy} (N/m)	K_{zz} (N/m)	$K_{\theta x}$ (Nm/rad)	$K_{\theta y}$ (Nm/rad)	c_a (Ns/m)	c_r (Ns/m)	c_t (Nms/rad)
PL1-A	1.61E+09	3.67E+09	8.60E+08	5.57E+06	6.49E+06	9.44E+03	1.65E+04	7.91E+02
PL1-B	1.60E+09	3.66E+09	8.99E+08	5.39E+06	7.15E+06	9.65E+03	1.65E+04	8.06E+02
PL2-A	1.60E+09	3.66E+09	8.63E+08	5.53E+06	6.56E+06	9.46E+03	1.65E+04	7.91E+02
PL2-B	1.60E+09	3.65E+09	8.95E+08	5.39E+06	7.09E+06	9.63E+03	1.65E+04	8.04E+02
PL3-A	1.59E+09	3.65E+09	8.55E+08	5.48E+06	6.50E+06	9.41E+03	1.65E+04	7.88E+02
PL3-B	1.59E+09	3.64E+09	8.88E+08	5.34E+06	7.05E+06	9.59E+03	1.65E+04	8.01E+02
PLC-A	8.24E+08	3.76E+08	5.51E+03	1.38E+04	6.02E+03	1.66E+01	5.49E+03	2.23E+01
PLC-B	3.50E+08	1.33E+09	1.30E+08	2.62E+06	3.97E+06	3.33E+03	8.46E+03	5.30E+02
LSS-A	1.93E+09	2.25E+09	9.74E+05	3.28E+04	3.92E+04	1.30E-03	6.01E+03	2.49E+01
LSS-B	8.86E+09	8.85E+09	1.68E+09	1.35E+07	1.35E+07	6.81E+03	1.56E+04	6.10E+02
LSS-C	9.56E+09	9.65E+09	1.82E+09	1.47E+07	1.49E+07	7.09E+03	1.63E+04	6.39E+02
ISS-A	1.49E+09	2.08E+09	0	7.07E+04	1.34E+05	0.00E+00	6.33E+03	4.79E+01
ISS-B	7.56E+09	7.55E+09	1.43E+09	5.82E+06	5.82E+06	7.58E+03	1.74E+04	4.83E+02
ISS-C	7.18E+09	7.17E+09	1.36E+09	5.47E+06	5.44E+06	7.39E+03	1.70E+04	4.68E+02
HSS-A	2.05E+09	1.56E+09	0	1.28E+05	6.73E+04	0.00E+00	6.37E+03	4.68E+01
HSS-B	3.70E+09	3.76E+09	6.65E+08	1.27E+06	1.29E+06	3.49E+03	8.28E+03	1.53E+02
HSS-C	4.38E+09	4.39E+09	7.81E+08	1.56E+06	1.56E+06	3.79E+03	8.97E+03	1.69E+02

Table 9-2: Bearing stiffness and damping properties

Gears

Table 9-3: Gear tooth contact stiffness and damping properties Table 9-3 displays the gear contact properties used in the VALDYN model.

Gears in contact	Contact stiffness (N/m ²)	Damping coefficient (Ns/m ²)
PL-RG	14.0	3.00E+05
PL-SU	14.0	5.52E+04
IN	13.1	1.45E+05
LS	13.1	4.91E+04

Table 9-3: Gear tooth contact stiffness and damping properties

Shaft properties

The shaft properties for the NREL gearbox are shown in Table 9-4.

Property	LSS	ISS	ISS2	MA	HSS
do (m)	0.185	0.16	0.3	0.325	0.103
di (m)	0.06	0	0.218	0.0635	0
L (m)	0.856	0.568	0.1	2.05	0.775
E (N/m ²)	2.00E+11	2.00E+11	2.00E+11	2.00E+11	2.00E+11
G (N/m ²)	8.00E+10	8.00E+10	8.00E+10	8.00E+10	8.00E+10
p (kg/m ²)	7810	7810	7810	7810	7810
A (m ²)	0.024	0.020	0.033	0.080	0.008
m (kg)	160.80	89.19	26.06	2050.40	50.44
Ixx (m ⁴)	5.686E-05	3.217E-05	2.867E-04	5.469E-04	5.525E-06
Iyy (m ⁴)	5.686E-05	3.217E-05	2.867E-04	5.469E-04	5.525E-06
I _p (m ⁴)	1.137E-04	6.434E-05	5.735E-04	7.936E-04	7.952E-04
I _m (kgm ²)	1.231	0.571	0.277	52.077	0.134
C _x (Ns/m)	4.022E+03	4.168E+03	9.104E+04	1.202E+04	4.022E+03
C _y (Ns/m)	4.022E+03	4.168E+03	9.104E+04	1.202E+04	4.022E+03
C _z (Ns/m)	2.833E+04	2.368E+04	3.929E+04	1.191E+05	2.833E+04
C _t (Ns/m/rad)	1.078E+02	6.778E+01	3.357E+02	1.197E+03	1.078E+02

Table 9-4: Shaft properties

Generator

The resistance torque applied at different generator rotational speeds ω , for the generator model used is illustrated in Figure 9-2. The input values calculated using equations 2.16-2.18 are shown in the figure.

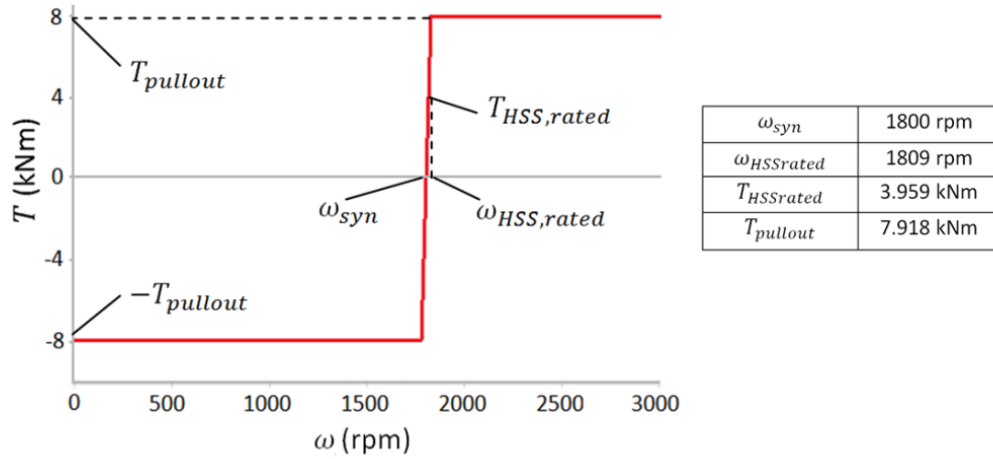


Figure 9-2: Generator resistance torque model used in dynamic model

Elastomer mount damping in x, y, z

Substituting in values for half of the total gearbox mass, which represents the value (m/n) from equation 3.36, and the rubber mount stiffness, we obtain a value of:

$$c = 110 \text{ kN/s.m}$$

Appendix D: Example shaft damping calculations using FEA

No shaft damping values were available, so Abaqus was used to set up a dynamic test to find the fraction of critical damping, ζ . The magnitude of the oscillation peaks is not important as it is the relative magnitude of two consecutive damped oscillation amplitudes that will enable this fraction to be calculated. Basic FE models were constructed of the length of the shaft connecting the two loading components on each. Examples of ISS2 displacements at a single time step are displayed below in the torsional and axial directions.

The first stage was to load the shaft, both:

- (i) Torsionally (Figure 9-3)
- (ii) Radially (Figure 9-4)

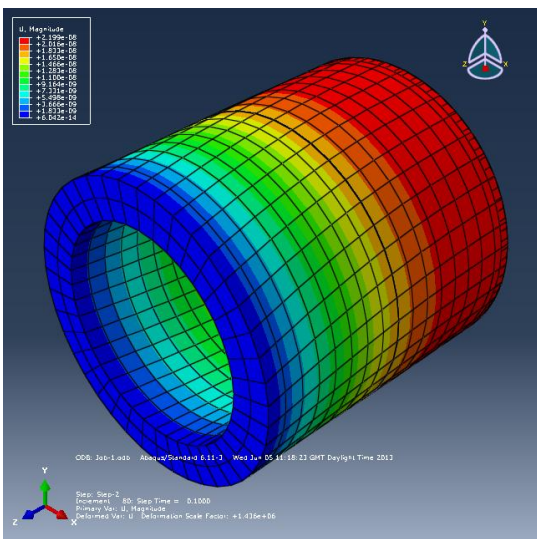


Figure 9-3: ISS2 under torsional load

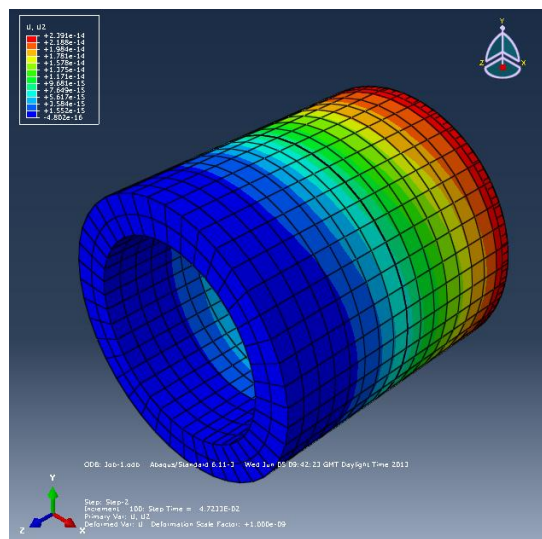


Figure 9-4: ISS2 under radial load

Once the shafts had been preloaded to an arbitrary load level, the preload was released, and their damping behaviour recorded over twenty seconds. The results at each time step in Abaqus were then plotted and fitted to a decaying sinusoidal damping curve (equation 3.34). The results can be Figure 9-5 and Figure 9-6 and amplitude results in Table 9-5 (note the units are arbitrary, as it is the ratio that is of interest, so are not shown). Table 9-5 also shows the results for equations 3.32 and 3.33, including the critical damping fraction.

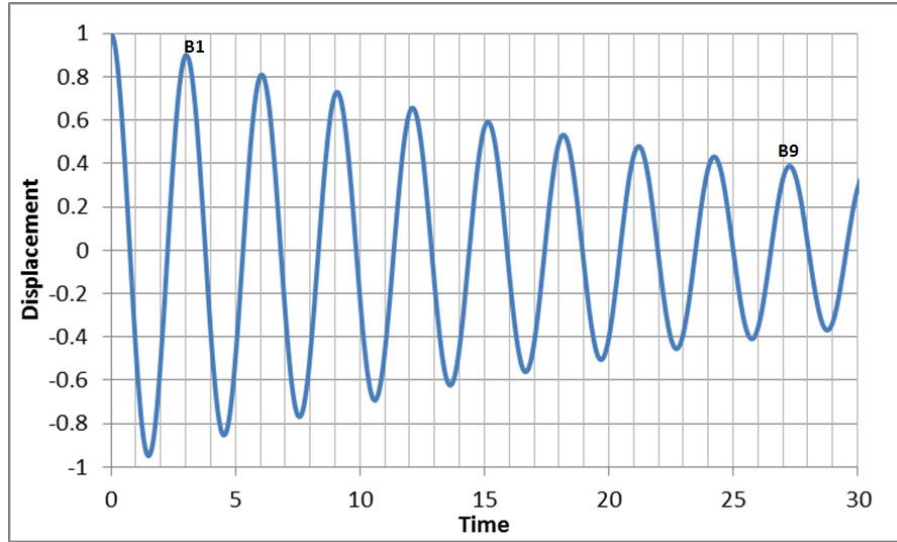


Figure 9-5: Torsional oscillation response of ISS2

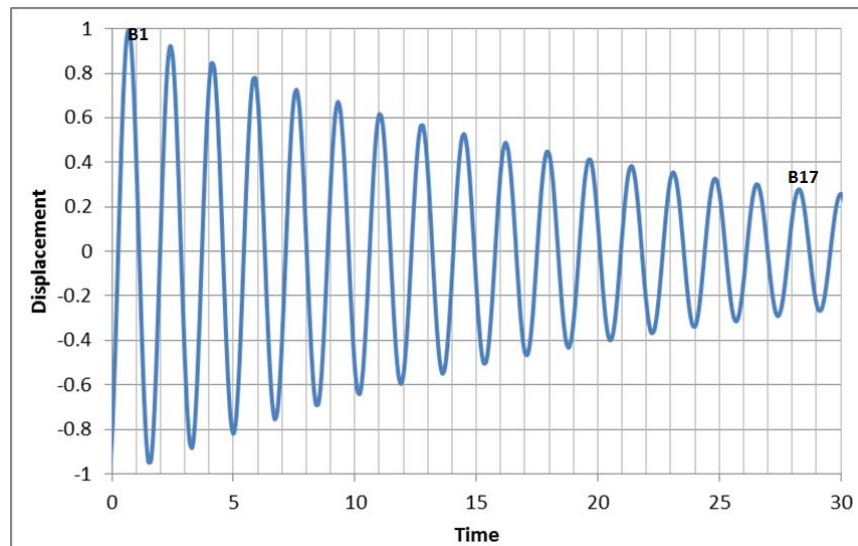


Figure 9-6: Radial oscillation response of ISS2

Amplitude	Torsional displacement	Linear displacement
B1	0.899	0.951
B9 (tor), B17 (rad)	0.388	0.282
δ	0.0934	0.135
ζ	0.0149	0.0215

Table 9-5: Shaft critical damping fraction calculation results

Appendix E - 600 kW gearbox information

This appendix contains images of the sectioned WTGB and the gearbox it was part of, including bearing geometry schematics. All images are shared with permission from our anonymous partner.

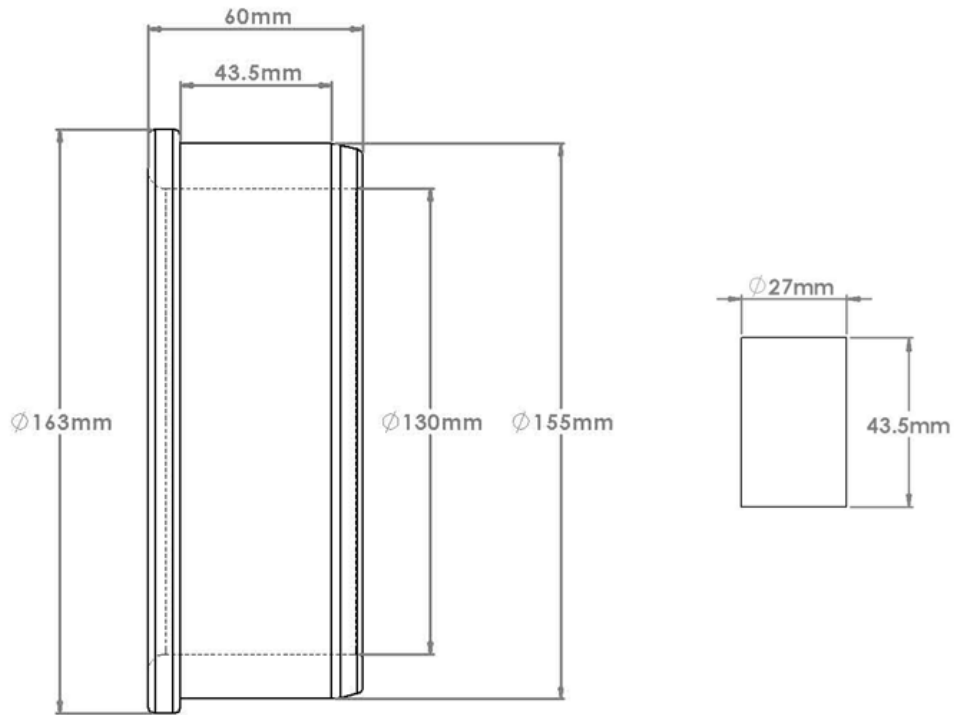


Figure 9-7: Dimensions of a) inner raceway b) cylindrical roller



Figure 9-8: Image showing surface damage and clear transition from undamaged to damaged region



Figure 9-9: Image showing undamaged region



Figure 9-10: Epicyclic stage ring gear

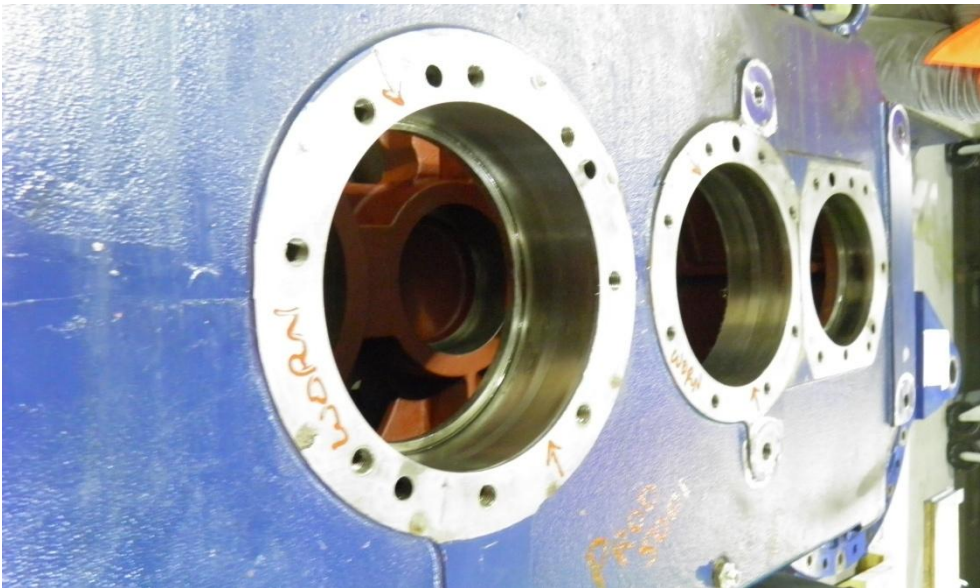


Figure 9-11: Gearbox housing shaft bearing mounting positions



Figure 9-12: Outer race, cage and rolling elements of failed planetary gear bearing



Figure 9-13: Wear scars observed on cylindrical rollers

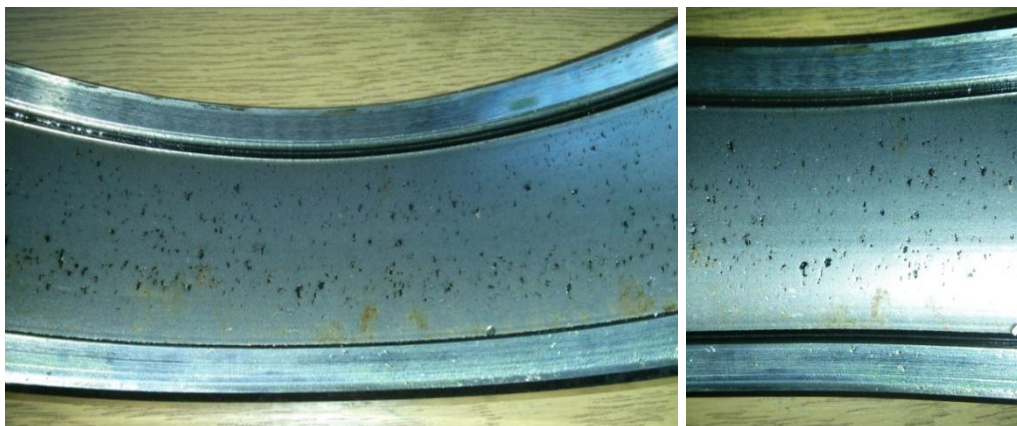


Figure 9-14: Smaller wear scars distributed over entire circumference of outer ring



Figure 9-15: Failed planetary gear



Figure 9-16: Low speed intermediate shaft

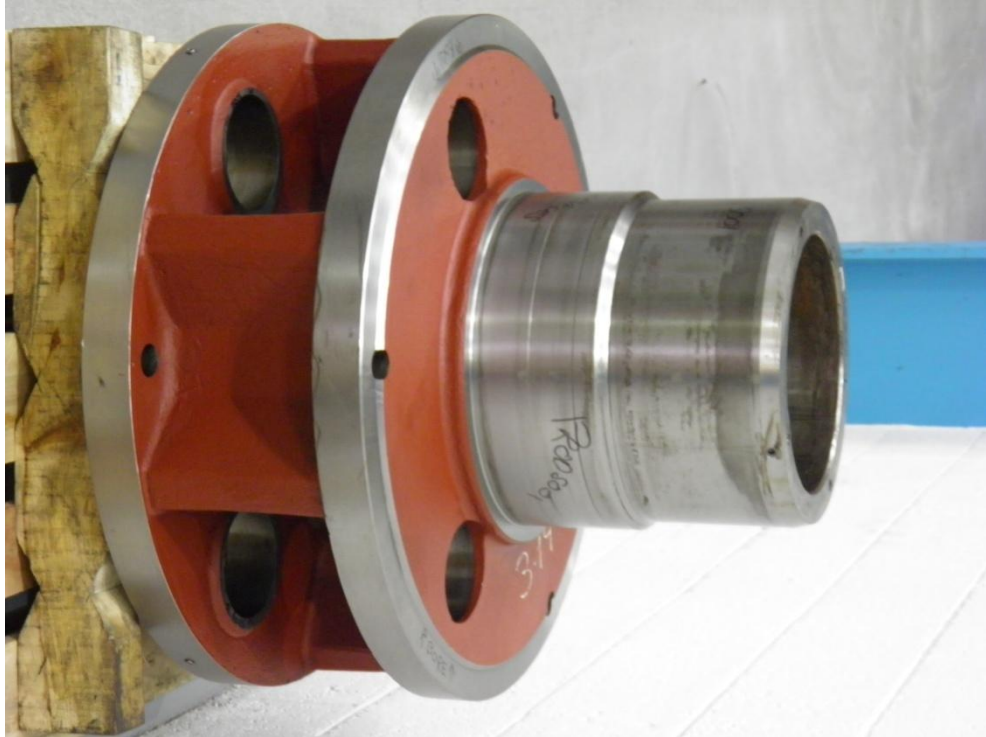


Figure 9-17: Planetary carrier

Appendix F: SUROS sample wear tracks

Optical microscope image montages of the analysed SUROS sample wear tracks are presented in Figure 9-18 - Figure 9-21.

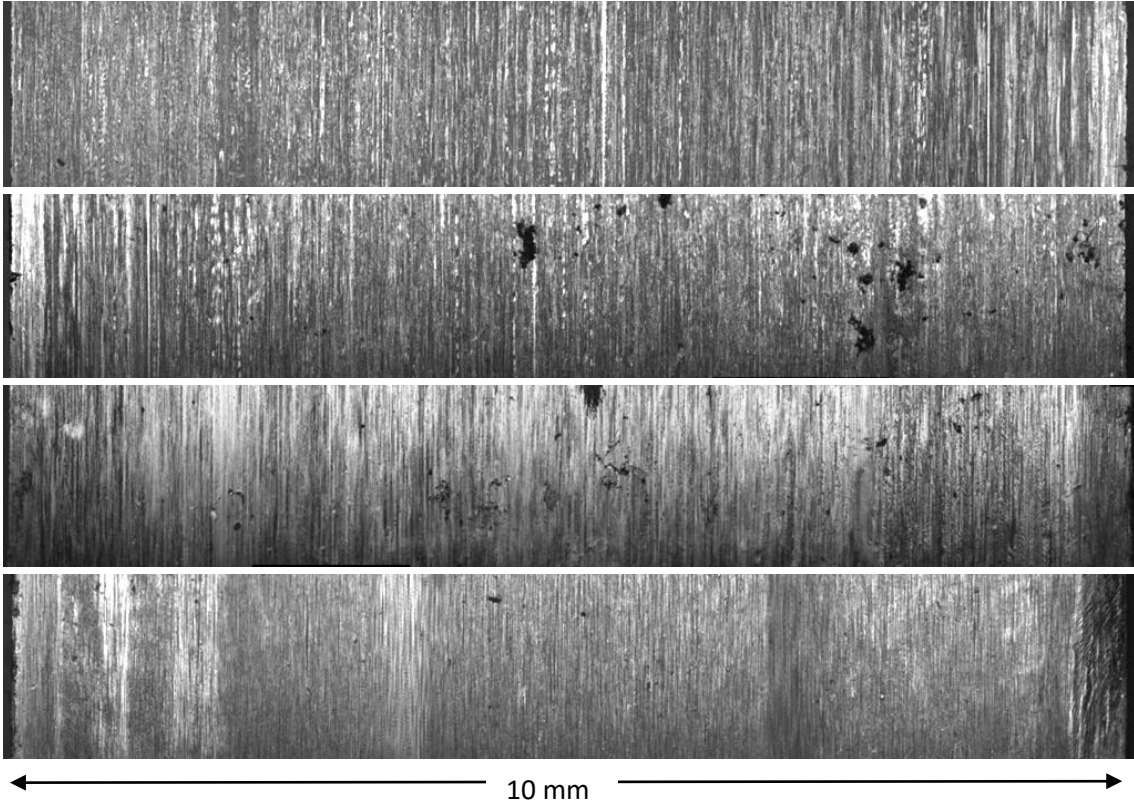


Figure 9-18: Wear tracks from SUROS discs 1-4

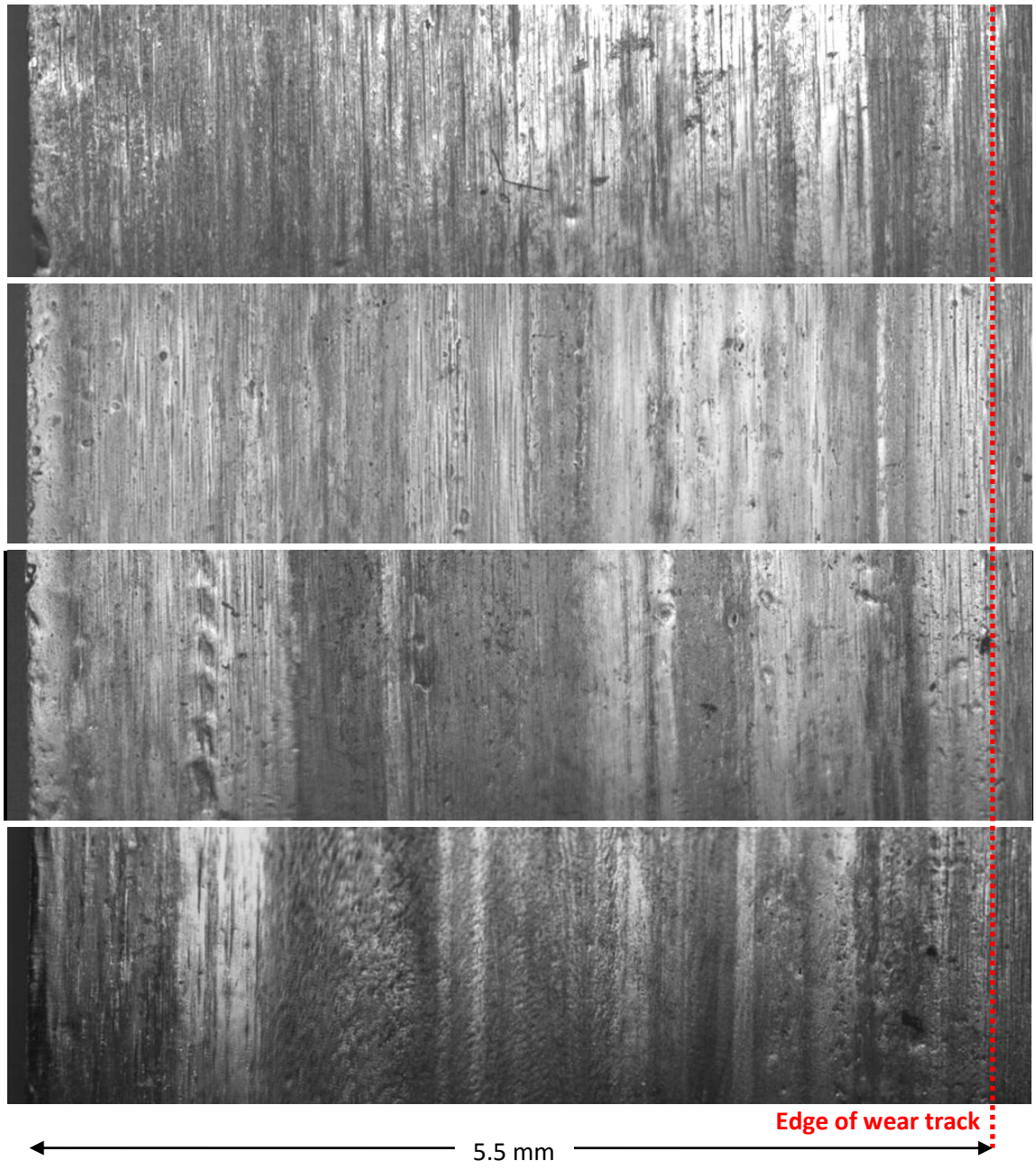


Figure 9-19: Wear tracks from SUROS discs 5-8

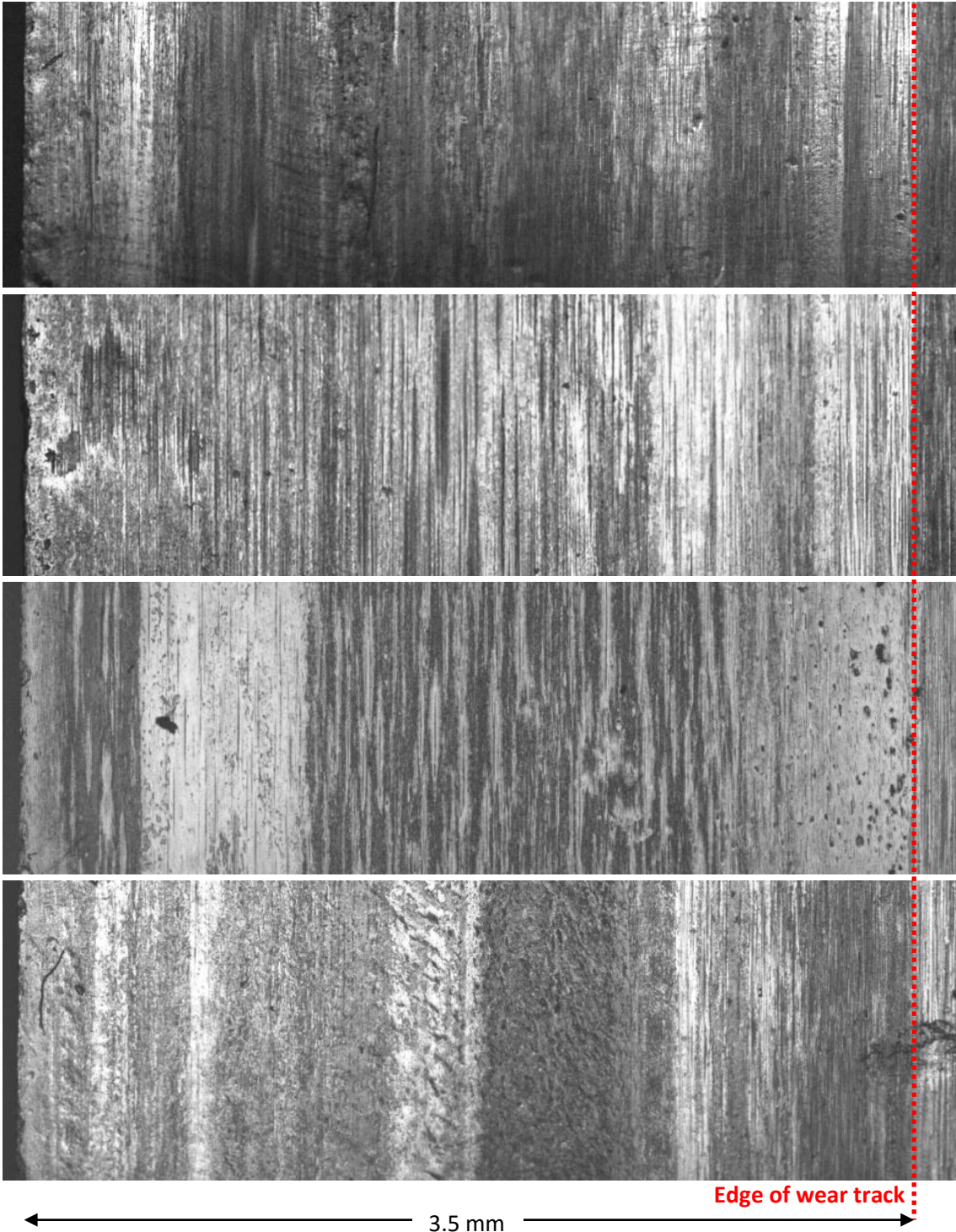


Figure 9-20: Wear tracks from SUROS discs 9-12

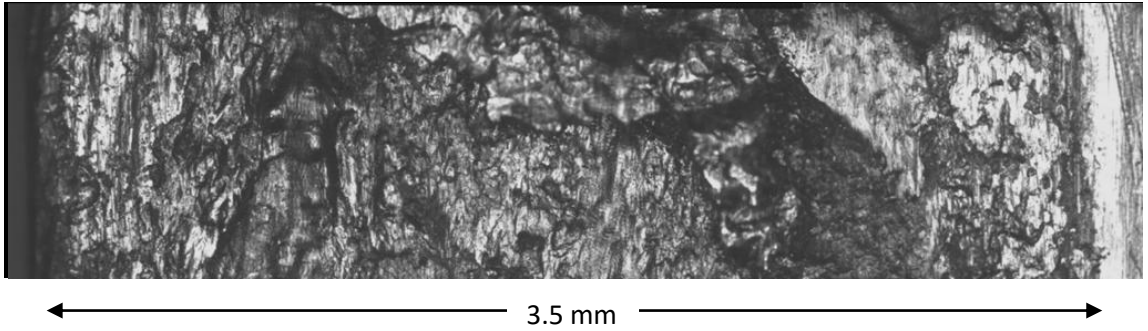


Figure 9-21: Wear track from failed test WEL producing SUROS disc